Numerical Study of Wall-Mounted Finite Span Wings

Jesse Lee Coombs

Faculty of Engineering, Computer and Mathematical Sciences
School of Mechanical Engineering
The University of Adelaide

A thesis submitted in fulfilment of the requirements for the degree of Doctor of Philosophy in engineering.

March 2017

Supervisors: Associate Professor Anthony C. Zander,
Associate Professor Con J. Doolan,
Dr. Danielle J. Moreau,
Dr. Laura A. Brooks

Submission date: November 7, 2016
Ammendment date: March 31, 2017

School of Mechanical Engineering
The University of Adleaide, 5055
South Australia, Australia

Typeset by the author using LaTeX
Printed in Australia.

Contents

List of Figures

List of Tables

Abstract

The extensive use of hydrofoils and airfoils in applications including domestic and military, air, water, and land vehicles, as well as air-conditioning and wind turbines, means that their design for minimally noisy and maximum aerodynamic performance, is not only an important issue for defence, but one with broader economic, health and environmental ramifications.

Wall-mounted finite span wing flows occur when a boundary layer developing on a surface encounters a hydrofoil or airfoil attached to that surface. Although fundamental to various engineering fields, there is a lack of insight into the underlying physics of these flows. Particularly important is the noise created by the complex flow structures associated with them.

The main objective of this work is to investigate the noise and associated flow structures of wall-mounted finite span wings and to develop noise prediction methods for these flows. A number of recent wall-mounted finite span wing experiments (Moreau et al., 2015; Moreau and Doolan, 2013) involving flat ended finite length wings attached to flat plates are simulated using three-dimensional Reynolds Averaged Navier Stokes (RANS) based methods, which provide greater insight into the complete flow structure than is available from the original experiments. The flow structures are observed and compared with experimental measurements. A flow topology model is developed to describe the observed tip vortex formation process for the zero angle of attack condition. Existing leading and trailing edge noise models that are suitable for predicting the noise from 2D airfoils are extended to be applicable for 3D airfoil applications, allowing spanwise variations in geometric and flow properties to be taken into account. Additionally, an isolated tip noise model is developed based on the size of the tip vortex obtained from RANS flow simulations. The developed noise models have been validated against experimental measurements and have been shown to agree well and thus provide a means for prediction of the noise produced by wall-mounted finite span wing flows. The increased understanding of the wall-mounted finite span wing flow structures and the increased capacity of the developed wall-mounted finite span wing flow noise modelling is expected to have applications in the design of airfoils and hydrofoils with improved aerodynamic and aeroacoustic performance.

Declaration

I certify that this work contains no material which has been accepted for the award of any other degree or diploma in my name, in any university or other tertiary institution and, to the best of my knowledge and belief, contains no material previously published or written by another person, except where due reference has been made in the text. In addition, I certify that no part of this work will, in the future, be used in a submission in my name, for any other degree or diploma in any university or other tertiary institution without the prior approval of the University of Adelaide and where applicable, any partner institution responsible for the joint-award of this degree. I give consent to this copy of my thesis when deposited in the University Library, being made available for loan and photocopying, subject to the provisions of the Copyright Act 1968. The author acknowledges that copyright of published works contained within this thesis resides with the copyright holder(s) of those works. I also give permission for the digital version of my thesis to be made available on the web, via the University's digital research repository, the Library Search and also through web search engines, unless permission has been granted.

Jesse Coombs

Acknowledgements

Thanks to my family, especially my mother, for all the many forms of support that I have been gifted.

I am indebted to my supervisors, Associate Professor Con J. Doolan, Associate Professor Anthony C. Zander, Dr. Laura A. Brooks, and Dr. Danielle J. Moreau, whose guidance, patience, and kindness, have been invaluable.

I am grateful also to Mr. Cristobal Albarracin Gonzalez, for his assistance, generally, and especially during the 3D-RSNM implementation phase.

My thanks to eResearch SA for use of the supercomputer facilities, as well as Andrew Hill and all the other eResearch SA staff for their instruction and assistance in making use of those facilities.

1 Introduction

Airfoils and hydrofoils, which will be referred to collectively as foils hereinafter, find extensive use in applications including domestic and military, air, water and land vehicles, air-conditioning and wind turbines. Therefore, their design for minimum noise and maximum efficiency is not only an issue of importance for defence, but also in broader economic and environmental areas.

Aviation traffic has been steadily increasing and is predicted to rise in the future (U.S. Department of Transportation Federal Aviation Administration Aviation Policy and Plans, 2011; Wenzel et al., 2015). Reducing fuel consumption through increasing the performance of airfoils is of economical and environmental concern. Along with the desire to reduce operating costs through reduction of fuel consumption, and in response to health concerns (Bronzaft et al., 1998; Kaltenbach et al., 2008) for those that live and work near airfields, noise reduction goals have been set (Lockard and Lilley, 2004). Achieving these goals is the subject of ongoing research and design work (Prats et al., 2011; Viswanathan et al., 2011).

Similarly to the aviation industry, fuel consumption reduction through increased efficiency is of concern to maritime industries. Noise reduction is an especially important consideration for military designs such as submarines (Defence Science and Technology Organisation, 2004).

The noise of electricity-producing wind turbines is one of the primary factors preventing their installation within close proximity to highly populated areas, and thus inhibits more widespread implementation (Rogers et al., 2006). Hence, akin to the situation in the aerospace industry, achieving noise reduction and increased efficiency of wind turbines is a subject of ongoing research.

The three aforementioned examples are part of a much broader trend, highlighting the kinds of benefits that could be expected to result from a better understanding of the flow and noise generated by airfoils.

Computational fluid dynamics (CFD) uses computers to perform calculations to numerically solve the equations which govern the behaviour of fluids to for fluid flow conditions such as velocity and pressure. CFD can be broadly categorised into three types of methods: Reynolds Averaged Navier-Stokes (RANS) methods, Large Eddy Simulation (LES) methods, and Direct Numerical Simulation (DNS) methods. These methods are listed in order of increasing accuracy, and also increased computational complexity. DNS results are extremely accurate, to the point of being considered equivalent to experimentally obtained results, and are obtained without the introduction of disturbances to the flow caused by some experimental measurement devices. However, the exceptionally large computing resources required, both in terms of total memory and processor time, to solve simulations of even the simplest flows, means that DNS and even LES are unsuitable for use in the design stage, given the current computing capabilities typically available to an industrial engineer. Because of this, almost all engineering CFD design utilises RANS methods.

RANS methods separate the flow conditions into average and fluctuating components. As a result of the Reynolds averaging process there are additional unknowns to solve for. A problem is said to be closed if there are enough known equations to solve for all the unknowns. In order to close the problem, and hence solve for the unknowns, additional equations are required. A turbulence model is a series of equations that provides a relationship between the various unknowns. There are many turbulence models in use, as no single model as yet provides uniformly superior results with minimal computational requirements for all flow situations. There are models of various complexities, and many have been refined for improved accuracy or suitability for a greater range of flow conditions over the course of their use. The evaluation of the relative and absolute performance of the various models for various flow conditions is an area of ongoing research. Improving the understanding and accuracy of turbulence models is not only of academic interest. A thorough understanding of the speed and accuracy of the various turbulence models is of immediate practical value due to their use in industrial design evaluation.

A possible method to achieve operational performance improvements in airfoils is by application of CFD to optimise their design. Such a process does, however, require computationally efficient and accurate modelling techniques to describe the flow, as well as any further parameters relevant to evaluating their performance. Therefore, it is of interest to determine the speed and accuracy of the turbulence models currently employed.

A wall-mounted finite span wing flow occurs when a boundary layer encounters a finite wing attached to the same surface. When the wing is considered to extend infinitely away from the wall, the flow is known as a junction flow. Due to the various aerodynamic and hydrodynamic applications in which wall-mounted finite span wing flows occur, being able to accurately model these flows and their features, as shown in Figure 1.1, is of immediate practical interest.

Despite the many applications in which wall-mounted finite span wing flows occur, there is insufficient understanding of the underlying physics of these flows. The present work contributes to this understanding, through observations of the tip vortex development process for flat ended wings, which are used to synthesise a tip vortex development flow topology model. The various noise sources in wall-mounted finite span wing flows include leading edge noise, turbulent boundary layer trailing edge noise, and tip noise. To ensure noise modelling can be part of an engineering design process, flow-induced-noise prediction methods must be both accurate and efficient. Hence it is necessary that the most effective noise modelling methods for the radiated sound of wall-mounted finite span wing flows be determined to assist those who need to analyse and design devices that incorporate them. Existing leading and trailing edge noise models that are suitable for predicting the noise from 2D airfoils are here extended to be applicable for 3D airfoils, allowing spanwise variations in geometric and flow properties to be taken into account. Specifically, the extensions developed and tested for surface pressure spectrum and RANS based statistical noise model methods for predicting trailing edge noise, as well as that for predicting leading edge noise based on the Amiet (1975) leading edge noise model, are novel noise prediction techniques for wall-mounted finite span wing flows.

The remainder of this document is structured as follows. Chapter 2 encompasses a literature review, as well as research gaps and project objectives. Chapter 3 details the numerical and noise modelling methodologies developed and used. Chapter 4 presents an investigation of the effectiveness of RANS based turbulence modelling for the junction region. Chapter 5 examines the behaviour of the proposed TE noise model developed in Chapter 3, validating it against a number of literature test cases. Chapter 6 presents an investigation into the flow and noise of a wall-mounted finite wing, providing insight into the tip vortex formation process as well as further validating the developed TE noise model on a case with 3D flow features. Chapter 7 proceeds to further validate the developed noise models against a series of experimental cases. Chapter 8 summarises the conclusions of the previous chapters, as well as suggesting avenues for future work.

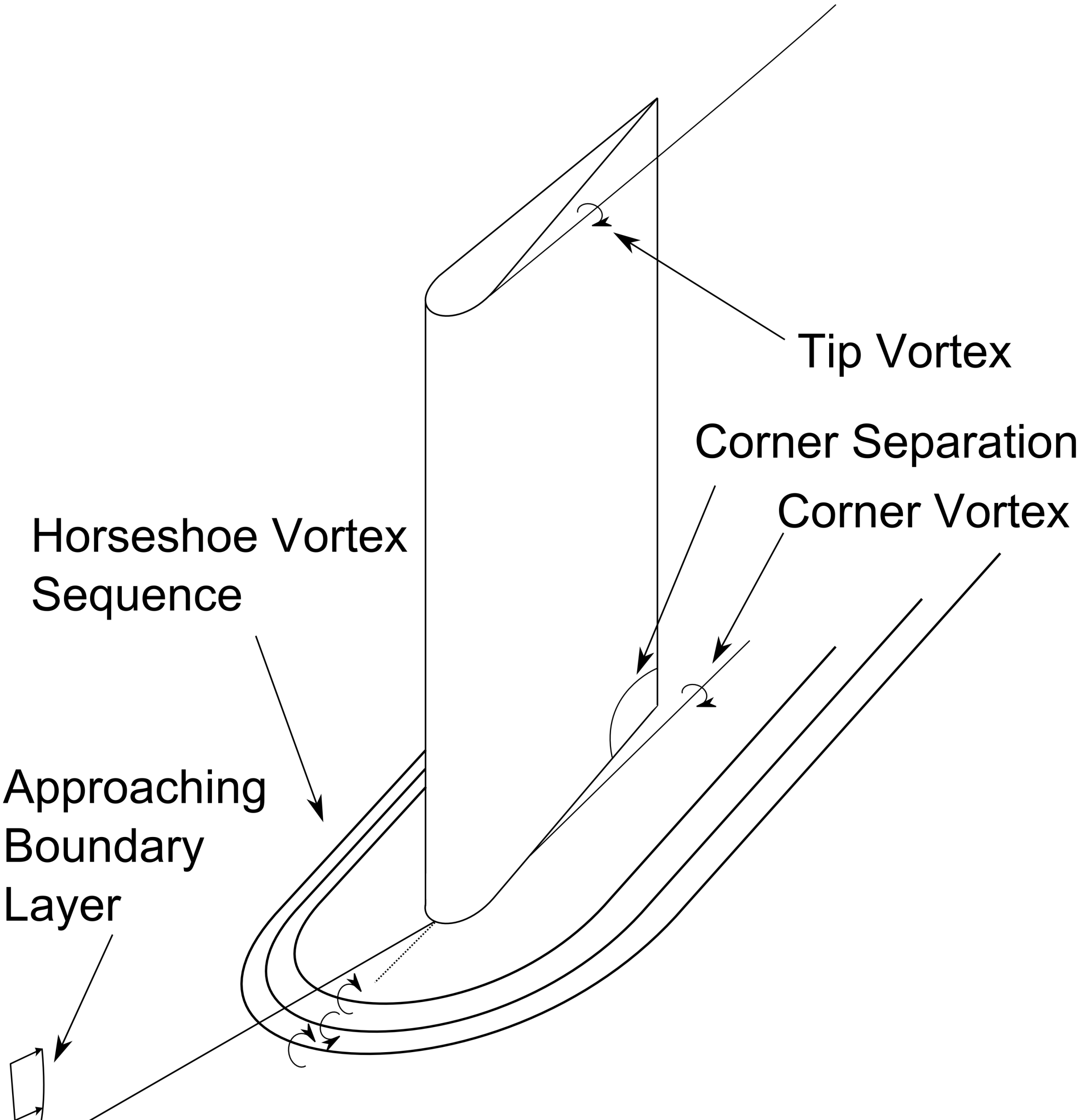

Figure 1.1: Schematic overview of a wall-mounted finite span wing flow, including horseshoe vortex, corner and tip vorticies.

1.1 Publications

Publications arising from this thesis are as follows:

J. L. Coombs, C. J. Doolan, D. J. Moreau, A. C. Zander, L. A. Brooks, "Assessment of turbulence models for a wing-in-junction flow", 18th Australasian Fluid Mechanics Conference, Launceston, Australia, 3 - 7 Dec, 2012.

C. J. Doolan, J. L. Coombs, D. J. Moreau, A. C. Zander, L. A. Brooks, "Prediction of noise from a wing-in-junction flow using computational fluid dynamics", Acoustics 2012, Fremantle, Western Australia, Australia, 21 - 23 Nov, 2012.

J. Coombs, C. Doolan, D. Moreau, A. Zander, L. Brooks, "Noise modelling of wing-in-junction flows", Acoustics 2013: Science, Technology and Amenity, Victor Harbor, South Australia, 2013.

D. J. Moreau, J. L. Coombs, C. J. Doolan, "On the Flow and Noise of a Two-Dimensional Step Element in a Turbulent Boundary Layer" In Y. Zhou, Y. Liu, L. Huang and D. Hodges (Eds.) Lecture Notes in Mechanical Engineering: Fluid-Structure-Sound Interactions and Control, pp. 225 - 230, Springer-Verlag, Berlin Heidelberg, 2014.

J. Coombs, B. Zajamsek, C. Doolan, Z. Prime, L. Brooks, D. Moreau, A. Zander, "Semi-empirical modelling of rotor aerodynamic noise", 3rd Symposium on Fluid-Structure-Sound Interactions and Control, Perth, Western Australia, 5 - 9 July 2015.

J. Coombs, C. Doolan, A. Zander, D. Moreau, L. Brooks, "Statistical estimation of trailing edge noise from finite wall-mounted airfoils", Acoustics 2016, Brisbane, Queensland, Australia, 9 - 11 Nov, 2016.

2 Literature Review

The current study involves investigation of wall-mounted finite span wing flows and their associated sound generation. This chapter reviews previous studies that are related to these subjects and is subdivided into seven sections. Section 2.1 gives an overview of wall-mounted finite span wing flows. Section 2.2 discusses turbulence modelling of wall-mounted finite span wings flows. The various junction flow noise mechanisms are introduced in Section 2.3, then discussed in detail along with methods for predicting the noise generated by these mechanisms in Sections 2.4, 2.5 and 2.6. Gaps identified within the literature reviewed in this thesis are detailed in Section 2.7.

2.1 Overview of Wall-Mounted Finite Span Wing Flow Features

Wall-mounted finite span wing flows exhibit complex flow structures due to the interaction of the incoming boundary layer with that developed by the flow obstructing body. Figure 1.1 illustrated the flow phenomena exhibited by wall-mounted finite span wing flows, including a horseshoe vortex sequence, tip and corner vortices, and corner separations. The relative strength and prominence of these features are known to be influenced by the flow Reynolds number, the relative bluntness and aspect ratio of the body, as well as properties of the incoming boundary layer (Khan et al., 1995; Fleming et al., 1991). The present work considers and limits itself to the discussion of turbulent junction flows; at lower Reynolds numbers the junction flow will be laminar. For a review of laminar junction flows, the reader is directed to Simpson (2001).

2.1.1 Horseshoe Vortex

A horseshoe vortex (or horseshoe vortex sequence) forms as a boundary layer approaches and interacts with an obstacle. The higher velocity flow from the top of the boundary layer flows down the obstacle face and then upstream, forming a vortex that is drawn around the obstacle into a necklace or horseshoe shape, after which the phenomenon is named. The horseshoe vortex, being linked to mean flow skew, is categorised as a secondary flow of the first kind according to Prandtl (Gand et al., 2010a). Depending on variables such as the incoming flow velocity, the incoming boundary layer height, as well as the geometry of the obstacle, the horseshoe vortex can occur as a single vortex with stationary position, a single vortex with significant oscillation of position, or a sequence of two or more vortices which may periodically merge and reform (Devenport and Simpson, 1990; Khan et al., 1995). Various authors (Shabaka and Bradshaw, 1981; Mehta, 1984; Brooks et al., 1989; Fleming et al., 1991) have found that the strength and location of horseshoe vortices are linked to the leading edge geometry. Fleming et al. (1991) proposed that this influence may be quantified by a quantity called the bluntness factor given by

$$BF = \frac{1}{2}\frac{R_0}{X_t}(\frac{t}{S_t} + \frac{S_t}{X_t}), \tag{2.1}$$

where t is the maximum thickness of the wing, which occurs at chordwise position X_t and at a distance from the leading edge along the airfoil surface S_t, while R_0 is the leading edge radius. A high bluntness factor is known to cause a strong horseshoe vortex while a low bluntness factor causes a weaker horseshoe vortex. Although a useful quantification, it is one that is not comprehensive as it does not take account of the angle of attack. At non-zero angles of attack, the flow typically encounters a leading edge of increased effective bluntness, and a stronger horseshoe vortex forms (Barber, 1987; Fleming et al., 1991). Wing sweep has also been found to influence the position of the horseshoe vortex (Rood and Anthony, 1985; Ahmed and Khan, 1995; Khan and Ahmed, 2002), with backswept wings exhibiting a vortex located nearer the leading edge and raised in the boundary layer. For forward swept wings the vortex is found further upstream.

Fleming et al. (1991) also proposed that the effect of the incoming boundary layer may be quantified by the momentum deficit factor

$$MDF = Re_t Re_{\theta_x}, \tag{2.2}$$

where Re_t and Re_{θ_x} are the Reynolds numbers based on wing thickness (t) and boundary layer momentum thickness (θ) at the location x where the MDF is calculated. Stronger horseshoe vortices are observed at higher momentum deficit factors.

2.1.2 Tip Vortex

Much work has been done investigating wing tip vortex formation and flow topology. Due to the relative ease of taking measurements in the wake, rather than in the immediate vicinity of the wing surface, many of the experimental studies are limited to measurements taken in the wake. A selection of the relevant literature, characterised by Reynolds number based on chord (Re_c) and angle of attack (AOA), is listed in Table 2.1. Many of the studies have used NACA 4-digit profile airfoils (Dacles-Mariani et al., 1995, 1996; Churchfield and Blaisdell, 2013; Chow et al., 1997; Srinivasan et al., 1988; Alsayed et al., 2010; Bailey et al., 2006; Duraisamy, 2005; Devenport et al., 1996; Jiang et al., 2008; Fleig and Arakawa, 2004; Malik, 2013; Giuni, 2013; Freymuth, 1993; Dacles-Mariani et al., 1993; Duraisamy et al., 2007; Brooks and Marcolini, 1986; Martin et al., 2003). At non-zero angles of attack for round ended tip geometries the tip vortex formation process and tip flow topology is reasonably well known, and has also been investigated for the flat-ended tip geometry. Other tip geometries have been investigated to a lesser extent, such as bevelled tips (Srinivasan et al., 1988); however, for these geometries, the tip vortex formation process and tip flow topology is not known.

The vortex formation process for non-zero angles of attack, for round ended tip geometries, is shown diagrammatically in Figure 2.1. Vortices with opposite rotational sense are referred to as contra-rotational, or counter-rotating, while those with the same rotational sense are known as co-rotational. The tip vortex formation process starts as flow is drawn around the tip from the pressure to the suction side. Near the leading edge, this process is achieved smoothly (Figure 2.1b); however, at or around the chordwise location of maximum thickness of the airfoil, the flow detaches from the surface. The exact location of the detachment shows significant dependence on airfoil thickness (Duraisamy, 2005). This has been attributed to a difference in pressure gradients resulting from the changing distance required to travel from the pressure to the suction side of the airfoil across the tip (Duraisamy, 2005). The detached flow rolls up as it completes the tip crossing and forms the primary tip vortex (Figure 2.1c). The crossflow velocity of the primary vortex near the airfoil surface induces outboard flow, which upon interaction with the primary vortex feeding sheet, forms into a secondary vortex which contra-rotates with respect to the primary vortex (Figure 2.1d). The secondary vortex then separates and is drawn into the primary vortex. In a similar process to the primary vortex, a tertiary vortex may form outboard of the secondary vortex which is contra-rotational to the secondary vortex (and hence co-rotational with the primary), which similarly lift, separate, and are drawn into the primary vortex further downstream (Figure 2.1e) (Giuni and Green, 2013).

Table 2.1: Tip flow literature operating conditions summary

Re_c Range	Tip Type †	AOA(s) [deg]	Investigation Type ⋆	Vortex observations	Other Notes / Salient Findings	Reference
4.6E6	R	10	E, N	Tip Vortex with secondary vortex		Dacles-Mariani et al. (1995)
1E6	R,F	4-12	E	Tip Vortex with secondary vortex		Anderson et al. (2000)
4.6E6	R	10	N	Tip Vortex with secondary vortex		Dacles-Mariani et al. (1996)
4.6E6	R	10	N	Primary Tip Vortex	Vortex turbulence properties very sensitive to turbulence model used	Churchfield and Blaisdell (2013)
4.6E6	R	10	E	Primary Tip Vortex		Chow et al. (1997)
1E6	R	N/A	N	Primary Tip Vortex	Bespoke wing with sweep, twist and taper	Mansour (1985)
2E6	F,O,R	5	N	Tip vortex and separate wake vortex sheet	Tip profiles significantly effect surface pressure profiles and vortex lift-off location	Srinivasan et al. (1988)
2.05E5	N/A	4	E	Single tip vortex		Alsayed et al. (2010)
2.4E5	F	8	E	Primary vortex with multiple secondary vortices		Bailey et al. (2006)
4.6E6	F,R	10	N	Primary vortex with secondary vortex		Duraisamy (2005)
5.3E5	F,R	2.5-7.5	E	Primary vortex with secondary vortex	Vortex core flow is laminar	Devenport et al. (1996)
4.6E6	R	10	N	Primary vortex with secondary vortex	Semi-infinite toward the root	Jiang et al. (2008)
4.06E5-2.87E6	R	0-11	N	Primary vortex and secondary vortex		Fleig and Arakawa (2004)
9.6E3-2.6E5	R	0-14.4	E	Primary vortex and secondary vortex		Brooks and Marcolini (1986)
6.9E5-1.4E6	F	0-10	E, N	N/A	No tip measurements; focus was junction flow	Malik (2013)
3.6E4-2.2E5	F	5-10	E	Primary vortex with multiple secondary vortices	Multiple secondary vortices	Shekarriz et al. (1993)
3000-12.7E5	F,R	0-20	E	#	Series of secondary vortices which are wrapped into the primary vortex	Giuni (2013)
5200	F	10-60	E	Primary vortex	Tip vortex seems to originate originate from front corner	Freymuth (1993)
4.6E6	R	10	N	Primary vortex and secondary vortex		Dacles-Mariani et al. (1993)
2.72E4‡	F	4.5	E, N	Secondary and tertiary vortices that result from crossflow separations near the blade tip		Duraisamy et al. (2007)
5E5	R	10	N	Tip Vortex with secondary and tertiary vortices		Uzun and Hussauni (2006)
1.2E6	R	12	N	Primary vortex and secondary vortex		Lombard et al. (2015)
2.72E5‡	F	4.5	N	Primary vortex and secondary vortex		Martin et al. (2003)
3.25E5	F	5 and 10	E, N	Single tip vortex	Excessive spatial dissipation of vortex, which increases with angle of attack	O'Regan et al. (2014)

† Tip Types are round ended (R), flat-ended (F), and other (O)

⋆ Investigation Types are experimental (E), numerical (N)

‡ Rotor measurement; Reynolds number based on tip velocity

For non-zero AOA: Tip vortex, as well as secondary and tertiary vortices. For 0 AOA with square and round ended tips: counter-rotating vortex pair, with the flat ended airfoil vortex pair having much greater intensity and possible weaker flanking pair of secondary vortices for the flat ended tip geometry.

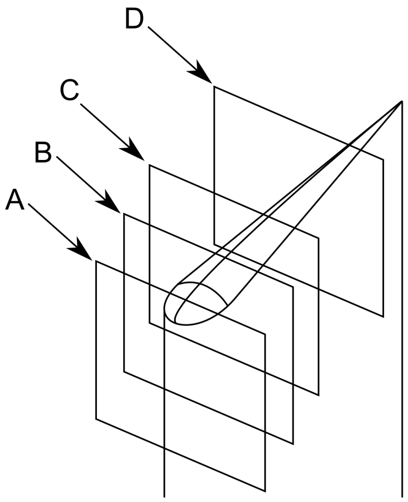

(a) Vortex development plane definition diagram

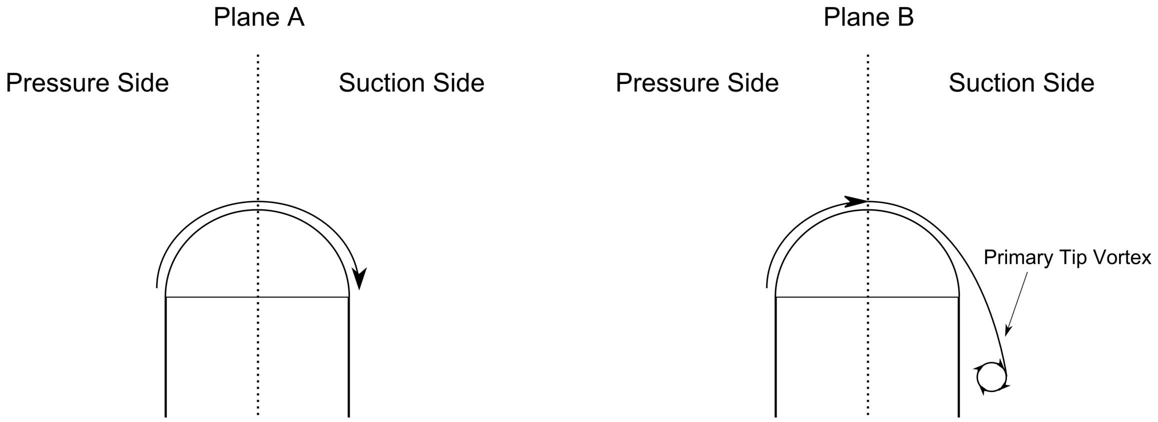

(b) Plane A (before chordwise location of maximum thickness)

(c) Plane B (at or about the chordwise location of maximum thickness)

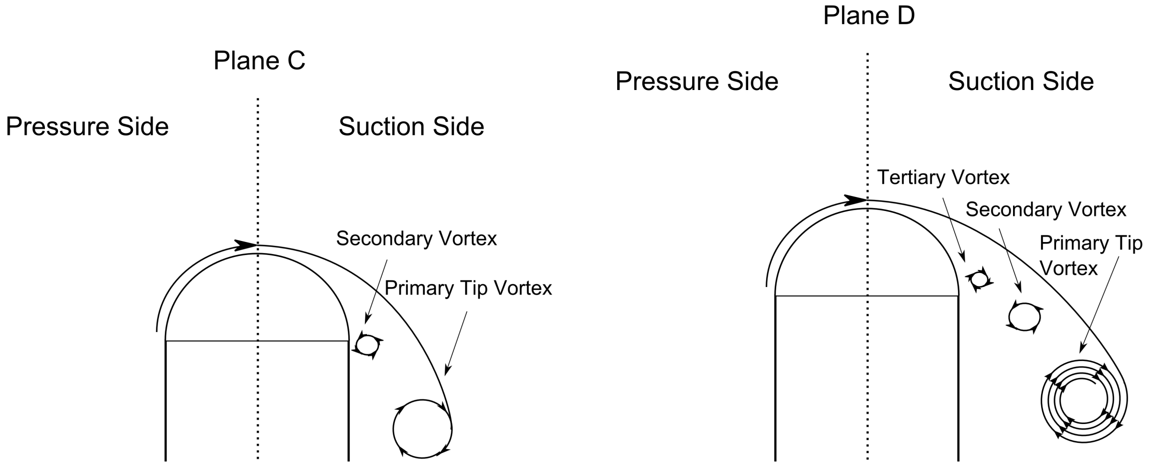

(d) Plane C (slightly downstream of the chordwise location of maximum thickness)

(e) Plane D (further downstream of the chordwise location of maximum thickness)

Figure 2.1: Round ended airfoil at non-zero AOA vortex formation process diagram.

Due to unfortunate naming conventions, a purely textual description of the flat-ended tip vortex formation process at non-zero AOA can be rather difficult to follow, and the reader is referred to Figure 2.2 to minimise confusion. For a flat-ended tip geometry, a pair of contra-rotating vortices, designated the leading vortex pair, are developed on the tip surface by inflow around the tip edge from both the pressure and suction sides crossing around the tip before the point of maximum wing thickness (Figure 2.2b). At or about the point of maximum wing thickness (Figure 2.2c), in a manner analogous to side tip vortex formation seen in simple circular cylinder tip flows, a second set of vortices develop; however, this pair of vortices are co-rotational. This pair of vorticies, referred to as side vortices, have a rotational sense corresponding to bulk flow being drawn from the pressure to suction side (Duraisamy, 2005). The suction and pressure side leading vortex pair both separate from the surface and form an additional set of contra-rotating (to each other as well as the leading vortex to which they owe their formation) secondary vortices, known as separation vortices (Figure 2.2d). From this point the pressure side separation vortex is increasingly suppressed as the co-rotational pressure side leading vortex merges with the pressure side side vortex. While on the suction side, the leading vortex is lifted further, until the suction side separation vortex and suction side side vortex merge, forming the tip primary vortex core, analogous to the primary vortex seen in the round ended airfoil tip vortex formation process. Just as in the round ended airfoil tip vortex formation process, the now merged suction side vortex (SSiV) and suction side separation vortex (SSeV) have crossflow velocity near the airfoil surface which induces outboard flow. The outboard flow causes the formation of a secondary vortex (Figure 2.2e). It is unknown if a contra-rotational tertiary vortex is caused by the detachment of the secondary vortex as it is drawn into the primary tip vortex. Finally, the tip primary vortex continues to separate from the corner, being fed by the merged pressure side leading vortex and side vortex which stretches to become analogous to the feeding sheet from the round ended tip topology (Figure 2.2f).

Summarising the information from Table 2.1 in terms of tip type and angle of attack results in Table 2.2, which highlights that although the vortex formation process is relatively well-understood for round ended and flat tips when at angles of attack, it has not been comprehensively reported on for flat ended tips when at zero angle of attack. Giuni and Green (2013) observed vortices in the near wake when at zero angle of attack, however there has been no detailed investigation into their formation process or the tip flow topology.

The bulk of the numerical studies have used time-averaged methods. However, Lombard et al. (2015) makes use of LES to investigate the wing tip vortex of a round-ended NACA 0012 profile airfoil at a Reynolds number, based on wing chord and freestream velocity, of 1.2×10^6 and angle of attack of 10 degrees, following the experimental work of Chow et al. (1997). However

Table 2.2: Tip vortex formation process knowledge

Airfoil tip type	Zero AOA	Non-zero AOA
Round ended tips	Brooks and Marcolini (1986) Fleig and Arakawa (2004) Giuni and Green (2013)	Dacles-Mariani et al. (1993), Churchfield and Blaisdell (2013) Chow et al. (1997), Srinivasan et al. (1988) Duraisamy (2005), Jiang et al. (2008) Fleig and Arakawa (2004), Brooks and Marcolini (1986) Giuni and Green (2013), Dacles-Mariani et al. (1993) Duraisamy et al. (2007), Uzun and Hussauni (2006) Devenport et al. (1996), Lombard et al. (2015) Anderson et al. (2000)
Flat ended tips	Giuni and Green (2013)	Srinivasan et al. (1988), Bailey et al. (2006) Duraisamy (2005), Devenport et al. (1996) Giuni and Green (2013), Shekarriz et al. (1993) Freymuth (1993), Martin et al. (2003) O'Regan et al. (2014), Anderson et al. (2000)

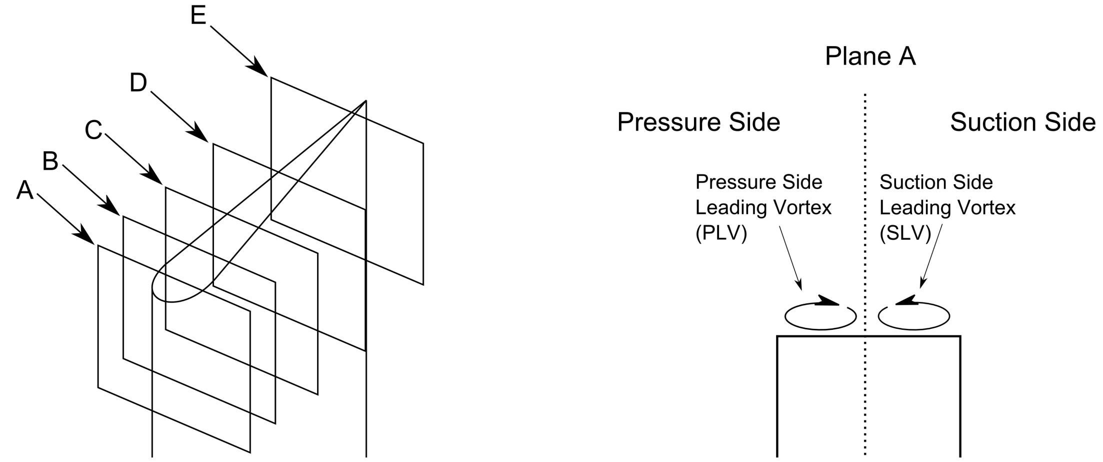

(a) Vortex development plane definition diagram

(b) Plane A (before chordwise location of maximum thickness)

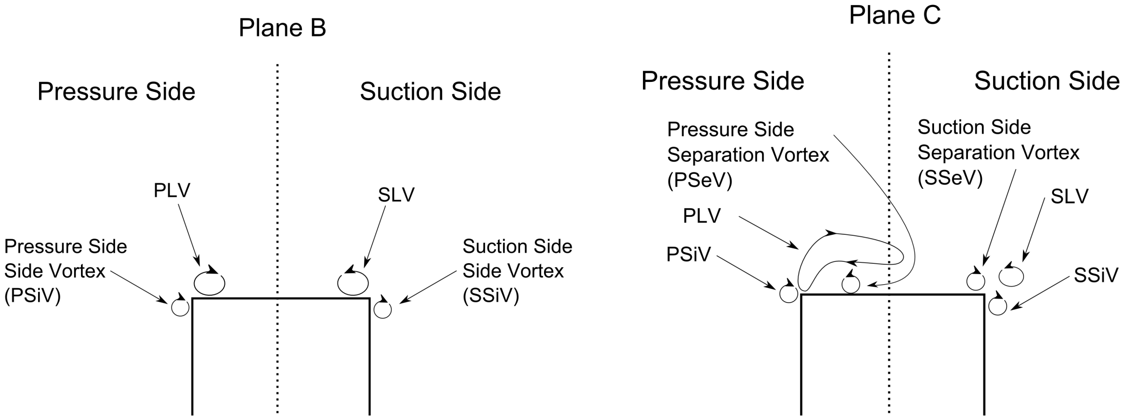

(c) Plane B (at or about the chordwise location of maximum thickness)

(d) Plane C (slightly downstream of the chordwise location of maximum thickness)

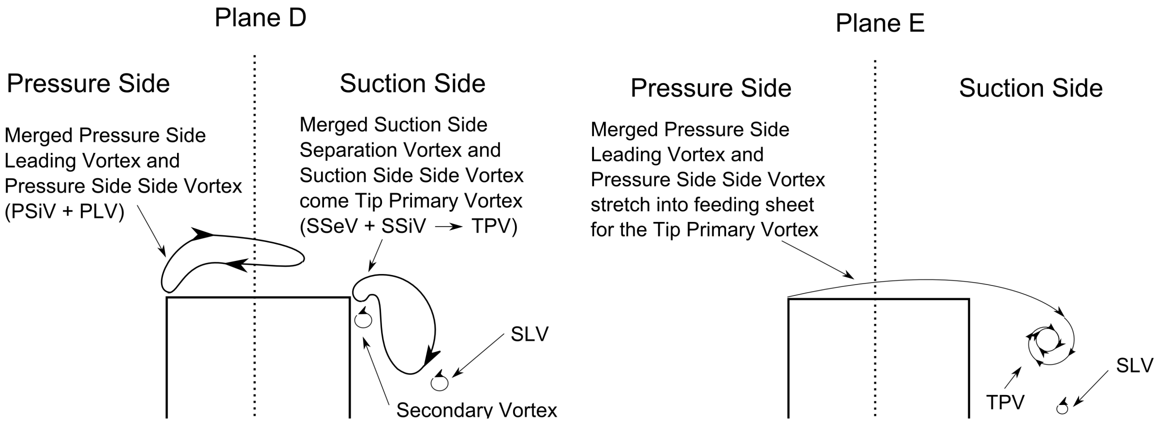

(e) Plane D (moderately downstream of the chordwise location of maximum thickness)

(f) Plane E (furthest downstream of the chordwise location of maximum thickness)

Figure 2.2: Flat-ended airfoil at non-zero AOA vortex formation process diagram.

Lombard et al. (2015) simplifies the problem by neglecting the boundary layer on the wall-mounting and instead uses a free slip condition on that boundary. Primary and secondary tip vortices were captured using the method. The properties of the secondary vortex were similar to those measured by Chow et al. (1997) along the length of the wing, but the secondary vortex properties did not find such good agreement in planes downstream of the wing (that is to say in the wake), which was attributed to inadequacy in the modelling of the interaction between the primary and secondary vortex.

2.1.3 Corner Vortex and Separation

Gessner (1973) experimentally investigated the flow between two perpendicular flat plates. Vortices induced by the interaction between the boundary layers of the two plates were observed. Gessner (1973) proposed a model to explain such separation, attributing corner vortex formation to gradients in Reynolds stresses, a finding supported by other investigations into corner flow between flat plates (Bragg, 1969; Nakayama and Rahai, 1984; Kornilov and Kharitonov, 1984). This means that corner vortex formation, being linked to gradients in Reynolds stresses, is categorised as a secondary flow of the second kind according to Prandtl. Gand et al. (2010b) proposed that the parallels between corner vortices and corner separations suggests that corner separations may also be secondary flows of the second kind according to Prandtl.

Based on flow visualisation of rectangular prism junction flows, Barber (1987) proposed a model linking horseshoe vortex development and that of corner separation. Barber (1987) suggested that larger, stronger, horseshoe vortices will draw higher momentum flow into the corner than would be otherwise present. The higher momentum fluid is better able to sustain the adverse pressure gradients without separating, and so produces a smaller corner separation.

It is known that the downstream evolution of the horseshoe vortex is influenced by flow angle of attack such that the suction side leg moves away from the wing as angle of attack increases (Gand et al., 2010a). At a greater distance, the vortex will have less of a stabilising effect and corner separation would be expected to increase. However, at increasing angle of attack the adverse pressure gradient would also increase, making it difficult to determine which factor is more significant.

The experimental study of Gand et al. (2015) found that increasing angle of attack results in progressive growth of the corner flow separation. Segregation of the effects of incoming boundary layer and Reynolds number on the flow found that corner flow separation strength increases for increasing Reynolds number, and that thickening of the incoming boundary layer results in a delayed, but larger, separation bubble.

2.1.4 Aspect Ratio and Boundary Layer Effects on Wall-Mounted Finite Span Wing Flow Structure

For wall-mounted square cylinders, it is known that as the incoming flat plate boundary layer increases it strengthens the base vortex, as well as increases the upwash from the obstacle base, and weakens the tip vortices (Wang et al., 2006); and that this effect is especially influential on the flow structure for very low aspect ratios. Similar effects could reasonably be expected for wall-mounted finite span airfoils, where at sufficiently low aspect ratios, extensive interaction between the base horseshoe and tip vortex structures would be anticipated, however, this has not been extensively investigated in terms of the effect on the flow. Although the influence of very low aspect ratio has not been investigated in terms of flow, Moreau et al. (2014) noted tonal noise generation suppression for airfoils of sufficiently low aspect ratios, and attributed this to the combined influence of junction and tip flow features.

The most pronounced effects of the boundary layer on wall-mounted finite span wing flow are by means of its known effects on the horseshoe vortex strength and position, and this was discussed in detail in Section 2.1.1.

2.1.5 Junction Flows Subject To Pressure Gradients

A favourable pressure gradient occurs when static pressure increases in the direction of the flow and conversely for adverse pressure gradient. Favourable pressure gradients (FPG) and adverse pressure gradients (APG) are encountered in a range of engineering applications, yet most wing-in-junction flow studies have been performed in zero pressure gradient (ZPG) flows. AGPs and FPGs are known to cause changes to boundary layer development, and properties such as mean velocities, turbulence production, and intensities, as well as skewness and inclination angle. For example, turbulent boundary layer skewness and flatness (Harun, 2012) are known to increase in an AGP, as does inclination angle (Krogstad and Skåre, 1995), while inclination angle decreases in an FGP (Dixit and Ramesh, 2010). Similarly turbulence production is known to increase in APG and decrease in FPG flows. The effect of pressure gradients on velocity and turbulence properties, such as two point space–time correlations (Krogstad and Skåre, 1995), could have significance for noise prediction models, due to many models being constructed based upon assumptions for ZPG flows. The effect of pressure gradient on approaching wall boundary layer as well as that on the wing, may in turn influence wing-in-junction flow structure due to changing the boundary layer to aspect ratio as discussed in Section 2.1.4. However, as investigation of streamlined wing-in-junction flows has concentrated on ZPG flows, these effects have not been reported in the literature.

2.2 CFD Modelling of Wall-Mounted Finite Span Wing Flows

Owing to the reduced computational requirements when simulating only the wing-wall junction region or only the tip region, many studies limit themselves to considering only one of these, rather than considering both. A selection of the computational studies involving tip flow from the literature were presented in Table 2.1 and discussed with reference to tip vortex formation in Section 2.1.2. What follows is a selection of the computational studies involving only the junction region.

Devenport and Simpson (1990) experimentally investigated the flow structure in the plane of symmetry upstream of the leading edge of the junction region of a ‘Rood’ wing mounted orthogonally to a flat plate, as shown in Figure 2.3. Their experiments revealed the oscillating but stable time dependent structure of the horseshoe vortex system that forms in the leading edge region. A number of subsequent studies of the same geometry (Fleming et al., 1991, 1993; Olcmen and Simpson, 1995b,a, 2006) further expanded locations where measurements were taken as well as the types of measurements taken, providing velocity and turbulence profiles not only along the upstream and downstream symmetry plane, but also in planes perpendicular to the plate and chord. Due to the extensive experimental measurements available, including detailed inlet flow conditions, as well as its geometric simplicity, reproduction of the Devenport and Simpson (1990) experiment proved to be an attractive case for investigating the performance of turbulence models on wing-in-junction flows. The 3D nature of the flow, and its inclusion of various flow features, such as the horseshoe vortex, make the Devenport and Simpson (1990) flow case a rich testing ground for RANS turbulence models. The case was adopted as the European Research Community On Flow Turbulence And Combustion (ERCOFTAC) case 08 of the 4th Workshop on Refining Flow Modeling (Bonnin et al., 1996), allowing for effective comparison between investigators, as all would be using the same specified boundary conditions. As a result of this, there have been many computational investigations of turbulence models undertaken for this case, comparing the results not only between each other, but also with the experimental measurements (Paciorri et al., 2005; Paik et al., 2007; Apsley and Leschziner, 2001; Chen, 1995; Devenport and Simpson, 1992; Parniex et al., 1998; Fu et al., 2007; Wong and Png, 2009). A selection of the literature relating to turbulence modelling of wing-in-junction flows is summarised in Table 2.3.

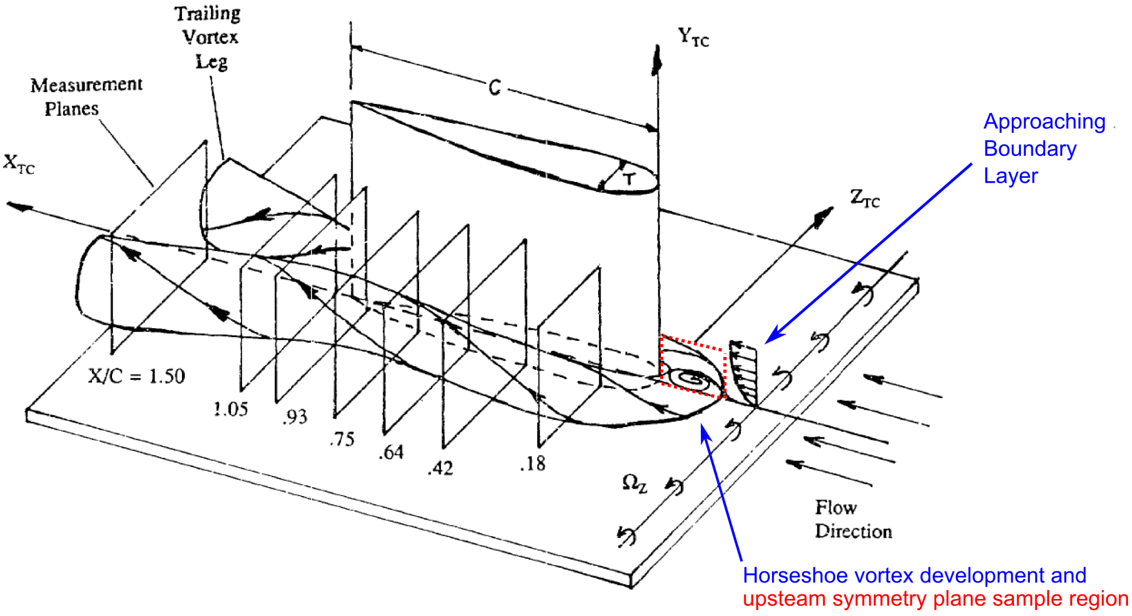

Figure 2.3: Devenport and Simpson (1990) experiment diagram, adapted from Fleming et al. (1993)

Table 2.3: CFD modelling of wing-in-junction flows literature operating conditions summary

Re_c	AOA(s)	Geometry	Base Experiment	Methodolgy(ies)	Salient Observation(s)	Reference
$\approx 5E5$	0	Rood Wing	Devenport and Simpson (1990)	RANS	Excessive production of eddy viscosity resulted in predicted horseshoe vortex that was smaller than that observed experimentally.	Paciorri et al. (2005)
$\approx 5E5$	0	Rood Wing	Devenport and Simpson (1990)	DES	DES like previous RANS results, predict plate pressure coefficient minima before wing maximum thickness location.	Paik et al. (2007)
$\approx 5E5$	0	Rood Wing	Devenport and Simpson (1990)	RANS	ALL models predict plate pressure coefficient minima before wing maximum thickness location. The Reynolds Stress Transport models produce better results than the majority of the linear and non-linear eddy viscosity models.	Apsley and Leschziner (2001)
$\approx 5E5$	0	Rood Wing	Devenport and Simpson (1990)	RANS	The RSMT model captured the appendage root vorticies, as well as the primary and secondary horseshoe vorticies.	Chen (1995)
$\approx 5E5$	0	Rood Wing	Devenport and Simpson (1990)	RANS	The V2F turbulence model, much more accurately than k-epsilon model results reported, predicts the right damping of turbulent transport in the horseshoe vortex region.	Parniex et al. (1998)
$\approx 5E5$	0	Rood Wing	Devenport and Simpson (1990)	RANS, DES, DDES	The DES approach resulted in flow separation, as well as vortex formation and breakdown occuring too early. DDES approach improved this.	Fu et al. (2007)
$\approx 5E5$	0	Rood Wing	Devenport and Simpson (1990)	LES	Of the LES models investigated the Dynamic Smagorinsky best captured the horseshoe vortex	Wong and Png (2009)
$3E5$	12	NACA0015	Bordji et al. (2014)	RANS	The unmodified Spalart-Allmaras model massively overpredicted the corner separation region, when modified with the quadratic constitutive relationship junction flow features were more effectively captured.HSV and corner vortices observed, and interactions between them and the wing boundary layer and wing skin friction respectively highlighted.	Bordji et al. (2014)
$2.8E5$	7, 10	NACA0012	Gand et al. (2010a)	RANS and LES	RANS unlike the LES, poorly predicted corner separation, however, RANS modelling was effective at studying the sensitivity for variations in the incoming boundary layer and angle of attack	Gand et al. (2010a)
$\approx 5E6$	0	DLR-F6 model aircraft	AIAA Drag Prediction Workshop	RANS	Primary tip vortex seen, quadratic constitutive relation improves prediction of corner separation	Yamamoto et al. (2012)
$\approx 5E6$	0	DLR-F6 model aircraft	AIAA Drag Prediction Workshop	RANS	Model with quadratic constitutive relationship is less sensitive to mesh refinement in the junction region than without	Dandois (2014)

Paciorri et al. (2005) computationally reproduced the Devenport and Simpson (1990) experiment as a semi-infinite wing using the Spalart-Allmaras and Lam and Bremhorst turbulence models on both structured and unstructured meshes. It was the only study of this case to the Author's knowledge that uses both structured and unstructured meshes, and found negligible differences between the results of the two. The Spalart-Allmaras model was found to significantly underpredict the intensity of the recirculation region upstream of the wing.

Apsley and Leschziner (2001) also computationally modelled the Devenport and Simpson (1990) experiment as a semi-infinite wing, using twelve turbulence models. All of the models investigated predicted the location of the region of lowest pressure coefficient on the plane surface to be upstream of, rather than at, the maximum thickness location of the wing as found in the experiment. This result is significant insofar as it suggests that such discrepancies are not due to the specific turbulence model selected, but rather due to some other aspect of the modelling process that is currently unknown. Of the turbulence models investigated by Apsley and Leschziner (2001), it should be mentioned that the $k - \epsilon$ model underpredicted the extent of the recirculation region in the upstream symmetry plane, and failed to accurately predict the turbulent kinetic energy intensity and distribution. The $k - \omega$-SST model overpredicted the downstream extent of the recirculation region, and also reduced the region height relative to the experimental results. The SST model did, however, do a much better job of predicting both the distribution and intensity of the turbulent kinetic energy. Similar results for the $k - \omega$-SST turbulence model were obtained by Fu et al. (2007).

Other computational results of Chen (1995); Parniex et al. (1998), and Devenport and Simpson (1992) showed generally good agreement with those of the experiment, with the more complex differential stress models performing best, although all models failed to predict the correct location of the region of lowest pressure coefficient on the flat plate around the wing.

As with the RANS turbulence modelling discussed above, LES of wall-mounted finite span wing flows has concentrated on the base of the junction, attempting to capture the horseshoe vortex rather than the tip region. Fu et al. (2007); Paik et al. (2007), and Wong and Png (2009) extended previous work by computationally reproducing the Devenport and Simpson (1990) experiment using not only RANS methods, but also time dependent delayed, standard direct eddy, and large eddy simulation methods respectively. Time dependent methods have been seen to more accurately capture flow features such as corner separation as well as better predict the flow and turbulence properties than equivalent RANS solutions. A significant portion of the improvement is attributed to time dependent methods being able to capture oscillation and merging processes for horseshoe vortex systems (Gand et al., 2010a; Fu et al., 2007; Paik et al., 2007). These studies all modelled the airfoil as semi-infinite away from the wing root, and although there are numerous LES investigations for finite square and circular cylinder junction flows of various aspect ratios, as well as LES of spanwise sections of true wing shapes, no full time dependent flow solutions of a wall-mounted finite span wing flow have been reported in the literature.

Corner vortex formation, being linked to gradients in Reynolds stresses, is not expected to be 'reproduced by any turbulence model that uses an isotropic eddy viscosity' (Bradshaw, 1987). Capturing such behaviours with time averaged methods requires the use of nonlinear eddy viscosity models or Reynolds stress models (Bradshaw, 1987; Speziale, 1987). Rather than introducing additional differential equations, such as is done in Reynolds stress models, it is possible to convert linear eddy viscosity models based on the Boussinesq assumption by means of nonlinear relations for the Reynolds stress. A method for doing so was proposed and applied by Spalart (2000), to adapt the Spalart-Allmaras turbulence model (Spalart and Allmaras, 1994). The result was found to significantly increase the accuracy of prediction of corner flow for a square duct over the base model. The method received little further attention until Yamamoto et al. (2012) used it on the DLR-F6 wing/body configuration used in the Second and Third Drag Prediction Workshops (Laflin et al., 2005; Vassberg et al., 2008), whereupon it has found a resurgence of interest. For example Dandois (2014) and Togiti et al. (2014) both used the method not only with the Spallart-Allmaras model but also with the $k-\omega$ SST model (Menter, 1994) on external flows. They found significant improvement over the original linear models, with the work of Dandois (2014) also applying the method to an internal flow, and again finding improvement over the base models. In comparing LES and RANS simulations with experimental measurements of the case, Gand et al. (2010a) found that although corner separation was not observed in the experimental measurements and LES simulation, that it was observed in the RANS simulation, even with a Reynolds stress turbulence model.

2.3 Wall-Mounted Finite Span Wing Flow Noise Components

Wall-mounted finite span wing flows may exhibit a number of noise production mechanisms, including leading edge noise, turbulent boundary layer trailing edge noise (TBL-TE), and tip noise. Depending on Reynolds number, angle of attack, as well as the airfoil geometry, other noise production mechanisms may also be present. At low to moderate Reynolds numbers, airfoil tonal noise can be a significant contributor to total noise, while at sufficiently high angles of attack and for certain airfoil trailing edge geometries respectively, stall-separation noise and bluntness-vortex-shedding noise may also make significant contributions. The present work considers sufficiently high Reynolds numbers, moderate angles of attack, and sharp trailing edged airfoils, such that the tonal, stall-separation and bluntness-vortex-shedding noise mechanisms are not relevant to the present discussion.

Owing to the more numerous and complex measurements and analysis required, segregating the various components from the total noise can be challenging. Therefore, the bulk of the previous investigations have focused on isolating a single noise component under the simplest conditions conceivable, which is often that of a 2D wing-flow condition. The work of Brooks et al. (1989) investigated the flow and noise generated by NACA0012 profile wings, in both 2D airfoil sections as well as those with a rounded end tip configuration. The study concentrated on the effects of Reynolds number, angle of attack and wing aspect ratio. The study resulted in increased understanding of the levels and directionality, as well as the development of noise prediction models for many of the noise production mechanisms.

Although many studies have concentrated on 2D wing-flow conditions, investigations of noise from wall-mounted finite span wing flows is not unheard-of. The work of Kendall (1978), in examining the noise produced by a wall-mounted NACA0012 airfoil, with semi-circularly rounded free end, with aspect ratio of 2.3 at a chord based Reynolds number of 2.8×10^5 and angles of attack ranging from 0 to 13 degrees, found the dominant noise sources to be a concentrated source located about the corner of the airfoil tip and trailing edge, as well as line sources observed along the trailing and leading edges. At the lowest frequencies reported, both the TE line source and tip-TE sources are apparent. As the frequency considered increases, the TE line source diminished, leaving only the tip-TE source, and at the highest frequencies reported, the tip source moves from the tip-TE to the midspan, and the leading edge line source becomes apparent. Kendall (1978) notes that the localisiation of the sources may be misleading of their actual extent, and that they are much more localised than in the presented results, due to limitations imposed on the measurement by the resolution of the acoustic mirror used when taking the directional measurements. Also worthy of mention is that Kendall (1978) suggests that the leading edge line source may not be due to the wall-mounted finite span wing flow, but rather may have been caused by in-flow fan noise.

The studies of Moreau et al. (2015) and Moreau et al. (2014), through the use of beamforming sound mapping, investigated the spectral and spacial contributions of wall-mounted finite span wing noise sources. Flat ended NACA0012 profile airfoils were used, with aspect ratios ranging from 0.2 to 3, and angles of attack from 0 to 12 degrees at chord based Reynolds numbers ranging from 9.2×10^4 to 1.6×10^6 were investigated. Agreement is seen with the results of Kendall (1978) in that at lower frequencies the dominant noise sources are a line source along the TE, as well as an additional source from the tip-TE, and that the tip noise source becomes dominant as the frequency considered is increased. Further analysis and discussion of the segregation of the various components presented in the results of Moreau et al. (2015) is conducted in Section 7.4.1.

What follows is a discussion of the individual noise production mechanisms present for wall-mounted finite span wing flows, as well as the prediction and modelling of the more significant components.

2.4 Turbulent Boundary Layer Trailing Edge Noise and Modelling

Turbulent boundary layer trailing edge noise is attributed to the interaction between flow turbulence created in the boundary layer of an airfoil, with the airfoil trailing edge. The airfoil trailing edge acts as an acoustic impedance discontinuity, from which a sound wave is scattered. This acoustic diffraction enhances the sound radiation occurring at the trailing edge, and was first addressed by Ffowcs-Williams and Hall (1970). Howe (1999) argued that rather than the surface pressure at the trailing edge, the trailing edge boundary layer ‘upwash’ velocity was the appropriate metric for determining trailing edge noise. Turbulent boundary layer trailing edge noise is one of the most significant noise production mechanisms for airfoil self noise in low Mach number, high Reynolds number conditions, and as such has received commensurate literature attention. On a theoretical basis, trailing edge noise is usually predicted using one of two alternative procedures. The first approximates the trailing edge as a semi-infinite rigid plate, which diffracts the boundary layer turbulence. The second uses the Lighthill (1952) acoustic analogy theory in combination with a Green’s function tailored to the trailing edge geometry to compute the far field noise from the vorticity in the edge flow. An alternative to predicting trailing edge noise, is with an empirical method. Empirical and semi-empirical methods attempt to model the TBL-TE noise based on geometric and/or flow properties. What follows is a more detailed discussion of these varied trailing edge noise prediction methods.

2.4.1 Empirical and Semi-Empirical Methods

The majority of trailing edge noise empirical and semi-empirical prediction methods may be thought of as falling into one of two categories, direct empirical methods, which attempt to use scaling arguments to predict the far field noise, such as the model of Brooks et al. (1989), and those that attempt to model the surface pressure spectrum near the TE and then propagate that to the far field using methods such as those of Amiet (1975) or Howe (1978).

Brooks et al. (1989) developed an empirical turbulent boundary layer trailing edge noise and separated flow model for predicting turbulent trailing edge noise for airfoils, often referred to as the 'BPM model', based on a series of experimental measurements on NACA 0012 profile airfoils covering a range of angles of attack and Reynolds numbers. The BPM model has found extensive use due to not only the relative simplicity of its formulation, but also because it requires only the geometric properties of the airfoil, the bulk flow velocity and angle of attack as scaling parameters. Other empirical models for turbulent trailing edge noise include those of Schlinker and Amiet (1981) and Fink (1979). All of these empirical models suffer from the limitation of only being valid for limited wing geometries, as well as limited angles of attack and Reynolds number ranges. However, such limitations are also common for the more complex surface pressure spectrum models. Although originally developed under the assumption of uniform spanwise geometric and flow properties, the BPM model is commonly applied to wings with non-uniform geometric and flow properties, by means of considering the wing to be composed of a number of spanwise sections with assumed uniform properties, applying the method to each section, and then summation of the results (Leloudas et al., 2007). Further detail of the BPM model, as well as its implementation and validation for the current study, is included in Section 3.5.

A popular type of semi-empirical method for predicting trailing edge noise is by means of surface pressure spectrum modelling. These models attempt to relate flow and geometric properties to a surface pressure spectrum at the trailing edge of the obstacle. The pressure spectrum at the trailing edge is then used to predict the far field noise by means of a propagation model. There exists a large number of different surface pressure spectrum models, including those of Herr et al. (2010); Goody (2004); Chase (1987); Smol'Yakov and Tkachenko (1991); Rozenberg (2007); Schlinker and Amiet (1981); Parchen and TNO-TH (1998).

A limitation of many of the earlier models based on measurements taken using flat plates is that they fail to account for the effects of adverse pressure gradients. Schlinker and Amiet (1981) attempted to generate a correction to account for such pressure gradient effects, however the correction does not take into account pressure gradients of varying strength, because the correction factor is constant. Rozenberg (2007) developed a more general method, which attempts to account for pressure gradients of varying strength. Although promising, the method requires evaluation of the wake's law parameter (Coles, 1956), which does not always have a solution. The predicted trailing edge surface pressure spectrum may then be used to determine the far field noise by means of methods such as those of Amiet (1975) or Howe (1978). A common limitation of these surface pressure spectrum methods is the assumption of uniform spanwise flow and geometric properties. Rozenberg (2007), using the Amiet (1975) far field propagation method, showed how the assumption of uniformity of spanwise geometry and flow properties may be overcome by considering the wing to be composed of a number of spanwise sections with assumed uniform properties. No attempt to use trailing edge surface pressure spectrum models and the Howe (1978) far field propagation method to account for spanwise variations of flow or geometric properties has been reported in the literature.

2.4.2 Prediction via Direct Simulation to the Far Field

It is possible to perform a trailing edge noise prediction by means of time dependent compressible flow simulations (DES/LES/DNS) which propagate the pressure fluctuations to desired observation point(s) in the far field. Recently, Ikeda et al. (2012) used DNS methods to investigate the aeroacoustic sound generated from the flow about a NACA 0012 airfoil, adding to the previous DNS studies of Sandberg et al. (2009) and Jones and Sandberg (2010). While LES studies include those of Wolf and Lele (2012); Wang and Moin (2000) and Marsden et al. (2007). Wang and Moin (2000) highlighted the need for accurate characterisation and representation of the in-flow turbulence and velocity conditions; a challenge which is even more difficult for junction flows than for semi-infinite wing sections. Although it is possible to directly compute the far field noise characteristics using time-dependent compressible flow simulations, a limiting factor is that in order to resolve the pressure fluctuation of wavelength λ requires at least four cells (de Villiers, 2006); a requirement that can cause it to be prohibitively computationally intensive to resolve even moderate frequencies in the far field. Similarly, in order for the acoustic fluctuations to be accurate in the far field, very accurate discretisation and numerics to minimise numerical dispersion and diffusion effects is required. Another source of computational effort is the fact that sampling of a numerical simulation is limited to the timestep of the simulation, and hence in order to resolve high frequencies exceptionally small timesteps are needed.

The need for small time-steps for resolving the high frequency components couples with the requirement that the simulation be run for long enough to provide a sufficient sample period to resolve the low frequency components, and this results in increased computational effort. Table 2.4 gives some of the operative conditions of the studies mentioned, including the spanwise extent of the simulation. It is worth considering the increase in computational effort that would be required to describe a more extensive span, such as would be required for wing-in-junction flow using time dependent compressible flow simulations. Although a powerful tool for the study of fundamental flow and noise research, the intense computational effort required renders such direct methods impractical for most industrial applications. This has driven the development of hybrid methods which operate in conjunction with much less computationally intensive time averaged CFD methods and are discussed presently.

Table 2.4: Summary of literature case operating conditions and simulated crossflow extent

Airfoil(s)	Re_C(s)	AOA(s) [degrees]	Maximum Simulated Span [C]	Reference
NACA0006 and NACA0012	10,000	0, 3.5	N/A	Ikeda et al. (2012)
NACA0006 and NACA0012	50,000	5, 7	0.2	Sandberg et al. (2009)
NACA0012 with serrations	50,000	5	0.2	Jones and Sandberg (2010)
NACA0012 and	408,000	5	0.1	Wolf and Lele (2012)
Flat strut	2,150,000	0	0.03	Wang and Moin (2000)
Flat strut	1,900,000	0	N/A	Marsden et al. (2007)

2.4.3 Hybrid Methods

Hybrid methods use CFD data as their input. This means there is crossover between semi-empirical methods and hybrid methods, as many of the semi-empirical models may use CFD predicted values for their scaling parameters, rather than physically measured properties. Alternatively, it may be possible to directly determine the quantity(s) required from the CFD. For example, an LES could be used to determine the flow properties for input into a surface pressure spectrum model, or the surface pressure spectrum itself could be determined from the LES. An example of this is the work of Winkler et al. (2012), which may then be combined with the usual methods (Amiet (1975) or Howe (1978)) to propagate the numerically obtained surface pressure spectrum to the far field. Such methods are advantageous when compared to directly resolving the pressure fluctuations to the far field in that only the regions of interest from which the relevant scaling parameters are obtained, need to be resolved in detail, and the far field location of interest where the noise is to be determined no longer needs to be within the CFD domain. Reduction of the computational domain in which time dependent solutions are sought is the basis of combined RANS/LES methods, such as the study of Terracol (2005) which used LES in only a small section of the domain. A section encompassing the region from which sources are sought and time averaged flow solutions for the rest of the domain. However such time accurate flow solutions are still too computationally intensive at moderate to high Reynolds numbers to find extensive use in practical applications.

Owing to the computational intensity of time dependent methods, hybrid methods which operate in conjunction with time averaged flow solution methods have received significant attention. Due to sound generation being a time dependent phenomenon, in order to use time averaged flow solutions as the basis of a noise calculation further modelling is required. Stochastic and statistical approaches are the most common modelling methods used. Stochastic methods for determining the required turbulence properties include the spatial convolution of spatio-temporal white-noise or summation of random Fourier modes (Kraichman, 1970; Ewert, 2008), as well as the stochastic model for surface-pressure covariance of Peltier and Hambric (2007), which accounts well for the changes wrought by adverse and favorable pressure gradients. Although earlier stochastic methods assumed homogeneous isotropic turbulence, Smirnov et al. (2001) extended the method to inhomogeneous anisotropic boundary layer flows. Statistical approaches attempt to model two point time and space correlation functions for turbulent velocity or surface pressure fluctuations, generally by best fit to experimental measurements, which once determined, may be used along with a flow solution to calculate the far field noise.

One example of using a surface pressure fluctuation model to predict far field noise is the work of Kamruzzaman et al. (2011), which extends the TNO model of Parchen and TNO-TH (1998) to account for turbulence anisotropy. It achieved good predictions for the spectral shape but had trouble predicting the correct sound pressure levels. Other hybrid pressure fluctuation methods include those of Glegg et al. (2008), Remmler et al. (2010) and Lee et al. (2005). A common limitation to these surface pressure spectrum methods is the assumption of uniform spanwise flow and geometric properties.

Although fewer in number than those using pressure fluctuations, and generally concentrating on jet noise, there are also approaches which calculate noise from velocity fluctuations, such as those of Tam and Auriault (1999) and Morris and Farassat (2002). As with the pressure spectra methods described previously, the velocity fluctuations can either be sampled directly from a suitable time dependent simulation, or else modelled based on average properties from a time averaged flow solution, or generated using empirical methods. An example of a velocity fluctuation method is the RANS based Statistical Noise Model (RSNM) method developed by Doolan et al. (2010), which is being used and investigated in this research and a further discussion of which is given presently.

2.4.4 2D RSNM

The RANS based Statistical Noise Model (RSNM) can be used to determine TBL-TE noise. The method is based on the theory of Ffowcs-Williams and Hall (1970), in which a Green's function approach is used to calculate the sound intensity in the far field, due to turbulent flow past a sharp trailing edge. The Green's function needs to be adapted to the problem geometry, and for a sharp, straight trailing edge a rigid half plane Green's function is used. The far field pressure fluctuations can be obtained by convolution of the source terms with the Green's function. These source terms could be determined by direct numerical simulation, however, due to the impracticality of such simulation, the method models these terms by using the mean flow data from RANS based simulation by means of a two-point space-time-correlation function model. A full derivation is given in Section 3.8.

To date, the method has been used successfully on a range of two-dimensional geometry-flow cases including sharp edged flat plates and various airfoils (Doolan et al., 2010; Albarracin et al., 2012a, 2011, 2012b); however, it has not previously been applied to more complex three-dimensional cases. Furthermore, the efficacy of the empirical constants and the assumed form of the turbulent velocity cross-spectrum for such cases is unknown. To date the RSNM method has been applied to RANS based turbulence modelling CFD results. However, extension of the method to utilise time dependent flow simulations should be possible though is yet to be investigated.

2.5 Tip Noise and Modelling

Tip vortex formation causes not only significant drag, but also high frequency broadband noise. George et al. (1980) developed the first physical explanation, attributing the tip noise to an increase in turbulent trailing-edge noise in the tip region due to the tip vortex. An alternative explanation, investigated by Hardin and Martin (1997) based on the work of Sen (1996) suggests that the primary vortex itself is perturbed from an equilibrium position, either by incoming turbulence or secondary vorticies, causing it to oscillate and become the noise source, radiating sound. Although a potentially promising model, it utilises a number of simplifications, such as assuming a 2D vortex and also relating to the tip geometry. These simplifications would be expected to make extending the model for more realistic flow and geometric properties difficult. The recent work of Moreau et al. (2015), in which beamforming sound maps were taken for a number of wing-in-junction flow cases, sheds light on both the spectral and spacial distribution of tip noise. For noise in the tip region, across all reported frequencies (frequencies corresponding to Strouhal numbers based on chord of 6.7 to 30), dominant sources were detected at the trailing edge tip. This supports the interpretation that tip noise is predominantly attributable to increases in turbulent trailing-edge noise in the tip region due to the tip vortex. However, at the highest frequencies reported (frequencies corresponding to Strouhal number based on chord of 30) moderate strength sources were also observed near the tip leading edge. These observations are not explained by the George et al. (1980) model, and additional mechanisms or a more complex model may be required for a complete description of tip noise.

Brooks and Marcolini (1986) used the George et al. (1980) explanation, in conjunction with their own experimental flow and noise measurements, to develop a tip noise model. The Brooks and Marcolini (1986) experiments involved flow and noise measurements on 2D and 3D configuration tripped NACA0012 airfoils in the low-turbulence potential core of a free jet located in an anechoic chamber. The 2D configuration airfoils were of uniform profile and spanned the jet exit nozzle. The 3D configuration airfoils, which had round ended tips defined by rotating the NACA 0012 profile about the chord line, only extended half way into the jet region. Airfoils of a range of chord lengths and a variety of flow speeds resulting in a Reynolds number based on chord (Re_c) range of $9,600 \lesssim Re_c \lesssim 260,000$, as well as at a range of angles of attack (geometric angles of attack (α_t) of $0 \leq \alpha_t \leq 14.4$) were investigated. Comparing the 2D and 3D configuration noise measurements allowed for estimation of the isolated tip noise component, while the flow measurements determined tip vortex size. The vortex size was used as a scaling parameter for a tip noise model. Using the experimental measurements of the tip vortex size for the flat ended airfoils of George and Chou (1984), the original tip noise model of Brooks and Marcolini (1986) was presented along with a proposed extension to allow for the prediction of tip noise for flat airfoils, although with the admission that there is 'no experimental confirmation' (Brooks et al., 1989) for this extension. Further details of the model, as well as its implementation and validation for the current study, is detailed in Section 3.4. Using the primary vortex size as the scaling parameter could be expected to be problematic for the zero AOA condition as the flow topology is different from that exhibited at non-zero angles of attack, as discussed in Section 2.1.2. Using a model based on that of Brooks and Marcolini (1986) but incorporating their own experimental noise measurements, Moreau et al. (2015) developed an isolated tip noise model, however, further testing is required into the effectiveness of the model for non-flat-ended tip geometries.

2.6 Leading Edge Noise and Modelling

Leading edge noise is caused by unsteady flow (such as turbulence) encountering the leading edge of an airfoil. The unsteady flow creates a fluctuating lift response. This fluctuating lift causes a measure of the flow energy to be radiated to the far field as sound. Devenport et al. (2010b) investigated the effect of airfoil thickness on leading edge noise, finding not only that the high frequency noise is substantially attenuated for thicker airfoils, but also that although leading edge noise varied little with angle of attack for isotropic inflow turbulence, that more significant leading edge noise increases were observed in the presence of anisotropic turbulence. This would suggest that wind tunnel grid-turbulence studies, and also isotropic turbulence calculations, could well be significantly underestimating angle of attack effects in practical applications, where anisotropic inflow turbulence is commonplace. More recently Geyer et al. (2012) used beamforming to investigate the reduction in leading edge noise which results when modifying an airfoil leading edge so as to be porous and comparing these to a non-porous reference. The sound maps of Geyer et al. (2012) show the spatial distribution of sound sources for leading edge noise, and shed light on the changes to this distribution resulting from changes in the inflow turbulence level. Amiet (1975) derived a model describing this sound generation process, as has Martinez and Widnall (1980). The Martinez and Widnall (1980) model was extended by Chapman (2003) for gusts of arbitrary shape, however the relative simplicity and generality of the Amiet (1975) model has lead to wider use than that of Martinez and Widnall (1980). A common limitation to these methods is the assumption of uniform spanwise flow and geometric properties of the wing.

2.7 Research Gaps

It is important to be able to accurately model the flow and noise generated by wall-mounted finite span wing flows because of the many engineering applications in which these flows occur. Wall-mounted finite span wing flows can exhibit a large number of complex flow phenomena, making flow modelling challenging. To date, wall-mounted finite span wing flow modelling has been predominantly via RANS based turbulence CFD modelling. Currently LES modelling has been limited to investigations treating the wing as semi-infinite towards either the tip or root. Determining which RANS based turbulence models are best able to predict these complex flow features is of interest for both practical applications as well as to provide insight into the models and to assist in furthering their development with a view to more completely capturing such flows.

Accurate noise predictions for wall-mounted finite span wing flows are of immediate practical interest. For the TE TBL noise mechanism, there are a number of empirical/semi-empirical methods which are unsuitable for realistic applications due to their requiring uniform geometric and flow properties. Many of these are commonly applied to airfoils with spanwise variation of flow, by means of subdividing the airfoil in the spanwise direction, and applying the respective models to each spanwise section, and summating the results. Such methods can fail to correctly capture the noise generated in the immediate vicinity of the wing tip and wing-wall junction, where the flow, and hence the noise it generates, is significantly different from that of the flow about a semi-infinite wing of uniform cross-section upon which the methods are based. No such adaptation of TE surface pressure spectrum methods, using the Howe (1978) far field propagation model, has to the author's knowledge been attempted. Similarly, the RSNM method, which has been used successfully on a range of two-dimensional geometry-flow cases, has not been applied to more complex three-dimensional cases.

Finally, the literature review revealed that although the tip vortex formation process is reasonably well understood for airfoils with round ended and flat tips at angles of attack, it has not been reported on in relation to flat tipped airfoils at zero angle of attack. The resulting aims of this research may be summarised as follows.

2.8 Thesis Aims

The gaps identified in Section 2.7 may be condensed to the following thesis aims:

- Aim 1: To investigate the strengths and limitations of RANS based turbulence models for predicting wall-mounted finite span wing flows and their suitability for noise modelling
- Aim 2: Develop and extend semi-analytical and RSNM techniques to take into account spanwise variations in wing geometry and flow properties, allowing them to be used to predict wall-mounted finite span wing flow noise
- Aim 3: Use the developed models to predict flow and noise from a number of wall-mounted finite span wing experiments
- Aim 4: To characterise the tip vortex formation process for flat ended airfoils at zero angle of attack

3 Methodologies

3.1 Introduction and Justification

This chapter details the numerical techniques used throughout the present work. These numerical techniques can be divided into two types, those centering around the flow and those relating to the noise. The first type involves simulating wing-in-junction flows within a finite computational domain, to allow investigation of wing-in-junction flow features. The second type are related to the prediction of wing-in-junction flow noise. The results from the flow simulations obtained using the first technique are often used to drive the noise prediction methods of the second technique, estimating the sound created in the flow domain and propagating it into the farfield.

3.2 Flow Modelling

Aims 1 and 3 of this work (see Section 2.7) necessitate the use of a Reynolds Averaged Navier Stokes (RANS) based flow modelling approach. RANS based turbulence modelling methods are therefore selected as the flow modelling approach in the present work. This section discusses the formulation and solution of such methods as relevant to the present work. The discussion begins with the governing equations and proceeds though their simplification and discretisation, as well as solution algorithms.

3.2.1 Governing Equations

Using conservation of mass, momentum, and energy, as well as the equation of state, it is possible to develop a series of equations that completely define a fluid and its motion [see for example Pope (2000), Versteeg and Malalasekera (2007) or Wilcox (2006)]. For a Newtonian, ideal gas with no external forces applied to it, conservation of mass requires

$$\frac{\partial \rho}{\partial t} + \frac{\partial}{\partial x_i}(\rho u_i) = 0, \tag{3.1}$$

while conservation of momentum requires

$$\frac{\partial}{\partial t}(\rho u_i) + \frac{\partial}{\partial x_j}(\rho u_i u_j) = -\frac{\partial p}{\partial x_i} + \frac{\partial}{\partial x_j}(2\mu s_{ij}), \tag{3.2}$$

where p and ρ are respectively the pressure and density of the fluid, x_i and u_i are respectively the index notation for Cartesian direction/position and velocity components, t is time, and s_{ij} is the strain rate tensor which is defined as

$$s_{ij} = \frac{1}{2}\left(\frac{\partial u_i}{\partial x_j} + \frac{\partial u_j}{\partial x_i}\right). \tag{3.3}$$

The present work involves flows of relatively low Mach number (M<0.3), and with negligible heating effects. This means that the fluid may be assumed to be incompressible, and allows Equations 3.1 and 3.2 to be reduced to

$$\frac{\partial u_i}{\partial x_i} = 0, \tag{3.4}$$

which is the simplified continuity equation, while the momentum equation becomes

$$\rho \frac{\partial u_i}{\partial t} + \rho u_j \frac{\partial u_i}{\partial x_j} = -\frac{\partial p}{\partial x_i} + \frac{\partial t_{ij}}{\partial x_j}, \tag{3.5}$$

where t_{ij} is the viscous stress tensor and is given by

$$t_{ij} = \mu \left(\frac{\partial u_i}{\partial x_j} + \frac{\partial u_j}{\partial x_i} \right), \tag{3.6}$$

and μ is the dynamic viscosity.

3.2.2 Reynolds Averaged Based Methods

RANS methods make use of Reynolds averaging to solve the Navier Stokes equations. Reynolds averaging is based on segregating the flow parameters into mean and varying components. This is done by using time, space or ensemble averaging. Wilcox (2006) explains the Reynolds averaging process in terms of time averaging, and it is this formulation that follows. The other averaging processes arrive at similar solutions by similar methods. The flow parameter is first separated into mean and varying components according to

$$\phi(\vec{x}, t) = \overline{\phi}(\vec{x}) + \phi'(\vec{x}, t), \tag{3.7}$$

where ϕ can be any flow parameter (eg. velocity), $\overline{\phi}$ is its time averaged mean component, and ϕ' is its time varying component. These are mathematically defined as

$$\overline{\phi}(\vec{x}) = \lim_{T \to \infty} \frac{1}{T} \int\limits_{t}^{t+T} \phi(\vec{x}, t) dt \quad , \quad \lim_{T \to \infty} \frac{1}{T} \int\limits_{t}^{t+T} \phi'(\vec{x}, t) dt = 0, \tag{3.8}$$

where T is the averaging period. This process is applied to Equations 3.4 and 3.5 and rearranged to yield

$$\frac{\partial \overline{u_i}}{\partial x_i} = 0 \tag{3.9}$$

and

$$\rho \frac{\partial \overline{u_i}}{\partial t} + \rho \overline{u_i} \frac{\partial \overline{u_i}}{\partial x_j} = -\frac{\partial \overline{p}}{\partial x_i} + \frac{\partial}{\partial x_j} \left(2\mu \overline{s}_{ji} - \rho \overline{u_i' u_j'} \right). \tag{3.10}$$

Equation 3.10 is known as the Reynolds-averaged Navier-Stokes equation. The quantity $-\rho \overline{u_i' u_j'}$ is known as the Reynolds-stress tensor, and τ_{ij} is the specific Reynolds-stress tensor and is defined as

$$\tau_{ij} = -\overline{u'_i u'_j} = \begin{pmatrix} \tau_{xx} & \tau_{xy} & \tau_{xz} \\ \tau_{yx} & \tau_{yy} & \tau_{yz} \\ \tau_{zx} & \tau_{zy} & \tau_{zz} \end{pmatrix}. \tag{3.11}$$

Noting that $\tau_{ij} = \tau_{ji}$, there are six new unknowns, which, when added to the original four unknowns, makes a total of ten. Given that there are only four equations, namely the continuity equation and conservation of momentum in each direction, the problem is not yet closed. In order to close the problem, additional equations are needed. Turbulence models are employed which attempt to provide approximations for the unknown correlations in terms of known flow properties. A discussion of turbulence modelling, as well as details of the RANS turbulence models used in the present study are given in Appendix C.

3.2.3 Discretisation and Solution

The Finite Volume Method

The finite volume method discretises partial differential equations into a series of algebraic equations which may then be solved numerically. This solution then corresponds to the solution of the original equations at pre-determined spacial/temporal positions. There are two components to the discretisation process, discretisation of the solution domain as well as equation discretisation. The equation discretisation allows transformation of the terms of the underlying equations into a form which may be evaluated numerically, while the discretisation of the solution domain describes the solution domain upon which the solutions of the underlying equations are sought. An example of a typical underlying equation would be conservation of mass, while an example of a solution domain would be some bounded physical space, such as a room. The finite volume method discretises the solution domain into a series of finite volumes of arbitrary shape. Such a collection of finite volume elements is known as a mesh. It is possible to have domain discretisations which change in time; however for the purposes of the following explanations, the finite volume elements are assumed to be stationary and unchanging with time. Similarly various possibilities exist with respect to the discretisation chosen, and the following discussion is limited to discretisations as used in the present work (with the OpenFOAM solver). The underlying equations of interest in the present work are those of conservation of mass, energy and momentum in the form of the Navier-Stokes equations for an incompressible fluid and the discussion is constrained to this.

Domain Discretisation

As already mentioned, the domain is discretised into a collection of finite volumes (V). These volumes do not overlap and completely fill the computational domain. Two typical adjoining control volumes are shown in Figure 3.1. Vector d is defined as that which connects the cell centroid of the first volume to that of the second. The joining face f has face normal vector A_f defined such as to have magnitude equal to the face area and direction facing outward from the volume being considered.

Equation Discretisation

To convert the underlying integral equations, with surface, volume, divergence and gradient integrals, such that they can be evaluated on the control volumes the following are used (for full derivations see Jasak (1996)):

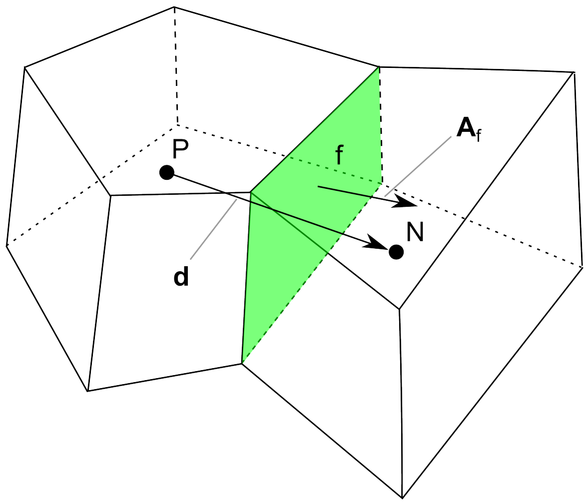

Figure 3.1: Diagram of arbitrary control volumes (with centroids P and N)

$$\begin{align}
\text{Surface integral:} \quad & \textstyle\int_f \phi(x)dA = \phi_f A_f, \tag{3.12}\\
\text{Volume integral:} \quad & \textstyle\int_{V_p} \phi(x)dV \approx \phi_P V_P, \tag{3.13}\\
\text{Gradient integral:} \quad & \textstyle\int_{V_p} \nabla\phi dV \approx \sum_f A_f \phi_f, \text{ and} \tag{3.14}\\
\text{Divergence integral:} \quad & \textstyle\int_{V_p} \nabla\cdot\phi(x)dV \approx \sum_f A_f \cdot \phi_f. \tag{3.15}\\
& \tag{3.16}
\end{align}$$

The discretisation of diffusion terms is achieved by

$$\int_{V_p} \nabla\cdot(\nu\nabla\phi)dV = \sum_f A\cdot(\nu\nabla\phi)_f = \sum_f \nu_f A\cdot(\nabla\phi)_f. \tag{3.17}$$

To evaluate this, ν_f is found by interpolation, while $A\cdot(\nabla\phi)_f$ will be a function of the domain discretisation and is given by

$$A\cdot(\nabla\phi)_f = |A|\frac{\phi_N - \phi_P}{|d|} + A_{\|_f}\cdot(\nabla\phi)_f \tag{3.18}$$

The most general case is shown in Figure 3.2, in which the joining face is not orthogonal to the vector connecting the two cell centroids, and showing the orthogonal and non-orthogonal components of the face area vector to the vector connecting the centroids. The non-orthogonal component is evaluated by taking the component of the gradient parallel to the face normal vector.

The discretisation of convection terms is achieved by

$$\int_{V_p} \nabla\cdot(u\phi)dV = \sum_f A\cdot(u\phi)_f. \tag{3.19}$$

Spatial Discretisation

In order to evaluate ϕ_f in Equation 3.19, a convection difference scheme needs to be selected. Central, upwind and blended differencing will be discussed, as although there are well known

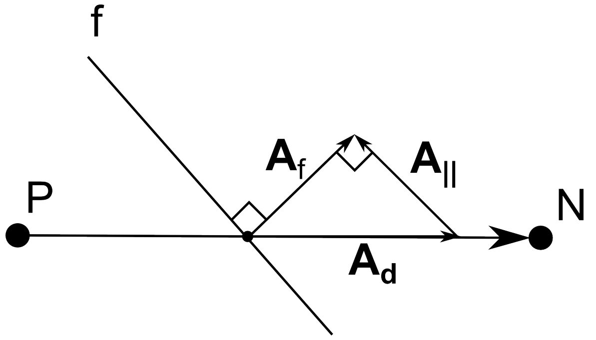

Figure 3.2: Face area vector decomposition for a non-orthogonal cell

methods with higher orders of accuracy, they are generally only practically applicable to structured meshes. Central differencing assumes linear variation of arbitrary quantity ϕ from its value in cell P (ϕ_P) to its value in cell N (ϕ_P) and arrives at the face value as

$$\phi_f = f_x \phi_P + (1 - f_x)\phi_N, \tag{3.20}$$

where $f_x = \frac{\overline{fN}}{\overline{PN}}$, where $\overline{fN}$ represents the distance between the location where the joining face intersects the line joining the cell centroids P and N, and $\overline{PN}$ represents the distance between the cell centroids. Central differencing is known to be second order accurate (Ferziger and Peric, 1995) but can cause unphysical oscillations in the solution for convection-dominated problems (Patankar, 1981), violating the boundedness of the solution. Upwind differencing instead assigns a value to ϕ_f that is equal to the cell value in the cell upwind. Unlike central differencing, solution boundedness is guaranteed; however, this is at the cost of increased numerical diffusion and so reduced solution accuracy. Blended differencing attempts to preserve both the boundedness offered by upwind differencing and the 2nd order accuracy offered by central differencing by blending the two together:

$$\phi_{f_{Blended}} = \gamma \phi_{f_{Upwind}} + (1 - \gamma)\phi_{f_{Central}} \tag{3.21}$$

where $0 \leq \gamma \leq 1$ and when taking values of 0 or 1 is purely central or upwind differencing respectively.

When the domain, equation and spatial discretisations discussed are combined, they are sufficient to completely convert the underlying equations into a form for numerical solution using a suitable method. The software suites and methods used for domain discretisation and numerical solution are discussed in the following.

OpenFOAM and Pointwise

The OpenFoam numerical simulation system was used to solve the governing equations. It is a finite volume discretisation approach with a wide variety of flexible discretisation solutions. The programming code is written in C++ language and the code can be changed to suit the specific fluid dynamics problem. The OpenFoam suite was selected due to scalability and availability on the computational resources available to the this study.

The Pointwise software suite was used for domain discretisation. It is capable of generating structured and unstructured meshes and outputting into a format immediately suitable for use with OpenFOAM.

Solution Algorithm

Now that the Navier-Stokes equations and suitable domain discretisations have been given, solution methods are discussed. The finalised RANS directisation of the Navier-Stokes system shows linear dependence between pressure and velocity. This can be solved using simultaneous or segregated approaches. Simultaneous methods are unpopular due to the extreme cost in terms of operations and memory requirements when compared to segregated methods. The SIMPLE algorithm (Patankar, 1981) is suitable for solving such steady state flow problems. The SIMPLE algorithm takes advantage of the fact that fully resolving the linear pressure-velocity coupling is not necessary when solving the steady state problem. Because of these properties it was selected as the solution algorithm to be used in the present work. The algorithm as implemented in OpenFOAM may be described as:

1. Set boundary conditions and initialisation of all fields.
2. To determine the new velocity field, use under-relaxing between the previous velocity field and that calculated based on the most recent pressure field.
3. To determine the new pressure field, use under-relaxing between the previous pressure field and that calculated based on the most recent velocity field.
4. If turbulence modelling is used, determine new turbulence variables, using under-relaxing between previous fields, and those calculated using the newest pressure and velocity fields.
5. Check if differences between the previous solution and new solution for all fields are smaller than set tolerance, if not return to Step 2.

3.2.4 Boundary Conditions and Wall Functions

The Dirichlet and Neumann boundary conditions, as well as the turbulence model wall functions, are detailed here as they have been used throughout the present work.

Boundary Conditions

Dirichlet type boundary conditions impose a fixed value for some quantity (ϕ) on a boundary,

$$\phi = C, \tag{3.22}$$

where C is the fixed value that is being imposed on the quantity (ϕ).

Neumann type boundary conditions impose a fixed value for on the derivative of some quantity (ϕ) on a boundary,

$$\frac{\partial \phi}{\partial \mathbf{n}} = C, \tag{3.23}$$

where $\mathbf{n}$ is the normal vector to the boundary upon which the fixed value of C is being imposed to the derivative of the quantity ϕ.

Wall functions

The boundary conditions relating to turbulence properties in RANS modelling depend not only on the specific turbulence model used, but also the spacial resolution of the flow near boundaries. Approaches may be divided into wall modelled and wall resolved approaches. Wall resolved approaches explicitly resolve the flow throughout the boundary layer, down through the buffer layer to the viscous sublayer. This allows for greater accuracy in the prediction of properties within and near the boundary layers, but comes at the cost of the increase in spacial resolution required in the spacial discretisation of the boundary layer. Wall modelled approaches make use of wall functions, which model the flow properties in the log-law region of the boundary layer, wherein the average velocity of a turbulent flow is known to be proportional to the logarithm of the distance from the wall (Von Karman, 1931). Both wall modelled and wall resolved approaches are used in the present work. Exact details of the wall functions used are given in Appendix D.

3.3 Noise Modelling

A number of models are developed and extended in order to allow them to be used to predict wing in junction flow noise. These will be compared not only against experimental noise measurements, but also against existing finite wing noise prediction methods from the literature. Firstly, Sections 3.4 and 3.5 detail the tip (Brooks and Marcolini, 1986) and trailing edge (Brooks et al., 1989) noise models used for comparison purposes. Section 3.6 details the TE surface pressure spectrum propagation model developed to extend existing 2D surface pressure spectrum methods, so as to be able to predict wing in junction flow noise. Section 3.7 details the LE noise prediction methodology developed to extend existing 2D LE noise prediction methods so as to be able to predict wing in junction flow noise. Finally, Section 3.8 details the new turbulent velocity cross-spectrum model and improved implementation for the RSNM, proposed to allow the method to be used to effectively and efficiently predict turbulent trailing edge noise for more complex three-dimensional cases.

3.4 BPM Tip Noise

Brooks and Marcolini (1986) developed an empirical airfoil tip vortex formation noise model by isolating airfoil high frequency broadband self-noise via comparison of 2D and 3D experimental airfoil acoustic data. The model returns the one-third octave band sound pressure levels in dB with reference to 20 micro-Pascals, and is given by

$$SPL_{TIP} = 10\log\left(\frac{M^2 M_{Max}^3 l^2 \overline{D}_h}{r_e^2}\right) - 30.5(\log St'' + 0.3)^2 + 126, \tag{3.24}$$

where M and M_{Max} are the Mach numbers based on freestream velocity, U and maximum velocity U_{Max}, both in metres per second, while r_e is the distance in metres from the midspan of the TE to the observation point at which the noise level is being calculated, and St'' is the Strouhal number given by

$$St'' = \frac{fl}{U_{Max}}, \tag{3.25}$$

l is the spanwise extent of the viscous core of the blade tip vortex in metres, $\overline{D}_h$ is a directivity function given by

$$\overline{D}_h = \overline{D}_h(\Theta_e, \Phi_e) \approx \frac{2sin(\Theta_e/2)sin^2(\Phi e)}{(1 + Mcos(\Theta_e))[1 + (M - M_c)cos(\Theta_e)]^2}, \tag{3.26}$$

where Θ_e and Φ_e are the angles between the chord-wise and chord-span-normal direction and the spanwise direction and the chord-span-normal direction respectively, and M_c is the convective Mach number.

The Brooks and Marcolini (1986) experiments were performed for airfoils with rounded tips, achieved by rotating the profile shape about the end of the span. For rounded tips a characteristic length (l) approximation for the extent of the viscous core of the blade tip vortex is given as

$$l/c \approx 0.008\alpha_{TIP}, \tag{3.27}$$

where α_{TIP} is the true angle of attack of the airfoil to the oncoming flow.

Additionally, to approximate the vortex core characteristic length for airfoils with flat tips, as is relevant to the present work, based on 'no experimental confirmation', Brooks and Marcolini (1986) gives

$$\frac{l}{C} = \begin{cases} 0.023 + 0.0169\alpha'_{TIP} & 0\text{degrees} \leq \alpha'_{TIP} \leq 2\text{degrees} \\ 0.0378 + 0.0095\alpha'_{TIP} & 2\text{degrees} > \alpha'_{TIP} \end{cases} \tag{3.28}$$

where α'_{TIP} is the corrected angle of attack calculated using sectional loading to account for tip loading characteristics differing from those of the reference case and C is the airfoil chord length. The redefined α'_{TIP} is given by

$$\alpha'_{TIP} = \lim_{\text{Location along span}\to\text{b}} \left[\frac{\frac{\partial L'}{\partial y}}{\frac{\partial L'}{\partial y_{Ref}}} \right] \alpha_{TIP}, \tag{3.29}$$

where L' is the lift per unit span, y is spanwise position, b is the extent of the wing in the spanwise direction ($s/2$), and the subscript $_{Ref}$ indicated with reference to the limiting $\lim_{AR\to\infty}$ case. Although useful in allowing for corrections for twist and other wing effects, Equation 3.29 is not immediately useful for practical applications. The present work, like that of Brooks and Marcolini (1986), is on uniform wings, and so fitting of the α'_{TIP} data presented in Brooks and Marcolini (1986) allows for the following approximation for wings of uniform profile with span:

$$\frac{\alpha'_{TIP}}{\alpha_{TIP}} = -0.8139 \times AR^{-0.5389} + 1.099, \tag{3.30}$$

where AR is the full span aspect ratio, taking account of the wing being attached to a flat plate, and treating the span as though it is of full span equal to twice that of the plate-attached wing. The fit has an R-squared value of 0.9997, and so should be a good approximation over the full span aspect ratio range of 2 to 24. The Brooks and Marcolini (1986) model, using the developed $\frac{\alpha'_{TIP}}{\alpha_{TIP}}$ fit, was verified against the predictions from the paper, and the results are given in Appendix B Figure B.1. The differences between the current implementation and the verification data are attributed to uncertainty in the experimental speed of sound (assumed to be 340m/s), as well as errors in interpolation of the data from the figure in the report and also experimental error and numerical approximations and assumptions.

3.5 BPM TE Noise

Brooks et al. (1989) developed an airfoil turbulent boundary layer trailing edge noise and separated flow model. This model is often referred to as the 'BPM model'. For angles of attack below a critical value, defined as the lesser of the maxima of an auxiliary function and 12.5°, the model returns the one-third octave band sound pressure levels in dB with reference to 20 micro-Pascals and is given as:

$$\mathrm{SPL}_{TE-Total} = 10log\left(10^{SPL_\alpha/10} + 10^{SPL_s/10} + 10^{SPL_p/10}\right), \tag{3.31}$$

where

$$\mathrm{SPL}_\alpha = 10log\left(\frac{\delta_s^* L M^5 \overline{D_h}}{r_e^2}\right) + B(St_s, St_2) + K_2 \tag{3.32}$$

is the noise component due to being at an angle of attack,

$$\mathrm{SPL}_s = 10log\left(\frac{\delta_s^* L M^5 \overline{D_h}}{r_e^2}\right) + A(St_s, St_1) + (K_1 - 3) \tag{3.33}$$

is the noise component due to the suction side of the airfoil,

$$\mathrm{SPL}_p = 10log\left(\frac{\delta_p^* L M^5 \overline{D_h}}{r_e^2}\right) + A(St_p, St_1) + (K_1 - 3) + \Delta K_1 \tag{3.34}$$

is the noise component due to the pressure side of the airfoil, L is the spanwise extent of the wetted airfoil in metres, M is the Mach number based on freestream velocity, St_p and St_s are respectively the Strouhal numbers based on the pressure and suction side displacement thicknesses δ_p^* and δ_s^*, both in metres, r_e is the observer distance from the trailing edge in metres, and K_1, ΔK_1, K_2, St_1 and A are the auxiliary equations based on chord Reynolds number, the Strouhal numbers and angle of attack, and $\overline{D_h}$ is a directivity function depending on observer position. For full details of the auxiliary functions refer to Brooks et al. (1989).

The current implementation of the model was verified against the predictions of the report, as well as against the independently developed implementation of the model in NAFNOISE, as shown in Appendix B Figure B.2. The test case was for a tripped rounded tip airfoil with chord of 15.24 cm, in flow of velocity 31.7 m/s. NAFNOISE was used with turbulent boundary layer heights calculated using the BPM model approximations (rather than other options, such as computing them with XFOIL). Agreement between the current implementation and NAFNOISE is good, and considered sufficient to validate the implementation. The differences between the current implementation and that of Brooks et al. (1989) are attributed to uncertainty in the experimental speed of sound (assumed to be 343m/s for NAFNOISE and the results shown for the current implementation), as well as errors in interpolation of the data from the figure in the report.

3.6 Herr TE Noise Model

3.6.1 Model Formulation

Herr et al. (2010) compared a number of semi-empirical prediction models for TE unsteady surface pressure power spectral densities with each other as well as experimental results. Such models in turn may be used to calculate the far field trailing-edge noise. The surface pressure power spectral densities model used for comparison in the current work is (Herr et al., 2010)

$$\frac{S_0(\omega)(u_e/\delta_{99})}{\tau_w^2} \approx \frac{3(\omega\delta_{99}/u_e)^2}{((\omega\delta_{99}/u_e)^2 + 1.8432)^{3/2} + (R_t^{-0.5}(\omega\delta_{99}/u_e)^7)}, \tag{3.35}$$

where δ_{99} is the 99% boundary layer thickness, u_e is the edge velocity, ω circular frequency, τ_w the trailing edge wall shear stress, $R_t = \delta^+ u_\tau/u_e \approx \delta^+ u_\tau/u_{\text{inf}}$ is the time scale ratio, $\delta^+ \approx \delta_{99}u_\tau/\nu_{\text{inf}}$ the ratio of outer-to-inner length scale, u_τ the wall friction velocity, and ν_{inf} and u_{inf} are the freestream viscosity and velocity respectively.

The surface pressure power spectral densities are used, in turn, to calculate the far field trailing-edge noise and this conversion is given by

$$S_F(r,\omega) \approx \frac{M_V b \delta_z(\omega) S_0(\omega)}{2\pi^2 r^2 (1 - M_V)}, \tag{3.36}$$

where $\delta_z(\omega) \approx V/\eta_z\omega$ are the spanwise correlation lengths, M_V is the (assumed constant) eddy convection Mach number ($M_V = V/c_{\text{inf}}$), η_z is an empirical constant of value 0.714, describing the spanwise coherence decay for a zero-pressure gradient turbulent boundary layer, as determined by Corcos (1964), and r is the distance from the trailing edge to the observer, which must be directly overhead the TE midspan, at which the sound is determined.

3.6.2 Implementation Verification

The model implementation was tested against the Herr et al. (2010) data for the properties shown in Table 3.1. The unsteady surface pressure power spectral density was calculated via Equation 3.36 using the input values from Table 3.1, and compared to those given in Herr et al. (2010) (Figure 10(d)), generated using $R_t = 51$ and 123, between which it falls, as shown in Appendix B Figure B.3. Similarly the farfield spectra based on the current implementation and that given in Herr et al. (2010) in Table 3.1 were compared, and this is shown in Appendix B Figure B.4. The agreement between them and the current implementation is considered

Table 3.1: Herr TE noise model validation data taken from Herr et al. (2010)

Quantity	Value
u_∞	40 m/s
$\frac{u_e}{u_\infty}$	0.98
r	1.15 m
b	0.8 m
δ_{99}	14.5 mm
u_τ	1.42 m/s
R_t	74.59

sufficient to validate the implementation.

3.6.3 Extension of Surface Pressure Spectrum Methods to Account for Spanwise Variation in Geometric and Flow Properties

In many applications the flow approaching a plate or an airfoil will not be uniform, such as in wind turbines and ducted fans. Surface pressure spectrum TBL-TE noise model methods are developed assuming uniform turbulence and flow properties, and so require modification to account for spanwise variation of flow and/or geometric properties. The modification proposed to account for such factors discretises the span into sectional elements. The noise from the entire span is then calculated by summing the contributions of each sectional element.

The method discretises the airfoil of span (b) into N sectional elements of width b_i and then the total TE noise due to all the sectional elements. Firstly the surface pressure power spectral density of the i$^{\text{th}}$ sectional element $S_{(0,i)}(\omega)$ is calculated using a surface pressure power spectral density model, such as that of Herr et al. (2010), as given in Equation 3.35. In practical applications the selection of model is expected to be driven by the object for which a TBL-TE noise estimate is sought; a flat plate surface pressure spectrum model, such as those of Herr et al. (2010); Goody (2004); Smol'Yakov and Tkachenko (1991) or Chase (1987) for estimating noise from zero pressure gradient turbulent boundary layers on flat plates, or an airfoil surface pressure spectrum model, such as that of Schlinker and Amiet (1981), for estimating noise from an airfoil. However, the farfield TBL-TE noise power spectral densities due to this sectional element, cannot be estimated by means of Equation 3.36, as the observation point will not be directly overhead the midspan of each of the strips. To arrive at an estimation for a more general observer position (θ, α, r) relative to the mid-span of the TE of the sectional element with convected turbulence over the trailing edge of velocity $V = (V_1, 0, V_3) = (Vcos(\beta), 0, Vsin(\beta))$ at angle β relative to the x_1 axis, as shown in Figure 3.3, we commence from the more general equation from which Equation 3.36 was derived, given as (Brooks and Hodgson, 1981)

$$\begin{aligned} S_F(\theta, \alpha, r, \omega) = &\frac{2}{\pi r^2}\frac{Vb}{c}\frac{sin(\alpha)sin^2(\frac{\theta}{2})cos\beta}{(1-M_{0R})^2(1-M_{VR})^2(1-M_{V_1}sin(\alpha))^2} \\ &\times \int_{-\infty}^{\infty} \Pi(\mu_1, \omega cos(\alpha)/c, \omega) d\mu_1 \end{aligned} \tag{3.37}$$

where $M_{0R} = U_\infty cos(\theta)/c$ is the Mach number of the freestream velocity in the observer direction, $M_{V_1} = V_1/c$ is the Mach number of the component of the convected turbulence velocity in the x_1 direction, M_{VR} is the Mach number of the convected turbulence velocity in the observer direction, and $\Pi(\mu_1, \omega cos(\alpha)/c, \omega)$ is the wavenumber-frequency spectrum of the pressure fluctuation on the plate or airfoil very close to the trailing edge in terms of the wavenumber μ_1 corresponding to the x_1 axis.

The approximation of Chandiramani (1974) is employed:

$$\int_{-\infty}^{\infty} \Pi(\mu_1, \omega cos(\alpha)/c, \omega) d\mu_1 \approx \int_{-\infty}^{\infty} \Pi(\mu_1, 0, \omega) d\mu_1 \approx l_3 S_0(\omega)/\pi. \tag{3.38}$$

Combining Equations 3.35, 3.37 and 3.38 allows for the determination of the farfield TBL-TE noise power spectral densities from the i$^{\text{th}}$ sectional element. If the entire span is discretised into N sectional elements of extent b_i then the total farfield TBL-TE noise power spectral densities $S_{F,T}$ will be given by

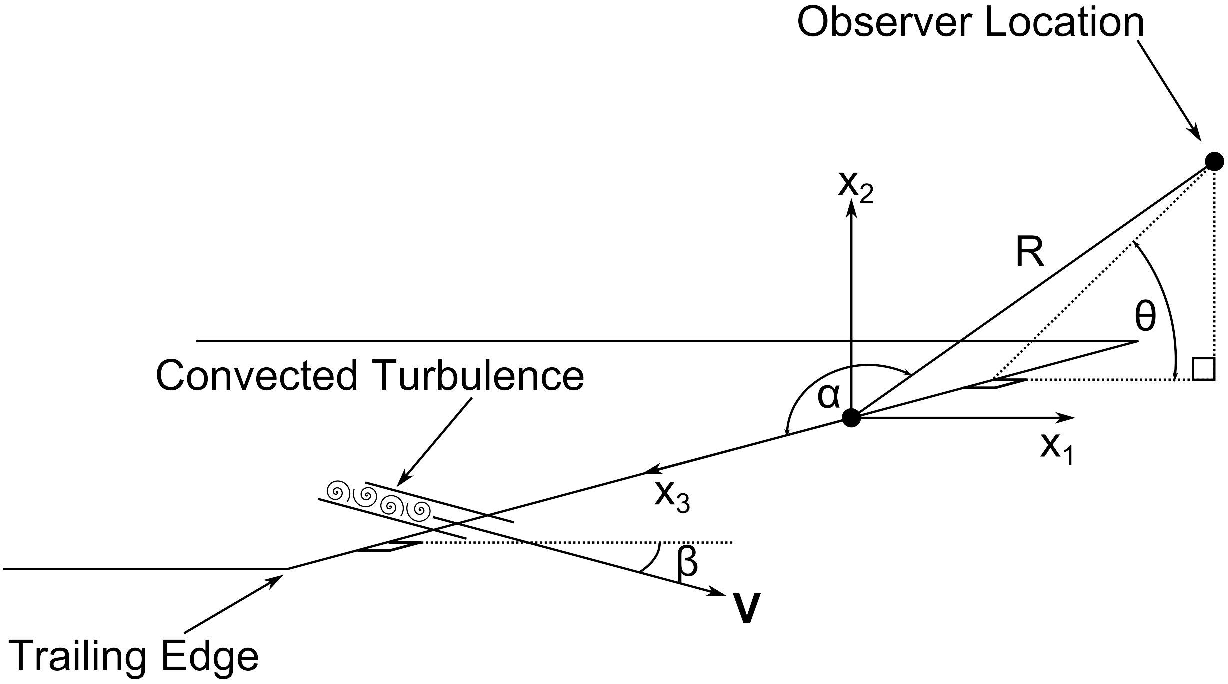

Figure 3.3: Diagram showing coordinate system, TE flow, and observer location

$$\begin{aligned} S_{F,T} &= \sum_{i=1}^{N} S_{F,i}(\theta, \alpha, r, \omega) \\ &= \sum_{i=1}^{N} \frac{2}{\pi^2 r^2} \frac{V_i b_i}{c} \frac{sin(\alpha) sin^2(\frac{\theta}{2}) cos\beta}{(1-M_{0R})^2 (1-M_{VR})^2 (1-M_{V_1 sin(\alpha)})} l_{3,i} S_{0,i}(\omega), \end{aligned} \tag{3.39}$$

where i subscripts have been added to any terms depending on the observer location, as the observer position is expressed relative to, and so is dependent on, each sectional element, as well as terms dependent on flow velocities, which may also change from sectional element to sectional element.

3.6.4 Extension Validation

The extended model was implemented and applied to the same case as in Section 3.6.2. The span was divided into $N = 2^J$ strips with $J = 0, 1, 2, 3, ...11$, the total TBL-TE noise farfield spectra calculated, and a selection of these are shown as well as the prediction results of Herr et al. (2010) in Appendix B Figure B.5. The overall sound pressure level (OASPL) was calculated across 1Hz $\leq f \leq 110,000$Hz (approximately the values at which the one-third octave band sound pressure levels drop below 0dB) for each total number of strips investigated. A selection of these results are given in Table 3.2. As can be seen, the result quickly converges with the result changing between $N = 1$ and $N = 2$ by less than 0.4%. These changes result from increasing accuracy of the spacial discretisation with increasing number of strips. The solution appears insensitive to the number of strips when $N > 8$, indicating the numerical method has become grid insensitive and converged. The relatively low number of strips required to achieve convergence in this case is attributed to the uniform flow and geometric properties, as well as position of the observation location relative to the trailing edge; it is expected that if such properties were non-uniform, or for observer locations that were less distant from the TE, a larger number of sectional elements would be required to achieve convergence.

Table 3.2: OASPL comparison for extension validation case

N	1	2	4	8	16	2056
OASPL [dB]	52.99	52.79	52.75	52.74	52.74	52.74

3.7 LE Noise Model Method

3.7.1 Theory of Amiet

Unsteady flow (such as turbulence) encountering the leading edge of an airfoil creates a fluctuating lift response. This fluctuating lift causes a measure of the flow energy to be radiated to the far-field as sound. Amiet (1975) derived a model describing this sound generation process, which produces the pressure power spectral density for far-field noise G_{pp} generated by the interaction of turbulence with the leading edge of an airfoil. This was extended to allow for spanwise variation of flow by Doolan et al. (2012), and details of the adapted model follow:

$$G_{pp,N}(\mathbf{x},\omega) = \sum_{i=1}^{N} \frac{2d}{N} \left(\frac{z_{a,i}\rho_0 U_0}{\sigma_i^2} \right)^2 (\frac{\omega b}{c_0})^2 |\mathcal{L}|^2 \phi_{ww,i}(\omega) l_{y,i}(\omega), \tag{3.40}$$

where d and b are the half-span and half-chord respectively, ρ_0 is the ambient fluid density, U_0 is the mean free stream flow velocity, $\omega = 2\pi f$ is the circular frequency, where f is the frequency in Hz, c_0 is the speed of sound of the ambient fluid, N the total number of spanwise sections (i), σ_i is the the far-field corrected distance of the i'th spanwise section and given by,

$$\sigma_i = \sqrt{x_{a,i}^2 + \beta^2 (y_{a,i}^2 + z_{a,i}^2)}, \tag{3.41}$$

in which $\beta = \sqrt{1 - M^2}$ is a compresibility term and $M = \frac{U_0}{c_0}$ is the Mach number of the flow, $\phi_{ww,i}$ is the vertical velocity turbulence spectrum of the i'th spanwise section, $l_{y,i}(\omega)$ is the spanwise correlation length scale of the i'th spanwise section (in this work, the Karman spectrum, and corresponding spanwise correlation length scale as defined in Amiet (1975) are used), and $\mathcal{L}$ is the airfoil response function which relates the fluctuating lift to noise. For full detail of the response function see Amiet (1975).

These RANS simulation data are linked to the Karman spectrum, and corresponding spanwise correlation length scale as defined in Amiet (1975) by means of turbulence intensity (Ti) and turbulent integral length scale L by means of (Wilcox, 2006),

$$Ti = \sqrt{\frac{2}{3} \frac{k}{U^2}}, \tag{3.42}$$

and,

$$L = C^* \frac{k^{\frac{3}{2}}}{\epsilon}, \tag{3.43}$$

where U is the mean local velocity, ϵ is the turbulent dissipation rate, and k is the turbulent kinetic energy, and C^* an empirical constant. Wilcox (2006) provides a value of $C^* = 0.09$.

3.7.2 Validation

The implementation of the model used in the present work was the same as that in Doolan et al. (2012), incorporating subsequent corrections to the Karman spectrum. Results using this implementation are compared against experimental results for a flow speed of 60 m/s as presented in Paterson and Amiet (1977). The noise was calculated at an observation point matching that of the experiment; that is, directly above the mid-span of the airfoil a distance of 2.25m from the model. The high frequency airfoil response function was used in the theory of Amiet using the von Karman turbulence model. In order to validate the stripwise implementation this was done dividing the airfoil span into a number of strips, N. The results for N=1, 5, 10, 25, 50, 100 and 1000 are compared in Figure 3.4. NOTE: All noise measurements presented, are given in dB with reference to 20 micro-Pascals unless otherwise specified.

Good agreement between the model and experimental results is achieved for frequencies up to approximately 1500 Hz. Results to not agree as well above this frequency possibly because (as discussed in Paterson and Amiet (1977)), the signal to noise ratio for the experiment at these frequencies was poor. Results did not show significant dependence on the number of strips used, varying by less than 0.1 dB when the number of strips was varied from 1 to 1000. The result it taken as sufficient to validate the method and implementation in the present work.

3.8 RSNM Detailed Description, 3D Adaptation, and Implementation

3.8.1 2D RSNM Detailed Description

Doolan et al. (2010) developed the RANS based Statistical Noise Model (RSNM) that can be used to determine TBL-TE noise. The method is based on the theory of Ffowcs-Williams and Hall (1970), in which a Green's function approach is used to calculate the sound intensity in the far field created by a turbulent flow past a sharp trailing edge. The Green's function is adapted to the problem geometry, and for a sharp, straight trailing edge, a rigid half plane Green's function is used. The far field pressure fluctuations are obtained by convolution of the source terms with the Green's function. These source terms may be determined by direct numerical simulation, however, due to the impractically large computational resources that would be involved, the method models these terms, using mean flow data from RANS-based simulation, and a two-point space-time-correlation function turbulent velocity model. A full derivation is given in (Albarracin et al., 2012a), while a brief overview is given here.

Begin by considering the Green's function for a rigid half plane (Macdonald, 1915),

$$G(r,\theta,\omega) = \frac{e^{-ikR}}{R}\left\{1 + \frac{2e^{i\pi/4}}{\sqrt{\pi}}(2kr_0\sin\phi)^{\frac{1}{2}}cos\frac{1}{2}\theta + O(kr_0)\right\} \tag{3.44}$$

in which $k = \omega/c_0$, ω is the angular frequency, c_0 is the speed of sound, R is the distance between the source and the observer locations, $O(kr_0)$ is an error term of the order of kr_0, r_0 is the distance from the edge to the source, and (r,θ,z) are the cylindrical coordinates of the observer as shown in Fig. 3.5, and in which the angle ϕ may be derived from

$$\sin\phi = \frac{r}{\sqrt{r^2 + (z-z_0)^2}}. \tag{3.45}$$

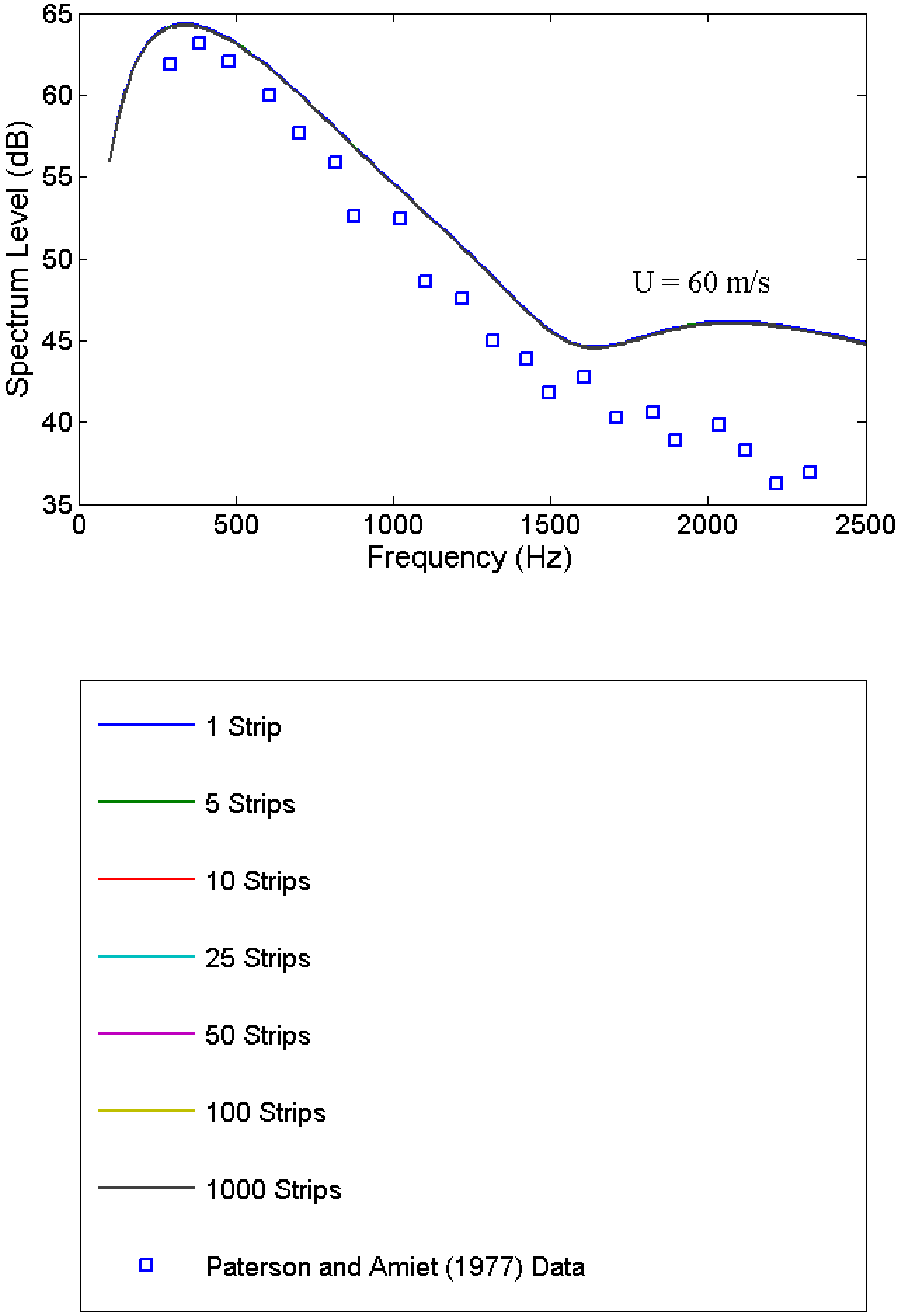

Figure 3.4: LE noise model method implementation validation

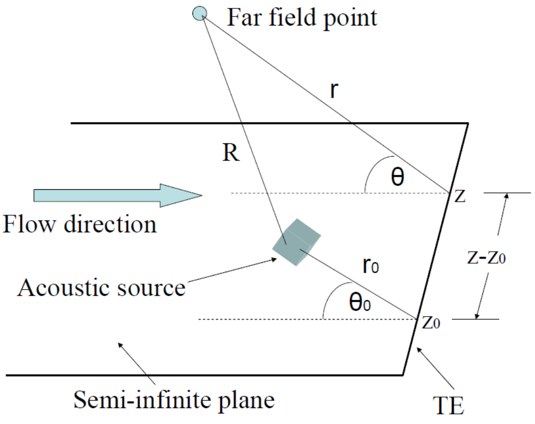

Figure 3.5: Cylindrical coordinate system centred at the trailing edge. Adapted from (Albarracin et al., 2012a)

Ffowcs-Williams and Hall (1970) showed that the half plane acoustic diffraction problem in frequency space is defined by the Helmholtz equation, and has the following solution,

$$4\pi p^*(\mathbf{x},\omega,\mathbf{y}) = \int\limits_V (\rho u_i u_j)^* \frac{\partial^2 G}{\partial y_i \partial y_j}\mathrm{dV} \tag{3.46}$$

where $\mathbf{x} = (r,\theta,z)$ is the location of the observer, $\mathbf{y} = (r_0,\theta_0,z_0)$ is the source region position, u_i are the velocity components with $i = 1,2,3$, f^* denotes the Fourier transform of f, and G is a Green's function tailored to the boundary conditions of the problem. Using the Green's function for a rigid half plane (Equation 3.44) and substituting this into Equation 3.46 obtains terms containing $(2kr_0)^{-3/2}$, $(2kr_0)^{-1/2}$ and $2kr_0$. For eddies close to the trailing edge (within one wavelength), $2kr_0 << 1$, and so $(2kr_0)^{-3/2}$ terms will dominate. Retaining only such terms produces

$$\begin{aligned} -4\pi p^*(\mathbf{x},\omega) = {} & k^2\frac{2e^{i\pi/4}}{\sqrt{\pi}}(\sin(\phi))^{\frac{1}{2}}\cos(\frac{1}{2}\theta) \\ & \times \int\limits_V \left\{\rho u_r^2\cos(\frac{1}{2}\theta_0) - \rho u_\theta^2\cos(\frac{1}{2}\theta_0) - 2\rho u_r u_\theta \sin(\frac{1}{2}\theta_0)\right\}^* \\ & \times (2kr_0)^{-\frac{3}{2}}\frac{e^{-ikR}}{R}\mathrm{dV}_0 \end{aligned} \tag{3.47}$$

where $\mathrm{dV}_0 = r_0\, dr_0\, d\theta_0\, dz_0$.

Again following Ffowcs-Williams and Hall (1970), the following approximations are made:

$$\begin{aligned} (u_r^2)^* &\approx 2\bar{U}_r u_r'^*, \\ (u_\theta^2)^* &\approx 2\bar{U}_\theta u_\theta'^*, \\ (u_r u_\theta)^* &\approx \bar{U}_r u_\theta'^* + \bar{U}_\theta u_r'^*, \end{aligned} \tag{3.48}$$

in which an overbar denotes time average and a prime denotes the fluctuating component as in a Reynolds decomposition ($u = \bar{U} + u'$). An additional simplification is made by assuming the fluctuating velocity components are related to each other by an anisotropy factor f_a such that

$$u_\theta'^* = f_a u_r'^*. \tag{3.49}$$

The function $F(\mathbf{y})$ is defined as

$$F(\mathbf{y}) = \left\{ (\bar{U}_r - f_a \bar{U}_\theta)\cos(\frac{1}{2}\theta_0) - (f_a \bar{U}_r + \bar{U}_\theta)\sin(\frac{1}{2}\theta_0) \right\}. \tag{3.50}$$

By employing the simplifications of Equation 3.48-3.49, applying the definition of Equation 3.50, and showing all dependencies on $\mathbf{y}$, Equation 3.47 becomes

$$\begin{aligned} -4\pi p^*(\mathbf{x},\omega,\mathbf{y}) = k^2 \frac{2e^{i\pi/4}}{\sqrt{\pi}} (\sin(\phi))^{\frac{1}{2}} \cos(\frac{1}{2}\theta) \times 2\rho_0 u_r'^*(\mathbf{y}) \\ \times \int\limits_{V(\mathbf{y})} \{F(\mathbf{y})\}^* \, (2kr_0)^{-\frac{3}{2}} \frac{e^{-ikR}}{R} \mathrm{dV}_0(\mathbf{y}) \end{aligned} \tag{3.51}$$

(Pressure) Power spectral density at position $\mathbf{x}$ in the far field may be written as,

$$S(\mathbf{x},\omega) = |p^*|^2 = p^*\hat{p}^* = p^*(\mathbf{x},\omega,\mathbf{y_1})\hat{p}^*(\mathbf{x},\omega,\mathbf{y_2}) \tag{3.52}$$

in which $\hat{p}$ is the complex conjugate of p.

Using the expression for $p^*(\mathbf{x},\omega,\mathbf{y})$ given by Equation 3.51 and substituting it into Equation 3.52, the power spectral density becomes

$$\begin{aligned} S(\mathbf{x},\omega) = \int\limits_{V(\mathbf{y1})} \int\limits_{V(\mathbf{y2})} \frac{2\rho_0^2 \omega \sin\phi \cos^2\frac{\theta}{2}}{\pi c r_0(\mathbf{y_1})^{3/2} r_0(\mathbf{y_2})^{3/2} R(\mathbf{y_1}) R(\mathbf{y_2})} \\ \times [u_r'^*(\mathbf{y_1})\hat{u}_r'^*(\mathbf{y_2})] F(\mathbf{y_1}) F(\mathbf{y_2}) \mathrm{dV}(\mathbf{y_2}) \mathrm{dV}(\mathbf{y_1}) \end{aligned} \tag{3.53}$$

The only unknown in the (pressure) power spectral density is the term $[u_r'^*(\mathbf{y_1})\hat{u}_r'^*(\mathbf{y_2})]$. This term is the turbulent velocity cross-spectrum,

$$\Phi(\mathbf{y_1},\mathbf{y_2},\omega) = [u_r'^*(\mathbf{y_1})\hat{u}_r'^*(\mathbf{y_2})] \tag{3.54}$$

In order to calculate the power spectral density at point $\mathbf{x}$ in the far field, a model for the turbulent velocity cross-spectrum is required. Estimation of this model is the subject of the following section.

3.8.2 Turbulent Velocity Cross-Spectrum of the Original 2D RSNM Model

The two point model used is that proposed by Morris and Farassat (2002) for turbulent jet flow in the form:

$$R_m\left(\mathbf{y_1},\eta,\tau\right) = Au_s^2 exp\left(-\frac{|\eta|^2}{l_s^2} - \omega_s^s \tau^2\right) \tag{3.55}$$

where $\mathbf{y_1}$ is the position of the first point, η is the separation between the two points ($\eta = \mathbf{y_2} - \mathbf{y_1}$), A is an empirical scalar value that determines the magnitude of the correlation, l_s the characteristic length scale of the flow, ω_s is a characteristic frequency, and u_s is a velocity scale that characterises the velocity fluctuations, and τ is the correlation time delay. Using this two point model the turbulent velocity cross-spectrum becomes:

$$
\begin{aligned}
\Phi\left(\mathbf{y_1},\eta,\tau\right) &= \int\limits_{-\infty}^{\infty} R_m\left(\mathbf{y_1},\eta,\tau\right) d\tau \\
&= \int\limits_{-\infty}^{\infty} Au_s^2\sqrt{\pi}\exp\left(-\frac{|\eta|^2}{l_s^2} - \omega_s^2\tau^2\right)\exp(i\omega\tau)d\tau \\
&= \frac{Au_s^2\sqrt{\pi}}{\omega_s}\exp\left(-\frac{|\eta|^2}{l_s^2}\right)\exp\left(-\frac{\omega}{4\omega_s^2}\right)
\end{aligned} \tag{3.56}
$$

and the cross spectrum is tied to the RANS turbulence properties by (Morris and Farassat, 2002):

$$
u_s = \sqrt{\frac{2k}{3}}, \omega_s = \frac{2\pi}{\tau_s}, \tau_s = \frac{c_\tau}{\epsilon}, l_s = \frac{c_l k^{\frac{3}{2}}}{\epsilon}, \tag{3.57}
$$

where k and ϵ are the RANS solution turbulent kinetic energy and turbulent dissipation, respectively, and where A, c_τ and c_l are semi-empirical parameters. For NACA0012 profile airfoils such as investigated here, these values have been found to take values of $A = 1/126$, $c_\tau = 0.11$ and $c_l = 0.012U_{ref} + 0.73$, where U_{ref} is the freestream flow velocity (Albarracin et al., 2012a).

To date the method has been used successfully on a range of two-dimensional geometry-flow cases, including sharp edged flat plates and various airfoils (Doolan et al., 2010; Albarracin et al., 2012a), where the effect of spanwise extent has been considered according using a Corcos (1964) based method as presented in Amiet (1976); however, it has not previously been applied to more complex three-dimensional cases and the efficacy of the empirical constants and the assumed form of the turbulent velocity cross-spectrum for such cases is unknown.

3.8.3 3D RSNM Adaptation

In order to extend the application of the RSNM method to three-dimensional cases, the following adaptation to the previously detailed turbulent velocity cross-spectrum was proposed:

$$
\begin{aligned}
\Phi\left(\mathbf{y_1},\eta,\omega\right) &= \overbrace{\frac{Au_s^2\sqrt{\pi}}{\omega_s} \quad \underbrace{\exp\left(-\frac{|\eta_{\mathbf{xy}}|^2}{l_{s_{xy}}^2}\right)}_{\text{Flow-plane-wise separation component }(\phi_{xy})} \quad \underbrace{\exp\left(-\frac{\omega}{4\omega_s^2}\right)}_{\text{Frequency dependence component }(\phi_\omega)}}^{\text{Same as original (Equation 3.56)}} \\
&\times \underbrace{\exp\left(-\frac{|\eta_{\mathbf{z}}|^2}{l_{s_z}^2}\right)}_{\text{Explicit spanwise separation component }(\phi_z)} \\
&= \frac{Au_s^2\sqrt{\pi}}{\omega_s}\phi_{xy}\phi_\omega\phi_z
\end{aligned} \tag{3.58}
$$

where the variables are as detailed previously, except that the distance between points, as well as the characteristic length scale of the flow, have been broken into 2D-equivalent and spanwise components labelled with the subscripts xy, and z, respectively. In this work, unless otherwise specified, the values for the semi-empirical constants A, c_τ and c_l are set to $A = 1/126$, $c_\tau = 0.11$ and $c_l = 0.012U_{ref} + 0.73$, where U_{ref} is the freestream flow velocity in accordance with Albarracin et al. (2012a). Such a form accounts for sources in a single way, rather than treating the flow-wise components using the RSNM approach, and the spanwise components using the Corcos (1964) based method as presented in Amiet (1976), as has been used in the work to date on RSNM (Doolan et al., 2010; Albarracin et al., 2012a). Although consistent in its treatment of flow-wise and spanwise sources, such a form allows for different correlation strengths to be applied to the different directional components, and it is suggested that future work could involve determining the dependence of these parameters on the airfoil geometry, flow Reynolds number and/or other factors. For the present study however, only modification of the spanwise coefficient will be investigated, with the semi-empirical constants A, c_τ and the flow-wise lengthscales $l_{s_{xy}}$ remaining the same as proposed by Albarracin et al. (2012a). This should show the capacity of the model to achieve accurate noise level predictions, without the need to investigate how to set all the semi-emperical values. It is unclear from the work of Albarracin et al. (2012a) the effect of modifying the spanwise extent of his computational domain has on the resulting noise, and it is possible that the value of the semi-empirical constants, especially the A value, are currently calibrated for a spanwise unit length in combination with the Amiet (1976) approach for accounting for spanwise extent. Study of how to set the semi-empirical length and timescale constants, could be undertaken numerically by using time resolved CFD methods, or experimentally. Such experimental investigations were being undertaken concurrently with the present work by Albarracin (2016) at the School of Mechanical Engineering at the University of Adelaide. Considering this, and the scope of the present study is to use time averaged RANS methods, further investigation of how to set these semi-empirical constants is beyond the scope of the present work.

The proposed model in this form is inappropriate for use when the spanwise distance between input points is approximately equal to or greater than the characteristic lengthscale in that same direction, requiring a spanwise discretisation that is less than this in order to function well. A purely textual description of the reasoning behind this failure condition can be rather difficult to follow, and the Author recommends reference to Figure 3.6. Consider a single acoustic cell (cell A) of volume V_A. Assume the RSNM method is being applied to the volume encompased by the cell. It can be seen by considering Equation 3.56, that for the two-point space-time-correlation function model considered in the original 2D RSNM model,

$$\Phi \propto \exp\left(-\frac{|\eta|^2}{l_s^2}\right). \tag{3.59}$$

For a single cell, the distance η will be zero, so

$$\begin{aligned} &\Phi \propto \exp\left(-\frac{|\eta|^2}{l_s^2}\right) \\ &\Phi \propto \exp\left(-\frac{|\mathbf{0}|^2}{l_s^2}\right) \\ &\Phi \propto 1 \end{aligned} \tag{3.60}$$

From Equation 3.53 it can be seen that the power spectral density

$$S(\mathbf{x},\omega) \propto \int_{V(\mathbf{y1})} \int_{V(\mathbf{y2})} \Phi \mathrm{dV}(\mathbf{y_2})\mathrm{dV}(\mathbf{y_1}). \tag{3.61}$$

Evaluating this in reference to cell A results in

$$S \propto V_A^2 \Phi. \tag{3.62}$$

When considering a single cell, the resulting power spectral density is proportional to the product of the square of the cell volume, and the two-point space-time-correlation term, that is to say, $S \propto V_A^2$.

Now assume that Cell A is split in the spanwise direction into two cells, named B and C, respectively, with equal volumes ($V_B = V_C = V_A/2$), and that the method is applied to the two volumes. The total sound is then determined by summation of the contributions from each volume due to each other volume. Consider first the calculation of the contributions from each volume due to itself. As the distance between each of the cells' centres and itself, is again zero, but the volumes are half that of the original, $\Phi_{\text{BB or CC}} \propto 1$ and $S \propto \left(\frac{V_A}{2}\right)^2 \Phi = \frac{V_A^2}{4}\Phi$. Secondly the contribution of each cell due to the other cell is determined. Assume too that the distance between the two cell centres is much greater than the characteristic lengthscale ($\eta_{\text{Cell B to Cell C}} >> l_s$). Under this assumption $\Phi \propto exp\left(-\frac{|\eta|^2}{l_s^2}\right) \approx 0$. Then summating all contributions leads to $S \propto 2 \times \frac{V_A^2}{4}\Phi = \frac{V_A^2}{2}\Phi$. This result can be seen to be equal to one half of the result achieved when considering a single cell. A seemingly contradictory result. However, if the distance between the cells, is assumed to be much smaller than characteristic length scale ($\eta_{CellAtoCellB} << l_s$), rather than much larger, then $\Phi \propto exp\left(-\frac{|\eta|^2}{l_s^2}\right) \approx 1$ and so the contributions due to each of the cells on the other becomes $S \propto \times \frac{V_A^2}{4}\Phi$. If all the contributions are then summated the result is $S \propto 4 \times \frac{V_A^2}{4}\Phi = V_A^2\Phi$, which can be seen to be the same as the result when considering only a single cell. This shows how when applied as originally presented, in order to function consistently, the spatial discretisation required, needs to be approximately the same or smaller than the characteristic lengthscale.

It would be impractical in most anticipated applications of the method, to have spanwise discretisation of a resolution approximately the same or smaller than the characteristic lengthscale, as it would significantly increase the computational effort of the CFD needed as an input, as well as the resulting noise calculation using RSNM. In order to address this shortcoming, the model was further modified in order to allow for larger spanwise discretisation by modifying the spanwise correlation term. The logic behind the modification is given in the following.

In order to correctly account for a cells correlation with itself (or another cell), what is desired is the average (spanwise) correlation, $\langle \phi_z \rangle)$, between points in the cell (or between the first and second cell). Consider point z_1 fixed at a cell centre. The cell is taken to have spanwise extent $[0, L]$. Consider point z_2 located randomly over the spanwise extent of the cell, that is to say $p(z_2)$ is uniform over $[0, L]$. Yielding probability density function

$$f_{z_2} = \frac{1}{L}, z \in [0, L], \text{else } f_{z_2} = 0 \tag{3.63}$$

The correlation between points z_1 and z_2 is given by the same function as before:

$$\phi_{z_1 z_2} = \exp\left(-\frac{|\eta_{\mathbf{z}}|^2}{l_{s_z}^2}\right). \tag{3.64}$$

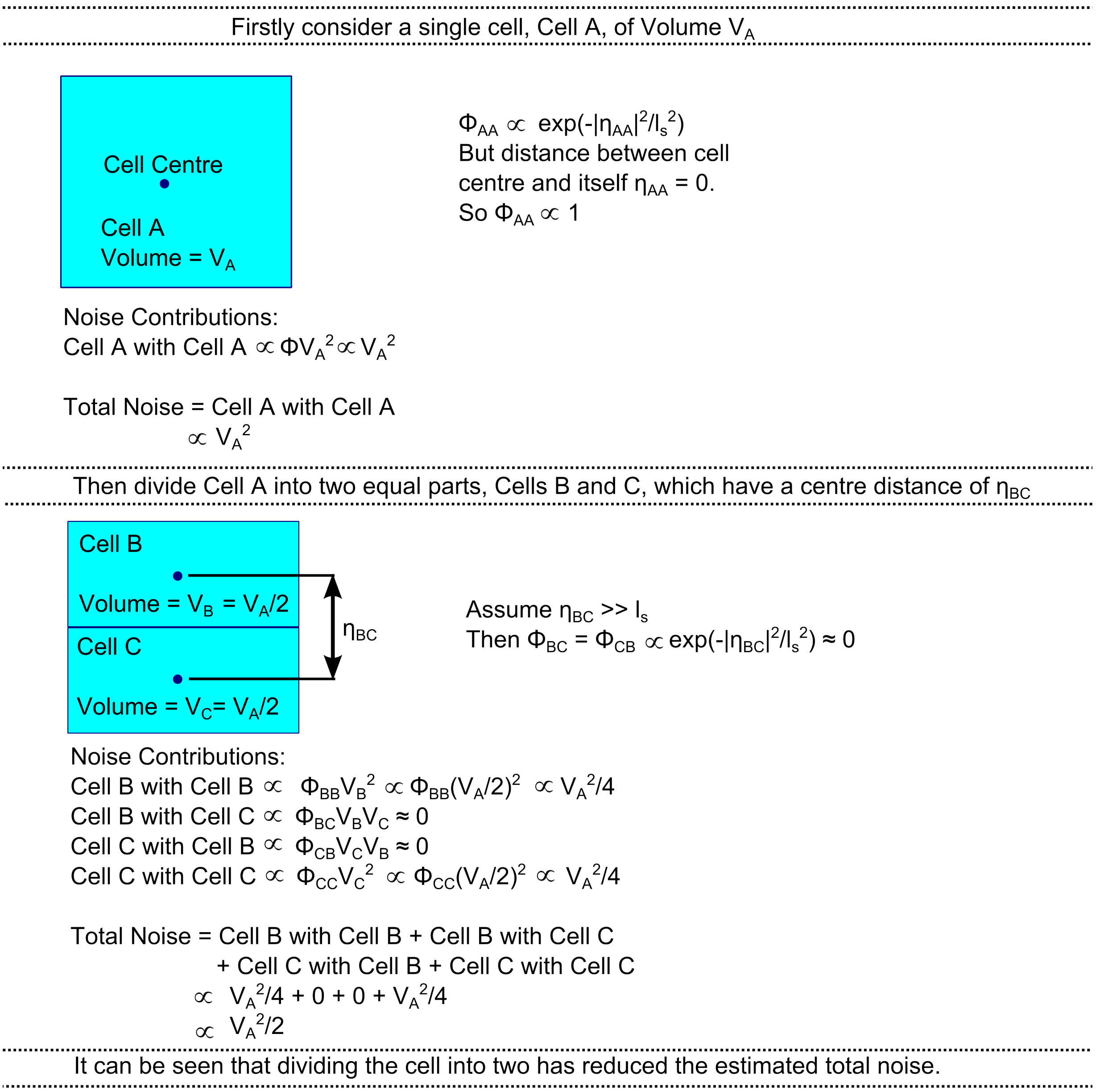

Firstly consider a single cell, Cell A, of Volume V_A

$\Phi_{AA} \propto \exp(-|\eta_{AA}|^2/l_s^2)$
But distance between cell centre and itself $\eta_{AA} = 0$.
So $\Phi_{AA} \propto 1$

Noise Contributions:
Cell A with Cell A $\propto \Phi V_A^2 \propto V_A^2$

Total Noise = Cell A with Cell A
$\propto V_A^2$

Then divide Cell A into two equal parts, Cells B and C, which have a centre distance of η_{BC}

Assume $\eta_{BC} >> l_s$
Then $\Phi_{BC} = \Phi_{CB} \propto \exp(-|\eta_{BC}|^2/l_s^2) \approx 0$

Noise Contributions:
Cell B with Cell B $\propto \Phi_{BB}V_B^2 \propto \Phi_{BB}(V_A/2)^2 \propto V_A^2/4$
Cell B with Cell C $\propto \Phi_{BC}V_BV_C \approx 0$
Cell C with Cell B $\propto \Phi_{CB}V_CV_B \approx 0$
Cell C with Cell C $\propto \Phi_{CC}V_C^2 \propto \Phi_{CC}(V_A/2)^2 \propto V_A^2/4$

Total Noise = Cell B with Cell B + Cell B with Cell C
+ Cell C with Cell B + Cell C with Cell C
$\propto V_A^2/4 + 0 + 0 + V_A^2/4$
$\propto V_A^2/2$

It can be seen that dividing the cell into two has reduced the estimated total noise.

Figure 3.6: Explanation of original RSNM model breakdown

Recalling that the location of z_2 is random on the cell's spanwise extent, correlation between z_2 and point z_1 located at the cell centre becomes:

$$\begin{aligned}\phi_{z_1z_2} &= \exp\left(-\frac{(\frac{L}{2}-z_2)^2}{l_{s_z}^2}\right) \text{ if } \frac{L}{2} \geq z_2 \text{ or else} \\ &= \exp\left(-\frac{(z_2-\frac{L}{2})^2}{l_{s_z}^2}\right) \text{ if } \frac{L}{2} \leq z_2\end{aligned} \tag{3.65}$$

The expectation value (or average) of the spanwise correlation is then:

$$
\begin{aligned}
\langle \phi_{z_1 z_2} \rangle &= \int_{-\infty}^{\infty} \phi_{z_1 z_2}(z_2) f_{z_2} dz_2 \\
&= \int_{0}^{L} \exp\left(-\frac{|\eta_{\mathbf{z}}|^2}{l_{s_z}^2}\right) \frac{1}{L}\, dz_2 \\
&= ... \\
&= \frac{l_{s_z}\sqrt{\pi}}{L} \mathrm{erf}\left(\frac{\frac{L}{2}}{l_{s_z}}\right),
\end{aligned}
\tag{3.66}
$$

where erf is the error function (also known as the Gauss error function). This may then be used to calcuate the average spanwise correlation for points within a cell, or for points between cells, by setting L as the spanwise extent of the cell, or the distance between the two cell centres respectively. This spanwise correlation correction is applied to a series of cases in Chapters 5, 6 and 7.

The success of the spanwise adaptation, along with the desire for the ability to make use of cells of larger extent in the x-y plane, drove the desire to apply a similar correction to the flow-plane-wise separation component (ϕ_{xy}). The x-y separation (η_{xy}), may be broken into orthogonal components (η_x and η_y), and in combination with exponential laws, allows the flow-plane-wise separation component to be broken into separate components (ϕ_x and ϕ_y):

$$
\begin{aligned}
\phi_{xy} = \exp\left(-\frac{|\eta_{\mathbf{xy}}|^2}{l_{s_{xy}}^2}\right) &= exp\left(-\frac{|\eta_{\mathbf{x}}|^2 + |\eta_{\mathbf{y}}|^2}{l_{s_{xy}}^2}\right) \\
= \exp\left(-\frac{|\eta_{\mathbf{x}}|^2}{l_{s_{xy}}^2}\right) \times exp\left(-\frac{|\eta_{\mathbf{y}}|^2}{l_{s_{xy}}^2}\right) &= \phi_x \times \phi_y
\end{aligned}
\tag{3.67}
$$

This results in a final version of the cross spectrum model:

$$
\Phi\left(\mathbf{y_1}, \eta, \omega\right) = \frac{A u_s^2 \sqrt{\pi}}{\omega_s} \phi_x \phi_y \phi_z \phi_\omega,
\tag{3.68}
$$

in which each direction component (ϕ_x, ϕ_y and ϕ_z) may have the expectation value correlation correction applied to them also, and doing so represents the complete extension to the RSNM method as developed in the present work. The complete extension is applied to a series of cases in Chapter 7.

3.8.4 Implementation

Converting Equation 3.53 for use with a RANS CFD solution by replacing the double spacial integrals with double summations over all volume elements of the computational grid produces:

$$
\begin{aligned}
S(\mathbf{x}, \omega) = \sum_{V(\mathbf{y1})} \sum_{V(\mathbf{y2})} & \frac{2\rho_0^2 \omega \sin\phi \cos^2\frac{\theta}{2}}{\pi c r_0(\mathbf{y_1})^{3/2} r_0(\mathbf{y_2})^{3/2} R(\mathbf{y_1}) R(\mathbf{y_2})} \\
& \times [u_r'^*(\mathbf{y_1}) \hat{u}_r'^*(\mathbf{y_2})] F(\mathbf{y_1}) F(\mathbf{y_2}) \mathrm{dV}(\mathbf{y_2}) \mathrm{dV}(\mathbf{y_1})
\end{aligned}
\tag{3.69}
$$

which is combined with the spanwise adapted cross spectrum model (Equation 3.58) and the modification for the spanwise term (3.66) to become,

$$\begin{aligned}
S(\mathbf{x},\omega) = &\sum_{V(\mathbf{y1})}\sum_{V(\mathbf{y2})} \frac{2\rho_0^2\omega\sin\phi\cos^2\frac{\theta}{2}}{\pi c r_0(\mathbf{y_1})^{3/2} r_0(\mathbf{y_2})^{3/2} R(\mathbf{y_1})R(\mathbf{y_2})} \\
&\times \frac{Au_s^2\sqrt{\pi}}{\omega_s} exp\left(-\frac{|\eta_{\mathbf{xy}}|}{l_{s_{xy}}^2}\right) exp\left(-\frac{|\eta_{\mathbf{z}}|}{l_{s_z}^2}\right) exp\left(-\frac{\omega}{4\omega_s^2}\right) \\
&\times F(\mathbf{y_1})F(\mathbf{y_2})\mathrm{dV}(\mathbf{y_2})\mathrm{dV}(\mathbf{y_1}) \\
= &\sum_{V(\mathbf{y1})}\sum_{V(\mathbf{y2})} \frac{2\rho_0^2\omega\sin\phi\cos^2\frac{\theta}{2}}{\pi c r_0(\mathbf{y_1})^{3/2} r_0(\mathbf{y_2})^{3/2} R(\mathbf{y_1})R(\mathbf{y_2})} \\
&\times \frac{Au_s^2\sqrt{\pi}}{\omega_s} exp\left(-\frac{|\eta_{\mathbf{xy}}|}{l_{s_{xy}}^2}\right) \left(\langle\phi_{z_1z_2}\rangle\right) exp\left(-\frac{\omega}{4\omega_s^2}\right) \\
&\times F(\mathbf{y_1})F(\mathbf{y_2})\mathrm{dV}(\mathbf{y_2})\mathrm{dV}(\mathbf{y_1})
\end{aligned} \tag{3.70}$$

which is tied to the RANS turbulence properties as already described by Equation 3.57, while the value L, within $\langle\phi_{z_1z_2}\rangle$, should be set to be the spanwise extent of $\mathrm{dV}(\mathbf{y_1})$.

Alternatively, Equation 3.69 may be combined with the final version of the cross spectrum model (Equation 3.68) and with expectation value corrections for each directional component (Equation 3.66) this becomes,

$$\begin{aligned}
S(\mathbf{x},\omega) = &\sum_{V(\mathbf{y1})}\sum_{V(\mathbf{y2})} \frac{2\rho_0^2\omega\sin\phi\cos^2\frac{\theta}{2}}{\pi c r_0(\mathbf{y_1})^{3/2} r_0(\mathbf{y_2})^{3/2} R(\mathbf{y_1})R(\mathbf{y_2})} \\
&\times \frac{Au_s^2\sqrt{\pi}}{\omega_s} exp\left(-\frac{|\eta_{\mathbf{x}}|}{l_{s_{xy}}^2}\right) exp\left(-\frac{|\eta_{\mathbf{y}}|}{l_{s_{xy}}^2}\right) exp\left(-\frac{|\eta_{\mathbf{z}}|}{l_{s_z}^2}\right) exp\left(-\frac{\omega}{4\omega_s^2}\right) \\
&\times F(\mathbf{y_1})F(\mathbf{y_2})\mathrm{dV}(\mathbf{y_2})\mathrm{dV}(\mathbf{y_1}) \\
= &\sum_{V(\mathbf{y1})}\sum_{V(\mathbf{y2})} \frac{2\rho_0^2\omega\sin\phi\cos^2\frac{\theta}{2}}{\pi c r_0(\mathbf{y_1})^{3/2} r_0(\mathbf{y_2})^{3/2} R(\mathbf{y_1})R(\mathbf{y_2})} \\
&\times \frac{Au_s^2\sqrt{\pi}}{\omega_s} \left(\langle\phi_{x_1x_2}\rangle\right)\left(\langle\phi_{y_1y_2}\rangle\right)\left(\langle\phi_{z_1z_2}\rangle\right) exp\left(-\frac{\omega}{4\omega_s^2}\right) \\
&\times F(\mathbf{y_1})F(\mathbf{y_2})\mathrm{dV}(\mathbf{y_2})\mathrm{dV}(\mathbf{y_1})
\end{aligned} \tag{3.71}$$

which is tied to the RANS turbulence properties as before.

4 Turbulence Model Verification and Validation

4.1 Study Aims

The aims of the turbulence model validation and comparison study are:

- To determine the required numerical techniques and mesh density required to obtain accurate simulations of wing-in-junction flows
- To apply the previously used k-ϵ, k-ω, k-ω SST and Spalart Allmaras models on the case, for validation of the flow modelling methods used through the present work, by means of comparison against previous results from the literature, and to expand upon the literature for this case through application and comparison of results obtained using the RNG k-ϵ, Realisable k-ϵ, LRR and Launder Gibson RSTM models. Many of these models are more recently developed and/or more complex than those previously applied to this case in the literature, and so may exhibit improved flow prediction performance.
- To compare all of the selected turbulence models' ability to accurately predict wing-in-junction flows and hence to determine the most suitable turbulence model(s) for wing-in-junction flows

These aims address the first of the thesis aims, namely to investigate the strengths and limitations of RANS based turbulence modelling for predicting wall-mounted finite span wing flows.

4.2 Background

As described in Section 2.2, reproducing the Devenport and Simpson (1990) experiment for investigating the performance of turbulence models, is attractive due to the extensive experimental measurements available, including detailed inlet flow conditions, as well as its geometric simplicity. For these reasons this experiment was adopted as the ERCOFTAC case 08, allowing for effective comparison between methods, as all would be using the provided boundary conditions specified in this case. This has resulted in numerous computational investigations of turbulence models undertaken for this case, comparing the results not only between each other, but also with the experimental results (Paciorri et al., 2005; Paik et al., 2007; Apsley and Leschziner, 2001; Chen, 1995; Devenport and Simpson, 1992; Parniex et al., 1998; Fu et al., 2007). Because of the wealth of experimental and computational results, the Devenport and Simpson (1990) experiment was selected to be the validation case for the present study.

4.3 Geometry and Boundary Locations

A RANS simulation of the Devenport and Simpson (1990) experiment, involving a Rood wing mounted on a flat plate, is undertaken. The wing is considered to be semi-infinite, with the wing extending the full vertical span of the computational domain. This simplification removes the wing tip, significantly reducing the grid size. As in the experiment, the geometry is a 'Rood' wing (a 3:2 elliptical nose connected at the point of maximum thickness to a NACA 0020 tail) attached to a flat plate bottom wall, as shown with coordinate system in Figure 4.1. There are standard suggested locations to place the boundary conditions given in the ERCOFTAC guidelines, in terms of the maximum thickness of the wing (T). The guidelines suggest that the geometric symmetry of the case be exploited to reduce the extent of the computational domain. By modelling only one side of the symmetry plane defined by the centre-chord-line of the wing, the number of cells required can be halved, and the computational requirements reduced. While the upstream and vertical boundary locations closely follow those of other numerical investigations (Paciorri et al., 2005; Paik et al., 2007; Apsley and Leschziner, 2001; Fu et al., 2007), the downstream and cross-stream boundary locations specified by the guidelines of $\frac{X}{T} = 10$ and $\frac{Z}{T} = 3.5$ respectively, are often deemed too short to be an appropriate distance for the boundaries and they have been extended to values as great as $\frac{X}{T} = 16$ and $\frac{Z}{T} = 18.24$ (Fu et al., 2007; Paciorri et al., 2005). The current study also uses cross-steam, vertical and downstream outlet boundary distances greater than those prescribed by the ERCOFTAC case guidelines. All the boundary distances used in the current study as well as the standard prescriptions are given in Table 4.1, in both wing thickness and chord (C) normalised units.

The suggested boundary locations, both downstream and cross-stream, have been increased, to provide more realistic distances at which the flow can be considered to be undisturbed. The vertical boundary distance is also larger than that suggested, and this was done to help minimise the effect of modelling the case as a semi-infinite wing; the extent of the domain needs to be large enough so that the top of the domain is a sufficient distance from the root of the wing.

The numerical results from the current study will be compared with Devenport and Simpson (1990) experimental measurements for flow velocity components, turbulent kinetic energy (k) and pressure, over the upstream symmetry plane, the near wing floor, as well as two cross-stream planes. These planes are shown in Figure 4.2. The first plane, referred to as 'Plane 05', is at the location of maximum thickness (the $\frac{X}{C} = 0.18$ plane) of the wing. The second plane, referred to as 'Plane 10', is located just downstream of the trailing edge of the wing, in the $\frac{X}{C} = 1.05$ plane.

In order to specify boundary conditions the outer surfaces of the computational domain have been sub-divided into the following sections: Wing, Floor, Roof, Symmetry Plane, Inlet and Outlet, as shown in Figure 4.3.

Table 4.1: Comparison of the ERCOFTAC suggested boundary distances and those implemented in the present study

Boundary	ERCOFTAC suggested distance $[\frac{1}{T}]$ $\{\frac{1}{C}\}$	Implemented Distance $[\frac{1}{T}]$ $\{\frac{1}{C}\}$
Upstream	[-18.24] {4.29}	[-18.24] {4.29}
Downstream	[10] {2.35}	[25.52] {6}
Cross-stream	[3.5] {0.82}	[14.88] {3.5}
Vertical	[3] {0.71}	[4.25] {1}

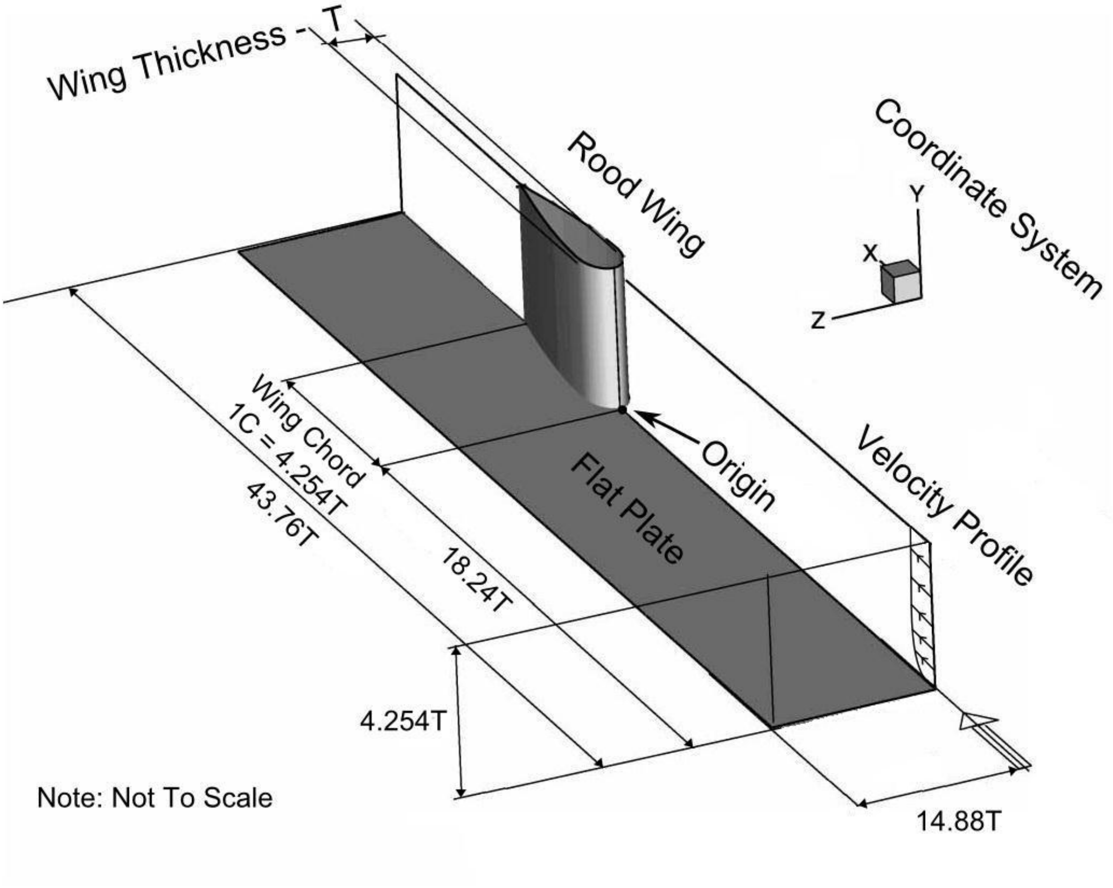

Figure 4.1: Computational Domain (adapted from (Paciorri et al., 2005))

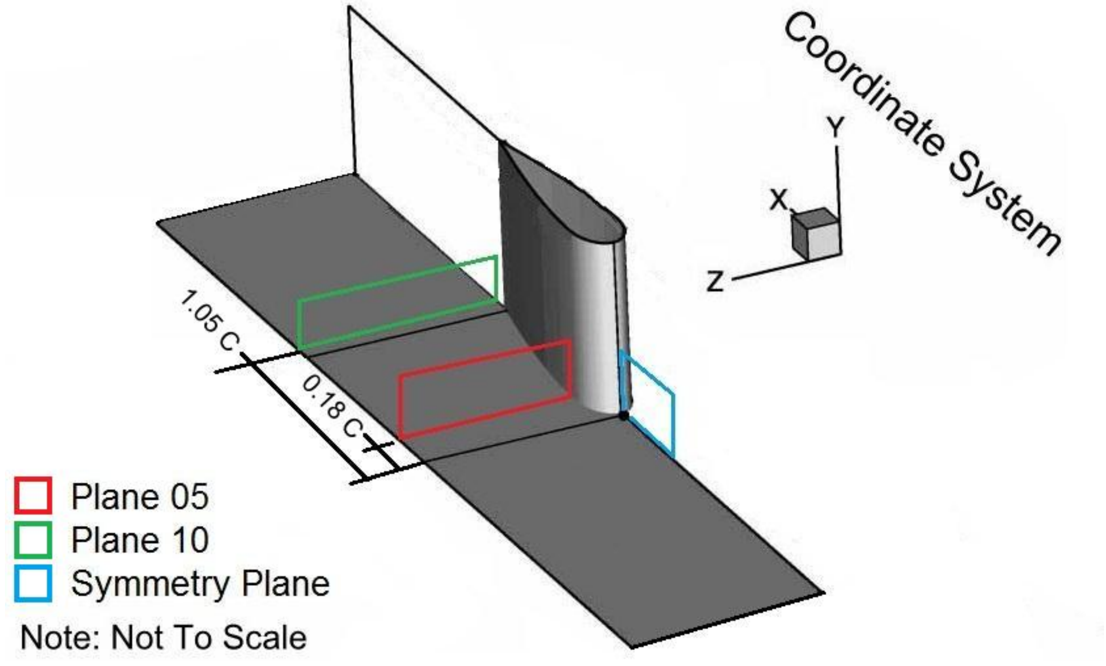

Figure 4.2: Comparison Planes (adapted from (Paciorri et al., 2005))

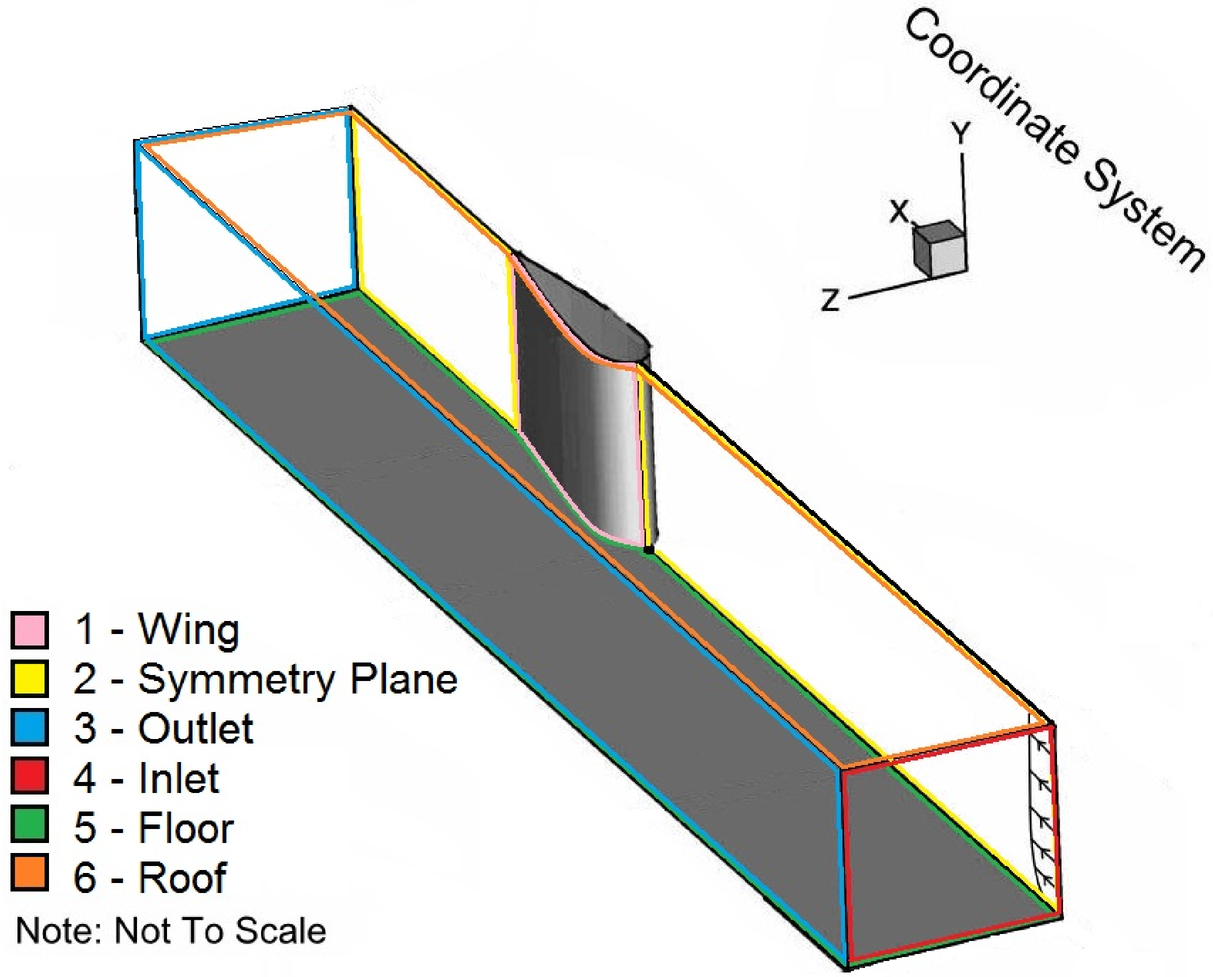

Figure 4.3: Surfaces for Boundary Conditions (adapted from (Paciorri et al., 2005))

4.4 Boundary Conditions

The technical details of the boundary conditions and wall functions used in the following are detailed in Appendix D.

4.4.1 Inlet Boundary Conditions

Velocity

The inlet velocity boundary condition is set to match the experimental data from Devenport and Simpson (1990) and corresponds to a zero pressure gradient developed flat-plate boundary layer. In order to implement this as the velocity boundary condition on the Inlet surface, a curve was fit to the experimental data and used as a continuous velocity boundary condition. To determine an appropriate functional representation of the velocity profile, the Matlab Curve Fitting toolbox was used. Table 4.2 shows the experimental data for the velocity profile. These were complemented by 30 linearly spaced padding values across the range $\frac{Y}{T} = [1.3, 4.25]$, each of which was given a freestream velocity $\frac{U}{U_{ref}} = 1$. The most appropriate form for the functional representation was determined to be

$$\frac{U}{U_{ref}}(\frac{Y}{T}) = \frac{0.9946 \times (\frac{Y}{T})^3 - 0.1183 \times (\frac{Y}{T})^2 + 0.01905 \times (\frac{Y}{T}) - 9.792 \times 10^{-7}}{(\frac{Y}{T})^3 - 0.1322 \times (\frac{Y}{T})^2 + 0.02262 \times (\frac{Y}{T}) + 0.0001117}. \tag{4.1}$$

Equation 4.1 is a rational function, a cubic polynomial divided by another cubic polynomial, and as such is continuous where the divisor polynomial is continuous. The divisor polynomial has roots $0.0663 \pm 0.4710i, -0.0005$ and so the functional representation is continuous over the height range $\frac{Y}{T} = [0, 4.254]$.

Equation 4.1 is considered to be a good representation of the non-dimensionalised velocity profile as a function of the non-dimensionalised height, with a resulting R^2 factor of 0.998 to

Table 4.2: Inlet Velocity Profile Data

$\frac{Y}{T}$	$\frac{U}{U_{ref}}$	$\frac{Y}{T}$	$\frac{U}{U_{ref}}$
0.0000	0.0000	0.0552	0.7637
0.0035	0.2869	0.0676	0.7907
0.0042	0.3647	0.0821	0.8123
0.0050	0.4257	0.1005	0.8400
0.0064	0.4827	0.1218	0.8736
0.0074	0.5150	0.1487	0.9042
0.0092	0.5523	0.1805	0.9334
0.0113	0.5850	0.2198	0.9662
0.0138	0.6092	0.2680	0.9957
0.0170	0.6297	0.3260	1.0110
0.0205	0.6489	0.3972	0.9985
0.0251	0.6741	0.4832	1.0150
0.0308	0.6960	0.5883	1.0020
0.0372	0.7160	0.7165	1.0050
0.0453	0.7381	0.8722	1.0140

both the original experimental data and the original data combined with added freesteam data points. The data, padding, and functional representation fit are shown in Figure 4.4. This velocity profile was implemented as the velocity boundary condition of the inlet.

Inlet Turbulence Properties k, ϵ, ω, $\tilde{\nu}$, R

Two possible methods of specifying the inlet turbulence properties are the characteristic length (l) and turbulence intensity (I) method (l-I method) and the eddy viscosity ratio method. The characteristic length and turbulence intensity method is commonly used for internal flows, such as ducts and pipes, for which good approximations to calculate a characteristic length from the physical features of the problem are known. For example, for fully developed pipe flow the turbulence length scale is 7% of the hydraulic diameter, and because of this, a turbulence length scale of 7% of the smallest characteristic geometric length for non-pipe flows is sometimes used as an initial approximation. However, for external flows, accurate general relationships are not available and the eddy viscosity ratio method is more appropriate. The eddy viscosity ratio ($\frac{\mu_T}{\mu}$) method attempts to estimate the influence of the turbulent viscosity, μ_T, compared to the molecular dynamic viscosity, μ. For true external aerodynamic flow cases a value for this ratio of 0.1-1 is a good approximation, while for wind-tunnel external flows values in the range 1-10 are appropriate. The equations for calculating the turbulence parameters are given by Equations 4.4-4.7, where the turbulent kinetic energy (k) is calculated from the velocity U, by

$$k = \frac{3}{2}(UI)^2. \tag{4.2}$$

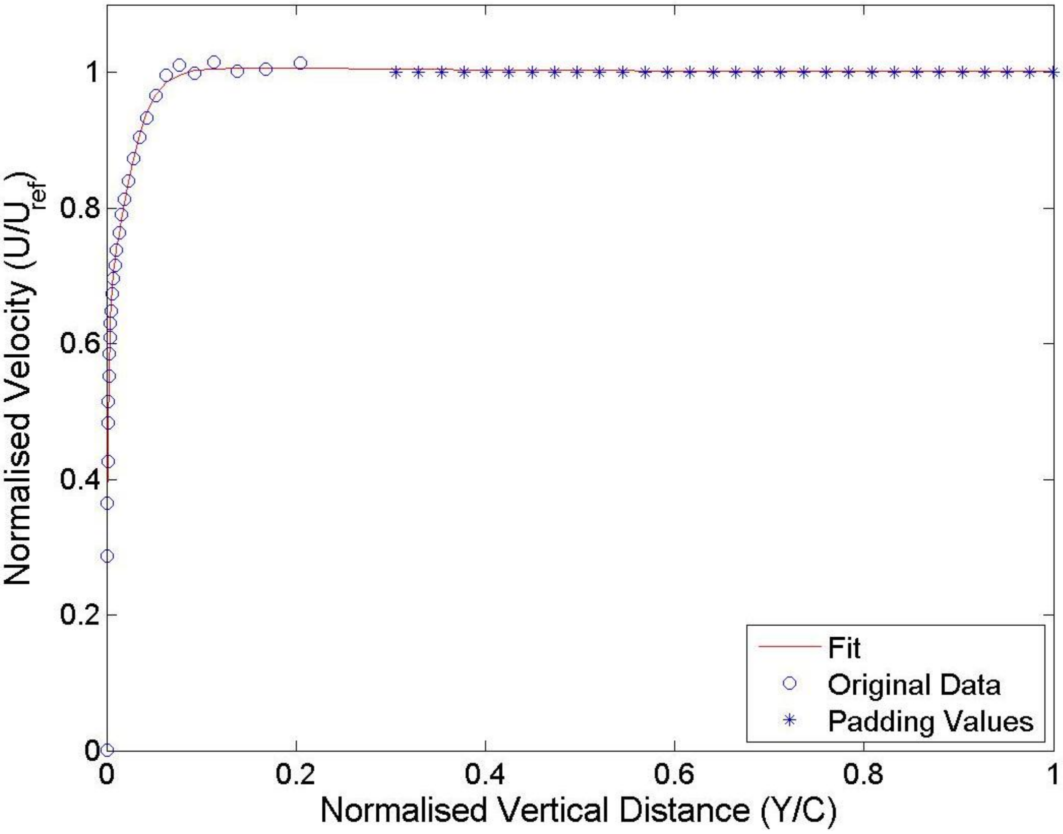

Figure 4.4: Functional Representation Curve Fit.

The dissipation rate ϵ can be defined from the turbulence length scale

$$\epsilon = C_\mu \frac{k^{\frac{3}{2}}}{l}, \tag{4.3}$$

or alternatively from the eddy viscosity ratio

$$\epsilon = C_\mu \frac{\rho k^2}{\mu} \frac{\mu}{\mu_T}, \tag{4.4}$$

where C_μ is a turbulence model constant which usually has a value of 0.09. The specific dissipation rate, ω, can be defined from the turbulent length scale

$$\omega = \frac{\sqrt{k}}{l}, \tag{4.5}$$

or alternatively from the eddy viscosity ratio

$$\omega = \frac{\rho k}{\mu} \frac{\mu}{\mu_t}. \tag{4.6}$$

The modified turbulent viscosity $\tilde{\nu}$ for use in the Spallart-Allmaras model is given by

$$\tilde{\nu} = \sqrt{\frac{3}{2}}(UIl). \tag{4.7}$$

The freestream turbulence intensity for the Devenport and Simpson (1990) experiment was measured to be 0.2%. Using this value, for a value of the characteristic length taken to be 7% of the wing thickness, and an eddy viscosity ratio of 1, the turbulence properties for the inlet can be calculated using the characteristic length and turbulence intensity method, and the results given by both of these methods are given in Table 4.3.

Table 4.3: Freestream Turbulent Parameters Estimation

Parameter	Characteristic *l*-*I* Method		$\frac{\mu_T}{\mu}$ Method	
Method Values	0.07 Wing Thickness	0.5 Boundary Layer Thickness	1	10
k	6e-6			
$\tilde{\nu}$	1.0500e-005	1.4010e-4	N/A	
ϵ	3.7792e-7	2.8324e-8	2.1724e-7	2.1724e-8
ω	0.6999	0.0525	0.4023	0.0402

The ranges of the estimated turbulence parameters values are given in Table 4.3. The fact that the ranges of ϵ and ω calculated using the two methods overlap significantly suggests that either approximation would be appropriate in this case. For the validation case, the eddy viscosity ratio method values (with $\frac{\mu_T}{\mu} = 1$) from Table 4.3 were used to specify the fixed value boundary values for the turbulence properties ω, ν_T, ϵ and k at the inlet. In order to provide a boundary condition for the Reynolds stress tensor turbulence parameter for the RSTM models, the Reynolds stresses were calculated at the inlet using the OpenFOAM$^{\text{TM}}$ post processing tool, called **R**, based on the results of the $k - \epsilon$ turbulence model runs.

Pressure p

As this validation case is being computed with the flow treated as incompressible, it is convenient to use relative pressure. Because of this, the boundary condition for pressure on the inlet and outlet is specified to be fixed at a value of zero.

Turbulent Eddy Viscosity ν_T

The eddy viscosity on the inlet was calculated from the other flow properties. The equations used depend on the specific turbulence model and these are given in Appendix C.

4.4.2 Wing and Floor Boundary Conditions

The wing and floor are both no-slip surfaces and so have fixed values of zero velocity applied. For k and R, the Reynolds stress components for the RSTM models, the OpenFOAM^{TM} kRqWallFunction was used, while for the Spalart-Allmaras model $\tilde{\nu}$ was set to a fixed value of zero, and ϵ and ω were set to use the OpenFOAM^{TM} epsilonWallFunction and omegaWallFunction for their respective boundary conditions. For pressure, a zero gradient boundary condition was used on the floor and wing surfaces. The OpenFOAM^{TM} nutkWallFunction was used as the boundary condition for the turbulent eddy viscosity on the floor and wall surfaces.

4.4.3 Symmetry Plane Boundary Conditions

The OpenFOAM^{TM} symmetryPlane boundary condition was used for all variables, including velocity, pressure, and the turbulence properties k, ϵ, ω, $\tilde{\nu}$ and R, as well as the turbulent eddy viscosity, ν_T, on the symmetry plane.

4.4.4 Outlet Boundary Conditions

A zero gradient boundary condition was used on the outlet surface for the velocity boundary condition. Turbulence Properties k, ϵ, ω and R also used the zero gradient boundary condition on the outlet surface. For the Spalart-Allmaras model the same fixed freesteam value of $\tilde{\nu}$ as specified at the inlet was used. For pressure, a fixed value boundary condition with value zero was used on the outlet surface. The turbulent eddy viscosity ν_T outlet boundary value was set to be calculated from the other properties.

4.4.5 Roof Boundary Conditions

A slip boundary condition was used for all parameters on the roof surface.

4.5 Grid Generation and Independence

The grids used in this investigation were generated using the blockMesh and snappyHexMesh grid generation tools of OpenFOAM^{TM} to produce multi-regioned multihedral grids consisting primarily of hexahedral elements for each region with prism and polyhedrals used to accurately model about and near the wing surface. Refinement regions, with increasing levels of refinement, were used close to the wing surface and specified in regions of interest, such as the recirculation-vortex region immediately upstream of the wing-wall junction. The refinement regions were used to reduce the total cell count and associated computational requirements. In order to ensure grid independence of the solution, five different grid densities were analysed. The grids, their cell composition breakdown and total cell count are given in Table 4.4. The refinement factor indicates the level of grid refinement and is a measure of the number of cells in each direction relative to the very coarse case.

Table 4.4: Grid Composition Information

Grid Name	Hexahedral Cells	Prism Cells	Polyhedral Cells	Total Number of Cells	Refinement Factor
Very Coarse	608293	3584	23387	6.35×10^5	1.00
Coarse	857863	4608	30672	8.93×10^5	1.14
Moderate	1694050	7040	47386	1.75×10^6	1.43
Fine	2858632	10752	67930	2.94×10^6	1.71
Very Fine	4534520	13888	92326	4.64×10^6	2.00

4.6 Residual Control

Table 4.5 shows the residual values required to be reached in order for the simulation to finish for all parameters for the various grid densities. Hence the simulations were run until the residuals for all the listed parameters were equal to or smaller than the values shown.

Table 4.5: Freestream Turbulent Parameters Residuals

Variable/Grid	Very Coarse	Coarse	Moderate	Fine	Very Fine
U, p	1e-7	1e-7	1e-7	1e-7	1e-7
$\tilde{\nu}$, k, ω, ϵ, R	1e-7	1e-7	1e-7	5e-8	5e-8

4.7 Turbulence Models

The turbulence models used in this investigation were the eight turbulence models described in Appendix C, namely the $k-\epsilon$, RNG $k-\epsilon$, Realisable $k-\epsilon$, $k-\omega$, $k-\omega$ SST, LRR, Launder-Gibson and Spalart-Allmaras models. As mentioned in Section 4.1 the k-ϵ, k-ω, k-ω SST and Spalart-Allmaras models had been identified, in the literature review as having been applied to simulate the Devenport and Simpson (1990) experiment previously. Therefore, they are suitable for validation of the results of the present study, by comparison against results using the same turbulence models from the literature. The RNG k-ϵ, Realisable k-ϵ, LRR and Launder Gibson RSTM models had not been applied to this case in the literature. These were implemented in this study to expand the base of turbulence models which have been applied to the case, and hence to help determine the most effective turbulence model(s) for wing-in-junction flows.

4.8 Results

4.8.1 General Results - Pressure

The pressure coefficient on the wing was compared with that of Devenport and Simpson (1990) for all models along the $Y/T = 0.13279$ plane. Figure 4.5 shows both the experimental results, as well as those for the very fine mesh solution using the Realisable k-ϵ model.

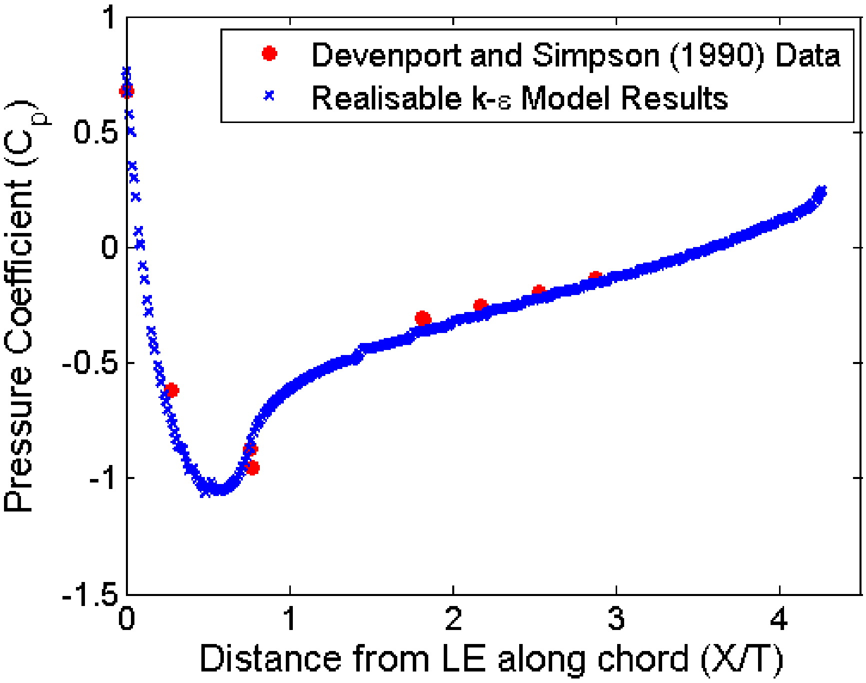

Figure 4.5: $Y/T = 0.13279$ plane comparison of the very fine mesh Realisable k-ϵ model solution and experimental wing pressure coefficient

By interpolation of the simulation results at identical locations to the experimental results, it is possible to quantify the error (E) of each model according to

$$E = \sum_{n}^{i=1} |C_i^{pS} - C_i^{pE}| \tag{4.8}$$

where n is the total number of points i at which the experimental pressure coefficient, C_i^{pE}, is compared to that of the simulation, C_i^{pS}. The calculated error for the very fine mesh solutions for each of the turbulence models are given in Table 4.6.

The ϵ-based models outperform the ω-based models as well as the Spalart-Allmaras model, with the Realisable $k - \epsilon$ performing best. The majority of the error can be attributed to the fact that all of the models predict the point of lowest pressure coefficient to be further forward than the experimental Devenport and Simpson (1990) results.

Table 4.6: Model pressure coefficient error

Pressure coefficient error for very fine mesh solutions	
Turbulence Model	**Error, E**
Realisable $k-\epsilon$	0.0705
RNG $k-\epsilon$	0.0711
$k-\epsilon$	0.0727
Launder-Gibson	0.0727
LRR	0.073
$k-\omega$ SST	0.0755
$k-\omega$	0.0771
Spalart-Allmaras	0.0916

4.8.2 General Results - Upstream Separation

The experimental results of Devenport and Simpson (1990) show that as the flow approaches the wing it separates at $X/T = -0.38919$ and recirculates. The separation point is strongly linked to viscous effects and turbulent flow, and hence is a sensitive parameter to use for turbulence model assessment. The locations of the separation points obtained from the experimental and the very fine mesh simulation results are given in Table 4.7.

The results shown do not provide a strong differentiation between the performance of the ϵ-based and ω-based models, however the simulated results, do tend to place the separation point too close to the leading edge of the wing, due to under-predicting the extent and intensity of the return flow, especially for the Spalart-Allmaras model which shows the greatest discrepancy with the experimental results.

4.8.3 General Results - Upstream Turbulent Kinetic Energy

The turbulent kinetic energy in the upstream symmetry plane was also compared, where the location and magnitude of the point of maximum kinetic energy is representative of the accu-

Table 4.7: Model pressure coefficient error

Separation point location for very fine mesh solutions		
Source of data	**Separation point location** $[X/T]$	**Error relative to experimental [%]**
Experimental*	-0.38919	0
Spalart-Allmaras	-0.17726	-54.45
$k-\epsilon$	-0.28407	-27.01
LRR	-0.31364	-19.41
Realisable $k-\epsilon$	-0.32994	-15.22
$k-\omega$	-0.33234	-14.61
Launder-Gibson	-0.40616	4.36
RNG $k-\epsilon$	-0.42634	9.55
$k-\omega$ SST	-0.4814	23.6928
* Devenport and Simpson (1990)		

racy of the models in predicting the position and intensity of the centre of the recirculation region. Figure 4.6 provides comparison of the performance of the models, in predicting both these quantities, by comparing the distance between the simulated and experimental point of maximum turbulent kinetic energy, R, as well as the ratio of maximum simulated to maximum experimental Devenport and Simpson (1990) turbulent kinetic energy. Results from other studies are given in Table 4.8 as well as Figure 4.6.

Table 4.8: Comparison of literature turbulent kinetic energy maximum amplitude and location

Reference	Turbulence Model	Maximum Turbulence Intensity $[k/U^2]$	Position of Point of Maximum Intensity	
			Y-Position $[Y/t]$	X-Position $[X/t]$
Fu et al. (2007)	$k-\omega$ WD+	$0.0496\pm^{0.0012}_{0.0012}$	$0.0316\pm^{0.0006}_{0.0006}$	$-0.25\pm^{0.05}_{0.05}$
Parniex et al. (1998)	V2F	$0.0402\pm^{0.0012}_{0.0012}$	$0.0288\pm^{0.0016}_{0.0016}$	$-0.2263\pm^{0.0016}_{0.0016}$
Apsley and Leschziner (2001)	$k-\omega$	$0.035\pm^{\infty}_{0}$	$0.0282\pm^{0.0167}_{0.0167}$	$-0.0904\pm^{0.0346}_{0.0462}$
Apsley and Leschziner (2001)	$k-\epsilon$	$0.035\pm^{\infty}_{0}$	$0.03\pm^{0.015}_{0.015}$	$-0.0827\pm^{0.0317}_{0.0317}$
Apsley and Leschziner (2001)	$k-\omega$ SST	$0.0175\pm^{0.0025}_{0.0025}$	$0.0275\pm^{0.0175}_{0.0175}$	$-0.2327\pm^{0.0423}_{0.0423}$
Apsley and Leschziner (2001)	Cubic $k-\epsilon$	$0.035\pm^{\infty}_{0}$	$0.0275\pm^{0.0188}_{0.0188}$	$-0.0731\pm^{0.0288}_{0.0288}$
Apsley and Leschziner (2001)	RSTM-W (Wilcox)	$0.0325\pm^{0.0025}_{0.0025}$	$0.0333\pm^{0.0128}_{0.0128}$	$-0.2038\pm^{0.0274}_{0.0274}$
Apsley and Leschziner (2001)	RSTM (Jakirlic)	$0.0275\pm^{0.0025}_{0.0025}$	$0.0333\pm^{0.0179}_{0.0179}$	$-0.3266\pm^{0.0928}_{0.0928}$
Apsley and Leschziner (2001)	RSTM+WF (Speziale et al.)	$0.0175\pm^{0.0025}_{0.0025}$	$0.0325\pm^{0.0175}_{0.0175}$	$-0.2242\pm^{0.1253}_{0.1253}$

As can be seen from the figure, aside from the $k-\epsilon$ model all the models significantly underpredict the intensity of the turbulent kinetic energy. As for the position of the maximum point, the figure shows that the Reynolds stress models perform best, while the ϵ-based models outperform the ω-based models.

4.8.4 $k-\epsilon$ Model

Pressure

Figure 4.7 shows the pressure coefficient results for the $k-\epsilon$ model for the finest grid density used. For ease of comparison, the experimental results of Devenport and Simpson (1990) are shown on the top half of the figure while the bottom half shows the computational result. As can be seen from the figure, the computational results match well with the experimental results, both quantitatively and qualitatively. For the computational results, the region of lowest pressure coefficient is not located at the point of maximum thickness of the wing, as

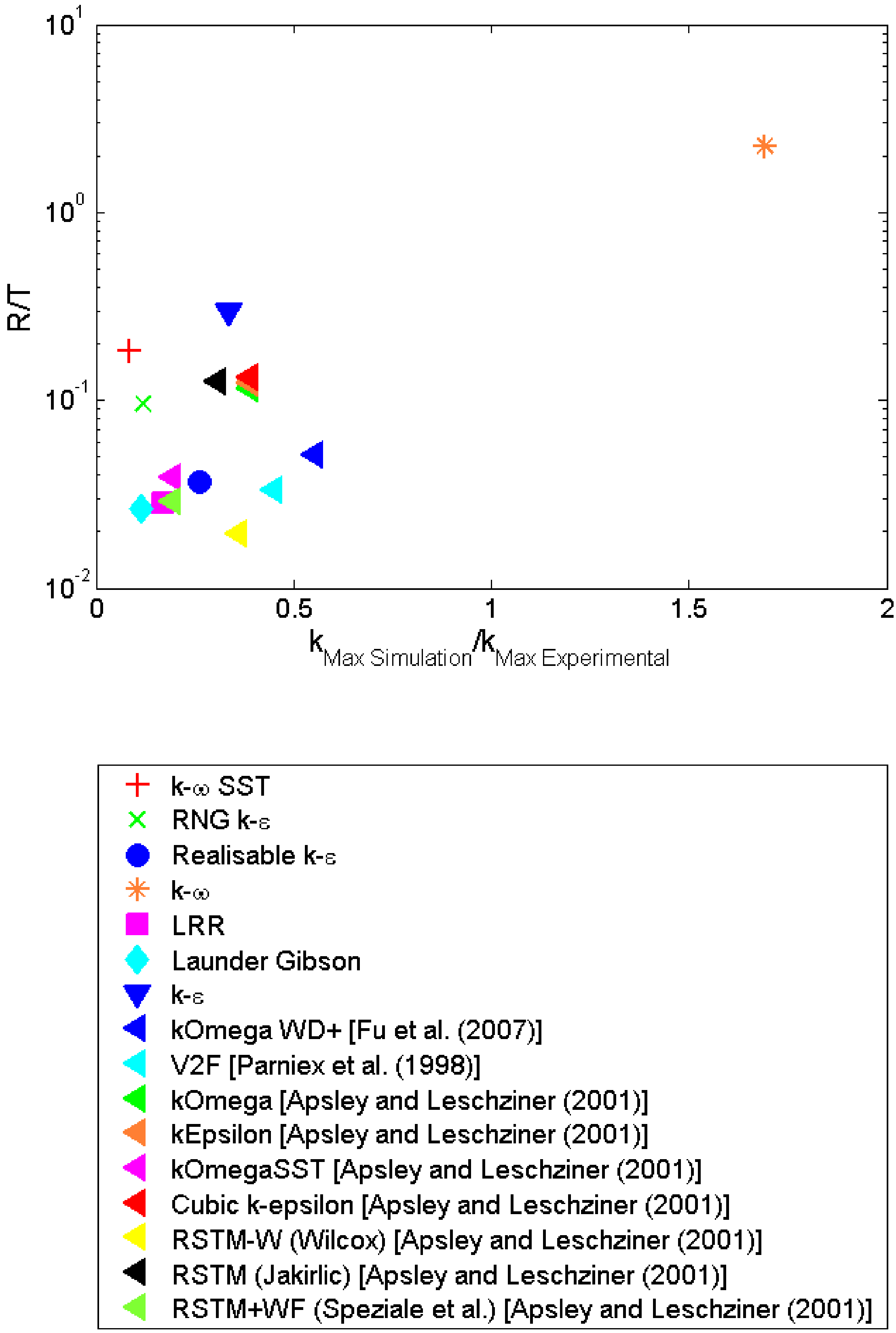

Figure 4.6: Plot of turbulent kinetic energy maximum amplitude and positional accuracy.

in the experiment, but slightly further upstream and of slightly reduced intensity. This result is consistent across all the turbulence models investigated here. Another noticeable difference between the computational and experimental results is the location where the contours meet the symmetry plane upstream of the leading edge. It is worth mentioning that these features are consistent with previous computational results obtained by Paik et al. (2007); Apsley and Leschziner (2001) and Paciorri et al. (2005).

Velocity

A feature sensitive to the type of turbulence model employed is the recirculation zone just ahead of the wing leading edge. Figure 4.8 shows the velocity vector field in the symmetry plane. Figure 4.8a is the experimental result, while Figure 4.8b is the result for the very fine grid mesh. The $k-\epsilon$ model does not successfully recreate the recirculation and vortex, failing to capture the upstream vertical velocity components and underestimating the reverse flow. This result is qualitatively and quantitatively similar to the previous result for the same turbulence model as applied by Apsley and Leschziner (2001).

In order to assess grid independence of the solution, the upstream velocity profiles in the symmetry plane have been compared with each other, as well as the experimental results. As can be seen in Figure 4.9 the computational results are consistent with the experimental results for all non-dimensional heights $\frac{Y}{T} \geq 0.3$, as well as consistent across the various grid densities. The only regions showing significant differences are those nearest the floor-wing intersection, where the numerical profiles approach the experimental result as the grid is refined.

In addition to the ability of a model to correctly predict the upstream generation of the vortex structure, its development as it is pulled downstream and around the wing is also important. To investigate this, contours for all three velocity components for the finest grid are compared with the experimental measurements at two cross-stream planes 05 and 10 as described in Section 4.3 and shown in Figure 4.2.

Figures 4.10 and 4.11 show good agreement between the experimental and computational results in both planes for the axial components of velocity except very close to the floor. The computational vertical velocity component, although smoother, also has reasonable agreement with the experimental data, except for under-predicting the magnitude of the near-wing flow in plane 05 and over-predicting it in plane 10. Cross-stream velocity components follow a similar trend of reasonable agreement but under-predict in plane 05 and over-predict in plane 10 the magnitude of the near floor flow. It is also worth mentioning that the peaked contour structure of the experiments along $\frac{Z}{T} = 1$ is significantly smoothed in the simulated flows, a result seen for all of the turbulence models investigated.

Turbulent Kinetic Energy

The computed turbulent kinetic energy for the finest grid will be compared to the experimental results in the upstream symmetry plane, as well as in planes 05 and 10. It is worth mentioning that as the experimental results for the upstream symmetry plane only measured two of the three turbulent kinetic energy components, the third has been approximated using a relationship for the velocity components for a fully developed flat plate boundary layer as prescribed by Wilcox (2006):

$$\bar{u'} : \bar{v'} : \bar{w'} \approx 4 : 2 : 3 \tag{4.9}$$

Figure 4.12 shows that the $k - \epsilon$ model does a poor job of predicting the upstream symmetry plane turbulent kinetic energy, with neither the profile shapes nor intensities being close to the experimental result, although the contour shapes are similar to the results of Apsley and Leschziner (2001). However, the agreement between the computational and experimental results is improved in plane 05, where they are qualitatively similar, although the looping structure centred along $\frac{Z}{T} = 0.95$ in the experiment is somewhat closer to the wing than in the numerical results, but its intensity is significantly under-predicted. The agreement further improves in plane 10, by which time qualitative agreement is clear except for the the experimental near-wing high intensity structure. The high intensity structure is predicted to be located much closer to the corner of the wing-floor junction, and still suffers from a reduced intensity relative to the experimental maximum.

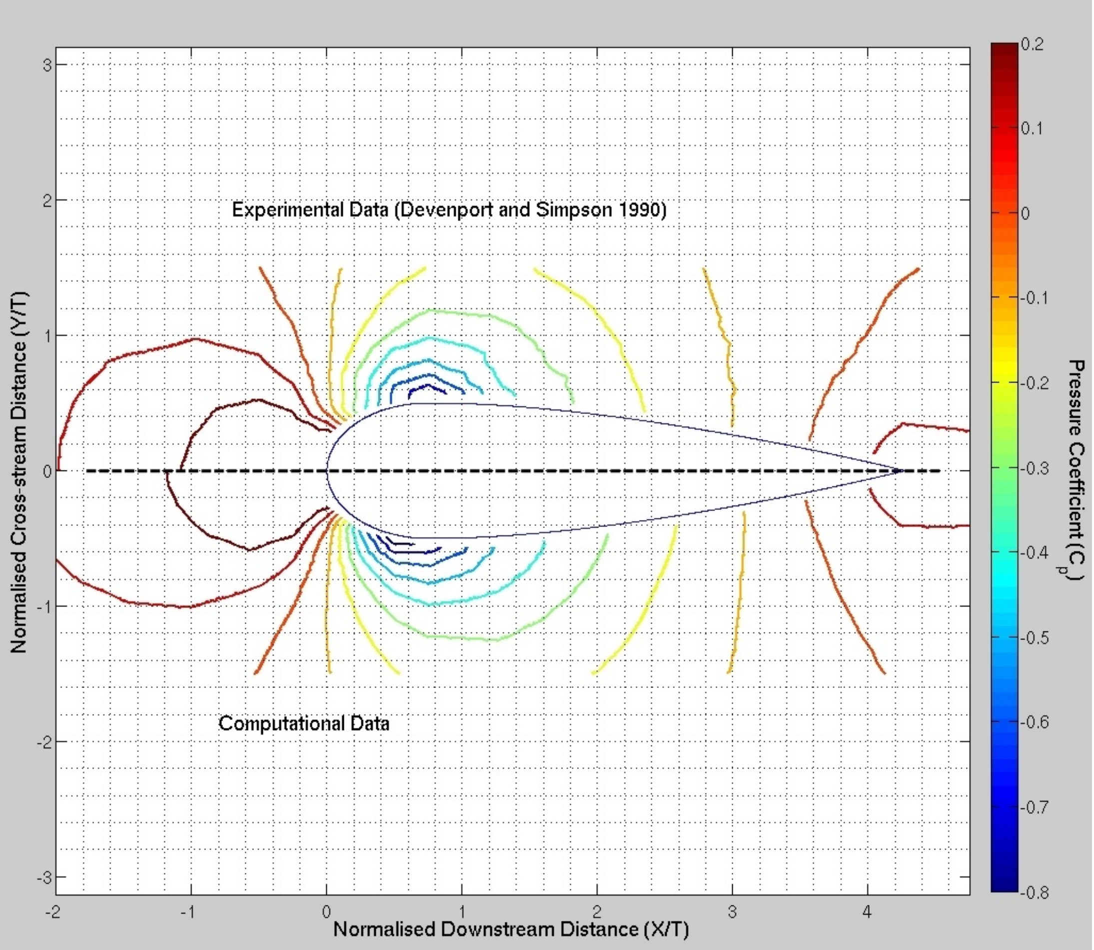

Figure 4.7: $k - \epsilon$ model very-fine grid flat plate pressure coefficient plot.

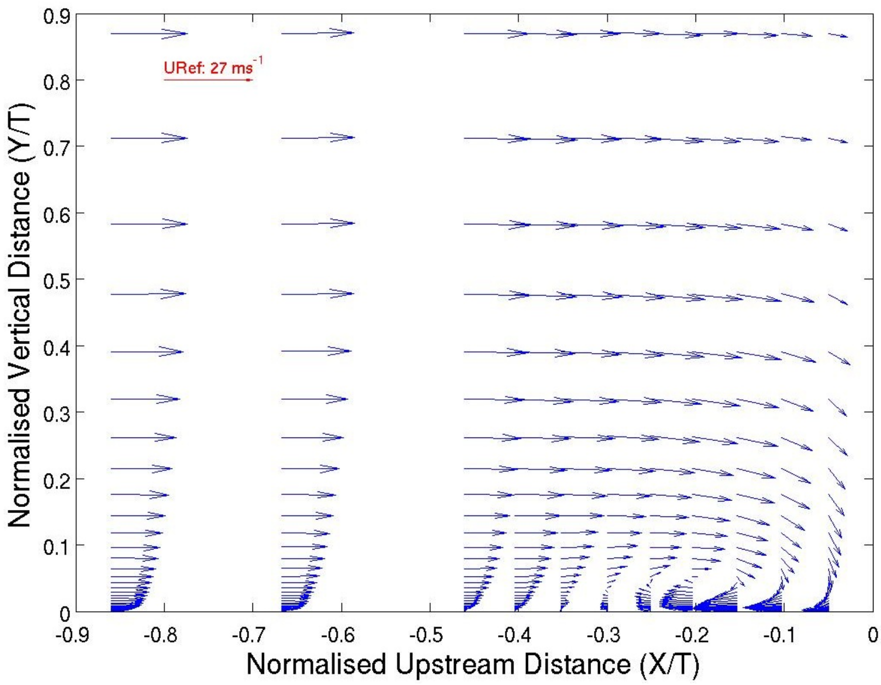

(a) Devenport and Simpson (1990) experiment upwind symmetry plane velocity vector plot.

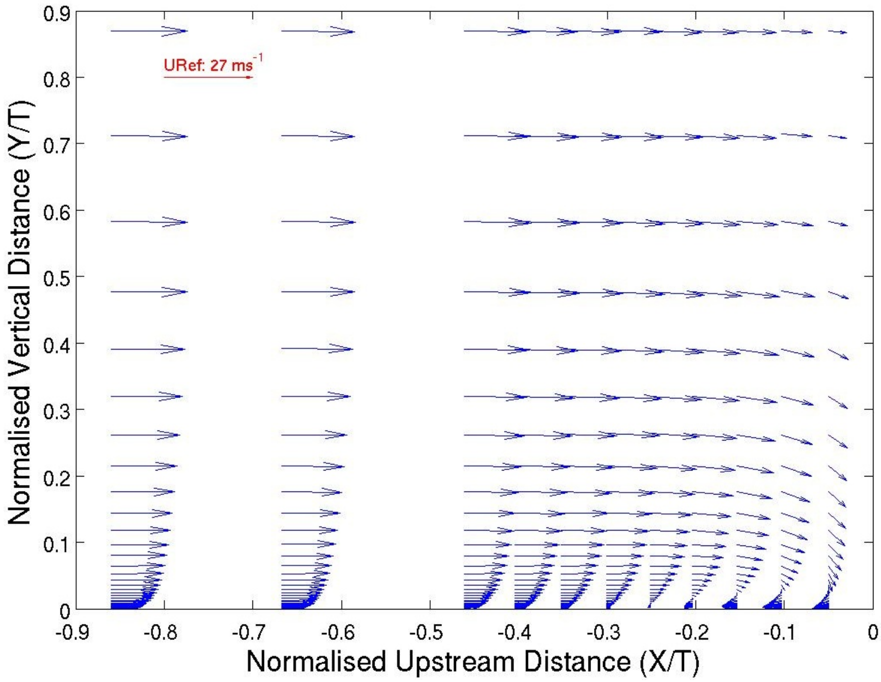

(b) $k - \epsilon$ model upwind symmetry plane velocity vector plot.

Figure 4.8: $k - \epsilon$ model upwind symmetry plane velocity vector plot compared with Devenport and Simpson (1990) experiment.

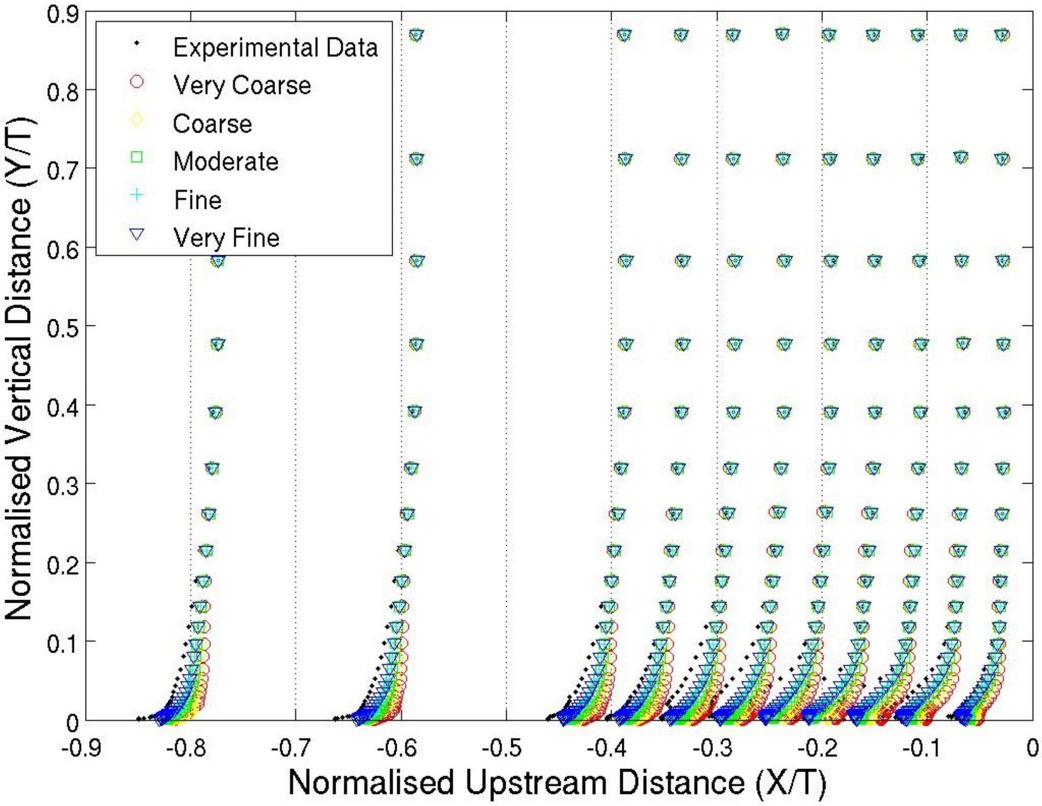

Figure 4.9: $k - \epsilon$ model grid dependence of upstream symmetry plane velocity profiles.

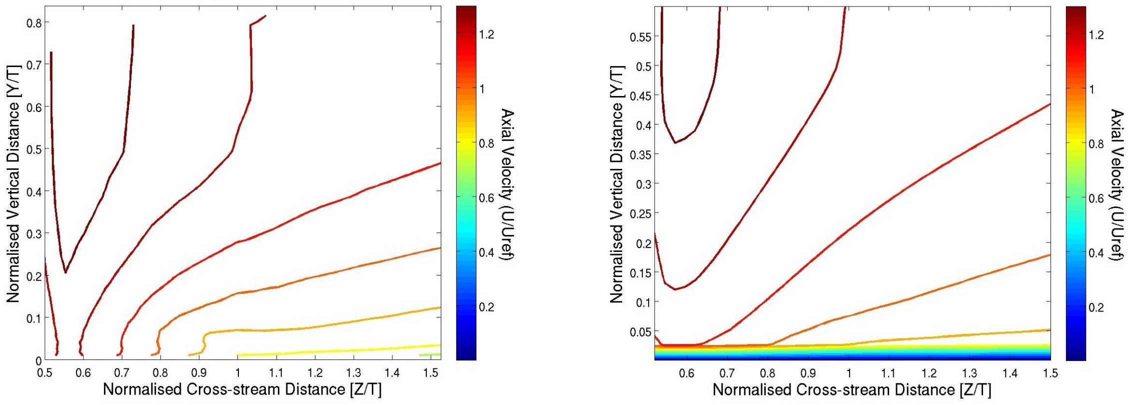

(a) Devenport and Simpson (1990) experiment plane 05 axial velocity contour plot.

(b) $k-\epsilon$ model plane 05 axial velocity contour plot.

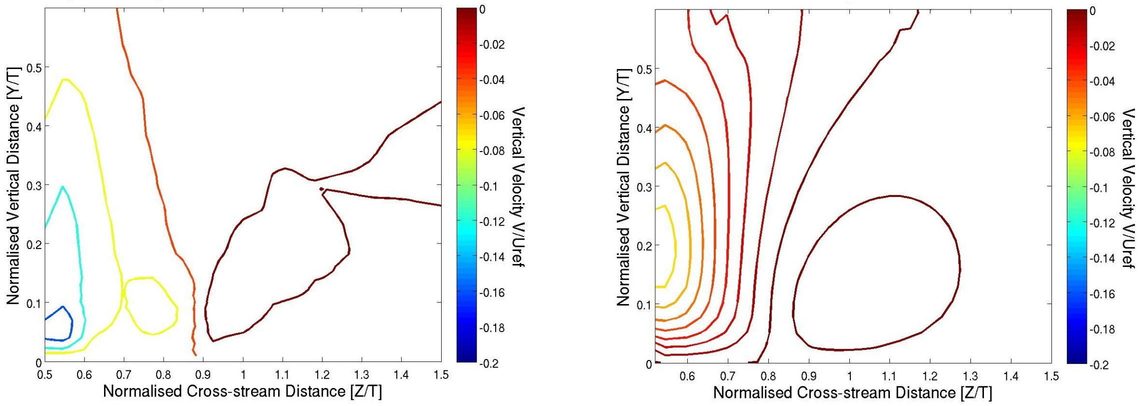

(c) Devenport and Simpson (1990) experiment plane 05 vertical velocity contour plot.

(d) $k-\epsilon$ model plane 05 vertical velocity contour plot.

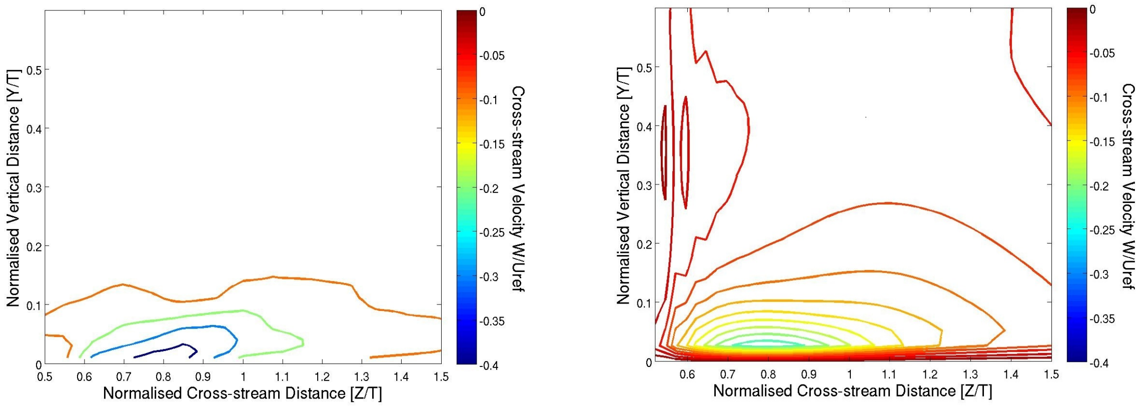

(e) Devenport and Simpson (1990) experiment plane 05 cross-stream velocity contour plot.

(f) $k-\epsilon$ model plane 05 cross-stream velocity contour plot.

Figure 4.10: $k-\epsilon$ model plane 05 velocity contour plots compared with Devenport and Simpson (1990) experiment.

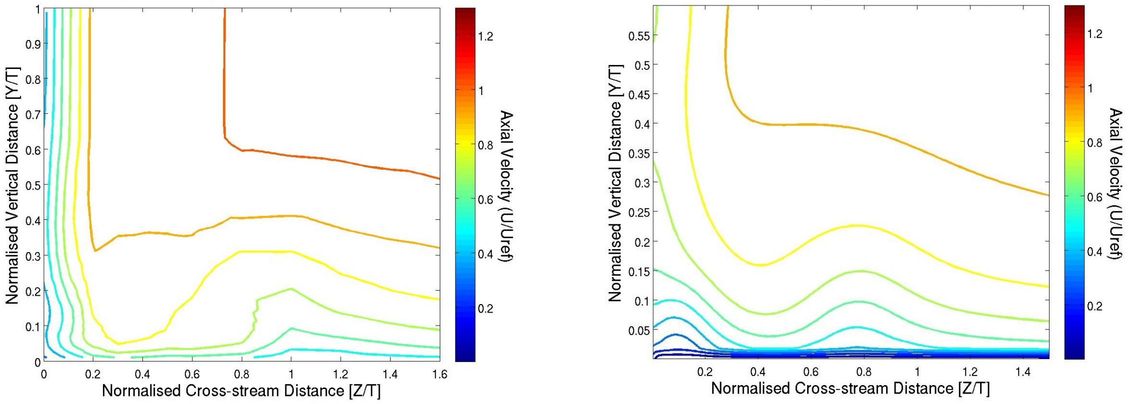

(a) Devenport and Simpson (1990) experiment plane 10 axial velocity contour plot.

(b) $k - \epsilon$ model plane 10 axial velocity contour plot.

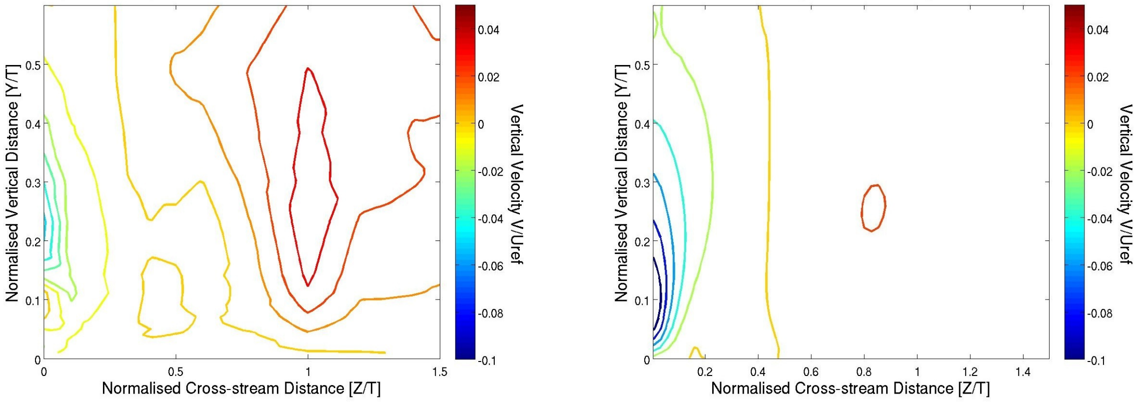

(c) Devenport and Simpson (1990) experiment plane 10 vertical velocity contour plot.

(d) $k - \epsilon$ model plane 10 vertical velocity contour plot.

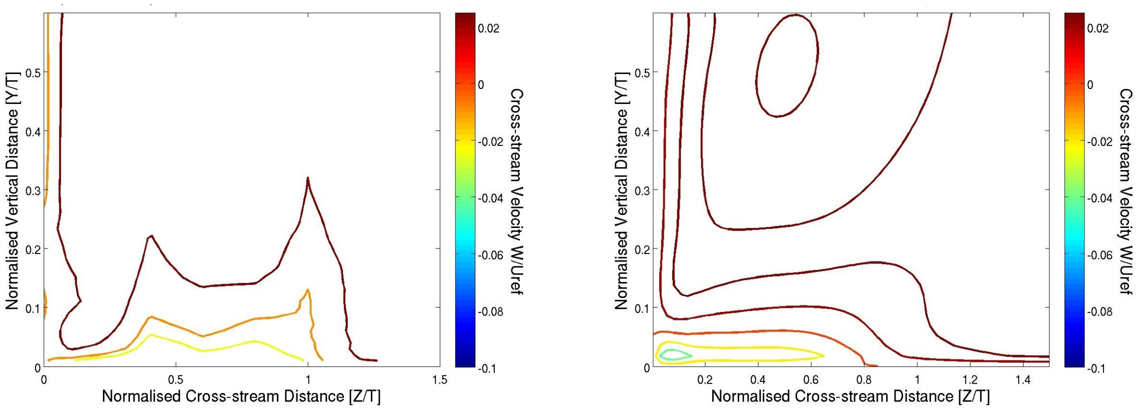

(e) Devenport and Simpson (1990) experiment plane 10 cross-stream velocity contour plot.

(f) $k - \epsilon$ model plane 10 cross-stream velocity contour plot.

Figure 4.11: $k - \epsilon$ model plane 10 velocity contour plots compared with Devenport and Simpson (1990) experiment.

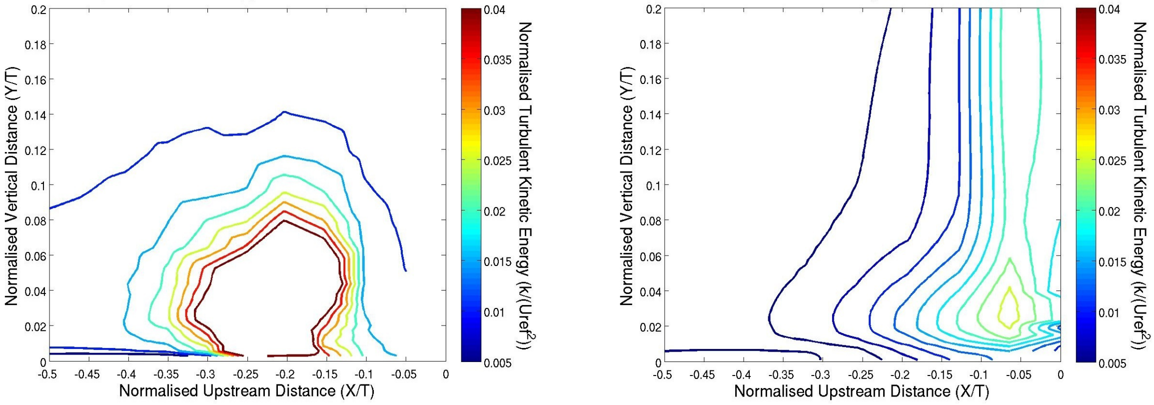

(a) Devenport and Simpson (1990) experiment upstream symmetry plane turbulent kinetic energy contour plot.

(b) $k-\epsilon$ model upstream symmetry plane turbulent kinetic energy contour plot.

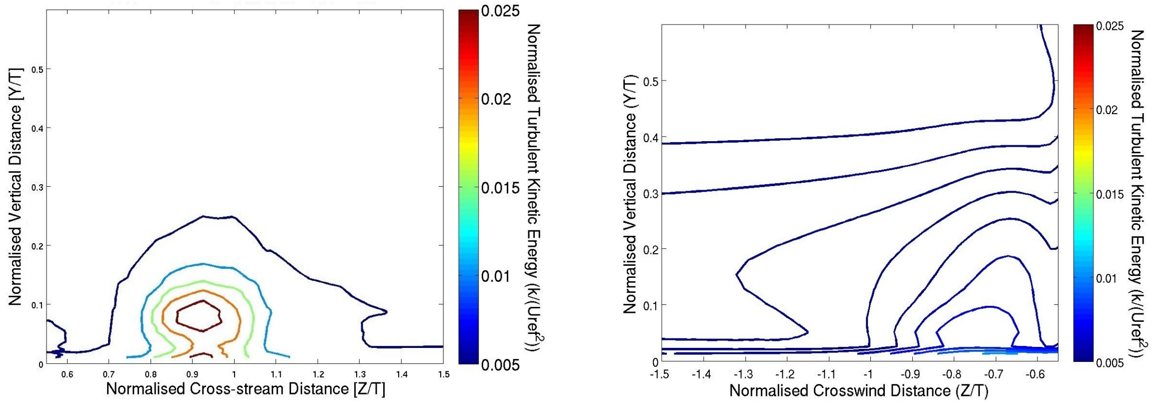

(c) Devenport and Simpson (1990) experiment plane 05 turbulent kinetic energy contour plot.

(d) $k-\epsilon$ model plane 05 turbulent kinetic energy contour plot.

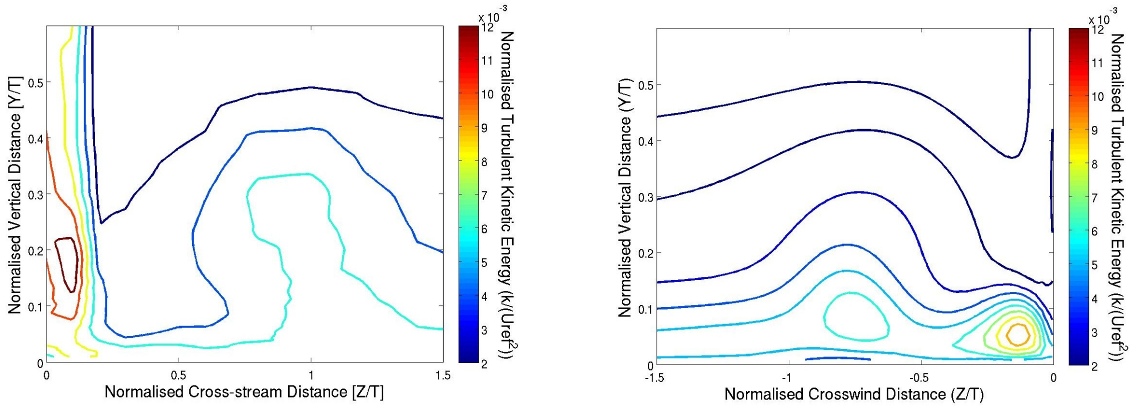

(e) Devenport and Simpson (1990) experiment plane 10 turbulent kinetic energy contour plot.

(f) $k-\epsilon$ model plane 10 turbulent kinetic energy contour plot.

Figure 4.12: $k-\epsilon$ model turbulent kinetic energy contour plots compared with Devenport and Simpson (1990) experiment.

4.8.5 Discussion of Other Model Results

Results for pressure, turbulent kinetic energy, and velocity are presented in Appendix C for the other models used in the study. Some of the more interesting of these are discussed presently. The realisable $k - \epsilon$ model, which to the author's knowledge has never been applied to this case before, achieves the closes match of all the models investigated, for upstream symmetry plane turbulent kinetic energy to the experimental results obtained by Devenport and Simpson (1990), this is given in Figure A.12b. The realisable $k - \epsilon$ also has good performance in predicting the turbulent kinetic energy in the two downstream planes, and so shows itself to be the model of choice where accurate predictions of turbulent kinetic energy level and distributions are required.
Most of the models significantly underpredict the extent of flow recirculation seen in the upstream symmetry plane. The exception to this is, as can be seen in Figure A.20, the $k - \omega$ SST model, which more than successfully captures the amount of recirculating flow, to the point of displaying too much recirculation. The flow returns too far upstream, and the vortex is more oblate and with a centre also further upstream than the experimental result, a result which is consistent with previous studies of this case that had used this model, such as Fu et al. (2007) and Apsley and Leschziner (2001).
The Spalart-Almarras model is the only one which does not, at least to some extent does not at least to some extent, predict the profile peak structure along $\frac{Z}{T} = 1$, as can be seen in Figure 4.11e. Which is attributed to the positioning and weakness of the core vortex the model produces in the upstream symmetry plane, with little recirculation and being positioned very close to the wing leading edge. Starting so close to the leading edge means that the vortex remains near the wing surface as the flow develops downstream, while a weaker initial vortex is not able to exert as strong an influence, and more easily dissipates as the downstream planes are reached.

4.8.6 Effect of Symmetry Plane - Non-symmetric Case Comparison

In order to check that modelling only half of the true situation by utilising the inherent symmetry of the problem, via the use of symmetry boundary conditions, did not have a significant effect on the results, a non-symmetric mesh that was equivalent to the finest mesh was developed. The full mesh case was run with the Realisable $k - \epsilon$ model on this mesh while using the same convergence criteria as for the very fine mesh of the symmetry utilising case. Figure 4.13 compares the pressure coefficient on the flat plate surrounding the wing, while Figures 4.14-4.17 give comparisons of the symmetry plane velocity and turbulent kinetic energy plots, as well as velocity component and turbulent kinetic energy contours for planes 05 and 10, for the symmetric and non-symmetric grid solutions.

The pressure plots shown in Figure 4.13 are similar in form, with both the symmetric and non-symmetric mesh results predicting the region of lowest pressure coefficient to be slightly further upstream of the true maximum thickness location. The symmetry utilising case underestimates the pressure coefficient in the upstream symmetry plane and at the trailing edge, whereas the full case overestimates them. This is consistent with previous results in the literature, specifically Paciorri et al. (2005), which compared the pressure coefficient in the upstream symmetry plane of the full mesh case as well as that utilising symmetry, and also found that the symmetry utilising solution locates the pressure contours further upstream than the full mesh case.

The velocity plots for the symmetry utilising and non-utilising cases shown in Figure 4.14 are very similar, with the only obvious differences being the reduction to zero of the near wall section of the $\frac{X}{T} = -0.85$ and -0.65 profiles, the slight reduction in near wall velocity magnitude, and slight differences in the vertical component of the recirculation, most noticeable on the upstream-flowing component of the $\frac{X}{T} = -0.25$ profile.

Although plane 05 axial and cross-stream contours shown in Figure 4.15 are quite similar, the vertical velocity contour for the full case's near wing contours, which have more tapered tops and greater magnitude than those of the symmetry utilising case, are closer to the experimental data. In plane 10, shown in Figure 4.16, the full case's near-wing vertical velocity contours are again more tapered, but show an even larger overestimation of the near-wing magnitude, than the symmetry plane utilising case does, while the plane 10 axial and cross-stream velocity components are again very similar.

The turbulent kinetic energy contours for both sets of results are of essentially identical shapes, with only small increases in the maximum magnitude of the symmetry utilising case, over that of the full case, serving to differentiate them.

The similarity of the results between the full mesh case and the symmetry plane condition utilising case are sufficiently small to warrant the use of the symmetry plane condition, given the halving of the number of cells required and the associated reduction in computational solution effort.

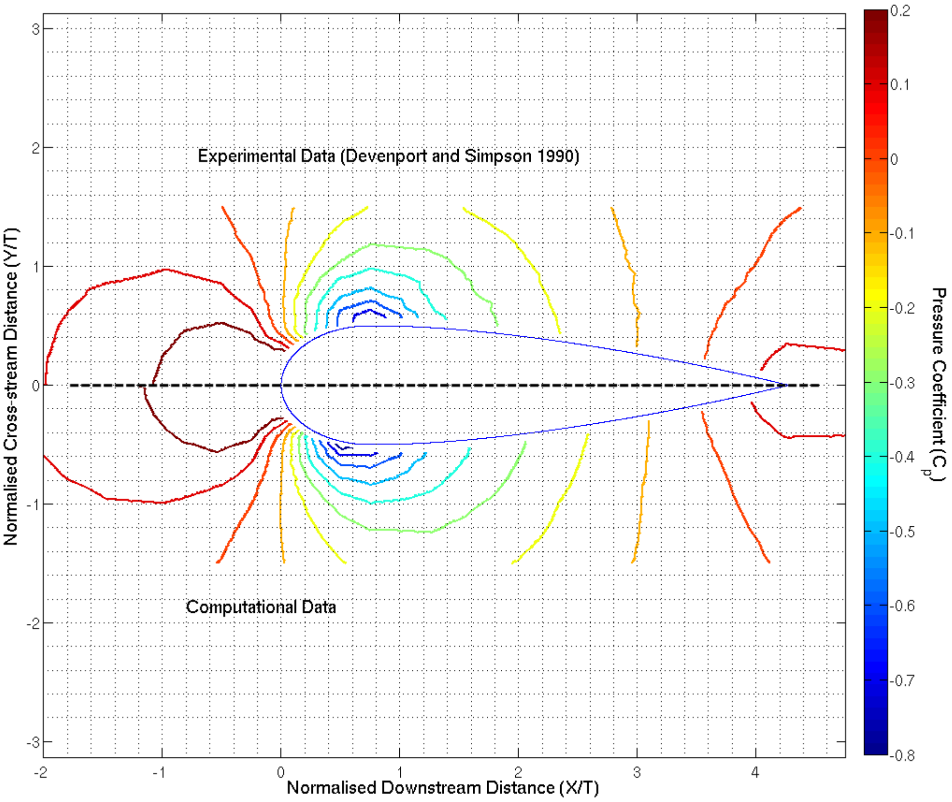

(a) Symmetry utilising case flat plate pressure coefficient contour plot.

(b) Non-symmetric case flat plate pressure coefficient contour plot.

Figure 4.13: Symmetry effect investigaton flat plate pressure coefficient contour plots.

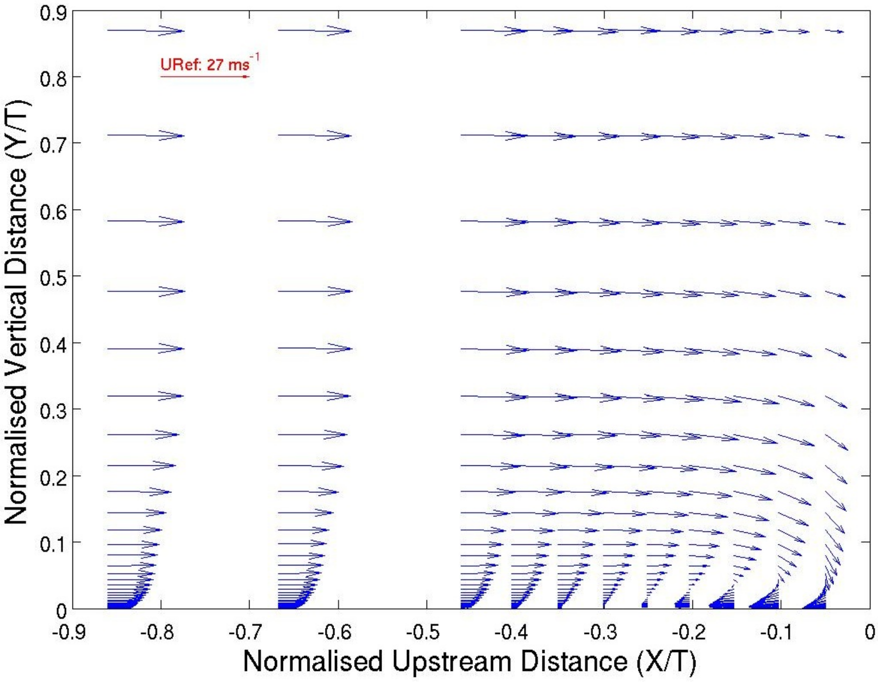

(a) Symmetry utilising case upwind symmetry plane velocity vector plot.

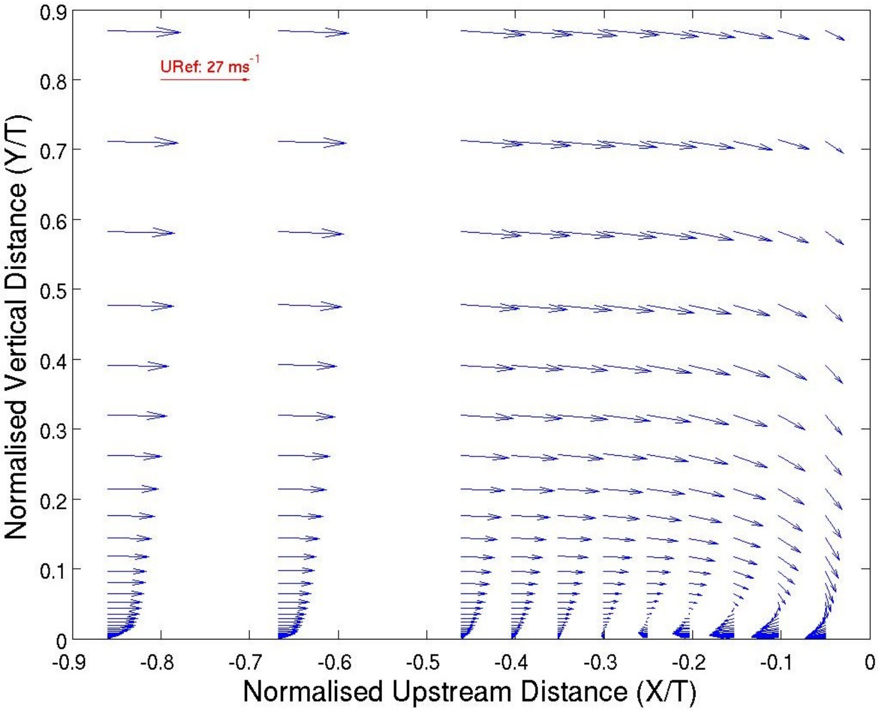

(b) Non-symmetric case upwind symmetry plane velocity vector plot.

Figure 4.14: Symmetry effect investigaton upwind symmetry plane velocity vector plots.

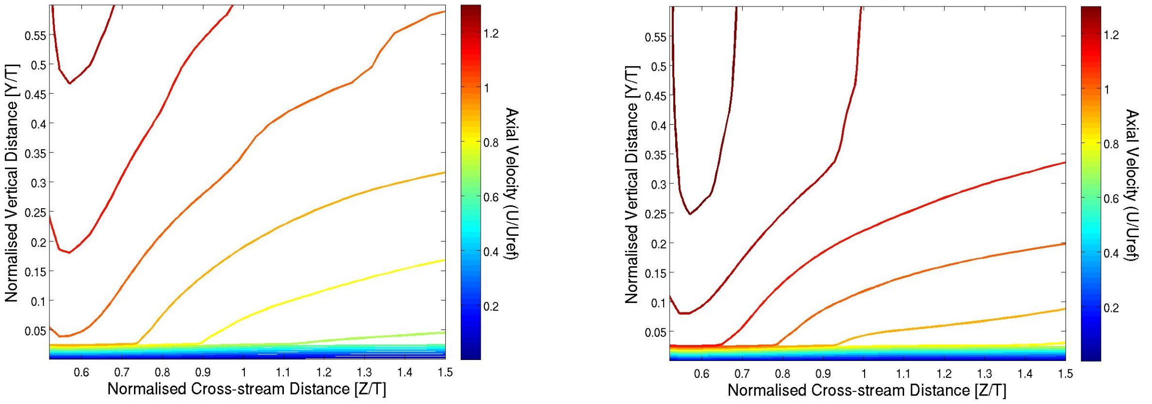

(a) Non-symmetric case plane 05 axial velocity contour plot.

(b) Symmetry utilising case plane 05 axial velocity contour plot.

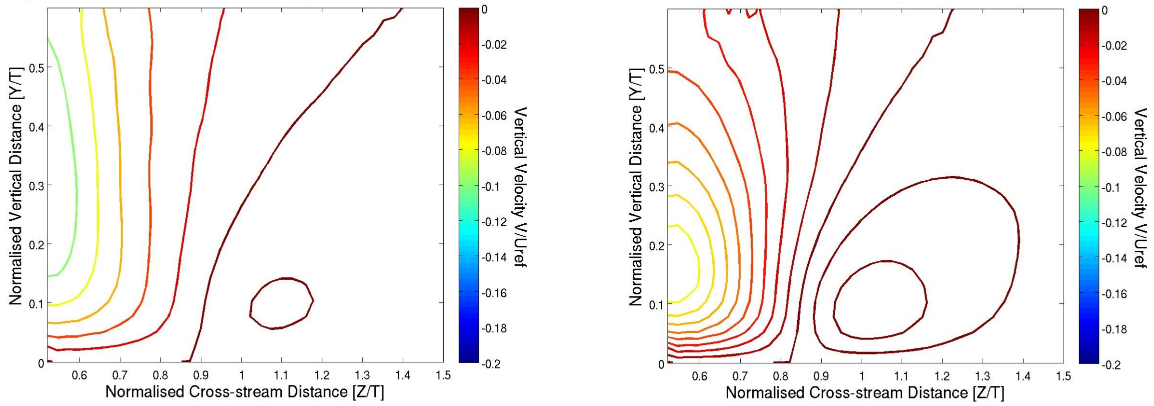

(c) Non-symmetric case plane 05 vertical velocity contour plot.

(d) Symmetry utilising case plane 05 vertical velocity contour plot.

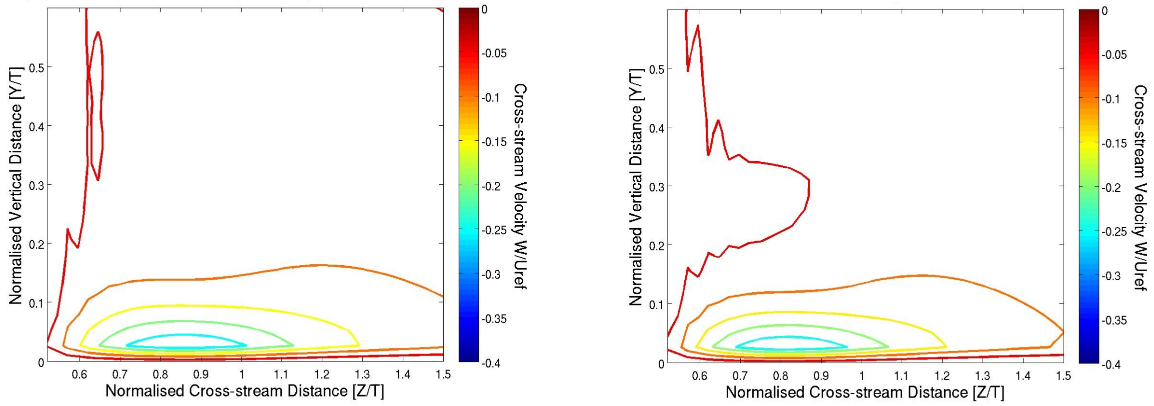

(e) Non-symmetric case plane 05 cross-stream velocity contour plot.

(f) Symmetry utilising case plane 05 cross-stream velocity contour plot.

Figure 4.15: Symmetry effect investigaton plane 05 velocity contour plots

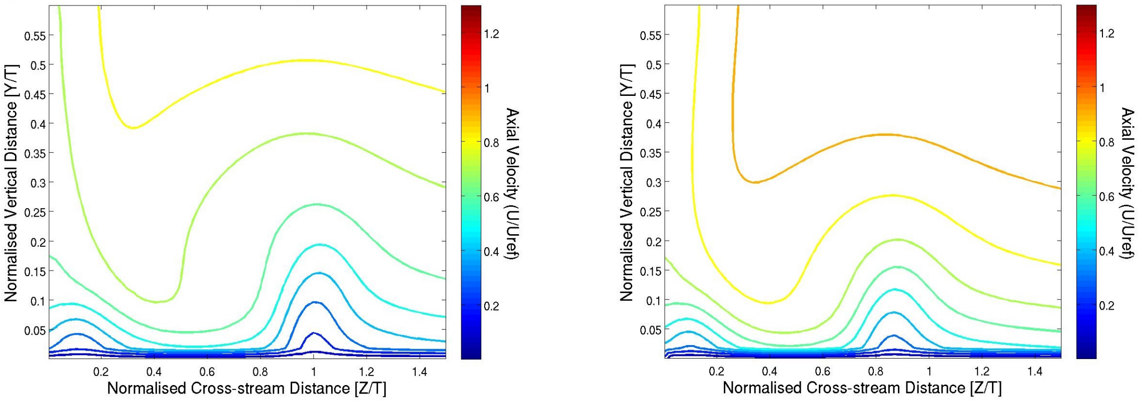

(a) Non-symmetric case plane 10 axial velocity contour plot.

(b) Symmetry utilising case plane 10 axial velocity contour plot.

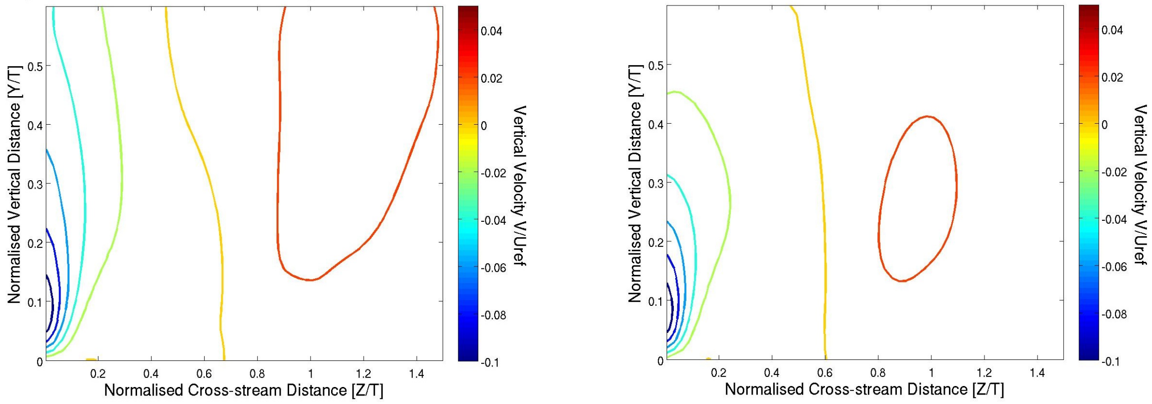

(c) Non-symmetric case plane 10 vertical velocity contour plot.

(d) Symmetry utilising case plane 10 vertical velocity contour plot.

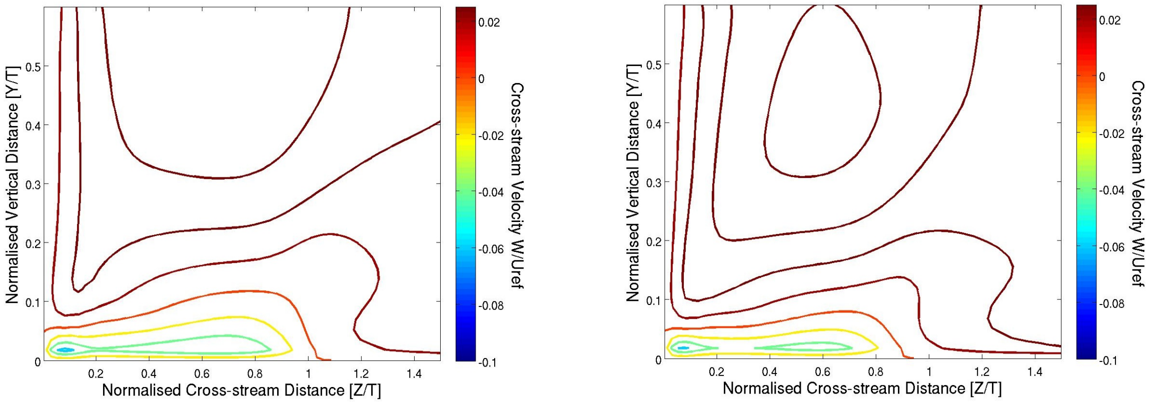

(e) Non-symmetric case plane 10 cross-stream velocity contour plot.

(f) Symmetry utilising case plane 10 cross-stream velocity contour plot.

Figure 4.16: Symmetry effect investigaton plane 10 velocity contour plots.

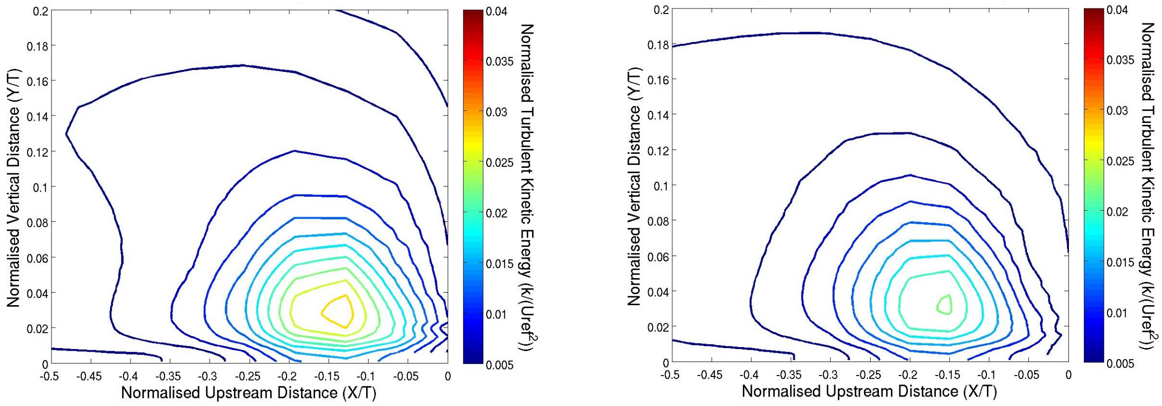

(a) Symmetry utilising case upstream symmetry plane turbulent kinetic energy contours plot.

(b) Non-symmetric case upstream symmetry plane turbulent kinetic energy contours plot.

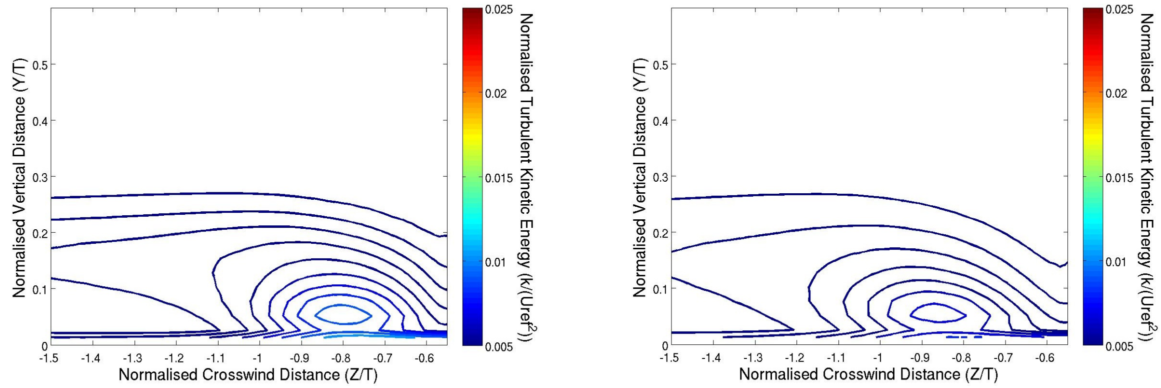

(c) Symmetry utilising case plane 05 turbulent kinetic energy contours plot.

(d) Non-symmetric case plane 05 turbulent kinetic energy contours plot.

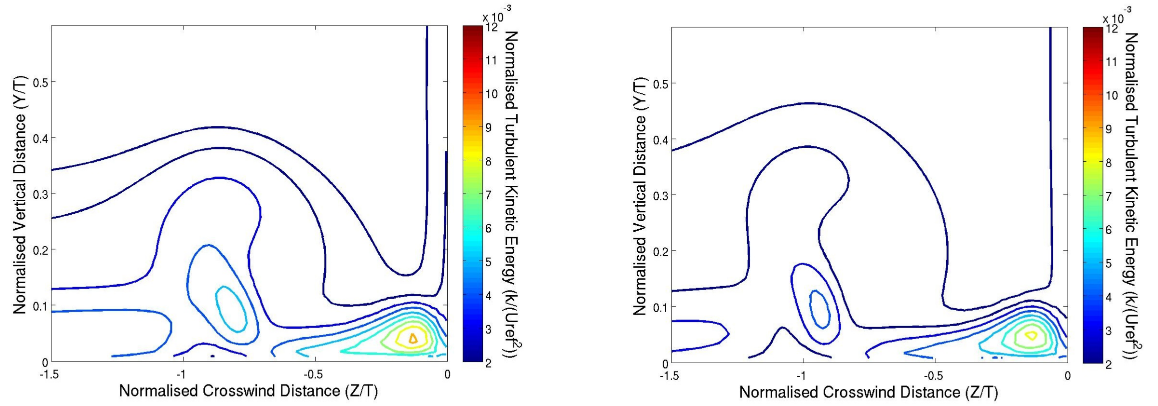

(e) Symmetry utilising case plane 10 turbulent kinetic energy contours plot.

(f) Non-symmetric case plane 10 turbulent kinetic energy contours plot.

Figure 4.17: Symmetry effect investigaton turbulent kinetic energy contour plots.

4.8.7 Semi-Infinite Wing Height Effect

As mentioned in Section 4.2 it was hoped that having a computational domain of increased vertical extent ($\frac{Y}{C} = 4.25$), would help to increase the accuracy of the simulations relative to those with smaller vertical dimension. In order to confirm this, and determine whether any trends result from raising and lowering the vertical domain, the finest mesh (see Table 4.4) was transformed by uniformly stretching/compressing it vertically and comparing the results. The transformation leaves the same total number of cells as well as cell composition. The height was varied from $\frac{Y}{T} = 1.75$-5.5 in units of $\frac{Y}{T} = 1.25$ for a total of 3 new values: $\frac{Y}{T} = 1.75$, 3 and 5.5, in addition to the value of 4.25 used for the validation case. These were all run using the Realisable $k - \epsilon$ model to the same residual specification as for the very fine mesh case, given in Table 4.5, from which they were adapted. As expected the results are largely self-similar, but with certain features showing increased agreement with the experimental results, as the height is increased.

Due to the difficulty of discerning any differences between the flat plate pressure coefficient of the various height cases, they have been omitted, and the results of the validation case $\frac{Y}{T} = 4.25$ as given in Figure A.7 serve to illustrate these results.

A feature sensitive to the type of turbulence modelling adopted, is the recirculation zone just ahead of the wing leading edge, and so any changes that occur as the semi-infinite wing height is varied should be observable by inspecting the velocity in this region. Figures 4.18 and 4.19 show the velocity vector field, and velocity profile plots, in the symmetry plane for the various heights' cases respectively. For all heights investigated, the Realisable $k - \epsilon$ model does a good job of recreating the recirculation and vortex, though it significantly underestimates the reverse flow. There are two trends apparent as the height is increased; upstream flow recirculation and the vertical velocity components of the recirculation region. The first trend is that as height is increased, the extent to which the flow recirculates upstream also increases, approaching the experimental value. This also has the effect of slightly reducing the velocity of the flow nearest the floor further upstream. The second trend is that as the height is increased, the vertical components of the recirculation region also grow. Although present and noticeable, it should be pointed out that these changes are relatively small when compared to the differences in predictions between the various models employed.

Figure 4.20 gives the upstream symmetry plane turbulent kinetic energy contours as predicted for the various heights. Even for the largest height differences, these contours show much greater similarity than the contours for any two differing turbulence models. There is a trend with increasing height on the outermost radius contours, where they are pulled inward, show slight decreases in magnitude, and bend towards a less smooth shape, as the height is increased.

It has been determined that, although largely similar, the results do show increased general agreement with the experimental results as the height of the domain is increased. This supports the selection of a larger than usually prescribed computational domain for the validation case, such as was selected in Section 4.2. It is worth noting, however, that such increases cannot be taken to extremes, as an increased domain size necessitates a larger number of cells, and hence has larger solution times. A balance must be struck between domain size selection and its computationally feasible meshing and solution.

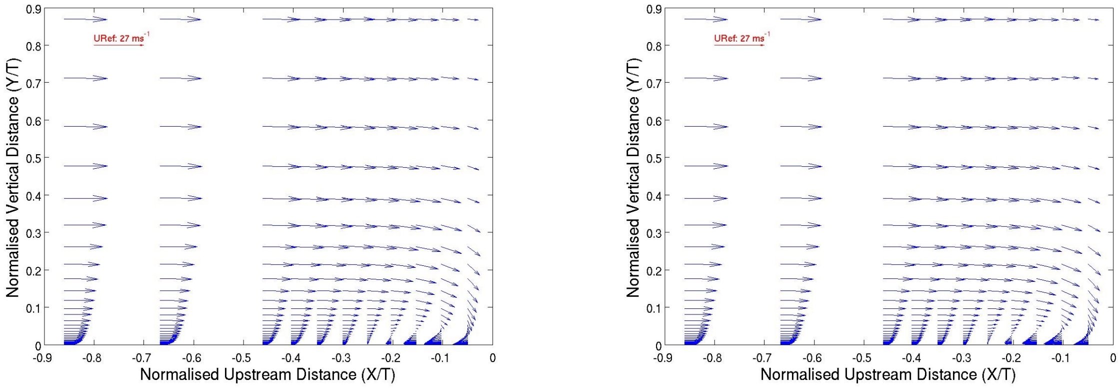

(a) Height $\frac{Y}{T} = 1.75$ upstream symmetry plane velocity vector plot.

(b) Height $\frac{Y}{T} = 3.0$ upstream symmetry plane velocity vector plot.

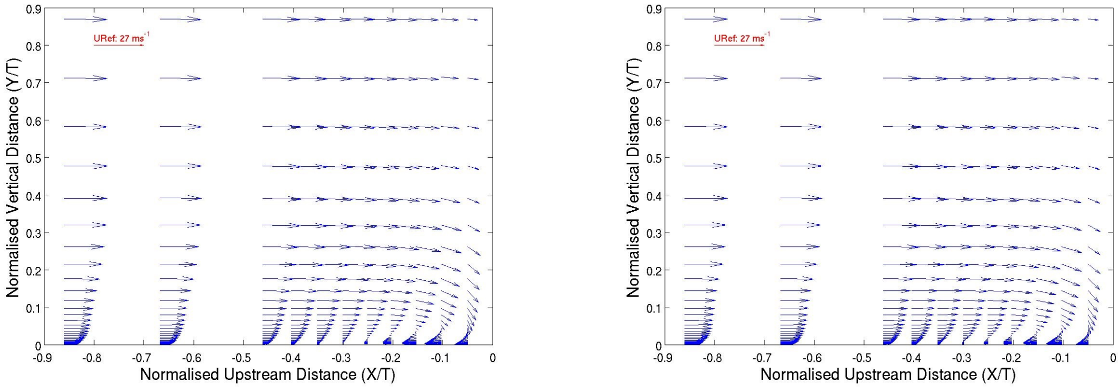

(c) Height $\frac{Y}{T} = 4.25$ upstream symmetry plane velocity vector plot.

(d) Height $\frac{Y}{T} = 5.5$ upstream symmetry plane velocity vector plot.

Figure 4.18: Height variation investigation upstream symmetry plane velocity vector plots.

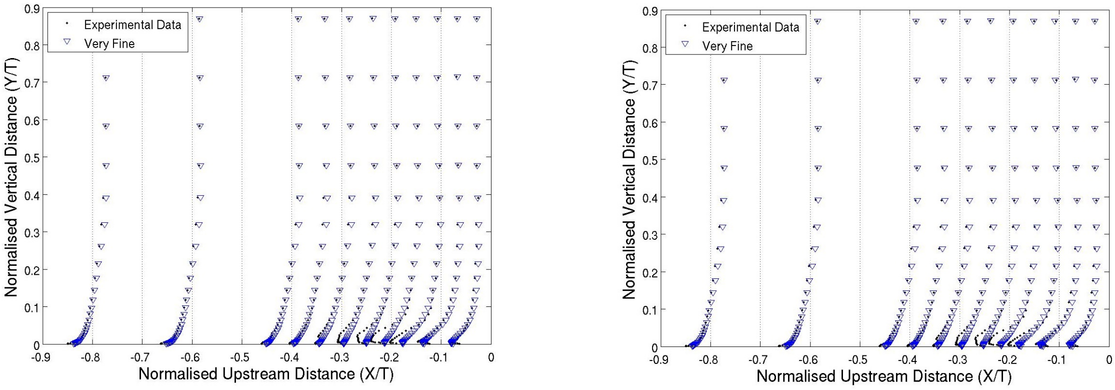

(a) Height $\frac{Y}{T} = 1.75$ upstream symmetry plane velocity profile plot.

(b) Height $\frac{Y}{T} = 3.0$ upstream symmetry plane velocity profile plot.

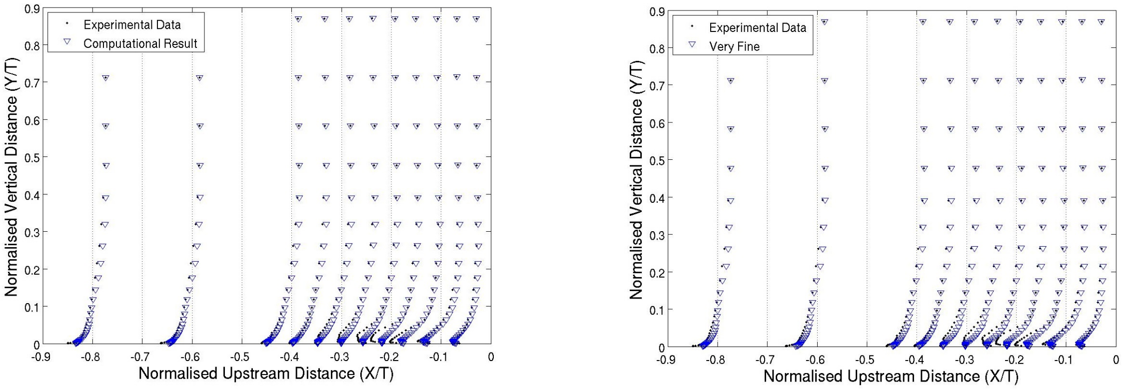

(c) Height $\frac{Y}{T} = 4.25$ upstream symmetry plane velocity profile plot.

(d) Height $\frac{Y}{T} = 5.5$ upstream symmetry plane velocity profile plot.

Figure 4.19: Height variation investigation upstream symmetry plane velocity profile plots.

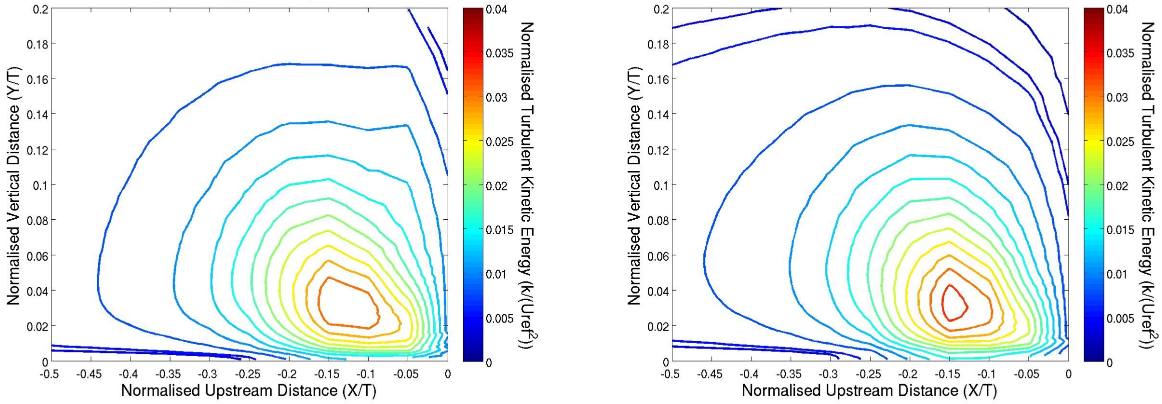

(a) Height $\frac{Y}{T} = 1.75$ upstream symmetry plane turbulent kinetic energy contour plot.

(b) Height $\frac{Y}{T} = 3.0$ upstream symmetry plane turbulent kinetic energy contour plot.

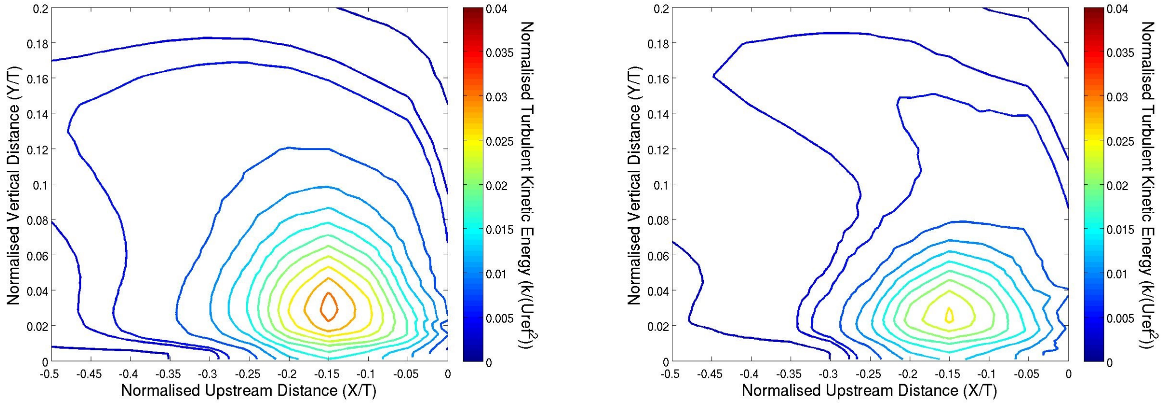

(c) Height $\frac{Y}{T} = 4.25$ upstream symmetry plane turbulent kinetic energy contour plot.

(d) Height $\frac{Y}{T} = 5.5$ upstream symmetry plane turbulent kinetic energy contour plot.

Figure 4.20: Height variation investigation upstream symmetry plane turbulent kinetic energy contour plots.

4.8.8 Compute Times

In order to compare the solution speed of the various models fairly, it is necessary to compare the coarsest grid run, as it is only the coarsest grid runs which are all initialised with the same values for the internal fields. All the cases were run with the same numerical settings, except for the non-mapped Launder-Gibson and LRR cases, which required significantly greater initial relaxation factors in order to converge from the standard initialisation condition.

By mapping the solution for one of the other models as the initialisation of the RSTM models, it is possible to achieve convergence with the less strict relaxation factors. Therefore it could be possible that a faster overall solution time may be achieved, by running one of the simpler models first from the standard initialisation condition, then mapping the solution over to an RSTM model and running it with looser relaxation numerics. Also considered was the effect of further adjusting the relaxation numerics of the RSTM cases, to see if a change in solution time could be achieved. These considerations were investigated by comparison between both the alternate methods, and unadjusted, unmapped results. All results are given in Figure 4.21. For the mapped solution times, the time of their own solution has been added to the time required to achieve the solution from which they were mapped, which is the $k-\epsilon$ case. As shown in Figure 4.21, the $k-\epsilon$ based models outperform the others in terms of solution speed, even the simpler Spalart-Allmaras model which, with the $k-\omega$ SST model, closely follow the $k-\epsilon$ based models. The plain $k-\omega$ model takes significantly longer than the other one and two equation models, but still significantly less time than either the mapped, or relaxed RSTM method. Comparison of the relaxation and mapping methods reveals that the mapping method results in faster solution times, compared to the unadjusted relaxation method, but slower solution times to the adjusted relaxation method.

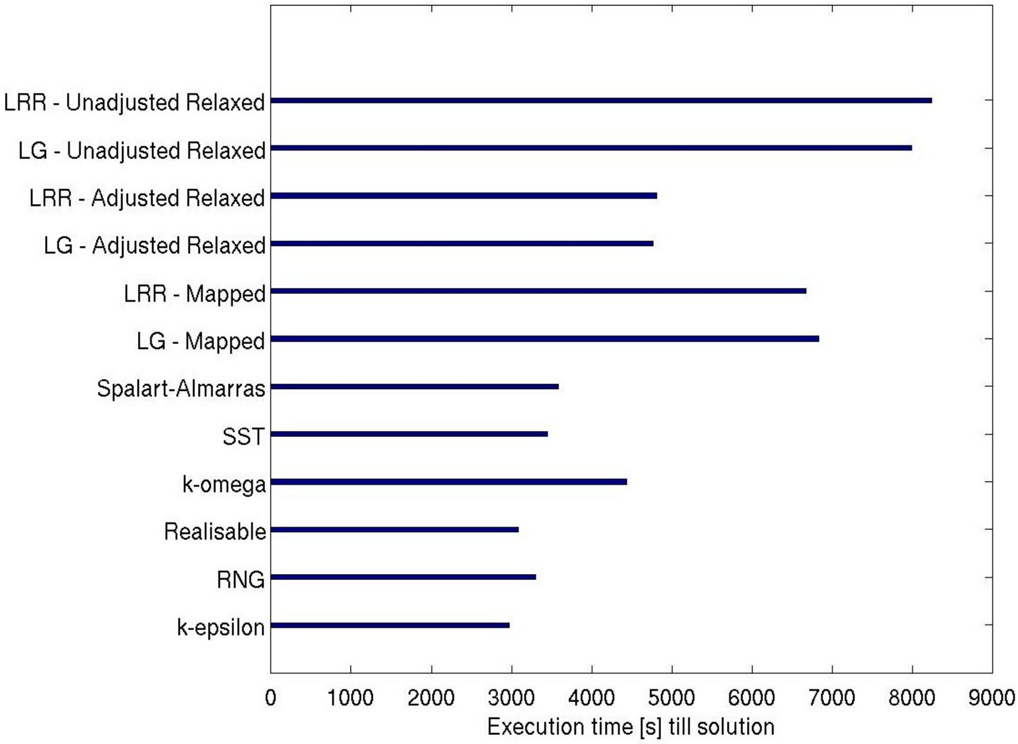

Figure 4.21: Coarsest Grid Solution Speed Comparison

4.9 Conclusions and Summary

A junction flow was investigated using RANS simulations and employing eight turbulence models. The results for the turbulence models which had been previously used in investigations of this case from the literature were compared with those obtained in this investigation. The results showed good agreement provinding confidence in the flow modelling methods used. For the models which had not, to the Author's knowledge, been used on this case previously, the results were compared with those of the other models and the experimental data of Devenport and Simpson (1990) and Devenport and Simpson (1992). Both the LRR and Launder-Gibson models showed better predictive results than most of the simpler one and two equation models, except for the Realisable $k - \epsilon$ model, which had the best performance of all the models used, for velocity, and kinetic energy results, and is arguably tied for best result with the LRR model for the flat plate pressure prediction. Although these results are for a semi-infinite wing-in-junction flow case, they provide justification for the selection of the Realisable $k - \epsilon$ model for the further work contained in this study on the basis of both accuracy and speed.

5 2D to 3D Test Cases

5.1 Introduction and Background

The aim of this chapter is to validate the implementation of the 3D-RSNM-TE noise prediction model as detailed in Section 3.8 as well as to investigate the performance of the model against a number of test cases from the literature. The method is applied to three test cases from the literature, namely a flat plate, a NACA 0012 airfoil, and a DU96 airfoil. The first test case, referred to as FP12, is based on the work of Albarracin et al. (2011, 2012b), in which the 2D RSNM method was applied to a sharp-edged symmetric flat strut following the work of Moreau et al. (2011). The second test case is based on the work of Albarracin et al. (2012a) regarding a NACA0012 profile airfoil following the work of Devenport et al. (2010a). The final test case is also based on the work of Albarracin et al. (2012a), regarding a DU96 profile airfoil and again follows the work of Devenport et al. (2010a).

5.2 Details and Methodologies

Salient details of the test cases are summarised in Table 5.1, and discussed at length in the following.

Table 5.1: Test Case Summary

Test Case Name	Geometric and Flow Properties					Mesh		
	Re_C	AOA [degrees]	Chord [m]	Span [m]	Ti [%]	Coarse [cells]	Moderate [cells]	Fine [cells]
FP12	5E5	0	0.2	0.45	1.6	4.8E5	1.96E6	7.68E6
NACA0012	4.02E6	0	0.914	1.8	0.05	1.13E5	4.52E5	7.68E6
DU96	2.165E6	3.1	0.914	1.8	0.05	3.47E5	1.39E6	5.55E6

The geometry of the first test case is a flat plate model with chord of $c = 200$ mm, span of $s = 450$ mm, thickness of $h = 5$ mm, circular leading edge with radius of $r = 2.5$ mm and symmetrical wedge-shaped trailing edge with an apex angle of 12°, shown in Figure 5.1. The geometry for the second test case is a NACA 0012 airfoil of chord 0.914 m and span 1.8 m, while the geometry for the third test case is a DU 96 (W-180) airfoil of chord 0.914 m and span 1.8 m.

For each of the test cases, 2D Low-Reynolds number RANS turbulence modelling simulations were performed, and the CFD flow results are compared with the experimental and CFD results from the literature. In all cases the 2D flow results are then sub-divided along the spanwise direction, as shown, using alternating shades of grey from white to black, in Figure 5.2, and the 3D-RSNM-TE method applied to the result to produce a TE noise prediction. In each test case the number of subdivisions considered (N) is given by $N = 2^J, J = 0, 1, 2, \ldots$, such that N varies from at least 32 to a maximum of 512. These values were chosen for ease of coding, as well as providing a simple and consistent refinement factor for convergence study. The noise predictions are then compared against noise measurements given in the literature.

The meshes used for each test case have CH mesh topologies (Laurence and Rodi, 1999) composed of hexahedral elements. The FP12 case mesh, examples of which are shown in Figures

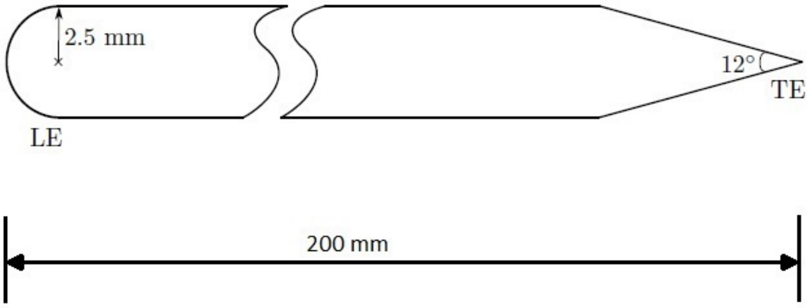

Figure 5.1: Schematic diagram of flat plate model geometry. Image adapted from Moreau et al. (2011).

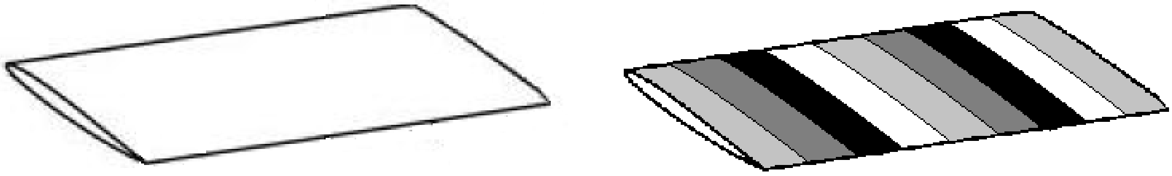

(a) Pre-Slicing TE of Plate

(b) Post-Slicing TE of Plate

Figure 5.2: Slicing process visualisation

5.3 and 5.4, takes advantage of the symmetry along the plate centerline, with the inlet extending one chord upstream as well as cross-stream of the plate; the same boundary locations used in the literature case (Albarracin et al., 2011). Three meshes were used with explicit cell doubling used between mesh levels, resulting in 480,000, 1,960,000, and 7,680,000 total cells for the coarse, moderate, and fine meshes respectively. The NACA0012 and DU96 case meshes are given in Figures 5.5 through 5.8. In each case, three meshes were used, again with explicit cell doubling used between mesh levels, resulting in 112,998, 451,992 and 1,807,968, and 346,580, 1,386,320 and 5,545,280 total cells for the coarse, moderate and fine meshes for the NACA0012 and DU96 cases, respectively.

For each case the inlet velocity boundary condition was set to be a uniform speed: 38 m/s for the FP12 case, 66 m/s for the NACA0012 case, and 29 m/s at 3.1 degrees angle of attack relative to the airfoil for the DU96 case. For each case the inlet turbulence intensities, 1.6%, 0.05% and 0.05% for the FP12, NACA0012 and DU96 cases, respectively, were used to set the uniform inlet turbulence properties using the eddy viscosity ratio (see Section 4.4.1) method with an assumed viscosity ratio of 1. For each case the inlet pressure boundary condition is specified to be a Neumann type boundary condition with zero spatial gradient in the (inlet) plane normal direction. The turbulence viscosity on the inlet was calculated from the flow and turbulence properties, according to the turbulence model used for the case. As part of a separate investigation, not detailed here, of which turbulence models produced the most accurate predictions for turbulence properties for use with the noise prediction method, the cases originally had a number of turbulence models applied. Only those producing the best results are detailed in the present work. The FP12 case was solved using a Low-Re implementation of the Launder-Sharma (Standard) k-ϵ model, while the NACA0012 and DU96 cases were both solved using the k-ω-SST model, full details of which are given in Appendix C. These models were selected based on a separate study into which turbulence models, k-ω or k-ϵ and meshing-modelling approaches, wall modelled or low-Re turbulence model utilising wall resolving, produce better

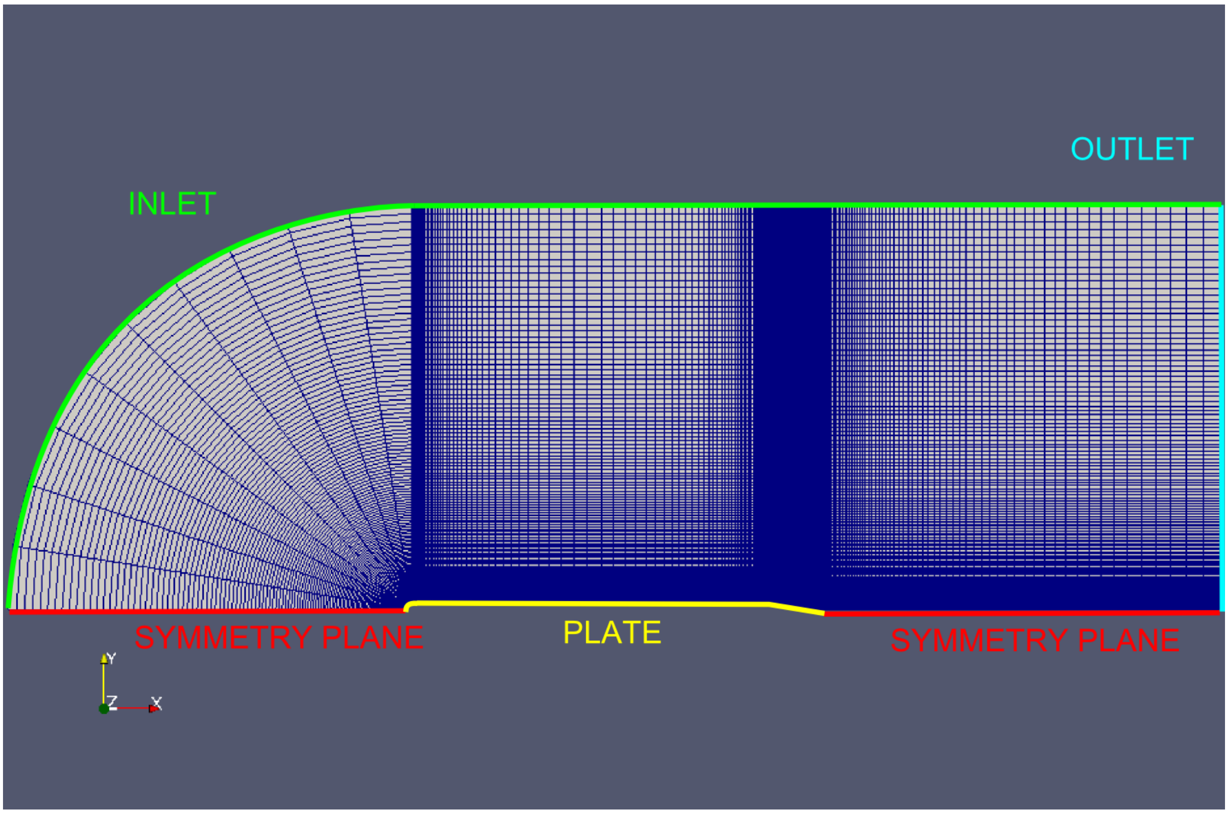

Figure 5.3: FP12 case mesh topology

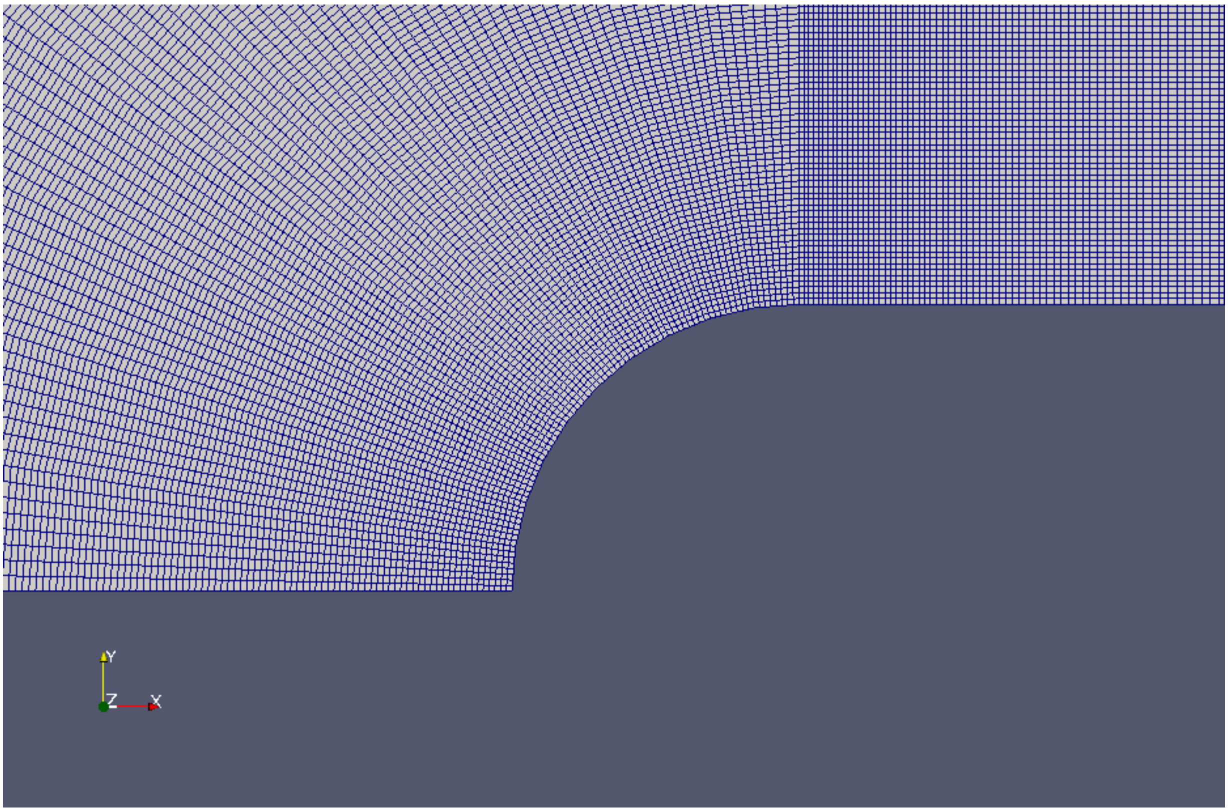

Figure 5.4: FP12 case coarse mesh LE closeup

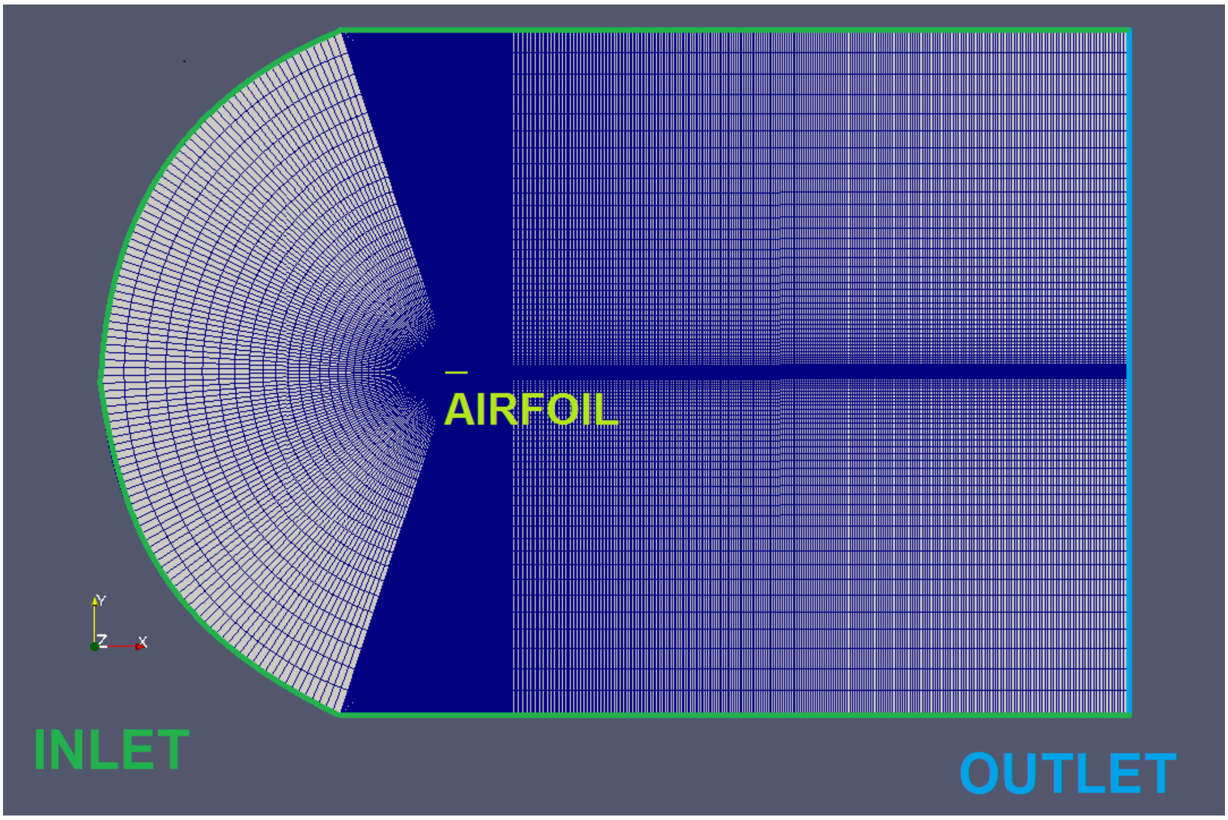

Figure 5.5: NACA0012 case mesh topology

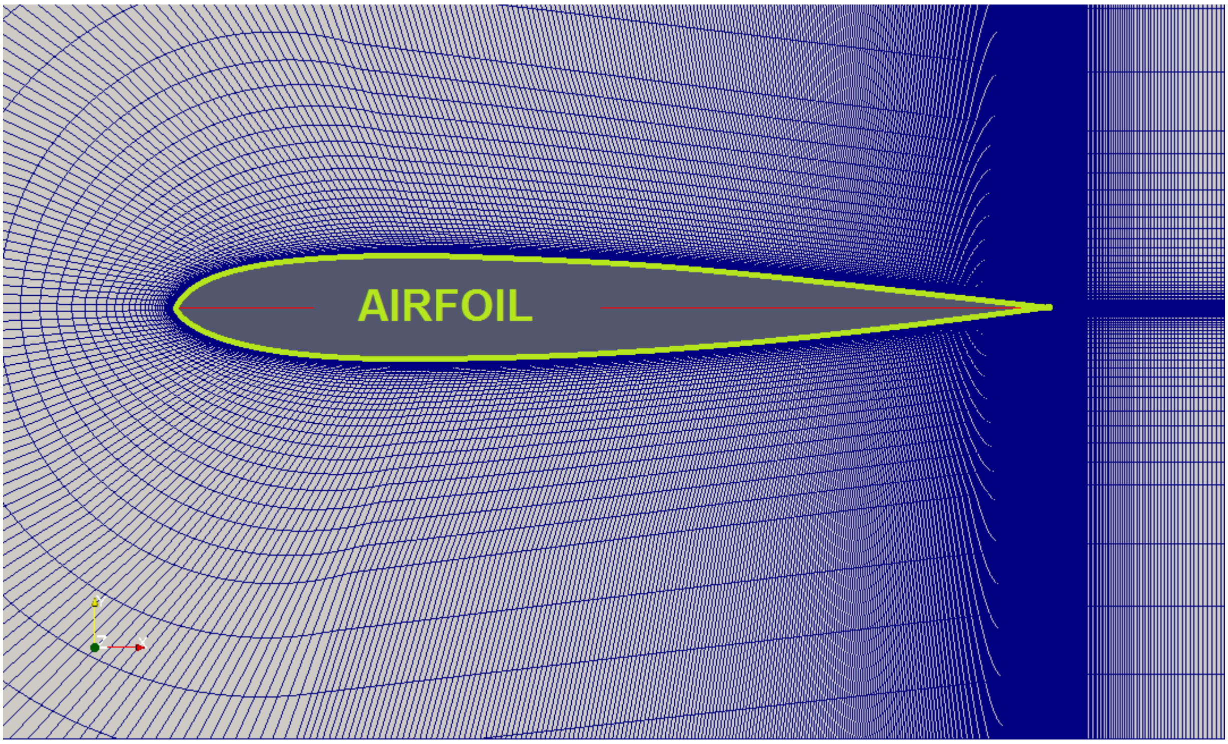

Figure 5.6: NACA0012 case coarse mesh LE closeup diagram

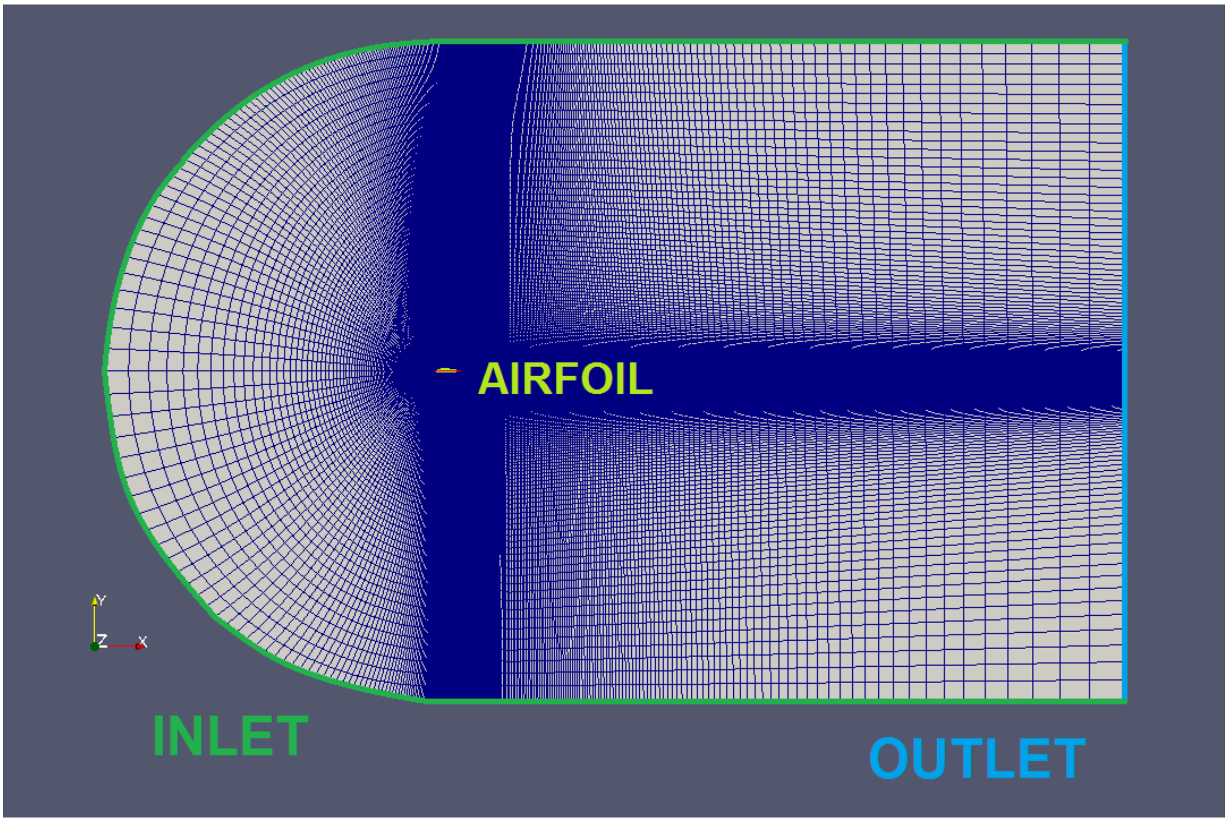

Figure 5.7: DU96 case mesh topology

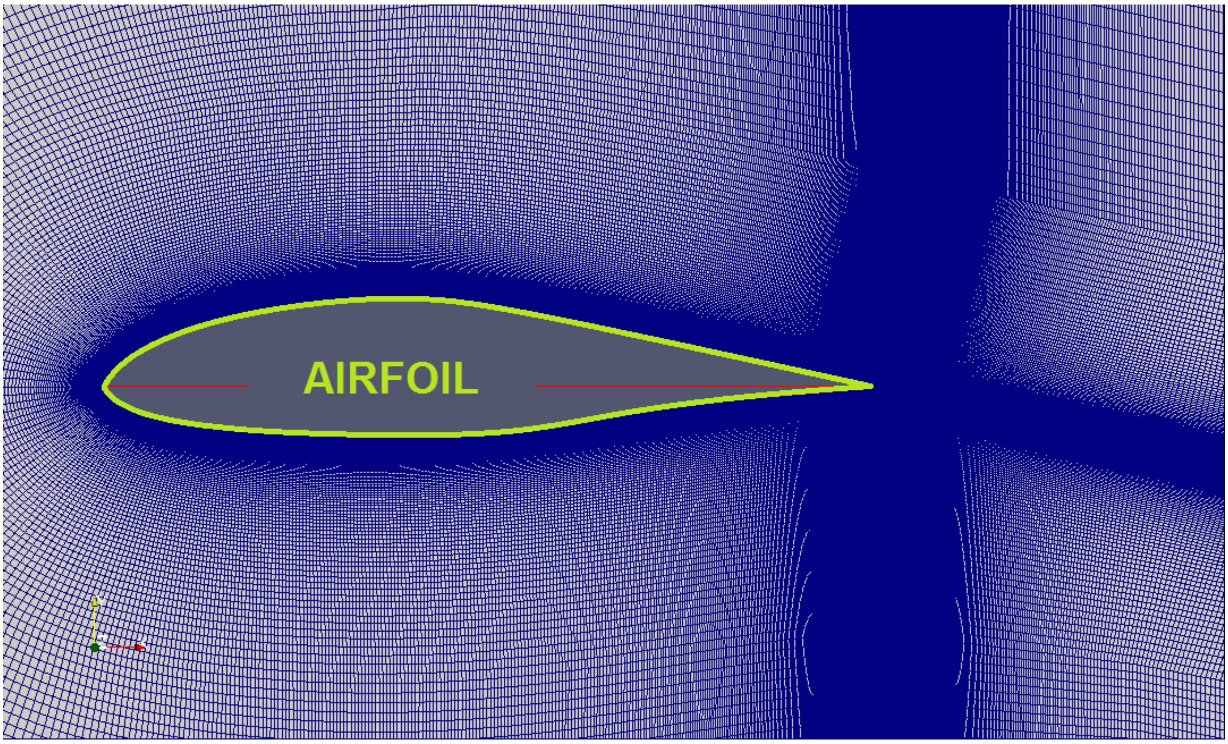

Figure 5.8: DU96 case coarse mesh LE closeup diagram

results with the RSNM method. Results favoured a wall resolving approach in all cases, but did not strongly differentiate between k-ω and k-ϵ based models. Results presented in this chapter use the most accurate turbulence model for each respective case as determined in the separate study, and reflect the finding of the study, weakly preferencing the k-ω-SST, but varying on a case by case basis.

The velocity boundary condition on the airfoils and flat plate were set as a Dirichlet-type boundary condition with fixed value for velocity at the surface of 0 m/s. The airfoil and plate turbulence viscosity boundary condition were set to be the OpenFOAM$^{\text{TM}}$ nutLowReWallFunction boundary condition. The airfoil and plate turbulent kinetic energy were set to be a Dirichlet-type boundary condition with fixed value of 1×10^{-10} for the FP12 case, while for the NACA012 and DU96 cases it was set using the OpenFOAM$^{\text{TM}}$ kLowReWallFunction. The FP12 case had the boundary condition for the dissipation rate ϵ at the plate set using a Neumann type boundary condition with zero spatial gradient in the plate normal direction, while the NACA0012 and DU96 cases specified the airfoil specific turbulence dissipation ω using the OpenFOAM$^{\text{TM}}$ omegaWallFunction. The boundary condition for pressure on the plate and airfoils was set to be a Neumann-type boundary condition, with zero spatial gradient in the surface normal direction.

The outlet boundary conditions for each case were specified using a Neumann-type boundary condition with zero spatial gradient in the (outlet) plane normal direction for the turbulence properties as well as velocity fields. The outlet boundary condition of pressure was specified as a Dirichlet type boundary condition with fixed value of zero. The symmetry plane for the FP12 case had the OpenFOAM$^{\text{TM}}$ symmetry plane boundary condition applied, which for the vector and scalar properties used in these simulations, reduces to Neumann-type boundary condition specifying zero spacial gradient in the direction normal to the symmetry plane.

For each case, the simulations were run until all residuals reached 10^{-6} or less. Linear interpolation schemes were used throughout, as was a second order accurate linear scheme for the discretisation of gradient terms. The velocity, turbulent kinetic energy, and dissipation fields divergence terms were discretised using a first-order-accurate upwind scheme. All Laplacian terms were discretised with the second-order-accurate linear scheme with explicit non-orthogonal correction. Finally, explicit non-orthogonal correction was performed when calculating surface normal gradient terms.The regions used for the RSNM calculations extended one boundary layer height upstream, downstream, as well as across-stream from the TE.

5.3 FP12 Case Grid Independence Study

In order to provide insight into the consistency and accuracy of the present results, a grid independence study was conducted on various quantities, and these are compared, where possible, to experimental values. For the FP12 test case, the boundary layer height (δ) was determined based on velocity profiles taken 0.7 mm downstream of the trailing edge of the plate, taken to be the location in the outer boundary layer where

$$\frac{\partial Ti}{y/c} \geq -0.1 \tag{5.1}$$

where Ti is the turbulence intensity and y/c is the wall distance normalised by chord. This method was chosen to match that used by Albarracin et al. (2011) to allow comparison of results to that work, as well as the experimental work of Moreau et al. (2011). The wall shear stress τ_w was determined at the trailing edge $\frac{x}{C} = 1$, and results for both the wall shear stress and boundary layer height are given in Table 5.2 and used in a grid independence study, the results of which are given in Table 5.3. The boundary layer height underpredicts that measured experimentally, but falls within the range of estimates achieved for this test case using a number of different CFD codes in the work of Albarracin et al. (2012b), in which boundary layer height estimates using the same method ranged from 5.7 to 7.9 mm. This boundary layer height will be sensitive to the mesh density and composition in the region where flow transitions from laminar to turbulent, as well as the ability of the turbulence model to capture this transition. The fact that the various RANS-based reproductions of this test case have all underpredicted this quantity suggests some regular error of the method, due to a failing of the various turbulence models used or other factors. As the present results fall within the range of those obtained in the literature, it is deemed sufficiently accurate for the purposes of this study.

Extending Richardson extrapolation, Roache (Roache, 1998) developed the concept of Grid Convergence Index (GCI) as a measure to provide uniform reporting of a grid refinement study. Richardson Extrapolation as well as the Grid Convergence Index and associated terms as used in the present work are detailed in Appendix E. Quantities of interest include the convergence ratio (R), the order of accuracy (p) limited where appropriate to the order of the finite-difference scheme used, and the fractional error (ϵ_h). Subscripts are used to indicate which mesh levels are being compared. For example in this Chapter GCI_{32} and ϵ_{21} indicate a Grid Convergence Index measure for the coarse and moderate mesh levels, and fractional error measure between the moderate and fine mesh levels, respectively. A GCI of less than 5% is generally considered sufficient (Wilcox, 2006).

The pressure coefficient along the plate surface (C_p) was also determined for each mesh solution, as shown in Figure 5.9, and the position and value of the extrema near the leading and trailing edges, the values of which are given in Table 5.4, were used in a grid independence study, the results of which are given in Table 5.3. The net pressure and viscous force experienced by the plate for each of the mesh solution values given in Table 5.4 were used in a grid convergence study, the results of which are also given in Table 5.3. The various quantities investigated show levels of consistency considered to be sufficiently grid independent for the purposes of the present work.

5.4 FP12 Case Validation Against Literature Results

In order to provide insight into the consistency and accuracy of the present results, they were compared against those from the literature. Velocity and turbulence intensity profiles sampled 0.7 mm downstream of the trailing edge in the simulation, were compared with the experimental and CFD results taken at the same location shown in the Albarracin et al. (2012b) study. Figure 5.10 shows the normalised flow velocity profiles 0.7 mm downstream of the trailing edge for the three mesh solutions, comparing them to the experimental data, while Figure 5.11 shows the result using the finest mesh, comparing it to the experimental data and also to the other CFD results, where it can be seen to closely match results achieved using Star-CCM+ in the work of Albarracin et al. (2012b). The differences in the innermost region of the boundary layer, between the various results of Albarracin et al. (2012b) and those of the present work, highlight that even when using the same turbulence model, differences can result from differing selection and application of wall functions, impacting on the resulting estimates for turbulence properties throughout the boundary layer. Figure 5.12 shows the normalised turbulence intensity profiles 0.7 mm downstream of the trailing edge for the three mesh solutions, comparing them to the

Table 5.2: FP12 case boundary layer heights and trailing edge wall shear stresses for different mesh solutions

Parameter	Coarse Mesh	Moderate Mesh	Fine Mesh	Experimental Value
δ (mm)	5.64	6.55	6.53	8.6
τ_w (mm)	4.118	5.299	4.358	n/a

Table 5.3: FP12 case grid convergence and independence results

Parameter	ϵ_{32}	ϵ_{21}	R	p	GCI_{32}	GCI_{21}
δ	-9.12×10^{-4}	2.03×10^{-5}	-0.0225	2 (5.49)	6.7427%	0.1291%
τ_w	-1.181	0.941	-0.797	2 (0.3274)	11.94%	7.40%
LE Extrema Position	0.0004	0.0007	0.4947	1.0153	9.0658%	4.8438%
LE Extrema Value	-0.118	-0.1168	1.0102	2 (-0.0146)	3.5116%	3.8738%
TE Extrema Position	0.0001	0.0002	0.4894	1.031	0.0319%	0.0156%
TE Extrema Value	-0.0147	0.0082	-0.5587	0.8398	9.1521%	5.4274%
F_x	-0.0585	0.0545	-0.9315	2 (-0.9315)	4.7794%	3.9938%
F_y	0.0058	-0.0953	-16.5178	2 (-4.046)	0.0398%	0.6582%

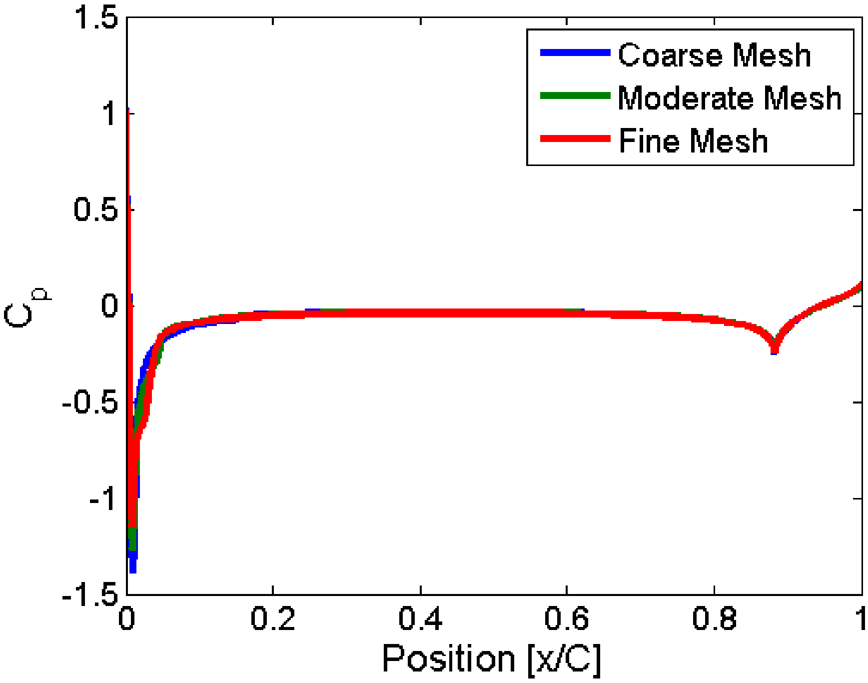

Figure 5.9: FP12 case plate surface pressure coefficient

experimental data, while Figure 5.13 shows the result using the finest mesh, comparing it to the experimental data and also to the other CFD results. Figure 5.13 shows that the correct profile shape is achieved, but that an underprediction in the absolute maximum level, as well as the freestream level, occurs when compared to the experimental data. The present results are comparable to those of Albarracin et al. (2012b), which proved suitable for application to the noise prediction method, and provides confidence in the present results.

5.5 NACA0012 Case Grid Independence Study

In order to provide insight into the consistency and accuracy of the present results, a grid independence study was conducted on various quantities and these were compared, where possible to experimental values. The boundary layer height for each mesh solution was determined and compared to expected results, based on the BPM empirical method (Brooks et al., 1989). Figure 5.14 shows the normalised flow velocity profiles at the trailing edge, for the three mesh solutions, while Figure 5.15 shows the same for turbulence intensity.

The boundary layer heights were determined according to Equation 5.1. The results all fell within the expected range based on the boundary layer heights estimated using the BPM method, both of which are given in Table 5.5. The pressure coefficient along the airfoil surface was also determined for each mesh solution, shown in Figure 5.16 along with that predicted using XFOIL for similar conditions ($M = 0.198$, $Re_C = 4.02E6$, $\alpha = 0$ degrees, tripped at $0.1C$). The position and value of the surface pressure profile extrema, values of which are given in Table 5.6, were used in a grid convergence study, the results of which are given in Table 5.7. The net pressure and viscous force experienced by the airfoil for each mesh solution was determined, and results are given in Table 5.6. The calculated drag, as well as the value of maximum turbulence intensity in the profiles at the TE, were used in a grid convergence study, the results of which are given in Table 5.7, the reader is reminded that the grid convergence index quantities were discussed in Section 5.3 and Richardson extrapolation is detailed in Appendix E. The various quantities investigated show levels of consistency such that the results are considered to be sufficiently grid independent for the purposes of the present work.

5.6 DU96 Case Grid Independence Study

In order to provide insight into the consistency and accuracy of the present results, they are compared against those from the literature. The pressure coefficient along the airfoil surface was determined for each mesh solution, shown in Figure 5.17 along with that predicted using XFOIL for similar conditions ($M = 0.087$, $Re_C = 2.165E6$, $\alpha = 3.1$ degrees, tripped at $0.1C$). The position and value of these surface pressure extrema are given in Table 5.8. The net pressure and viscous drag and lift forces experienced by the airfoil was determined for each mesh solution, and the results are given in Table 5.9. This drag force corresponds to a drag coefficient of 0.588. No drag measurement was made by Devenport et al. (2010a) for 3.1 degrees angle of attack at this Reynolds number, but results for the Reynolds numbers at which measurements were obtained, for this angle of attack, along with the present results, are shown in Figure 5.18. Both the position and value of the surface pressure profile LE extrema, as well as the drag force values given in Tables 5.8 and 5.9, were used in a grid convergence study, the results of which are given in Table 5.10, the reader is reminded that the grid convergence index quantities were discussed in Section 5.3 and Richardson extrapolation is detailed in Appendix E. The various quantities investigated show levels of consistency such that the results are considered to be

Table 5.4: FP12 case plate surface pressure coefficient extrema

Parameter	Coarse Mesh	Moderate Mesh	Fine Mesh
LE Extrema Position [x/C]	0.0096	0.0089	0.0085
LE Extrema Value [C_p]	-1.3864	-1.2695	-1.1515
TE Extrema Position [x/C]	0.8815	0.8812	0.8811
TE Extrema Value [C_p]	-0.2541	-0.2394	-0.2477
F_x [N]	0.5101	0.5687	0.5142
F_y [N]	6.0417	6.0359	6.1313

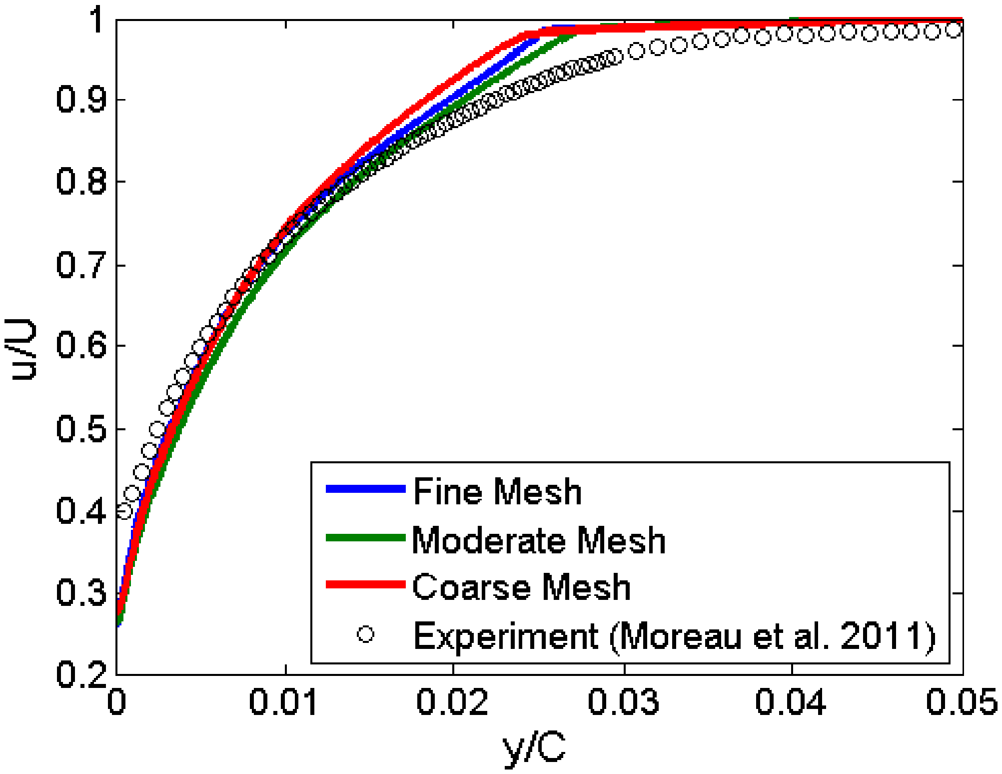

Figure 5.10: FP12 case comparison of velocity profiles at $\frac{X}{C} = 1.00$ for different mesh solutions with experimental data

Table 5.5: NACA0012 case boundary layer heights for different mesh solutions

	RANS Result		BPM Prediction	
	Coarse Mesh	Fine Mesh	Untripped	Tripped
δ (mm)	0.0273	0.0246	0.0175	0.0301

Table 5.6: NACA0012 case pressure coefficent and force results

Parameter	Coarse Mesh	Moderate Mesh	Fine Mesh
Extrema Position [x/C]	0.1247	0.1219	0.1206
Extrema Value [C_p]	-0.419	-0.415	-0.414
Drag force [N]	22.2	24.0	26.2

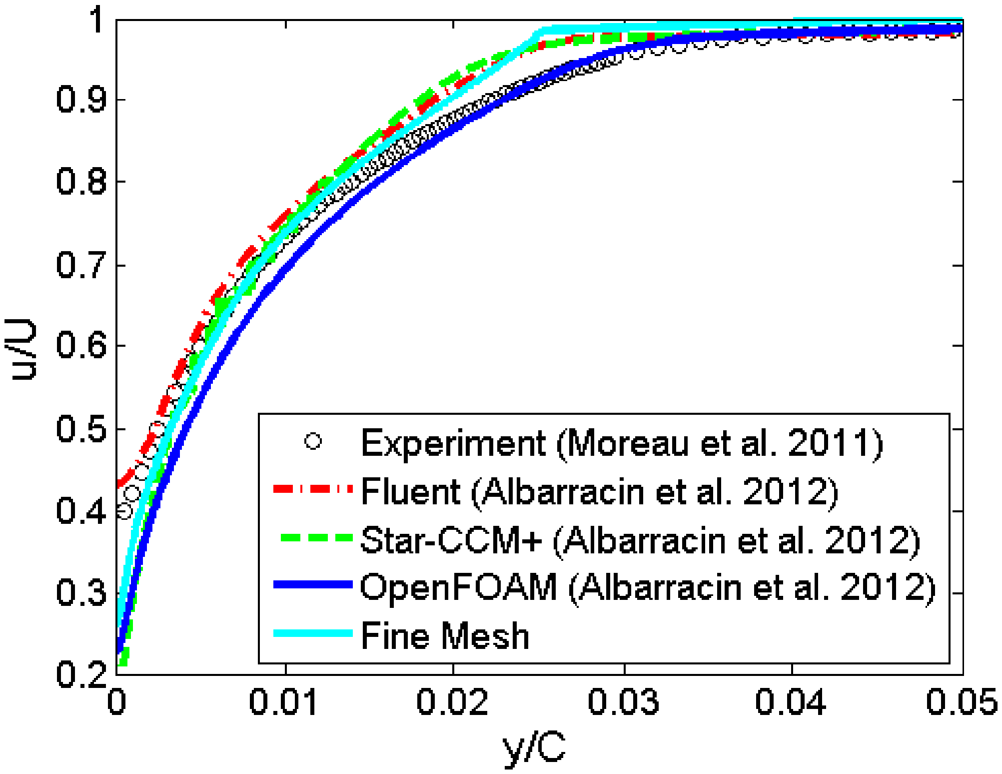

Figure 5.11: FP12 case comparison of fine mesh velocity profile to those of the literature at $\frac{X}{C} = 1.00$

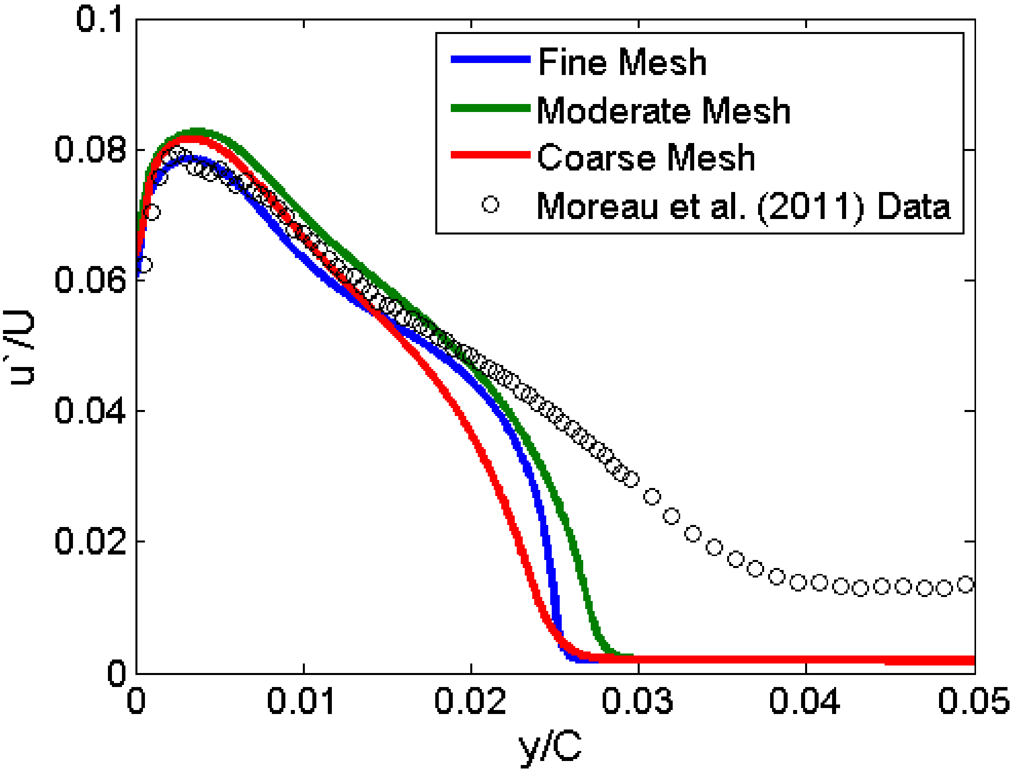

Figure 5.12: FP12 case comparison of turbulence intensity profiles for different mesh solutions with experimental data at $\frac{X}{C} = 1.00$

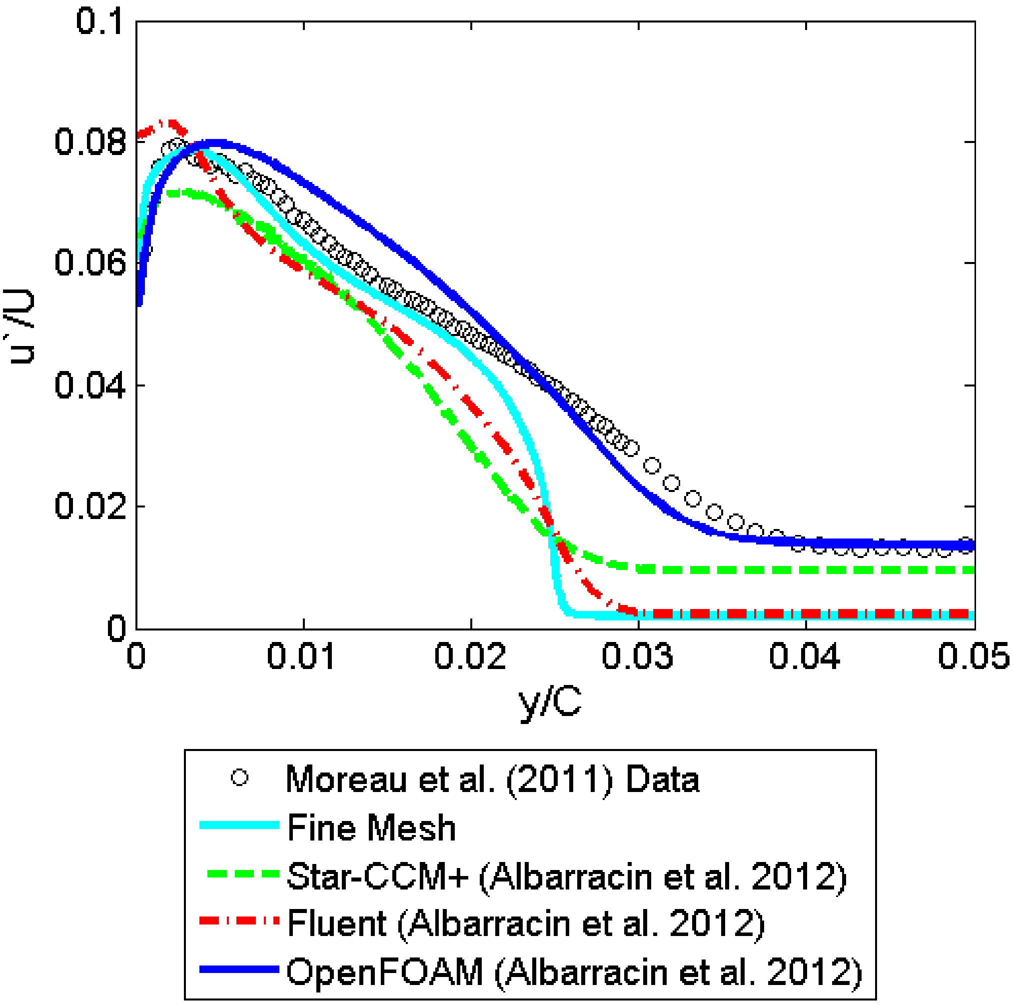

Figure 5.13: FP12 case comparison of fine mesh turbulence intensity profiles to those of the literature at $\frac{X}{C} = 1.00$

Table 5.7: NACA0012 case grid convergence and independence study results

Parameter	ϵ_{32}	ϵ_{21}	R	p	GCI_{32}	GCI_{21}
Cp Extrema Position	-0.0025	-0.0013	2	2 (-1)	0.4734%	0.9361%
Cp Extrema Value	-0.0039	-0.0011	3.48	2 (-1.8)	0.1128%	0.3909%
Drag Force	1.834	2.135	0.859	2 (0.219)	3.398%	3.180%
Ti Max Value	0.0008	-0.0062	-0.122	2 (3.04)	4.8048%	0.5256%

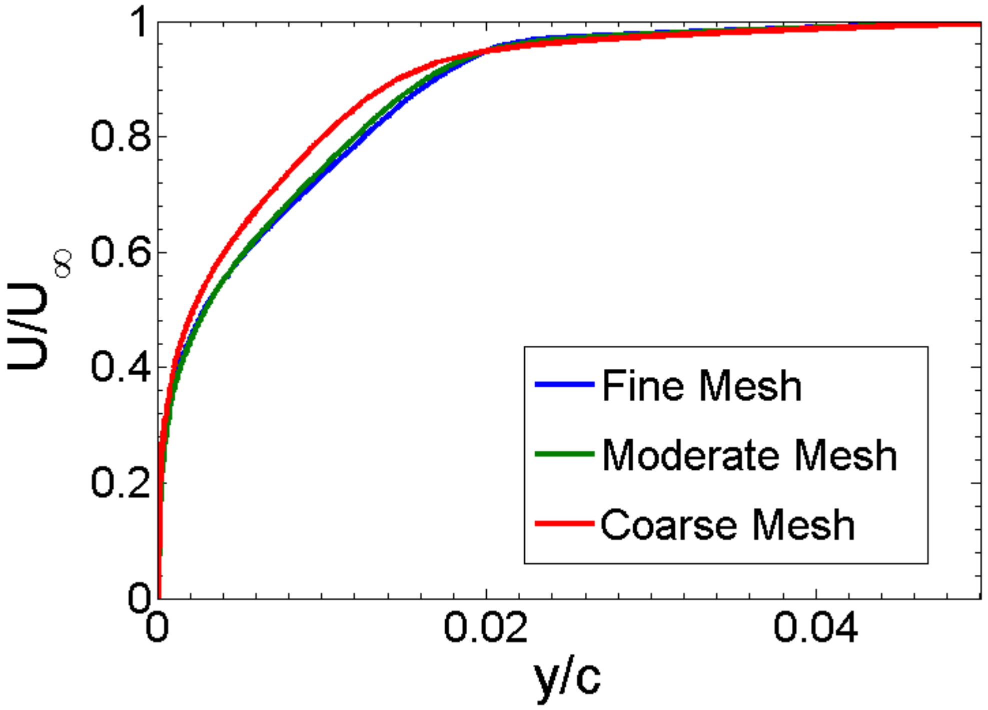

Figure 5.14: NACA0012 case comparison of velocity profiles for different mesh solutions at $\frac{X}{C} = 1$

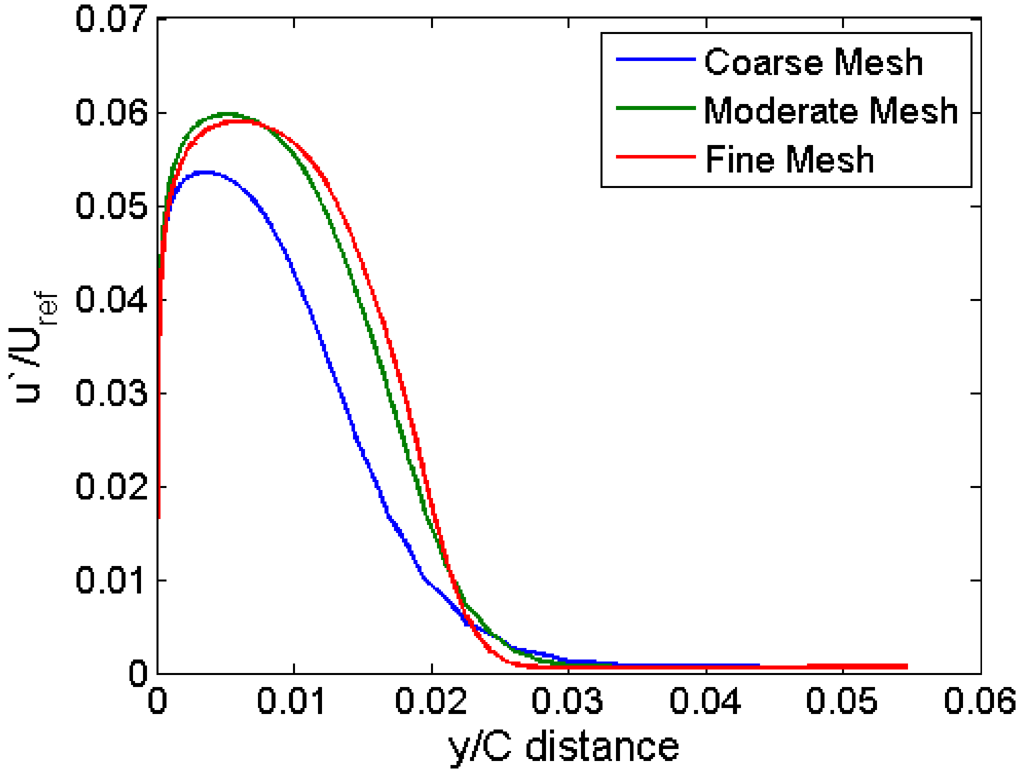

Figure 5.15: NACA0012 case comparison of turbulence intensity velocity profiles for different mesh solutions at $\frac{X}{C} = 1$

sufficiently grid independent for the purposes of the present work.

5.7 DU96 Case Validation Against Literature Results

In order to provide insight into the consistency and accuracy of the present results, they were compared against those from the literature. Although Devenport et al. (2010a) did not take velocity measurements for this exact case, measurements were taken for otherwise the same conditions, but at a somewhat reduced Reynolds number of 1,570,000 (compared to 2,165,000 for the present case). The velocity and turbulence intensity profiles were determined 1.9 mm downstream of wing trailing edge for the coarse mesh solution, and compared against those of Devenport et al. (2010a) in Figures 5.19 and 5.20 respectively. The greatest differences between the experimental and CFD predicted velocity profiles occur in the outer boundary layer of the pressure side, a result also seen in the work of Albarracin et al. (2012a). The greatest differences between the experimental and CFD predicted turbulence intensity (see Figure 5.20) are seen in the outermost part of the boundary layer, with the experimental levels taking longer to decay to freestream levels than those of the RANS predictions. The present results, being comparable to those of Albarracin et al. (2012a), which exactly matched the reduced experimental Reynolds number, and which proved suitable for application of the RSNM method, provides confidence in the present results for the same purposes.

5.8 3D RSNM Results

For the three test cases, the noise predictions are made at virtual observer positions, so as to match the location of the microphones used in the experiments reported in the literature (Moreau et al., 2011; Devenport et al., 2010a), against which the model predictions are compared. For each test case, the microphones were located at 90 degrees, directly above the midspan of the TE of the airfoil/plate, at distances of 585 mm, 3 m and 3 m for the FP12, NACA0012 and DU96 cases respectively. Further details of the microphone measurements can be found in Moreau et al. (2011) for the FP12 case, and Devenport et al. (2010a) for the NACA0012 and DU96 cases respectively. Acoustic predictions will be shown for each test case, first using the basic 3D-RSNM-TE method (see Equation 3.58), then using the 3D-RSNM-TE method with expectation value correction (see Equation 3.66), and finally, using the 3D-RSNM-TE method with expectation value correction, and optimising the model parameters (refer to Section 3.8.3 for a discussion on setting and selection of empirical constants).

Results using the basic 3D-RSNM-TE method applied to the FP12, NACA0012, and DU96 cases are given in Figures 5.21 through 5.23 respectively. In each case, a reduction of ~3dB for each doubling of the number of spanwise divisions considered is observed. This was expected based on the predicted breakdown condition for the basic model, explained in detail in Section 3.8.

Noise prediction results obtained using the 3D-RSNM-TE method with expectation value correction applied to the FP12, NACA0012, and DU96 cases are given in Figures 5.24 though 5.26 respectively. It can be seen that the expectation value correction eliminates the ~3dB for each doubling of the number of spanwise divisions considered. A more complete description of the numerical cause of this, as well as how the expectation value methodology was developed to overcome this, is discussed in Section 3.8. Any remaining variation between the results for

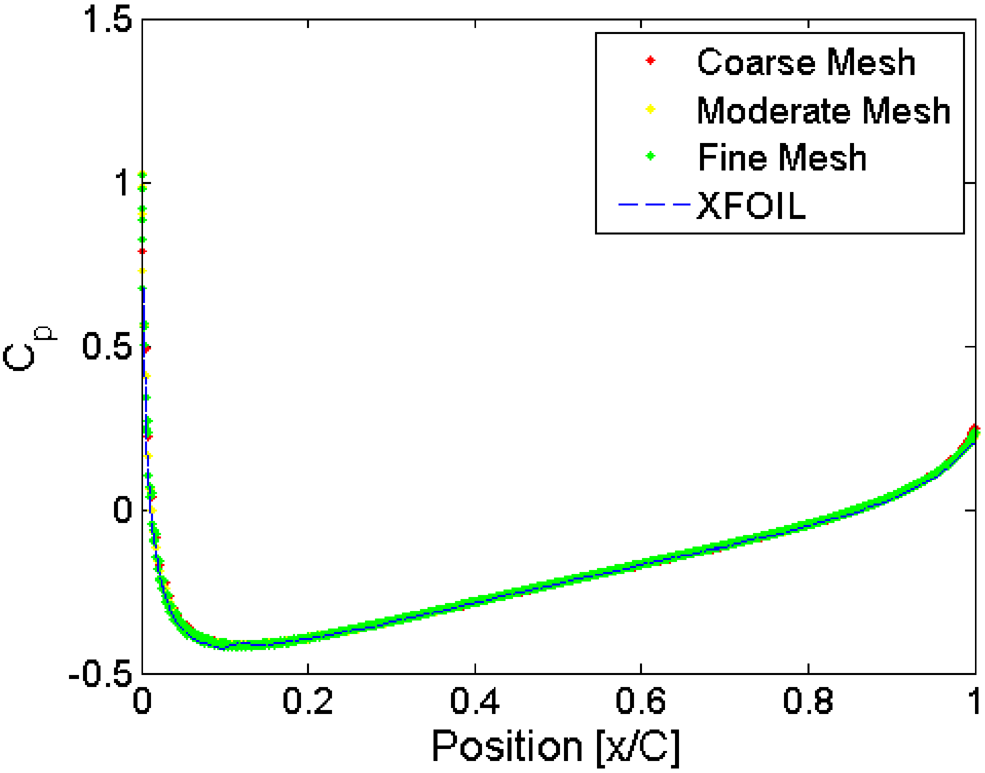

Figure 5.16: NACA0012 case comparison of aerofoil surface pressure coefficient for different mesh solutions

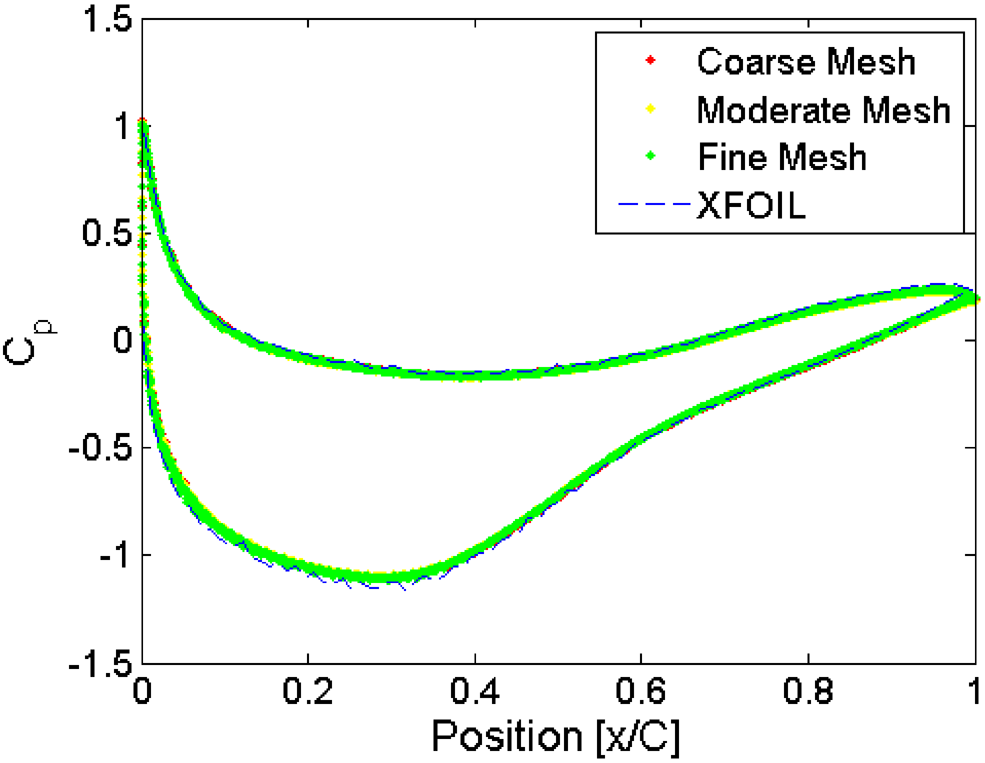

Figure 5.17: DU96 case comparison of aerofoil surface pressure coefficient for different mesh solutions

Table 5.8: DU96 case airfoil surface pressure coefficient extrema

Parameter	Coarse Mesh	Moderate Mesh	Fine Mesh
Pressure Side Extrema Position [x/C]	0.0012	0.0012	0.0015
Pressure Side Extrema Value [C_p]	1.024	1.011	1.007
Suction Side Extrema Position [x/C]	0.2627	0.2522	0.2722
Suction Side Extrema Value [C_p]	-1.109	-1.107	-1.117

Table 5.9: DU96 case forces acting on aerofoil

Parameter	Coarse Mesh	Moderate Mesh	Fine Mesh
Drag force [N]	14.32	13.15	11.23
Lift force [N]	499.8	492.8	498.7

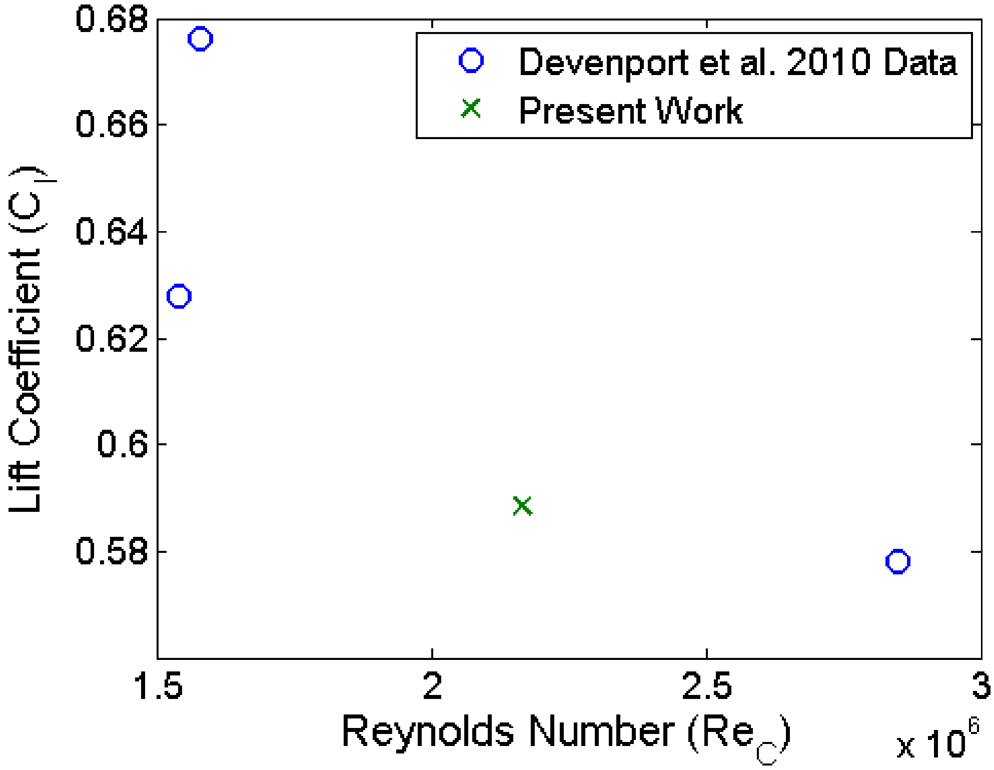

Figure 5.18: DU96 case comparison drag coefficient with nearest experimental measurements

Table 5.10: DU96 case grid convergence and independence results

Parameter	ϵ_{32}	ϵ_{21}	R	p	GCI_{32}	GCI_{21}
Pressure Side Extrema Value	0.0127	0.0035	0.2775	1.849	0.5966%	0.1677%
Suction Side Extrema Value	0.0018	-0.0106	-5.85	2 (-2.55)	0.0680%	0.3986%
Drag Force	1.1693	1.9209	1.6427	2 (-0.7161)	3.4021%	6.0855%
Lift Force	6.9327	-5.8548	-0.8445	2 (0.2438)	0.5779%	0.495%

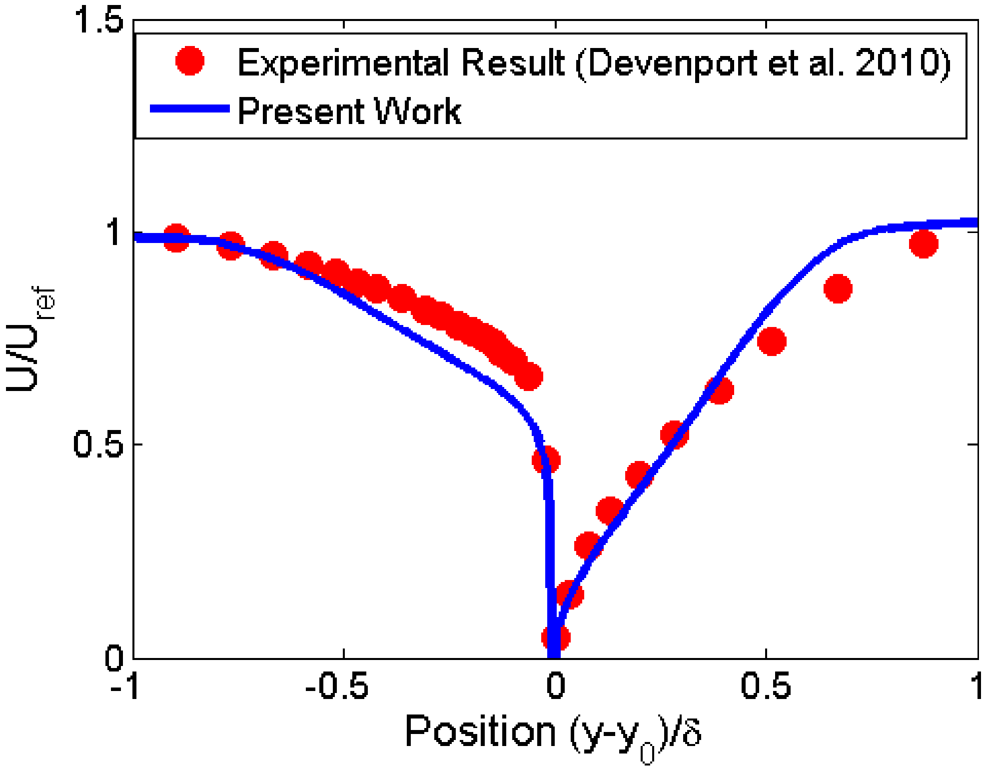

Figure 5.19: DU96 case comparison of simulated near trailing edge velocity profile at $Re_c = 2,165,000$ with experimental measurements at $Re_c = 1,570,000$

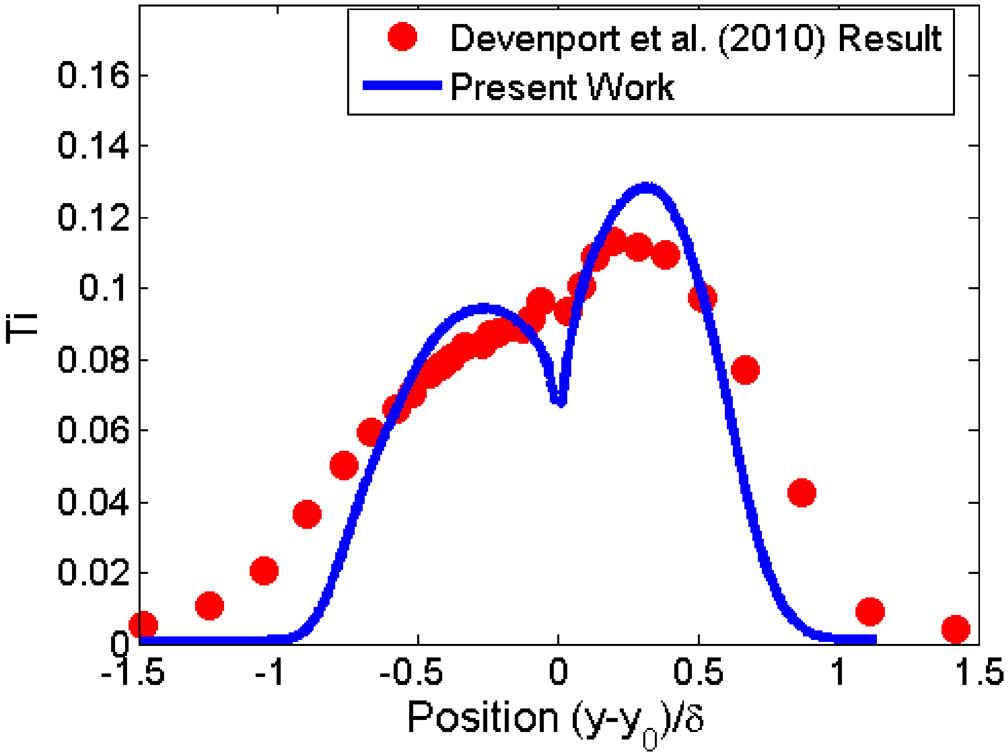

Figure 5.20: DU96 case comparison of near trailing edge turbulence intensity profile at $Re_c = 2,165,000$ with experimental measurements at $Re_c = 1,570,000$

differing number of divisions considered is expected to be attributed to increased spatial discretisation accuracy in calculating the distances and angles between the sources and observer, rather than inadequacy of the expectation value model. The absolute levels predicted when using the expectation value method, and setting the spanwise lengthscale parameter to have a value the same as that for the flowwise lengthscale constant, as suggested by Albarracin et al. (2012a), namely $C_{l_z} = C_{l_{xy}} = 0.11$, only produces good agreement in terms of absolute noise levels for the DU96 case; significant underprediction is seen in the FP12 and NACA0012 cases. However, the spanwise correlation time and lengthscales are not necessarily expected to be the same as those for the planeflow components, and so would have different characteristic length scale values. Varying the characteristic spanwise lengthscale parameter C_{l_z}, allows greater agreement with the absolute noise level to be achieved. Raising C_{l_z} increases the amplitude of the predicted noise, while decreasing C_{l_z} decreases the amplitude of the predicted noise, leaving the shape unchanged. Empirically optimised results for the C_{l_z} value are shown for the FP12 and NACA0012 cases, using values of $C_{l_z} \approx 7$ and $C_{l_z} \approx 2$, in Figures 5.27 and 5.28 respectively. These values were determined by a parametric study in which the noise calculation was run with the C_{l_z} value varied from 0.0011 to 110, and visually inspecting the resulting spectra to find the value providing the best fit to the experimental data; the same method as was used by Albarracin et al. (2012a) to determine the $C_{l_{xy}} = 0.11$ value.

Finally, the Herr trailing edge noise model, discussed in Section 3.6, is applied to the FP12 case, as a means of comparison of the effectiveness of the 3D RSNM method against others from the literature. Noise prediction results obtained using the Herr method for each mesh solution, are compared against the experimental literature results (Moreau et al., 2011), as well as previous 2D RSNM (Albarracin, 2014) and the RSNM methods developed here, in Figure 5.29. It can be seen that the predictions resulting from the use of the Herr model do not show significant mesh dependence, changing less than 2 dB between mesh solutions, and that the 3D RSNM model has the best agreement with the experimental data from 2 kHz to 10 kHz. At frequencies of less than 500 Hz, the experimental results of Moreau et al. (2011) have significantly higher levels than predicted by both the literature models as well as those presented here, this is attributed to a facility effect, as the flow becomes decreasingly anechoic as these lower frequencies.

5.9 Conclusions

The 3D-RSNM-TE model was applied to a number of test cases from the literature. The originally propsed RSNM implementation was predicted in Section 3.8.3 to have a deficiency in that it does not produce an accurate prediction when the spanwise distance between input points is approximately equal to or greater than the characteristic lengthscale in that same direction, a deficiency which was predicted would result in an halfing of predicted noise when doubling the discretising spatial division. This was observed, and was shown to be mitigated by using the spanwise expectation value methodology to more accurately account for the self correlation of an acoustic cell, through modification of the spanwise correlation term. Although the expectation value methodology produces a noise prediction that has much less dependence on the acoustic grid, significant variance was found between the predicted and experimental sound pressure levels. This variance could be attributed to the semi-empirical model values inherited from 2D RSNM. Initially, the spanwise correlation lengthscale coefficient, was taken to have the same value as that of the flow-plane. In order to show the capacity of the model to achieve accurate noise level predictions when setting all the semi-empirical model values appropriately, and investigation was performed into the effect of modifying the spanwise correlation lengthscale.

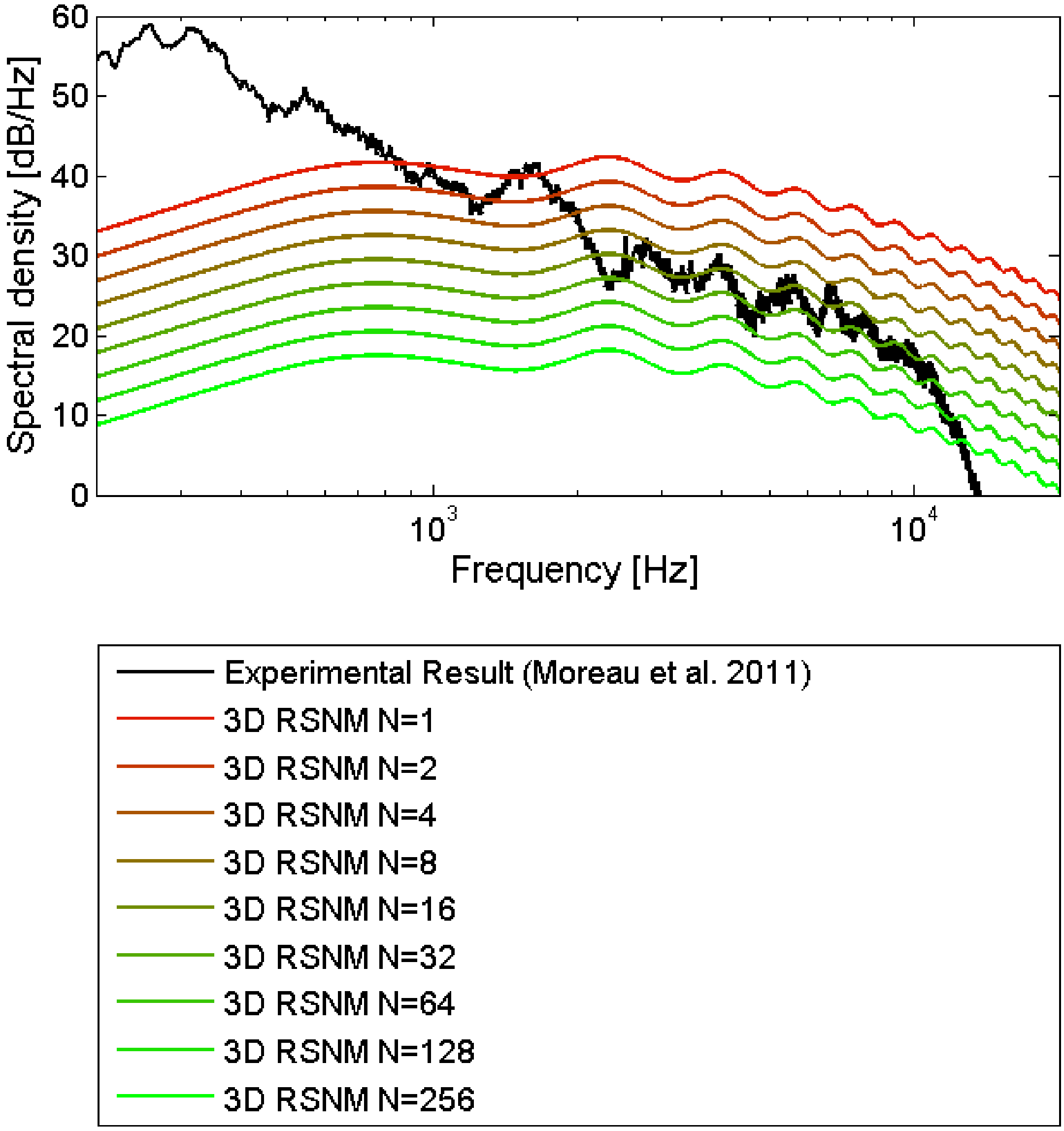

Figure 5.21: FP12 case baseline RSNM TE noise prediction

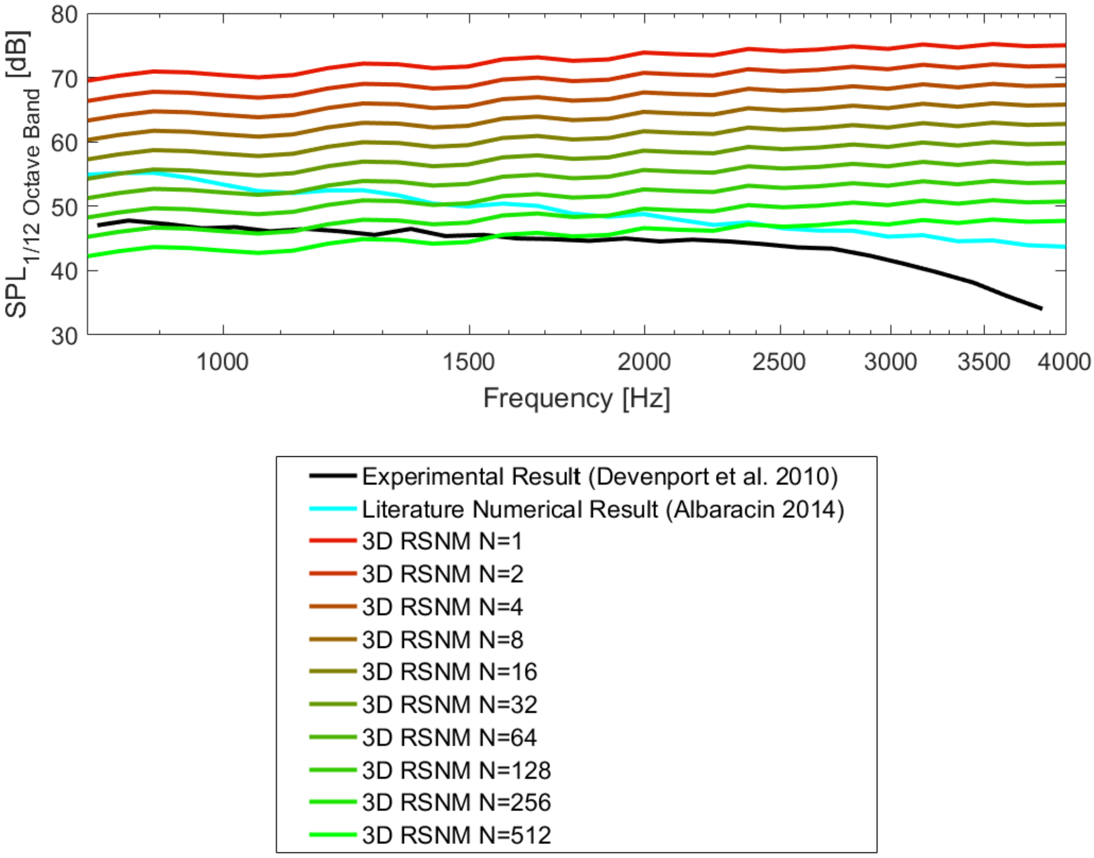

Figure 5.22: NACA0012 case baseline RSNM TE noise prediction

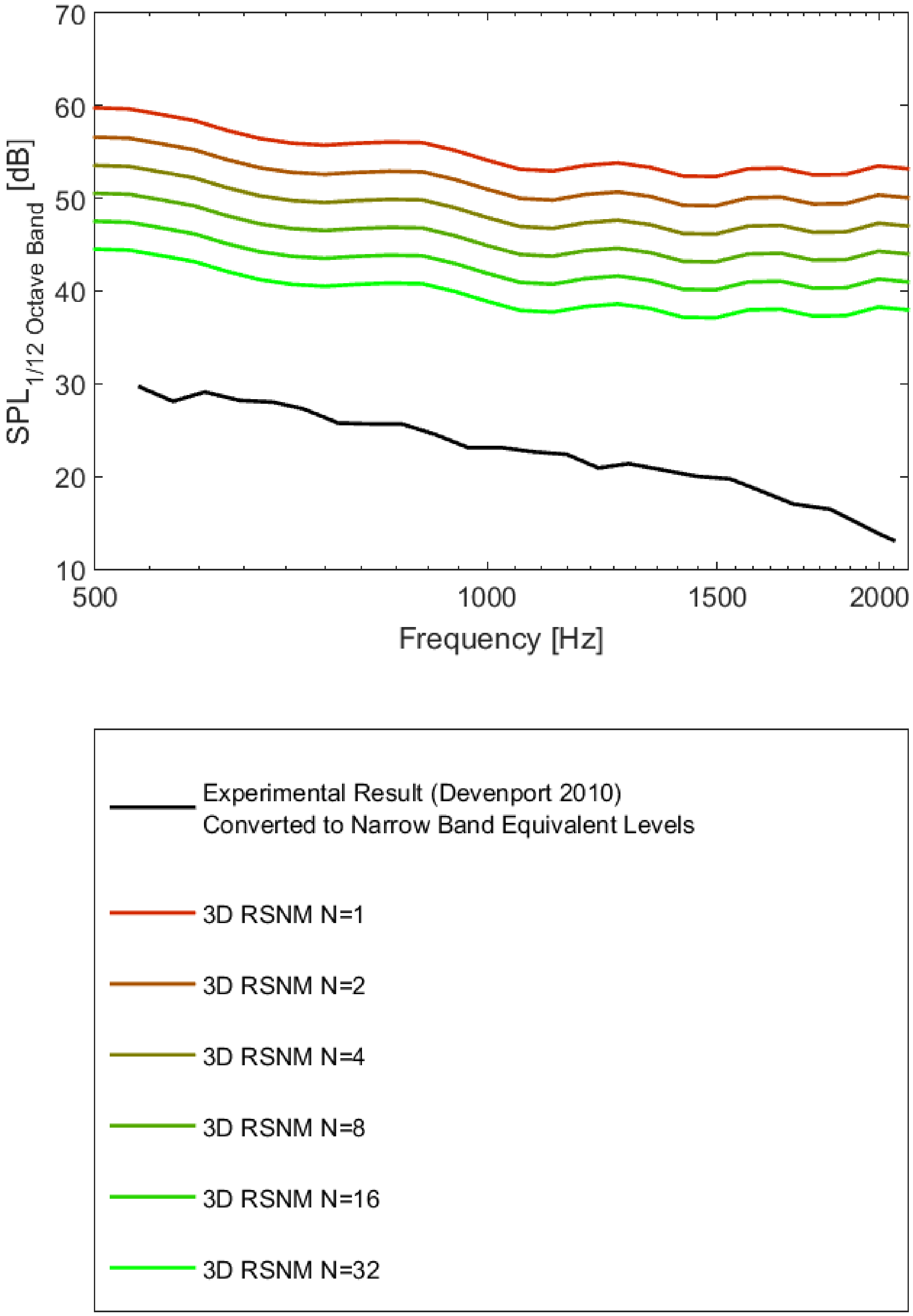

Figure 5.23: DU96 case baseline RSNM TE noise prediction

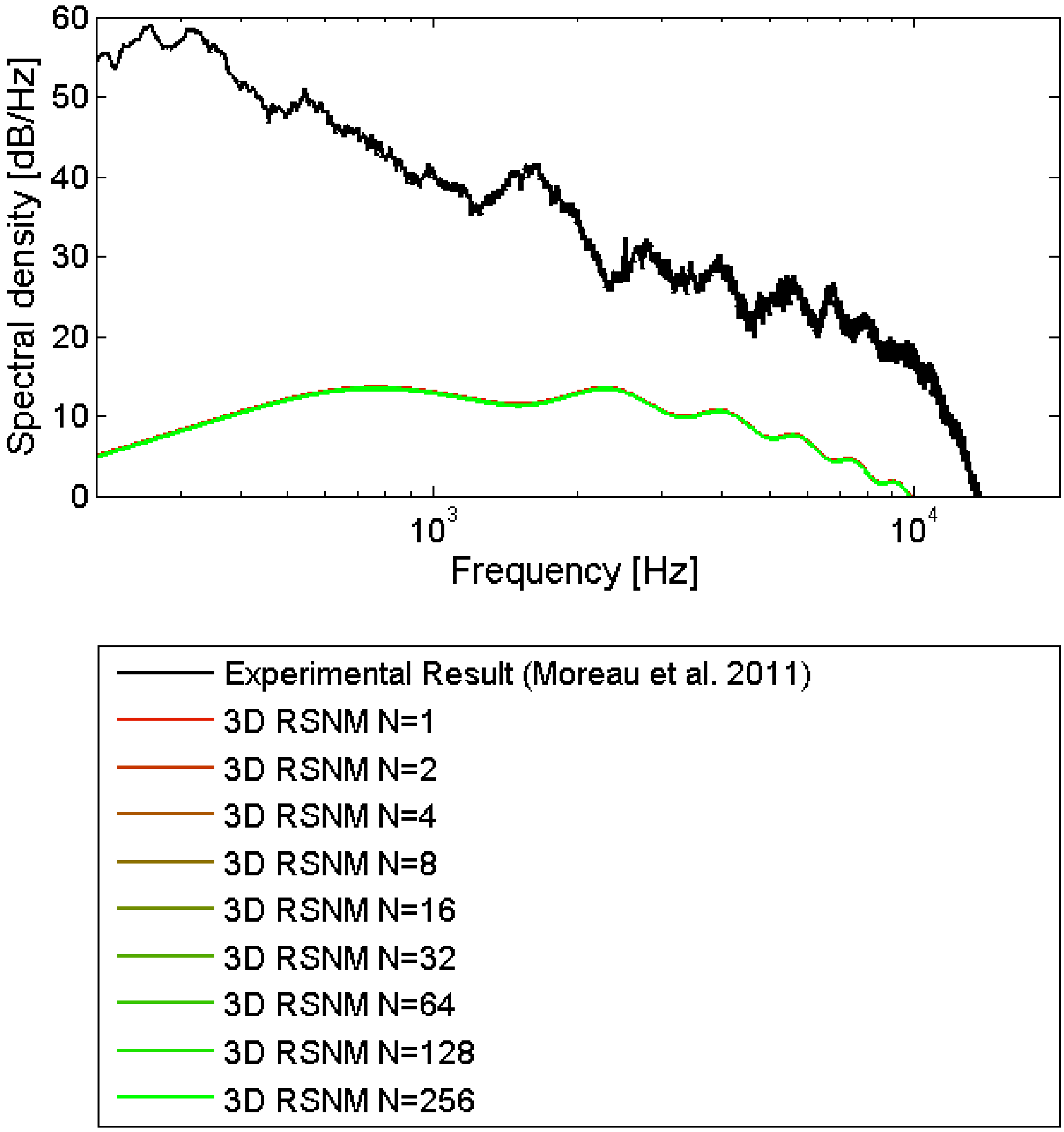

Figure 5.24: FP12 RSNM TE noise prediction with expectation value correction

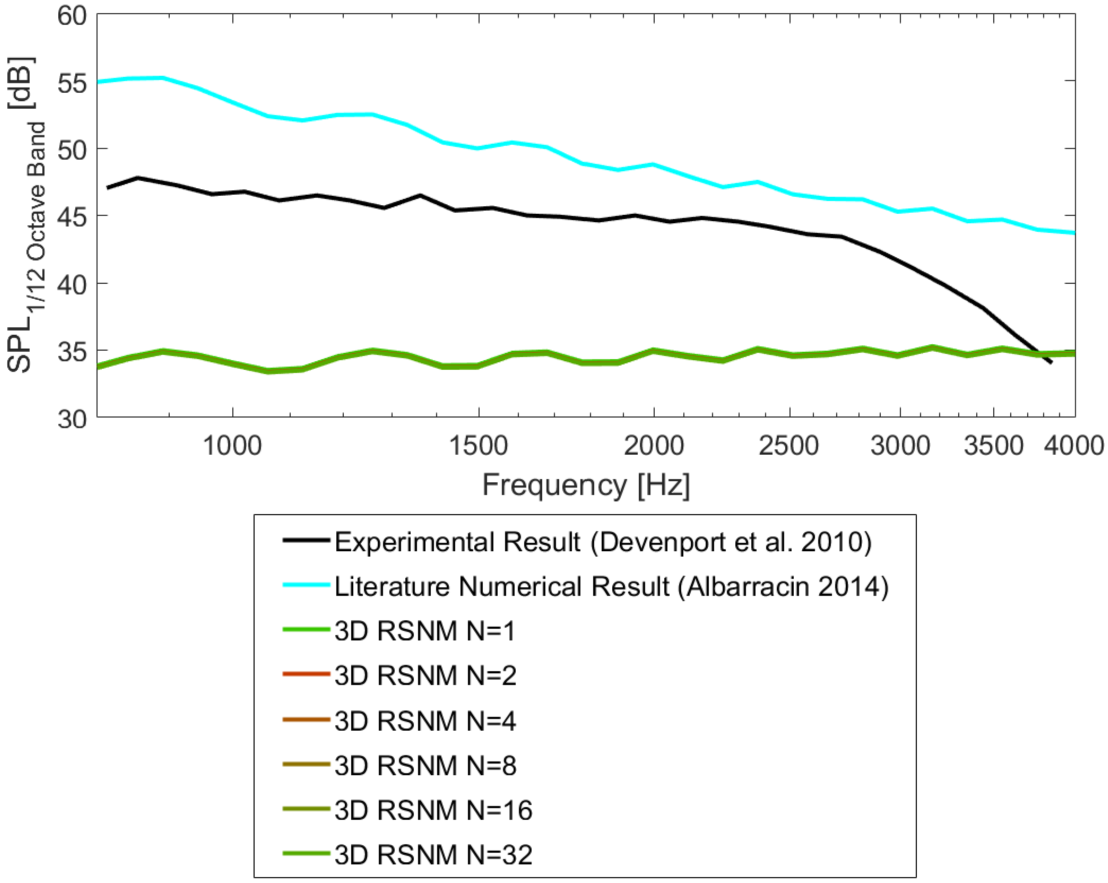

Figure 5.25: NACA0012 RSNM TE noise prediction with expectation value correction

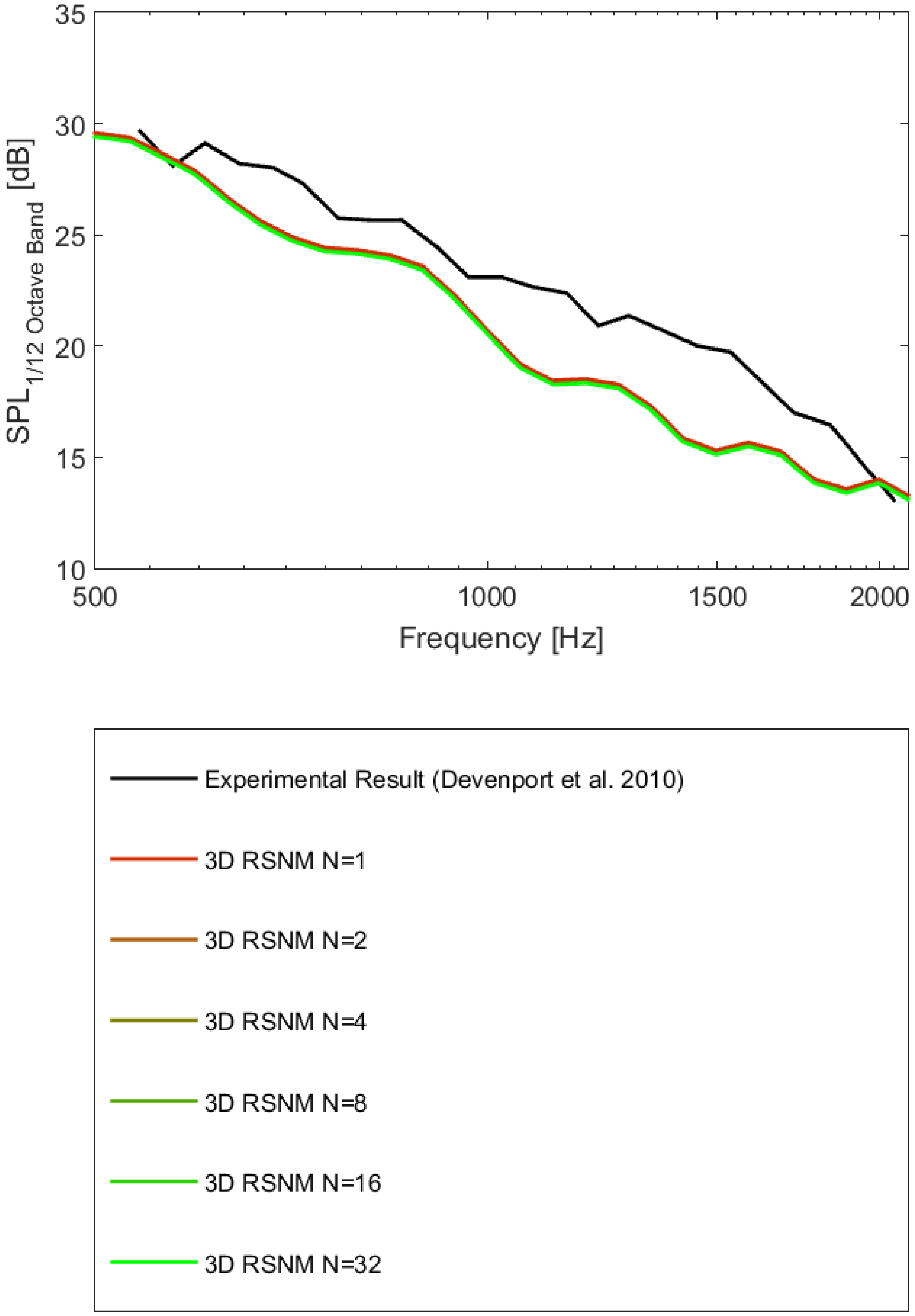

Figure 5.26: DU96 RSNM TE noise prediction with expectation value correction

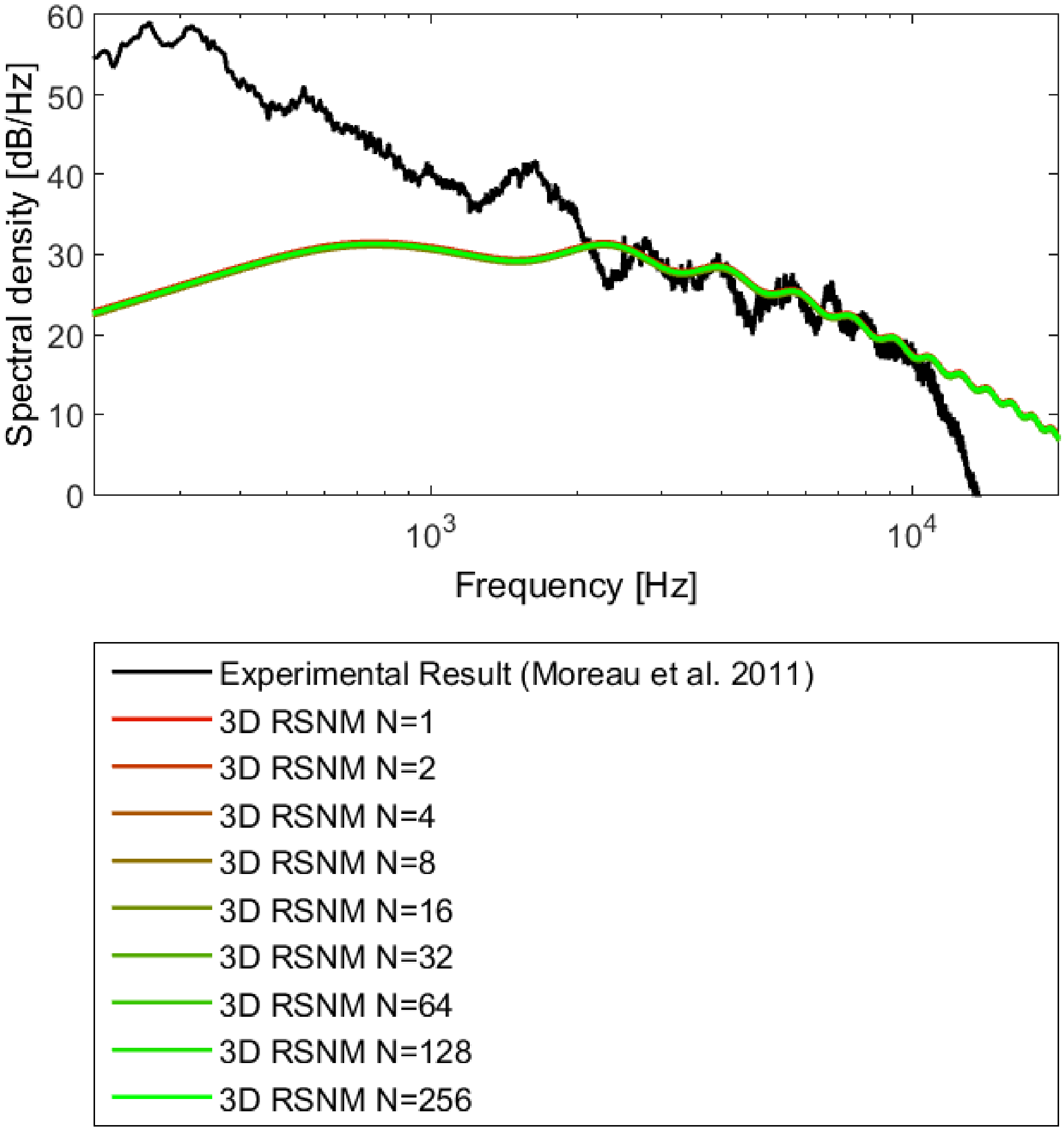

Figure 5.27: FP12 RSNM TE noise prediction with expectation value correction and optimised $C_{l_z} = 7$

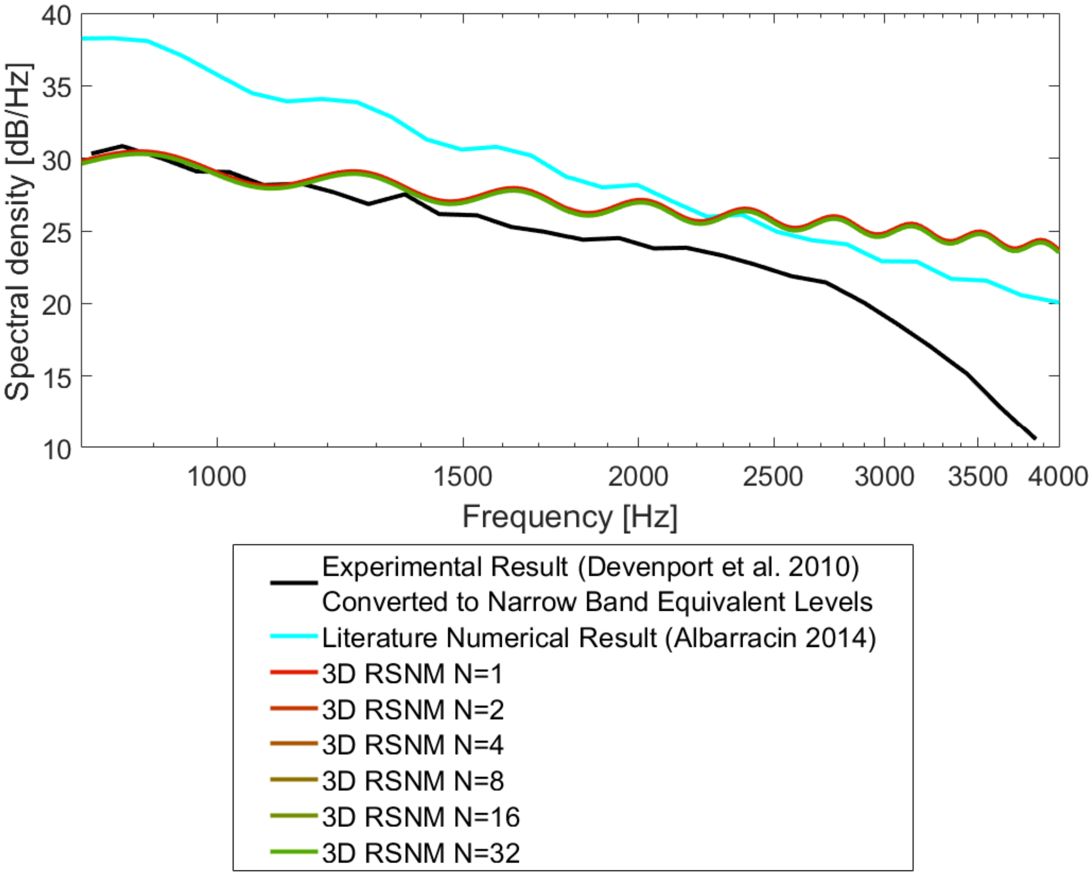

Figure 5.28: NACA0012 RSNM TE noise prediction with expectation value correction and optimised $C_{l_z} = 2$

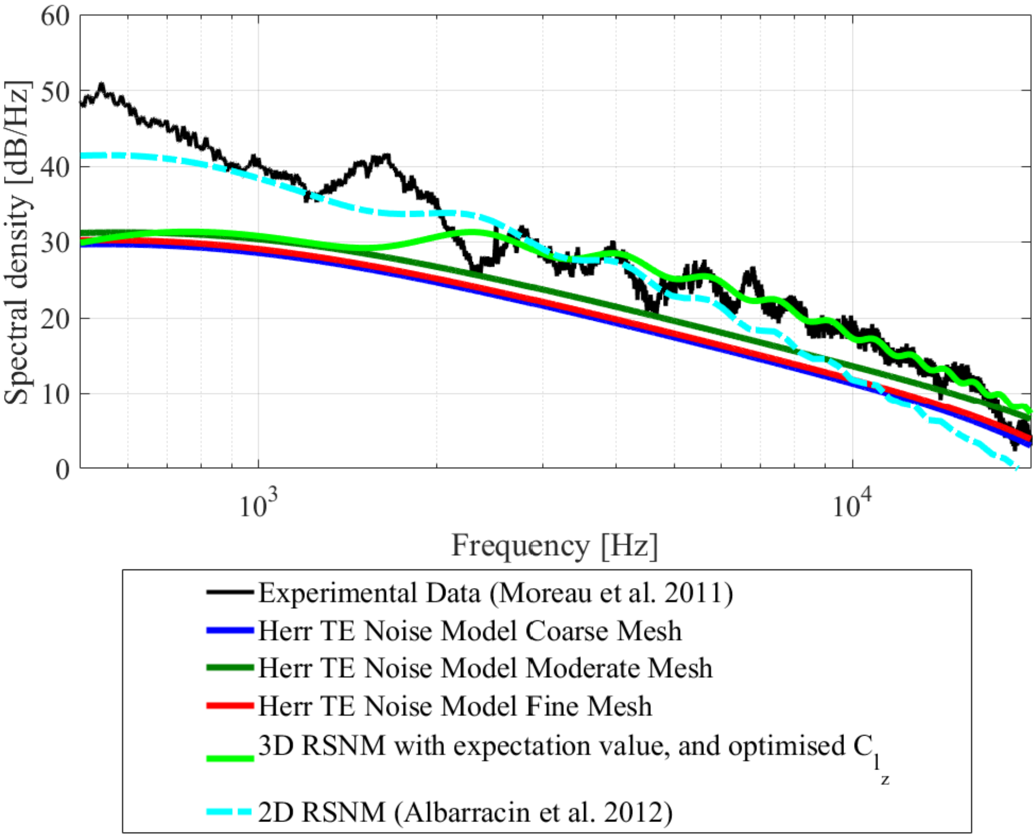

Figure 5.29: NACA0012 case comparison of optimised 3D RSNM TE, with alernative noise modelling methods

Variation of this parameter was found to allow for significantly improved agreement between predicted and experimental absolute levels, however, the value of C_{l_z} required differed in each case. Accurate setting of the model semi-empirical constants is thus found to be instrumental to the accuracy of the 3D-RSNM-TE model, and determining if these terms are a function of other flow or geometric properties is identified as an avenue of future work. Study of how to set the semi-empirical length and timescale constants, could be undertaken numerically using time resolved CFD methods, or experimentally. Experimental measurements expected to be capable of this were being undertaken concurrently with the present work by Albarracin (2016) at the University of Adelaide School of Mechanical Engineering. This may allow for better noise predictions, rather than a model developed by analogy to those for turbulent jets. The success of the incorporation of the expectation value correction for spanwise correlation terms, suggests that extending the concept to the flow-plane terms may also be of value. The spanwise expectation value method will be of immediate practical interest on the basis of allowing significant reductions in the required acoustic grid resolution, greatly reducing the computational effort involved.

6 University of Adelaide Anechoic Wind Tunnel Case

6.1 Introduction

In this chapter the developed and extended RSNM is used to predict the noise from the Moreau and Doolan (2013) wing in junction experiment which provides a suitable experimental data set against which to compare flow and noise predictions. This directly addresses the third thesis aim (see Section 2.7), which is to apply the developed noise modelling techniques to recent wing in junction experiments. The flow structure about the tip of a wing when at zero angle of attack is investigated, and this is used to address the fourth thesis aim, to characterise the tip vortex formation process for flat ended airfoils at zero angle of attack.

The 3DRSNM-TE method was applied on cases involving 2D flow data in Section 5. The present chapter considers a case with 3D flow features or wing geometry, the specific type of features and variation for which the model was developed. The case, described in detail in Section 6.2.1, considers a wall mounted NACA0012 profile wing, with aspect ratio 1, at a freesteam flow velocity and chord based Reynolds number of 161,000.

6.2 Methodology

Low Reynolds number turbulence modelling RANS simulations were performed, as detailed in Section 6.3. CFD flow data, as well as trailing and leading edge noise predictions made from the CFD flow data using the 3DRSNM-TE and Amiet based leading edge noise prediction methods detailed in Sections 3.8 and 3.7 respectively, are compared with experimental flow and noise measurements in Sections 6.4.6 and 6.4.7 respectively.

6.2.1 Experimental Details

Salient details of the experimental test case are summarised in Table 6.1 and discussed in the following.

The case follows the work of Moreau and Doolan (2013) which placed a wall mounted NACA0012 profile wing with chord and span each equal to 69 mm in 35 m/s flow, as shown in Figure 6.1. The wing is mounted to a wall which has an attached turbulent boundary layer. The wall boundary layer was measured to be 9.7 mm high at a distance 60 mm upstream of the wing

Table 6.1: Test Case Summary

Freestream flow speed	35 m/s
Chord	69 mm
Chord based Reynolds number	161,000
AOA	0
Span	69 mm
Wing Aspect Ratio	1
Junction Boundary Layer Height[†]	9.7 mm
Freestream Turbulence Intensity	0.3%
[†] Junction boundary layer height as measured 60 mm upstream of the airfoil leading edge.	

leading edge. The experimental data against which comparisons will be made, was gathered in the University of Adelaide anechoic wind tunnel. In the experiment, the airfoil was tripped at 10% chord using a 12 mm wide serrated strip of double sided tape covered in fine sand. Acoustic data were recorded at a single observation location using a B&K 1/2" microphone (Model No. 4190) located at a distance of 500 mm above a point at the middle of the chord at the free end of the airfoil. Additionally, hot-wire anemometry (using a TSI 1210-T1.5 single-wire probe) was used to measure velocity profiles in the near trailing edge wake. The samples were taken 1 mm downstream of the trailing edge, with one profile taken along the length of the airfoil span, and three profiles taken at wall normal distances of 39 mm, 64 mm and 69 mm, as shown in Figure 6.2. Interested readers are directed to Moreau and Doolan (2013) for further experimental details.

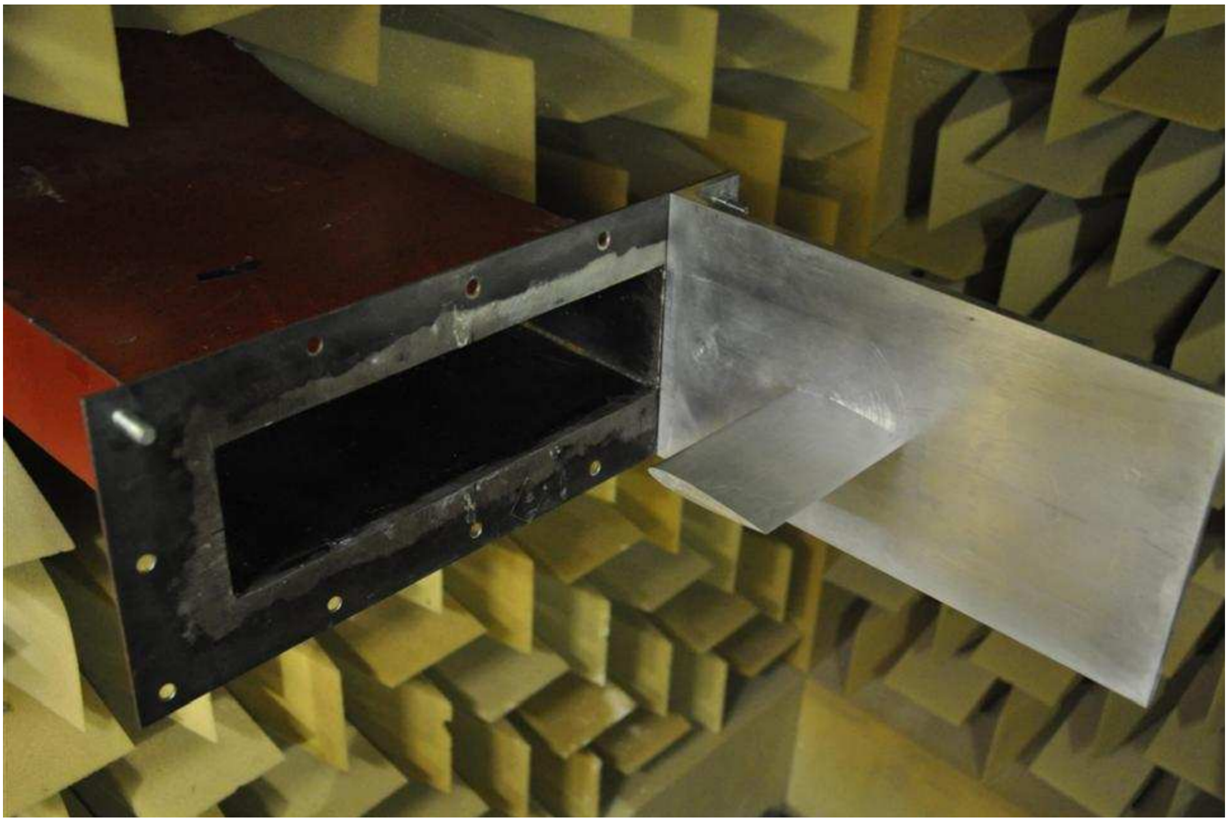

Figure 6.1: Moreau and Doolan (2013) experimental set-up, adapted from Moreau and Doolan (2013)

6.3 Modelling Details

The flow was treated as incompressible and solved using the OpenFOAM$^{\mathrm{TM}}$code, and the Semi-Implicit Method for Pressure-Linked Equations algorithm. The RANS equations were solved using, for closure, the k-ω-SST model, detailed in Appendix C. Wall functions for turbulence properties (turbulent eddy viscocity, ν_T, specific dissipation, ω, and turbulent kinetic energy, k) were used thoughout, and are detailed in Appendix D.

The geometry is a finite NACA 0012 wing attached at angle of attack of 0 degrees to a flat plate wall as shown in Figure 6.3, with cartesian coordinate system, with origin at the wing-leading-edge-junction interface. The wing chord (C) and span (S) are both 69 mm.

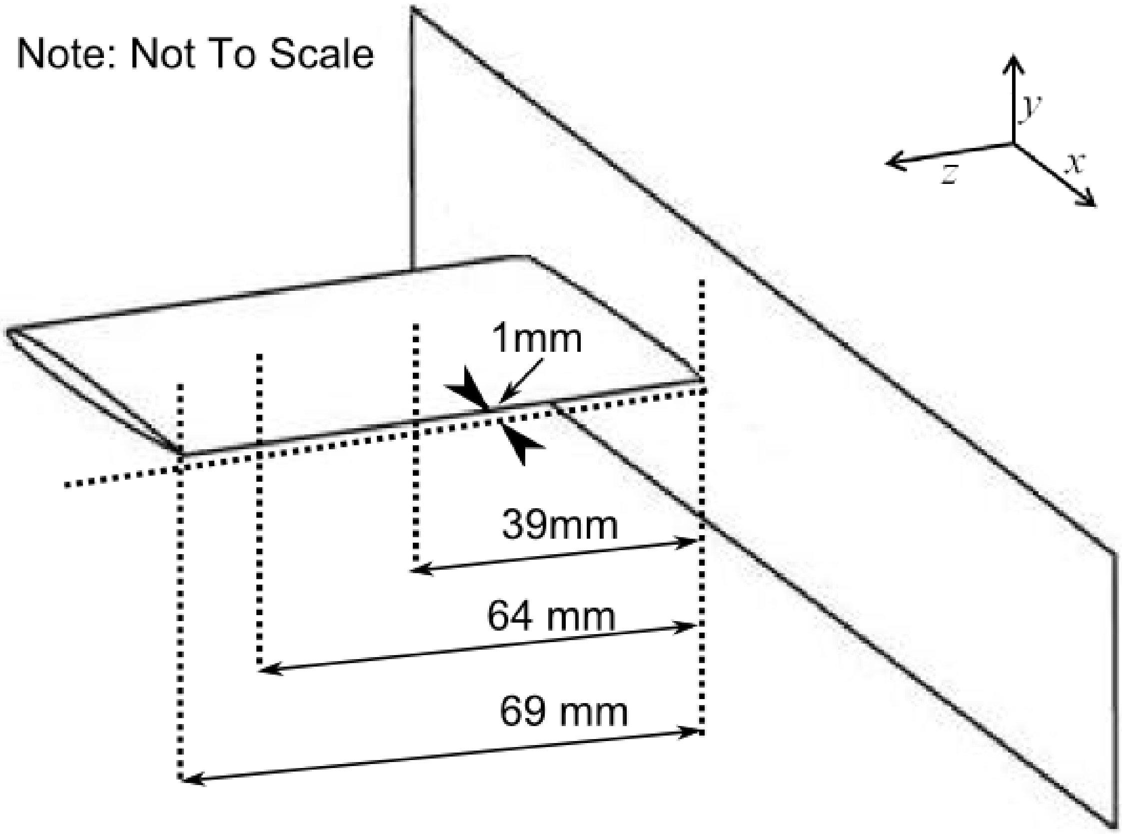

Figure 6.2: University of Adelaide anechoic wind tunnel case sample locations for comparison with Moreau and Doolan (2013) experimental results

6.3.1 Boundary Locations and Conditions

The four boundaries on this domain are the solid surface formed by the wing-plate, the outlet which consists of the Y-Z plane at X=15C as well as the X-Z planes at Y=±2.5C, the top X-Z plane at Z=10C, and the inlet at X=-6.845C in the Y-Z plane. The top X-Z plane had a slip boundary condition applied to it while the wing-plate pair was given a no-slip condition. There was a zero-gradient condition applied on the outlet. The inlet had a uniform velocity of 35 m/s, with turbulence properties estimated using the eddy viscosity ratio method with an assumed eddy viscosity ratio of unity and turbulence intensity set to 0.3%, matching the intensity of the wind tunnel facility used in the experiments of Moreau and Doolan (2013), resulting in values of turbulent kinetic energy, $k = 0.0165375$ m^{2}s^{-2}, and specific turbulence dissipation, $\omega = 1102.5$ s^{-1}, for the inlet. The eddy viscosity on the inlet was calculated from the other flow properties. The boundary layer height on the flat plate in absence of the airfoil was measured experimentally as $\delta = 9.7$ mm at a distance 60 mm upstream of the location equivalent to the position of the leading edge of the airfoil. The inlet position for the simulation was set so that uniform inlet boundary conditions would develop a flat plate boundary layer, with height matching this experimental measurement, based on the flat plate turbulent boundary layer power law equation (Cebeci and Bradshaw, 1977), $\frac{\delta}{x} = 0.37 R_x^{-0.2}$, where δ is

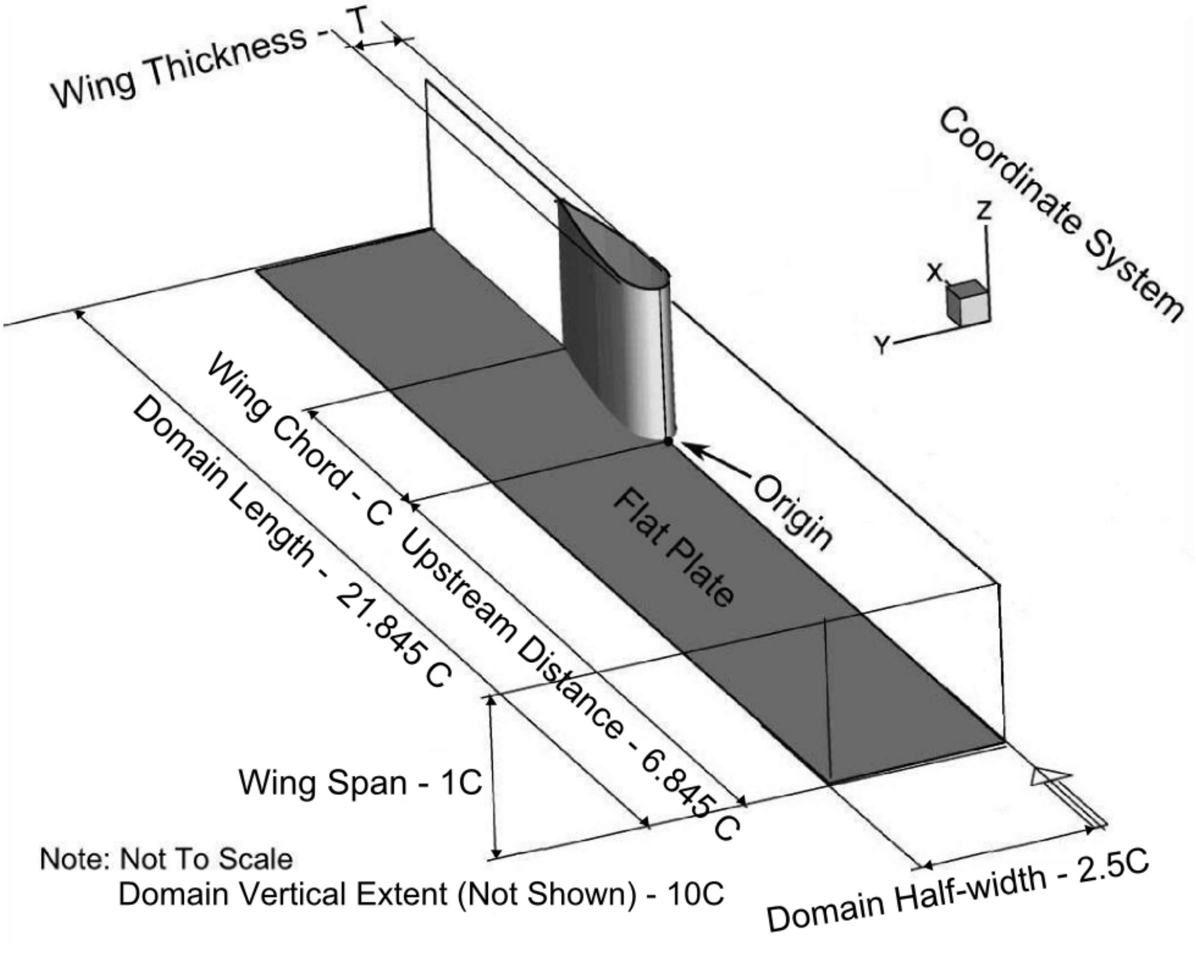

Figure 6.3: University of Adelaide anechoic wind tunnel case computational domain

the boundary layer height, x the flat plate distance, and R_x the Reynolds number based on the flat plate distance. When this is solved for the measured 9.7 mm boundary layer height, and added to the 60 mm that the measurement was taken upstream of the airfoil location, a total upstream distance of 0.4723 m (6.845 C) is determined to be required in order to match the experimental and simulation boundary layer heights.

The airfoil and plate are treated as no-slip surfaces and thus have a fixed value of zero velocity applied. The turbulent kinetic energy was also given a Dirichlet type boundary condition, imposing a fixed value of 1e-8 m^2s^{-2}, while for pressure, a zero gradient boundary condition was used. The OpenFOAM^{TM} nutLowReWallFunction (see Appendix D) was used as the boundary condition for the turbulent eddy viscosity on the wing surface and the specific turbulence dissipation had the omegaWallFunction (see Appendix D) applied. A zero gradient boundary condition was used on the outlet surface for the velocity boundary condition. For turbulent kinetic energy and dissipation on the outlet surface the zero gradient boundary condition was also used. For pressure, a fixed value boundary condition with value zero was used on the outlet surface. The turbulent eddy viscosity ν_T outlet boundary value was set to be calculated from the other properties.

6.3.2 Grid Generation

The grids used in this investigation have a structured CH-type mesh topology near the wing and in the far-field region, with a connecting unstructured region, an example of which is shown in Figure 6.4. Three meshes were used with 10.72×10^6, 17.1×10^6 and $24.0\ \times10^6$ total cells for the coarse, moderate, and fine meshes, respectively. The minimum, maximum and average y^+ values on the wing and plate surfaces are given in Table 6.2.

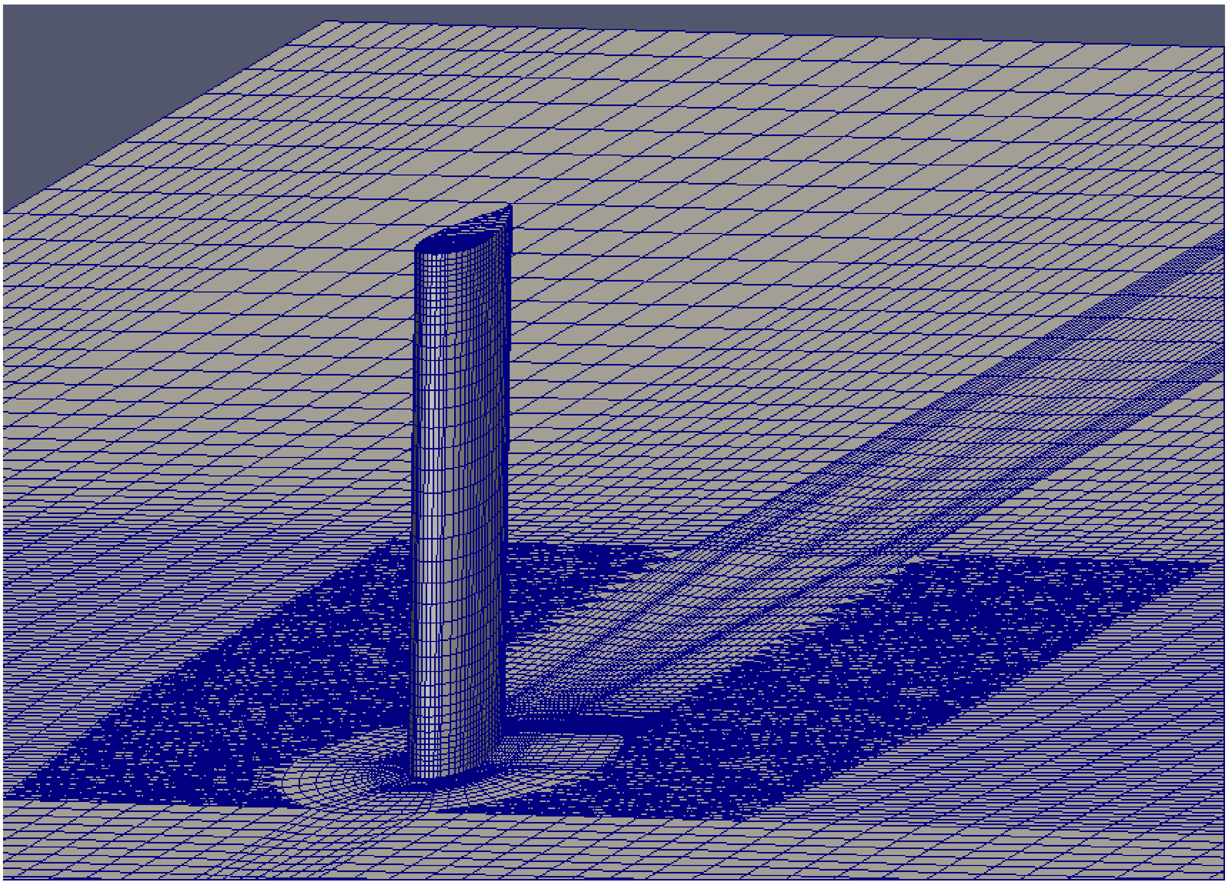

Figure 6.4: University of Adelaide anechoic wind tunnel case coarse mesh example

Table 6.2: University of Adelaide anechoic wind tunnel case mesh y^+ statistics

Wing (Plate)	Coarse Mesh	Moderate Mesh	Fine Mesh
Min. y^+	0.00992 (0.016704)	0.00958 (0.014372)	0.00705 (0.010606)
Max y^+	3.8108 (2.3367)	3.9151 (1.8684)	3.4830 (1.5604)
Ave. y^+	0.58959 (0.89784)	0.54459 (0.73997)	0.47377 (0.60985)

6.3.3 Residual Control and Numerical Methods

The simulation was run until all residuals reached 10^{-5} or less. Linear interpolation schemes were used throughout, as was a second order accurate linear scheme for the discretisation of gradient terms. The divergence terms for the velocity, turbulent kinetic energy, and dissipation fields were discretised using a first order accurate upwind scheme. All Laplacian terms were discretised with the second order accurate linear scheme with explicit non-orthogonal correction. Explicit non-orthogonal correction was performed when calculating surface normal gradient terms.

6.4 Results and Analysis

6.4.1 Grid Independence Results

The forces exerted on the wing, the wing TE boundary layer height, the location and intensity of the wing surface pressure coefficient were investigated as measures of the grid independence for the CFD results. The boundary layer height at the wing TE was determined at a plate normal distance (z) of 39 mm for each mesh solution, corresponding to the location in the outer boundary layer where

$$\frac{\partial Ti}{y/c} \geq -0.1, \tag{6.1}$$

where Ti is the turbulence intensity and y/c is the wall distance normalised by chord. The CFD results are compared in Table 6.3 and with boundary layer heights estimated using the BPM method for a 2D airfoil of the same chord and freesteam flow velocity, as well as those based on experimental hot wire measurements. The experimental and simulated results fall within the range expected based on the BPM model. Furthermore, the simulation results are consistent, exhibiting changes in value between the coarse and moderate, and moderate and fine meshes of 1.26% and 0.95%, respectively.

The values for total force (pressure and viscous) on the wing were extracted from each simulation and are given in Table 6.4. The symmetry of the case should result in $Fy = 0$, towards which the result tend. The drag (Fx) and spanwise (Fz) forces change by less than 1.9% and 1.1% between the moderate and fine mesh solutions, respectively. The mid-span ($z = 34.5$ mm plain) pressure coefficient for each mesh solution is given in Figure 6.5 along with that predicted using XFOIL for similar conditions ($M = 0.3$, $Re_C = 161000$, $\alpha = 0$, tripped at $0.1C$), while Table 6.5 gives the location and minimum value of the pressure coefficient for each mesh solution. The position and minimum value change by 0.486% and 0.147%, respectively, between the moderate and fine solutions.

Table 6.3: University of Adelaide anechoic wind tunnel case boundary layer heights comparison

	Coarse Mesh	Moderate Mesh	Fine Mesh	Experimental Value	BPM Estimate (Tripped-Untripped)
δ (mm)	3.16	3.12	3.15	3.44	2.38-4.1

6.4.2 Flow Visualisation and Structure

Figure 6.6 visualises isocontours of $Q = 1.225 \times 10^8[\frac{c}{U_\infty}]$, coloured by velocity magnitude, and exposes four strong tube-like regions of vortical flow around the wing tip. An additional structure can also be seen at the base of the wing, which starts upstream of the LE of the wing-plate junction, and extends along that junction interface. Figure 6.7 shows the static pressure

Table 6.4: University of Adelaide anechoic wind tunnel case forces on the wing

Parameter	Coarse Mesh	Moderate Mesh	Fine Mesh
Fx [N]	5.97×10^{-2}	6.60×10^{-2}	6.48×10^{-2}
Fy [N]	6.54×10^{-4}	1.69×10^{-5}	-2.97×10^{-4}
Fz [N]	2.75×10^{-2}	2.76×10^{-2}	2.73×10^{-2}

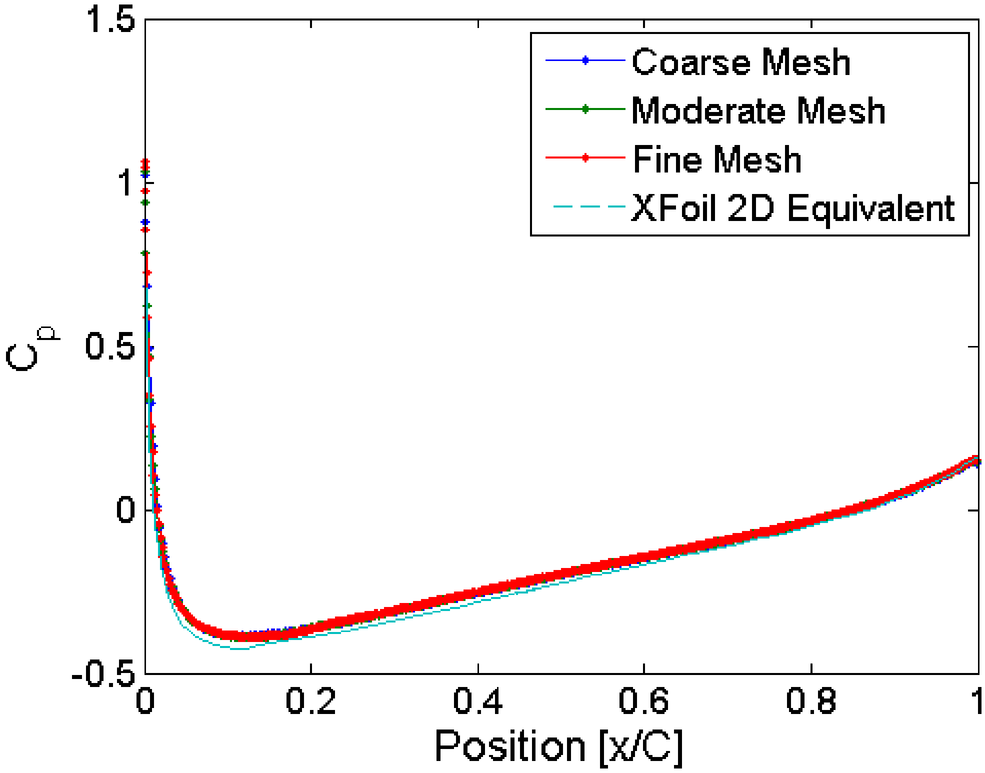

Figure 6.5: Comparison of midspan pressure coefficient for different mesh solutions

Table 6.5: Midspan pressure coefficient extrema and location

Parameter	Coarse Mesh	Moderate Mesh	Fine Mesh
$C_{p_{min}}$	-0.3170	-0.3188	-0.3172
$\frac{x}{C}\vert C_{p_{min}}$	0.1136	0.1286	0.1288

coefficient on the flat plate, the portside of the wing, and the wing tip. Local maxima regions occur along the wing leading edge as well as just before the point of maximum thickness along the span of the wing, and on the forwardmost section of the wing tip flat end. The pressure coefficient is relatively uniform along the wing in the spanwise direction, although some effect can be seen at the wing-plate junction, as well as at the wing tip. The largest variations are seen at the tip, in a region extending from the point of maximum wing thickness to the trailing edge, matching the location of one of the tube-like regions of vortical flow from Figure 6.6. Figures 6.8 and 6.9 show flow velocity components in the wing symmetry plane (U_y velocity component omitted as it is approximately zero in the symmetry plane). A region of positive vertical velocity can be seen downstream of the TE-tip and extending downstream. Figures 6.10-6.12 give the velocity components in the maximum thickness plane. Figures 6.13-6.16 give the velocity components as well as the magnitude of the vorticity in a plane 1 mm downstream of the TE. Normalised axial velocity and normalised x-plane vorticity are compared to the experimental measurements of Giuni and Green (2013), which are also for flat-ended NACA 0012 wall mounted airfoil, but at a somewhat higher chord based Reynolds number, Re_C = 740,000, than that of the present work, in Figures 6.17 and 6.18 respectively. Unfortunately the results of the present work are not made over precisely the same spatial ranges, and using exactly the same contour levels as the results of Giuni and Green (2013). Additionally, Giuni and Green (2013) do not have ticks on either the spatial axes nor the contour colourbars, which makes exact comparisons with the results problematic. However, the present results have been made as easily comparable as possible, given these limitations. It is also worth mentioning that these comparisons are made using a secondary co-ordinate system (x_2, y_2, z_2) which is aligned with the primary coordinate system, but with offsets, such that the origin is at the airfoil TE-tip interface, and such that the relationship between the primary and secondary coordinate system is given by

$$\begin{bmatrix} x_1 \\ y_1 \\ z_1 \end{bmatrix} = \begin{bmatrix} 1 & 0 & 0 \\ 0 & 1 & 0 \\ 0 & 0 & 1 \end{bmatrix} \times \begin{bmatrix} x_2 \\ y_2 \\ z_2 \end{bmatrix} + \begin{bmatrix} C \\ 0 \\ C \end{bmatrix}. \tag{6.2}$$

This gives a right-handed secondary coordinate system that is otherwise equivalent to the left-handed system of Giuni and Green (2013) but for the different sense of the y-axis. The low axial velocity regions of the present work and that of Giuni and Green (2013) have the same structure, although it can be seen from Figure 6.17 that larger and more intense low flow regions are observed in the present work.

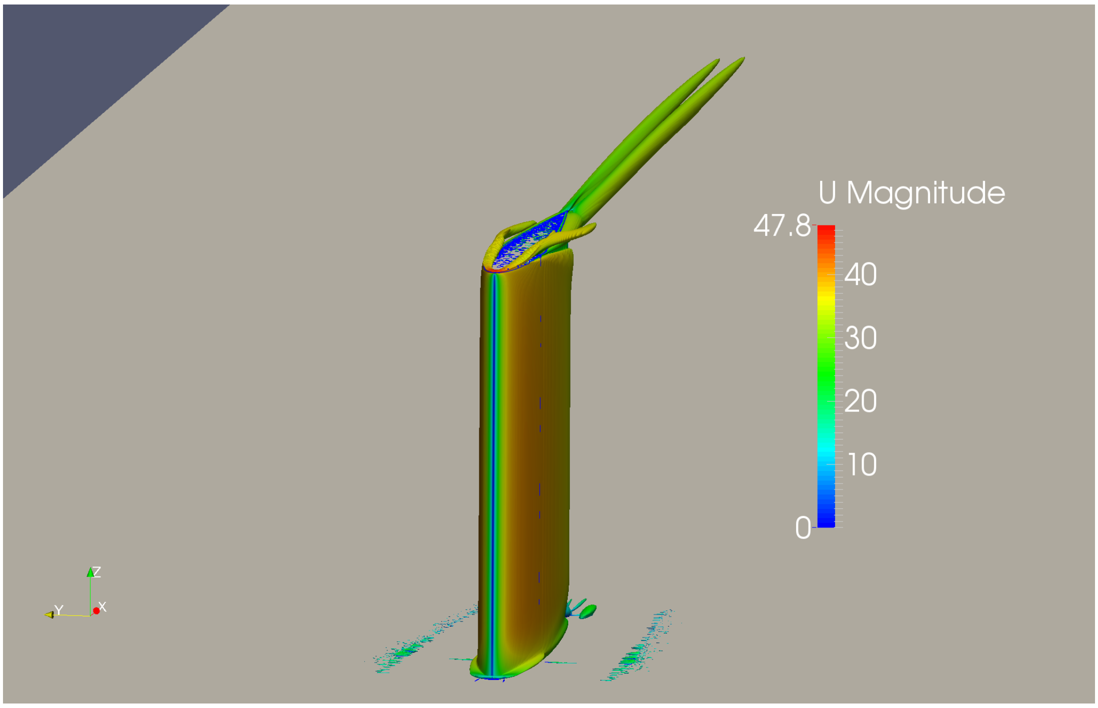

Figure 6.6: University of Adelaide anechoic wind tunnel case flow visualistion of isocontours of Q coloured by flow velocity magnitude

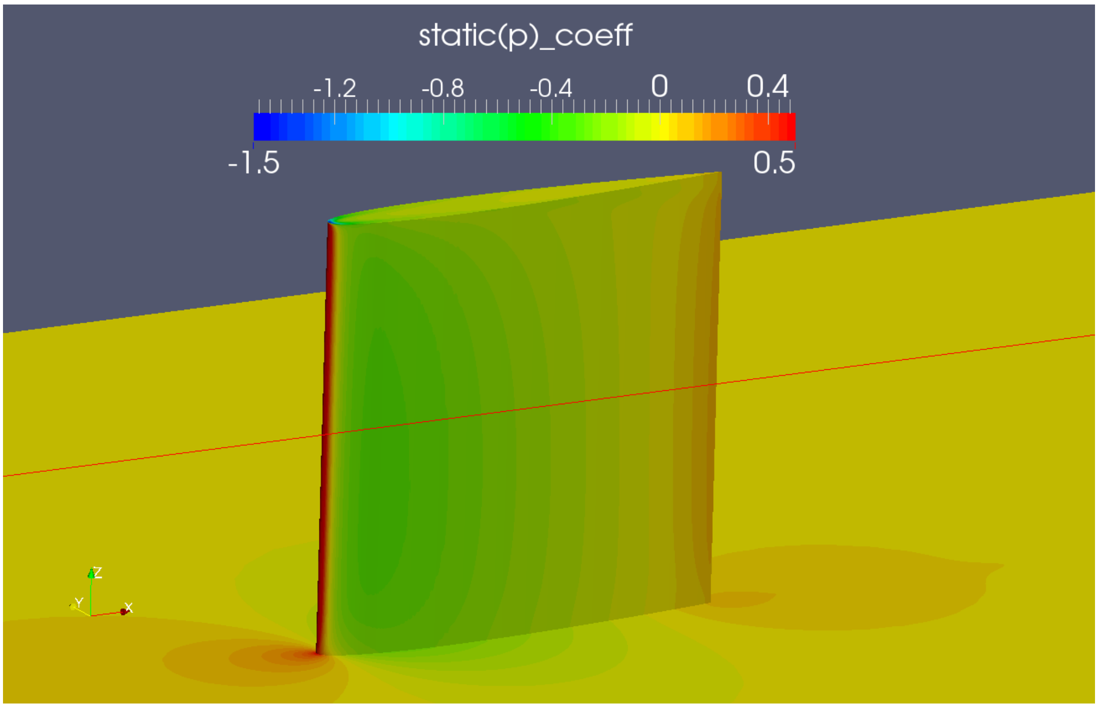

Figure 6.7: University of Adelaide anechoic wind tunnel case wing and flat plate static pressure coefficient visualisation

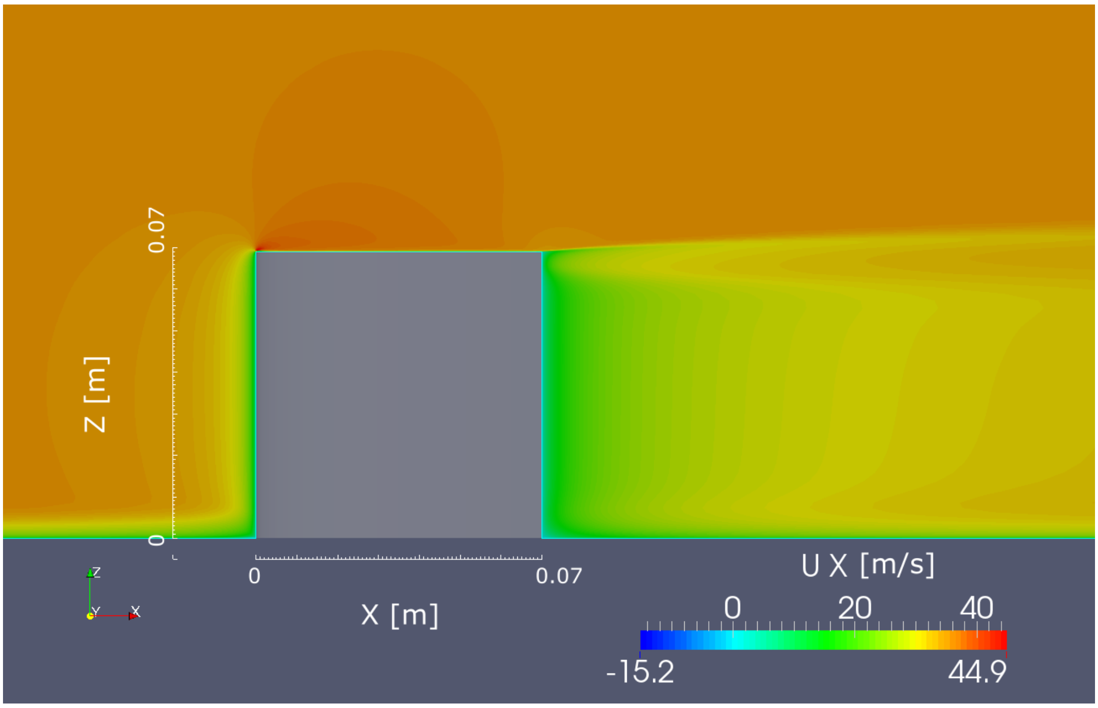

Figure 6.8: University of Adelaide anechoic wind tunnel case visualisation of U_x in the wing symmetry plane

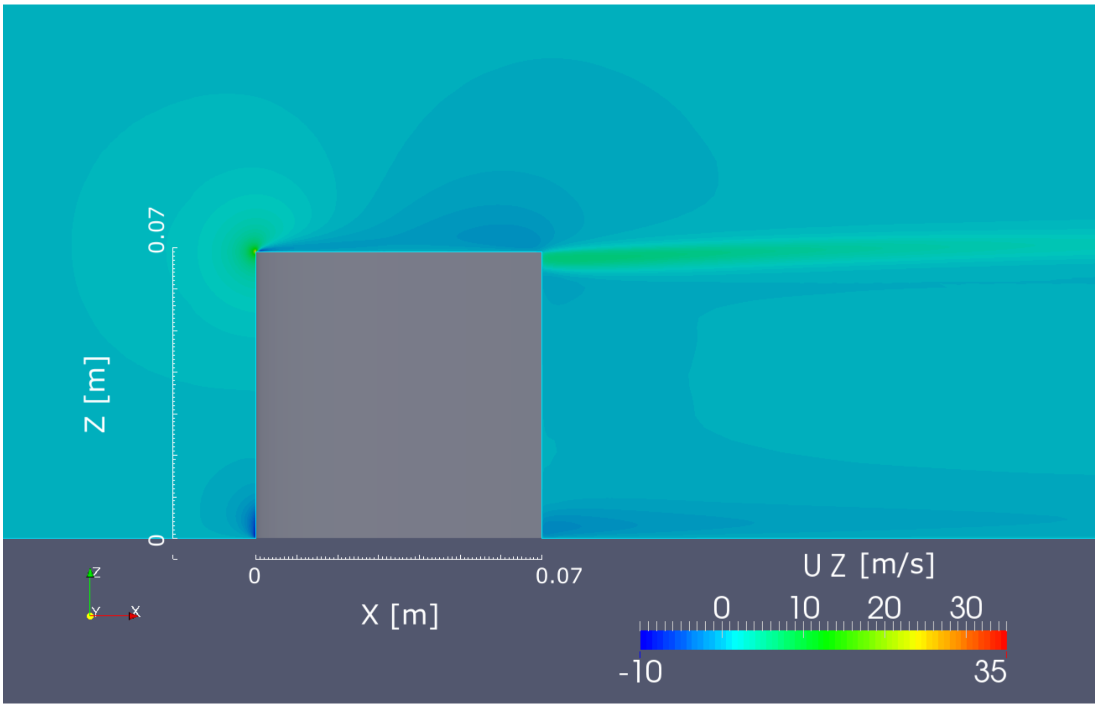

Figure 6.9: University of Adelaide anechoic wind tunnel case visualisation of U_z in the wing symmetry plane

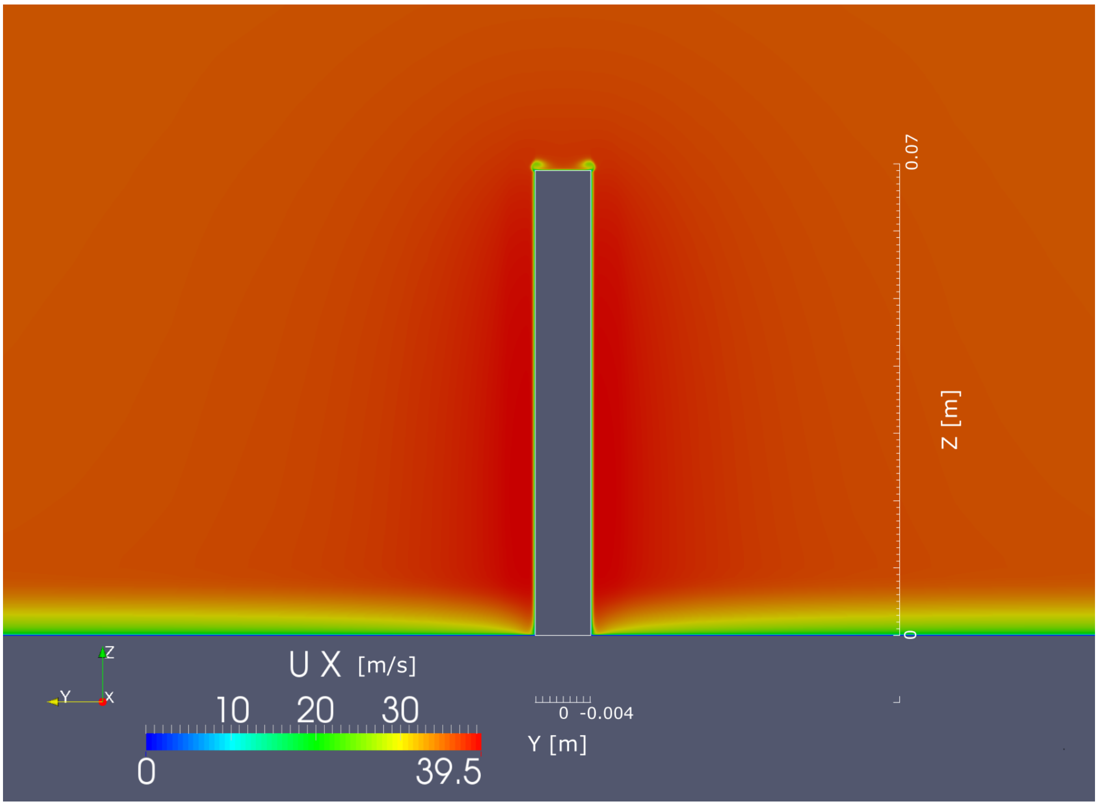

Figure 6.10: University of Adelaide anechoic wind tunnel case visualisation of U_x in the maximum thickness plane

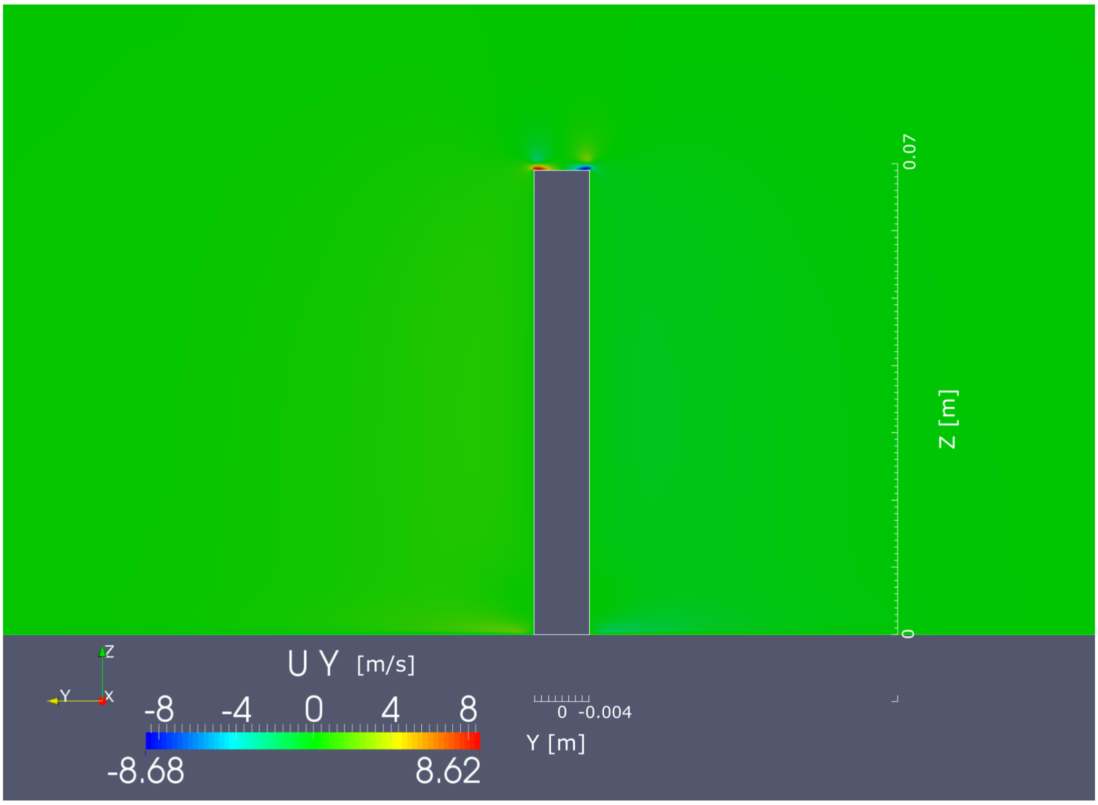

Figure 6.11: University of Adelaide anechoic wind tunnel case visualisation of U_y in the maximum thickness plane

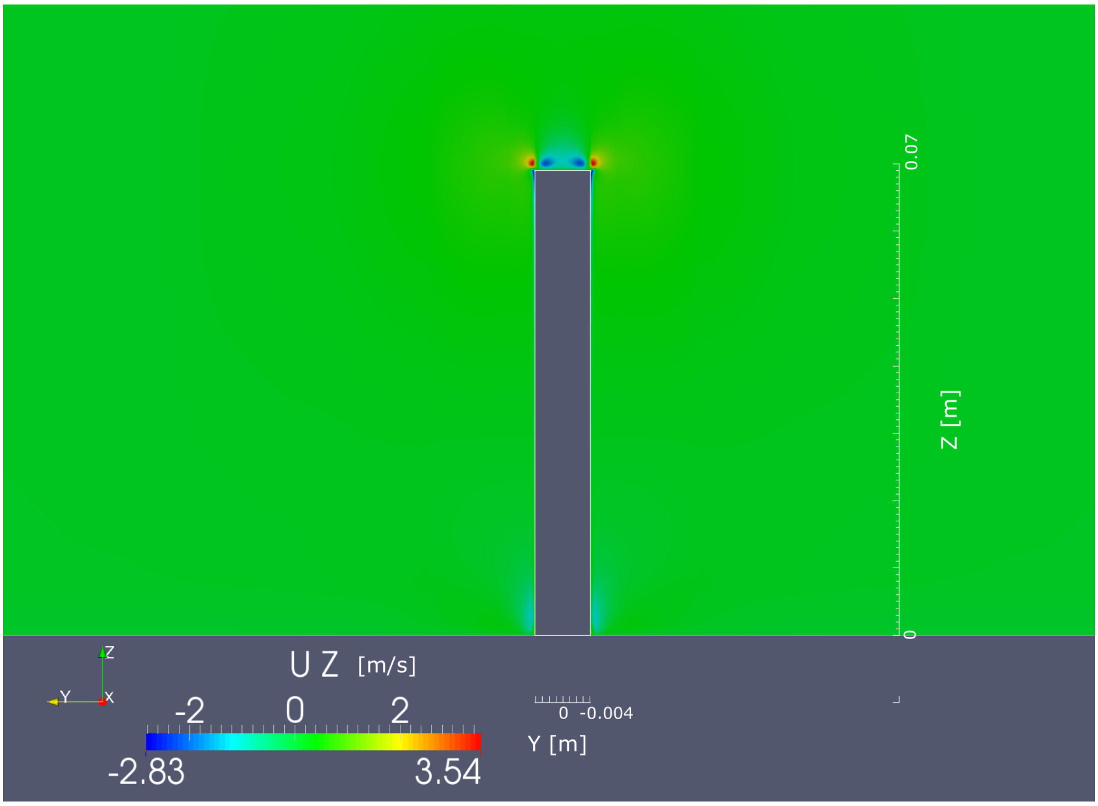

Figure 6.12: University of Adelaide anechoic wind tunnel case visualisation of U_z in the maximum thickness plane

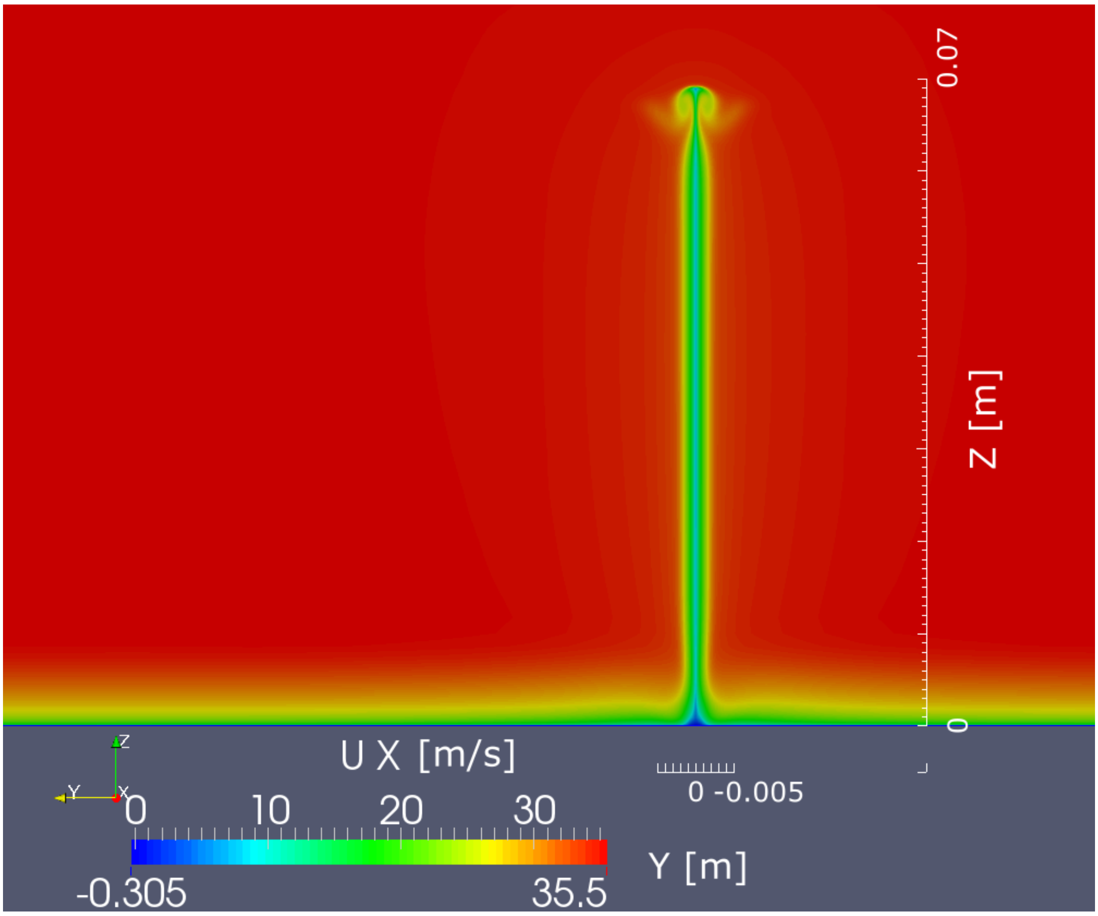

Figure 6.13: University of Adelaide anechoic wind tunnel case visualisation of U_x in a plane 1mm downstream of the TE

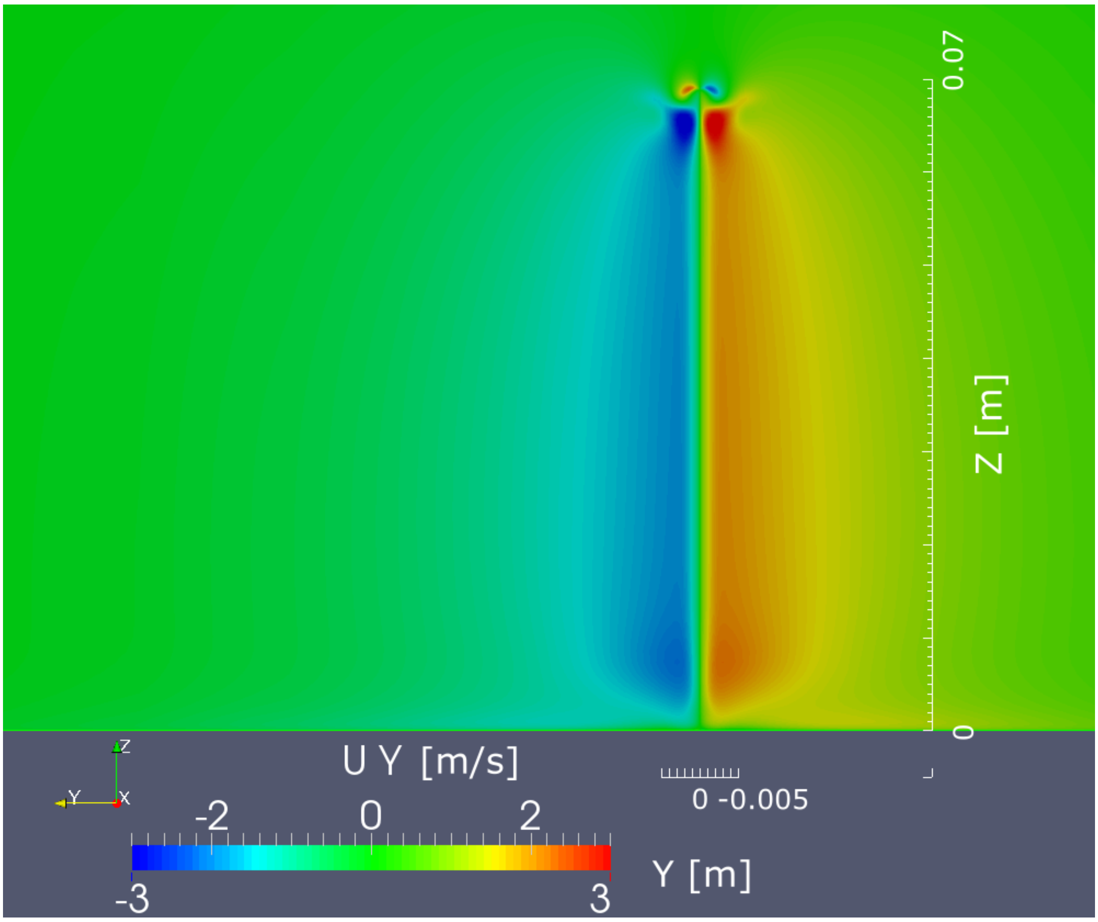

Figure 6.14: University of Adelaide anechoic wind tunnel case visualisation of U_y in a plane 1mm downstream of the TE

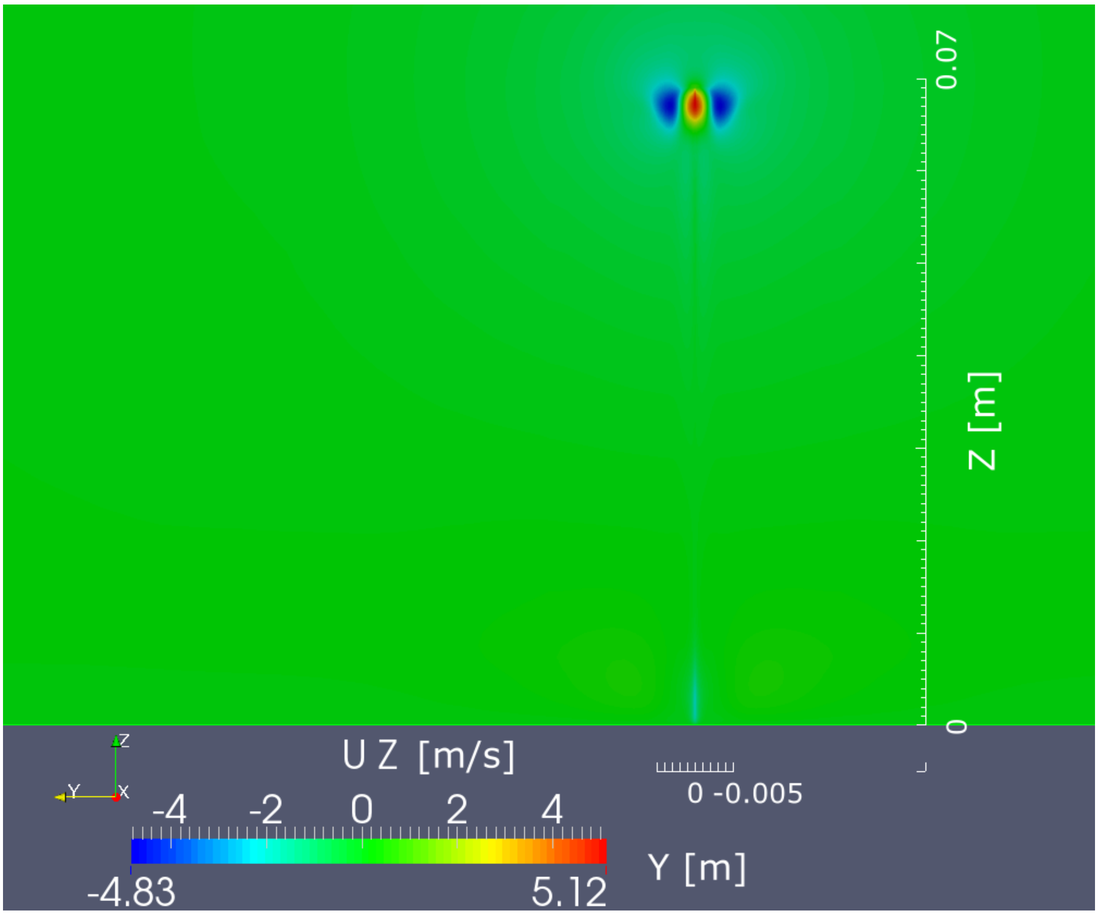

Figure 6.15: University of Adelaide anechoic wind tunnel case visualisation of U_z in a plane 1mm downstream of the TE

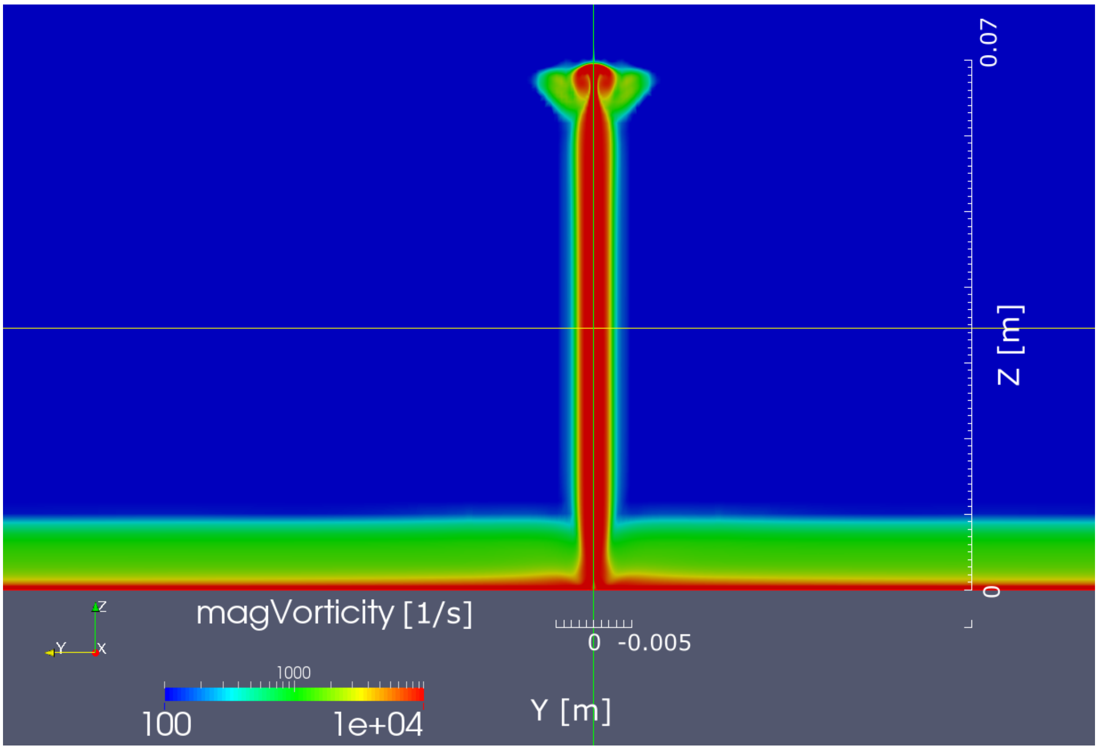

Figure 6.16: Visualisation of the magnitude of vorticity in a plane 1mm downstream of the TE

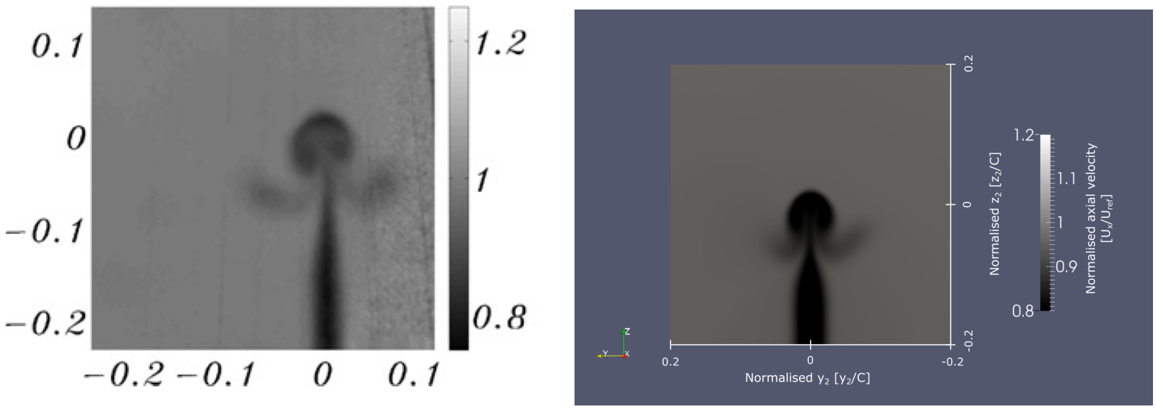

(a) Result of Giuni and Green (2013) (b) Fine mesh normalised axial velocity

Figure 6.17: Comparison of University of Adelaide anechoic wind tunnel case fine mesh normalised axial velocity one quarter chord downstream of the TE with experimental results of Giuni and Green (2013) in chord normalised coordinates

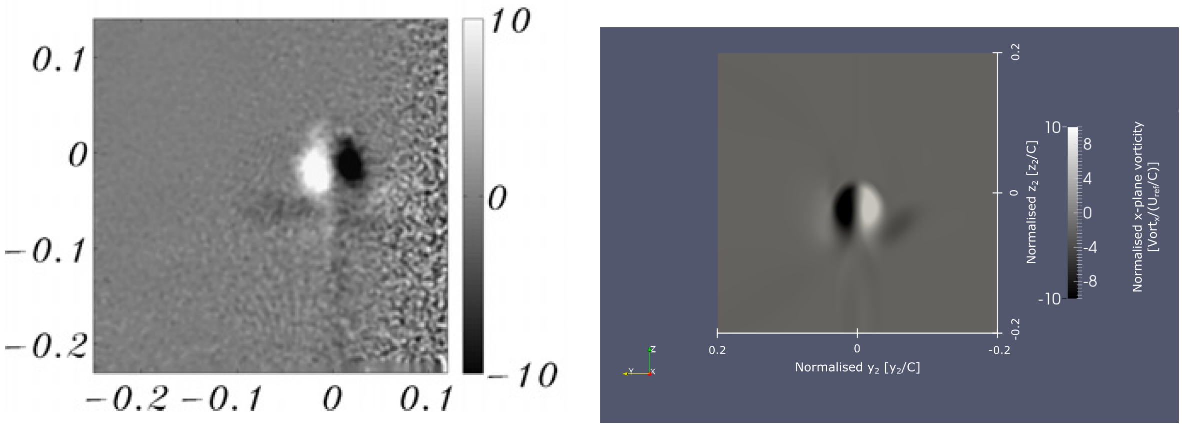

(a) Result of Giuni and Green (2013) (b) Fine mesh normalised x-plane vorticity

Figure 6.18: Comparison of University of Adelaide anechoic wind tunnel case fine mesh normalised x-plane vorticity one quarter chord downstream of the TE with experimental results of Giuni and Green (2013) in chord normalised coordinates

6.4.3 Tip Flow Topology

The literature review of tip vortices given in Section 2.1.2 highlighted that although the tip vortex formation process was understood for rounded airfoils, and flat ended airfoils when at angles of attack, there has been no detailed investigation of the tip vortex formation process for flat ended airfoils at zero angle of attack. Results for the flow in the tip region are presented and used to develop a topology model of tip vortices for flat ended airfoils at zero angle of attack.

Vorticity magnitude results from the fine mesh solution corresponding to $y - z$ planes taken at $x = [0.017, 0.035, 0.05, 0.07]$ (meters) are given in Figures 6.19-6.22 respectively. A tip flow topology model has been developed from inspection of the CFD results. A purely textual description of the flat-ended tip vortex formation process can be rather difficult to follow, and frequent reference to Figure 6.23 is recommended to minimize potential confusion. The explanation will consider the flow on a series of planes along the chord, as indicated in Figure 6.23a. Plane A is representative of a plane very close to the leading edge. Plane B is representative of a plane about midway between the leading edge and the maximum thickness plane. Plane C corresponds to the maximum thickness plane. Plane D is representative of a plane somewhat downstream of the maximum thickness plane. Finally, Plane E is representative of a plane at the trailing edge, and Plane F a plane in the near wake. At Plane A, shown in Figure 6.23b, located very near the leading edge, a pair of contra-rotating vortices, designated the leading vortex pair, are developed on the tip surface by inflow around the tip edge crossing around the tip before the point of maximum wing thickness. As the wing thickens (Figure 6.23c), the leading vortex pair stay near the tip edge, which results in them moving away from the chord line as can be seen in Figure 6.19. At the point of maximum wing thickness (Figure 6.23d), the flow over the tip edge reverses, and begins flowing from the tip back down the wing span. This causes the leading vortex pair to be drawn away from the tip-edge, away from the chord line, as well as inboard (towards the root of the wing), and causes the formation of a new pair of vortices, designated the proximal vortices, on the other side of the tip-edge, on the span-surface, which are contra-rotational to each other, as well as the leading vortex nearest them. As the wing thickness futher reduces (Figure 6.23e), the leading vortex pair continue to move further away from the chord line and inboard, while the ongoing flow from the tip, feeds and strengthens the proximal vortices, which stay near the tip edge, moving inward towards the chord line. This can be seen from the changes between Figures 6.20 and 6.21. At the wing trailing edge, the proximal vorticies, no longer separated on either side of the wing, meet and begin to be drawn outboard by upwash (Figure 6.23f), which corresponds to the results shown in Figure 6.22.

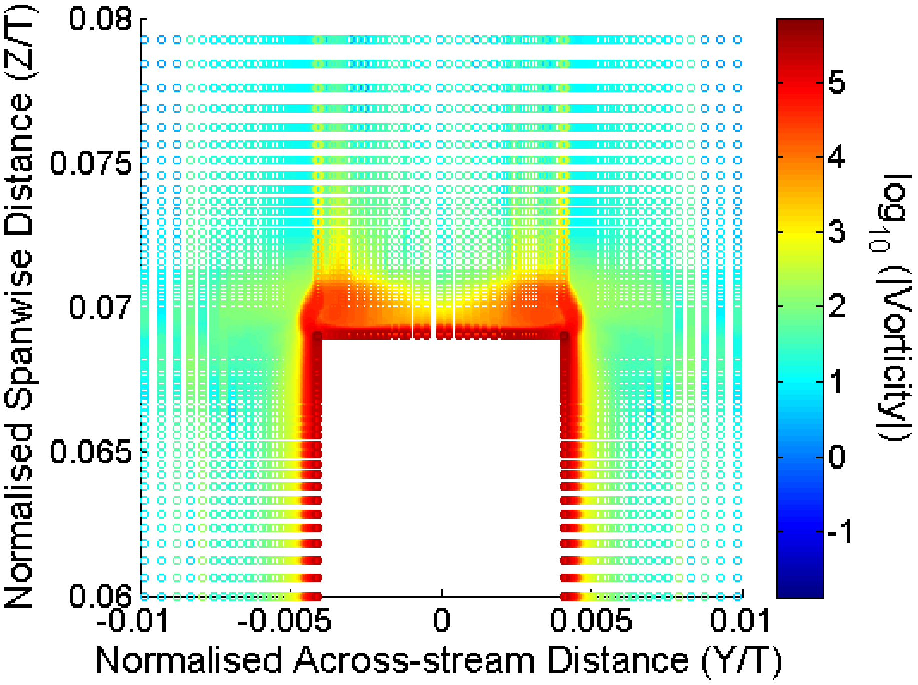

Figure 6.19: University of Adelaide anechoic Wind Tunnel Case $x = 0.017$ vorticity magnitude

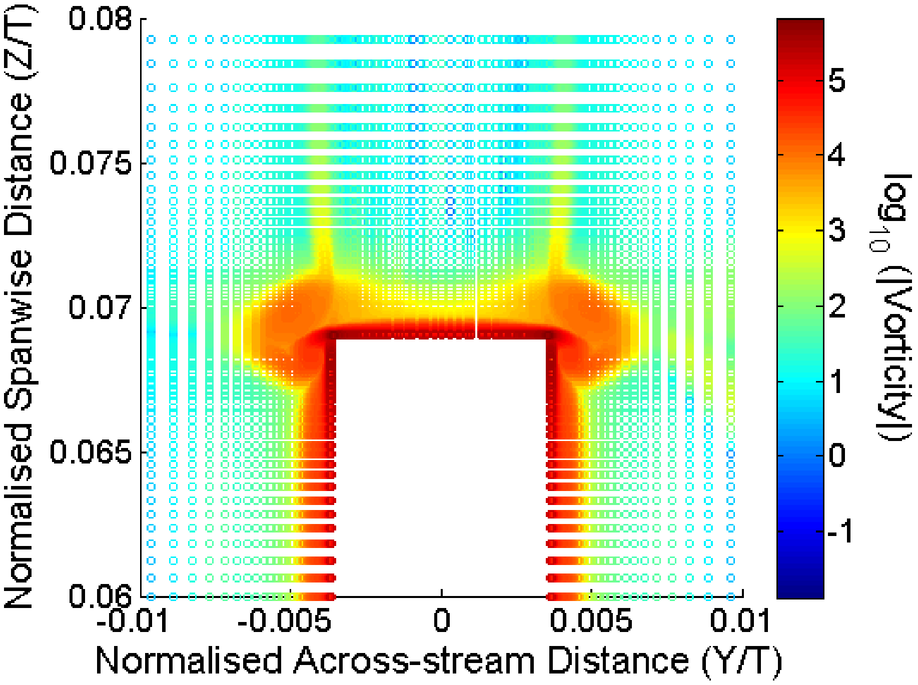

Figure 6.20: University of Adelaide anechoic Wind Tunnel Case $x = 0.035$ vorticity magnitude

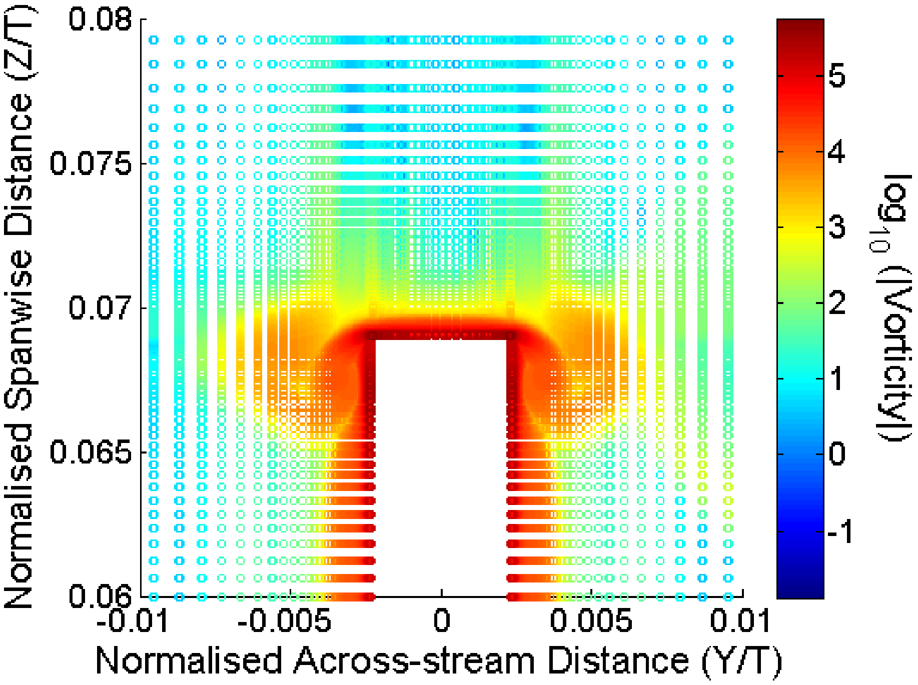

Figure 6.21: University of Adelaide anechoic Wind Tunnel Case $x = 0.05$ vorticity magnitude

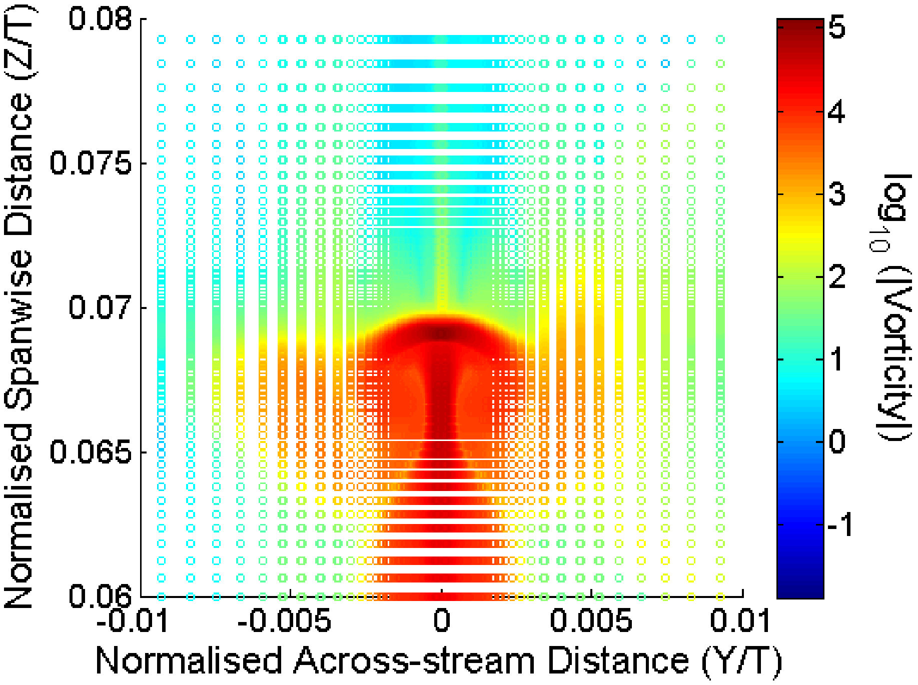

Figure 6.22: University of Adelaide Anechoic Wind Tunnel Case $x = 0.07$ vorticity magnitude

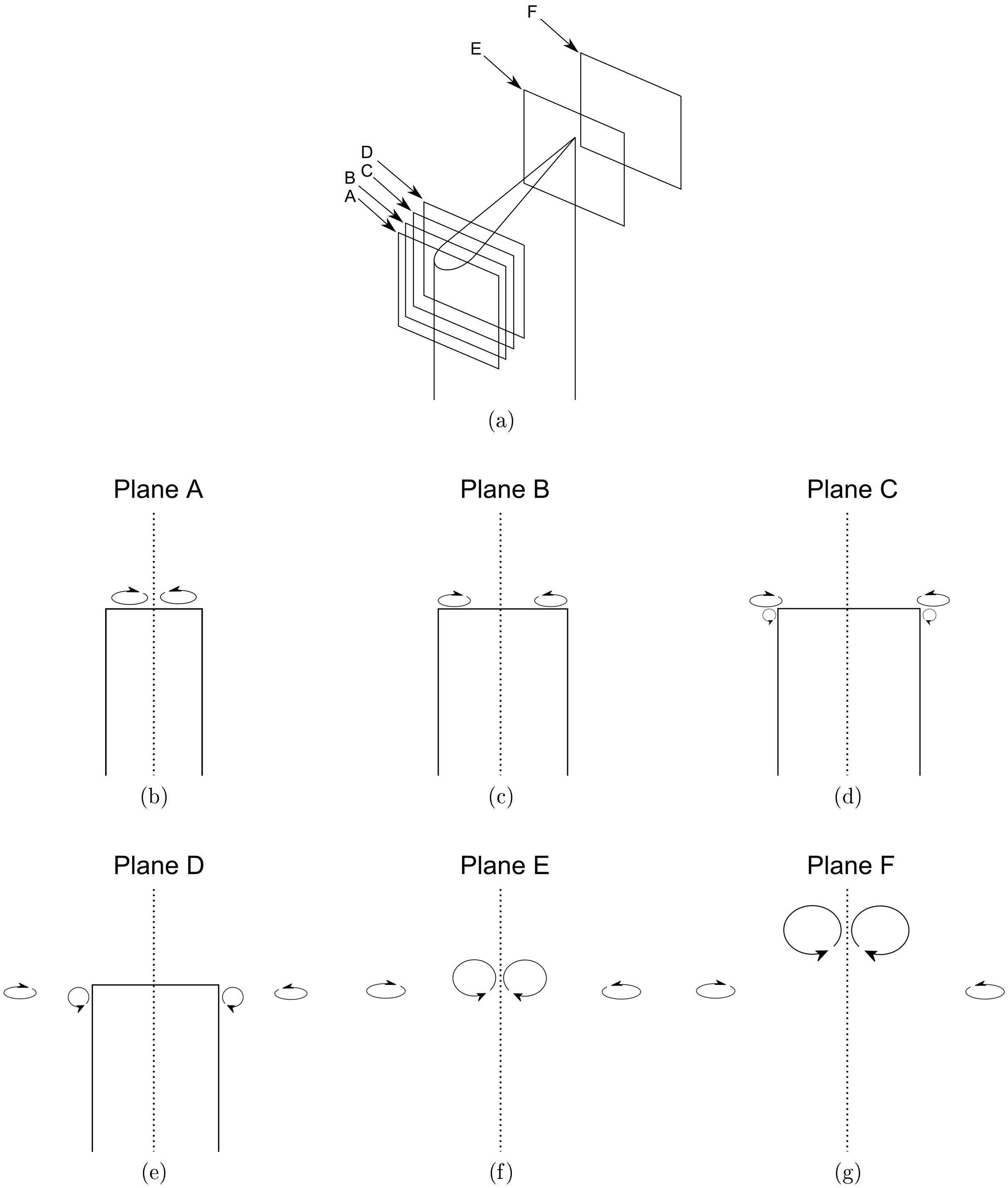

(a)

(b)

(c)

(d)

(e)

(f)

(g)

Figure 6.23: Flat ended airfoil at zero AOA vortex formation process diagram
a) Vortex development plane definition diagram
b-g) Vortex representative planes as labelled

6.4.4 Pressure Fields

The flat plate pressure results shown in Figure 6.25 do not place the region of lowest pressure coefficient slightly upstream of the point of maximum thickness of the wing, where it would be expected. This deviation was also seen in Chapter 4, and is commonly seen for RANS CFD predictions for wing in junction flows, having also been encountered in the studies of Paik et al. (2007); Apsley and Leschziner (2001) and Paciorri et al. (2005). The pressure coefficient on the port side of the wing, given in Figure 6.24, is relatively uniform along the wing in the spanwise direction. At the wing-plate junction as well as at the tip, the positive pressure coefficient regions at the leading and trailing edges are much smaller than those of the relatively uniform midspan region. The strongest variations in pressure coefficient from that at the midspan are seen at the tip, in a region extending from the point of maximum wing thickness to the trailing edge, which corresponds to the region influenced by the proximal vorticies discussed in Section 6.4.3, and was seen in the oil-film visualisation of Moreau et al. (2014) for conditions otherwise similar to the present work, except for a wing of aspect ratio 2.

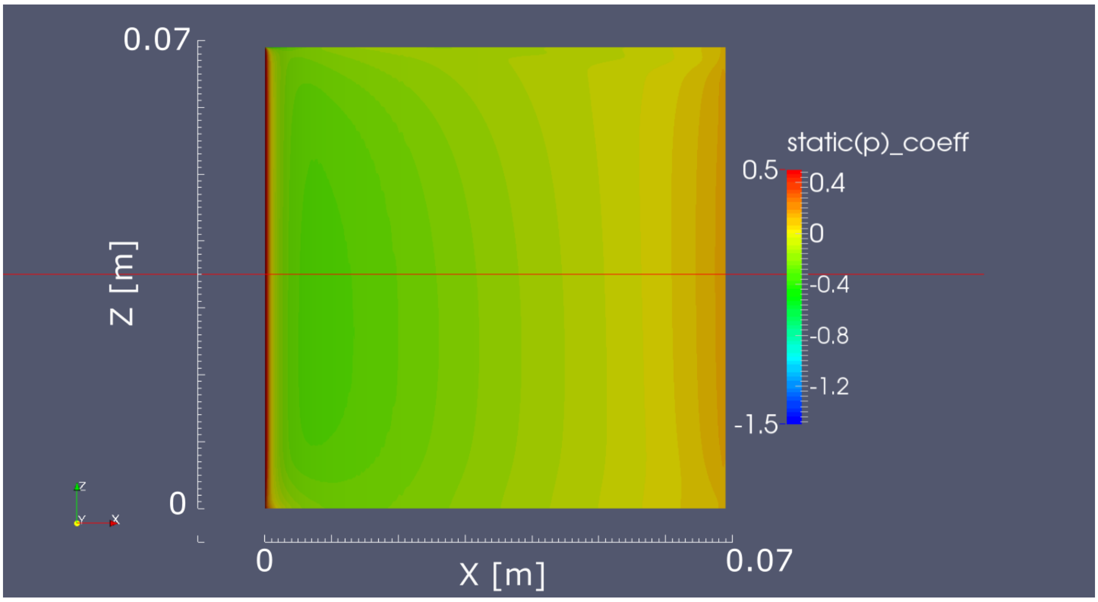

Figure 6.24: University of Adelaide anechoic wind tunnel case wing port side static pressure coefficient visualisation

6.4.5 Comparison of Simulated and Experimental Velocity Fields

Figure 6.2 showed the locations at which experimental velocity measurements were taken against which the CFD results will be compared. Velocity ($U_{Mag} = |u|$), as well as turbulent kinetic energy (k), will be compared. A spanwise sample taken in the chordwise symmetry plane 1 mm downstream of the TE is shown in Figures 6.26 and 6.28. The simulated symmetry plane velocity profile shows good qualitative agreement with that measured experimentally, with a rise from $z/C = 0$ to a relatively steady region, until the tip-region at about $z/C = 1$, although quantitatively the velocity is somewhat underpredicted. This velocity has been found to be sensitive to the sample location due to the extreme proximity of the sample to the wing surface. If samples taken a further $+1$ mm downstream are compared against those of the experiment, significantly improved quantitative agreement is found, as shown in Figure 6.27. This can also be seen in Figure 6.30 which gives the fine mesh solution downstream sample distance

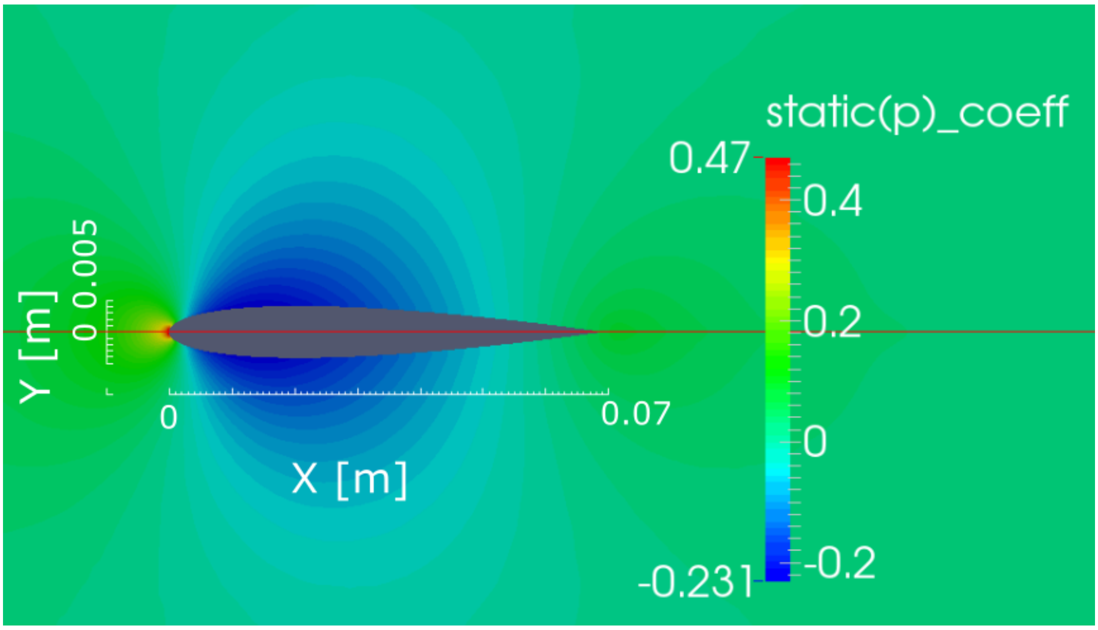

Figure 6.25: University of Adelaide anechoic wind tunnel case flat plate static pressure coefficient visualisation

dependence for the 39 mm wall normal distance velocity profiles. However this is thought to be a consistent result of the RANS modelling, as lower velocities are also seen when comparing these results to the experimental results of Giuni and Green (2013), as already discussed in relation to Figure 6.17. The turbulent kinetic energy shows similar qualitative agreement and only slightly quantitative overprediction. Samples taken at plate normal distances (z) of 39, 64 and 69 mm, also taken 1mm downstream of the TE are given in Figures 6.29-6.35. The velocity profiles of the plate normal sample set have reasonable agreement with those measured experimentally, except at the symmetry line, where noticeable underprediction occurs. Similarly the intensity of the turbulence profiles shows good qualitative agreement, being of the same shape, though with somewhat smaller widths and having higher intensities than those measured experimentally. It should be noted that the experimental measurements only measured two velocity components, and for comparison to the simulation the third component was estimated assuming a 4:2:3 ratio between u' : v' : w', which is known to hold for flat plate boundary layers (Wilcox, 2006). Furthermore, the TSI 1210-T1.5 single wire probe used in the physical experiment of Moreau and Doolan (2013) has 1.3 mm width making it susceptible to spacial averaging. The reader is also reminded of the simplifying assumptions of a sharp trailing edge used in the CFD compared with the blunt trailing edge in the physical experiment, as well as the induced transition to turbulent flow in the experiments by means of 12 mm wide serrated strip of double sided tape covered in fine sand when compared to the natural transition of the CFD implementation, which is controlled by the ability of the turbulence model to capture the laminar to turbulent flow transition. The challenges of ensuring 0 degree angle of attack exactly in a physical experiment, as well as complete symmetry of model shape, surface finish, incoming flow, and tripping, mean it is unsurprising that the experimental measurements of Moreau and Doolan (2013) and Giuni and Green (2013) both exhibit greater asymmetry than seen in the CFD results.

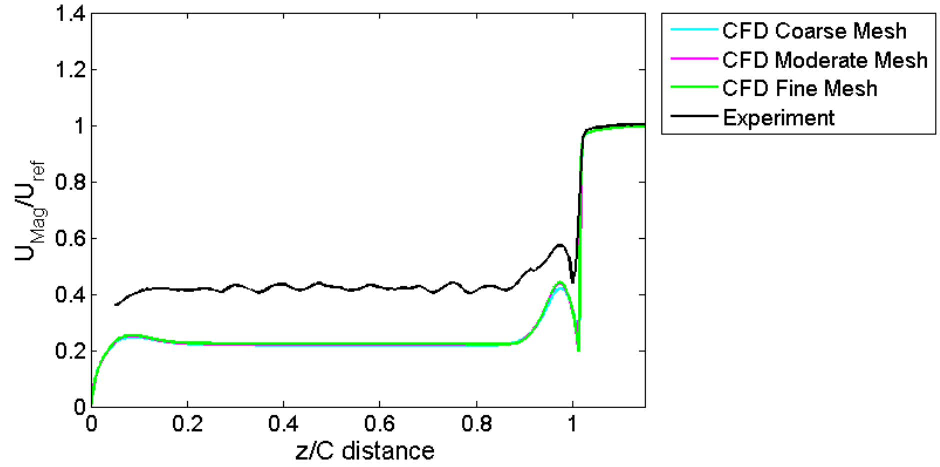

Figure 6.26: University of Adelaide anechoic wind tunnel case symmetry plane velocity profile comparison

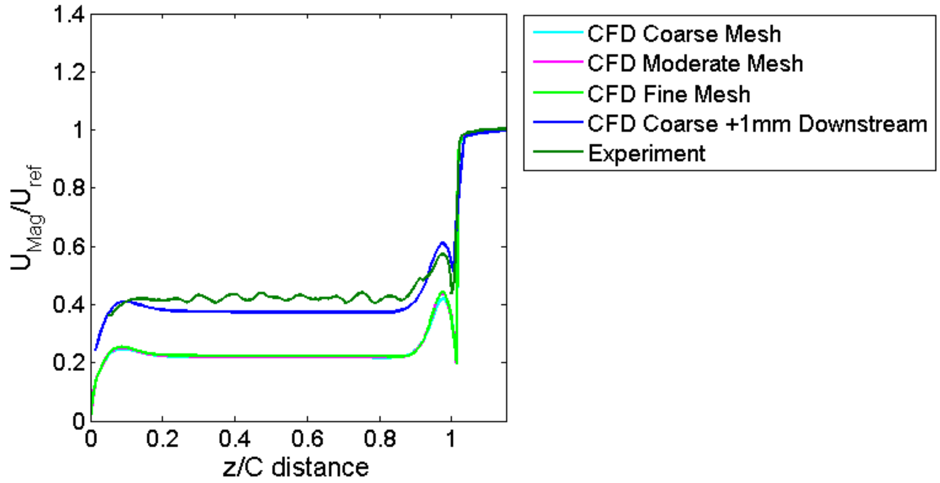

Figure 6.27: University of Adelaide anechoic wind tunnel case symmetry plane velocity profile comparison showing sample distance dependence

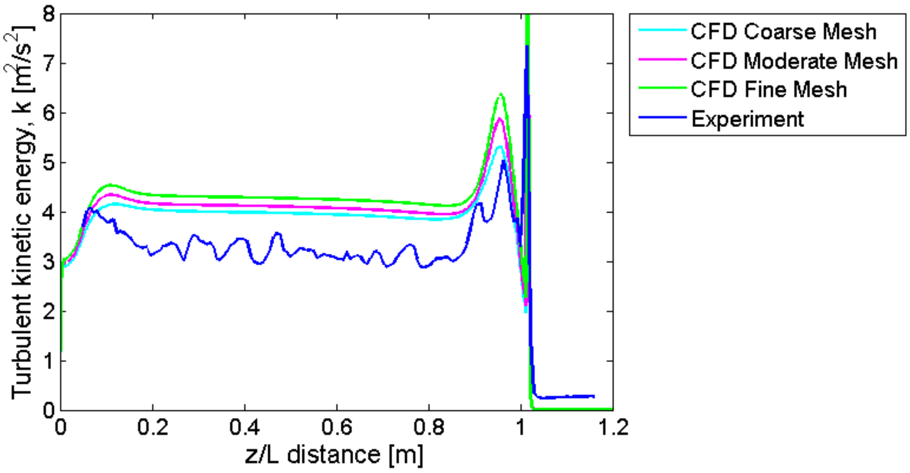

Figure 6.28: University of Adelaide anechoic wind tunnel case symmetry plane turbulence kinetic energy profiles

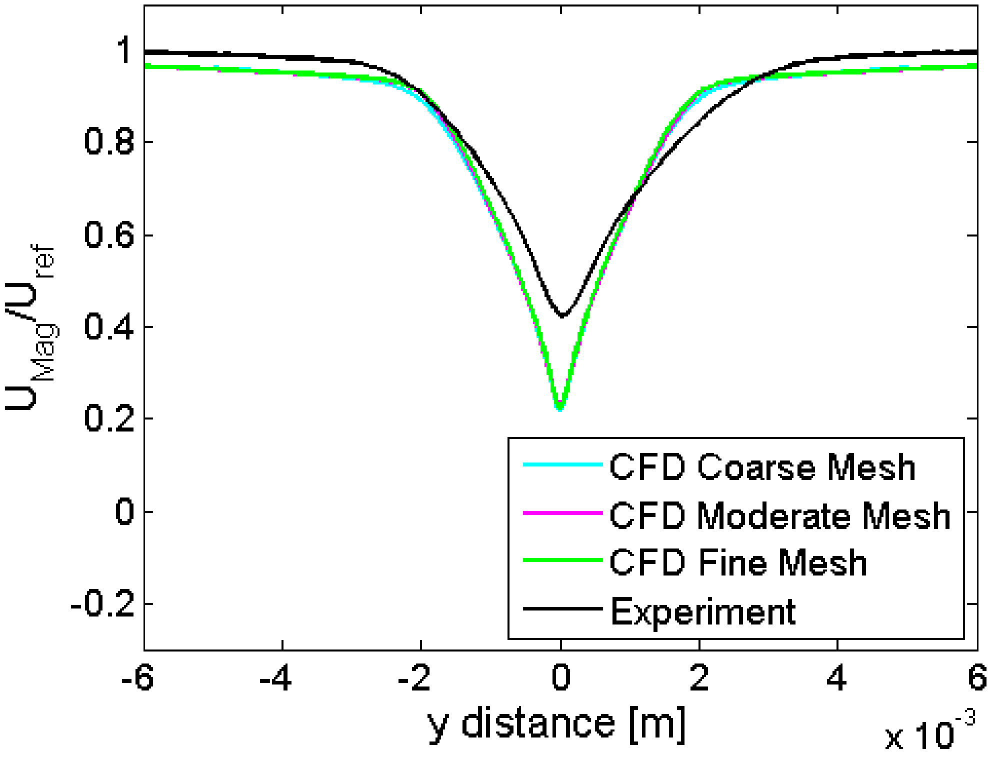

Figure 6.29: University of Adelaide anechoic wind tunnel case 39mm plane velocity profile comparison

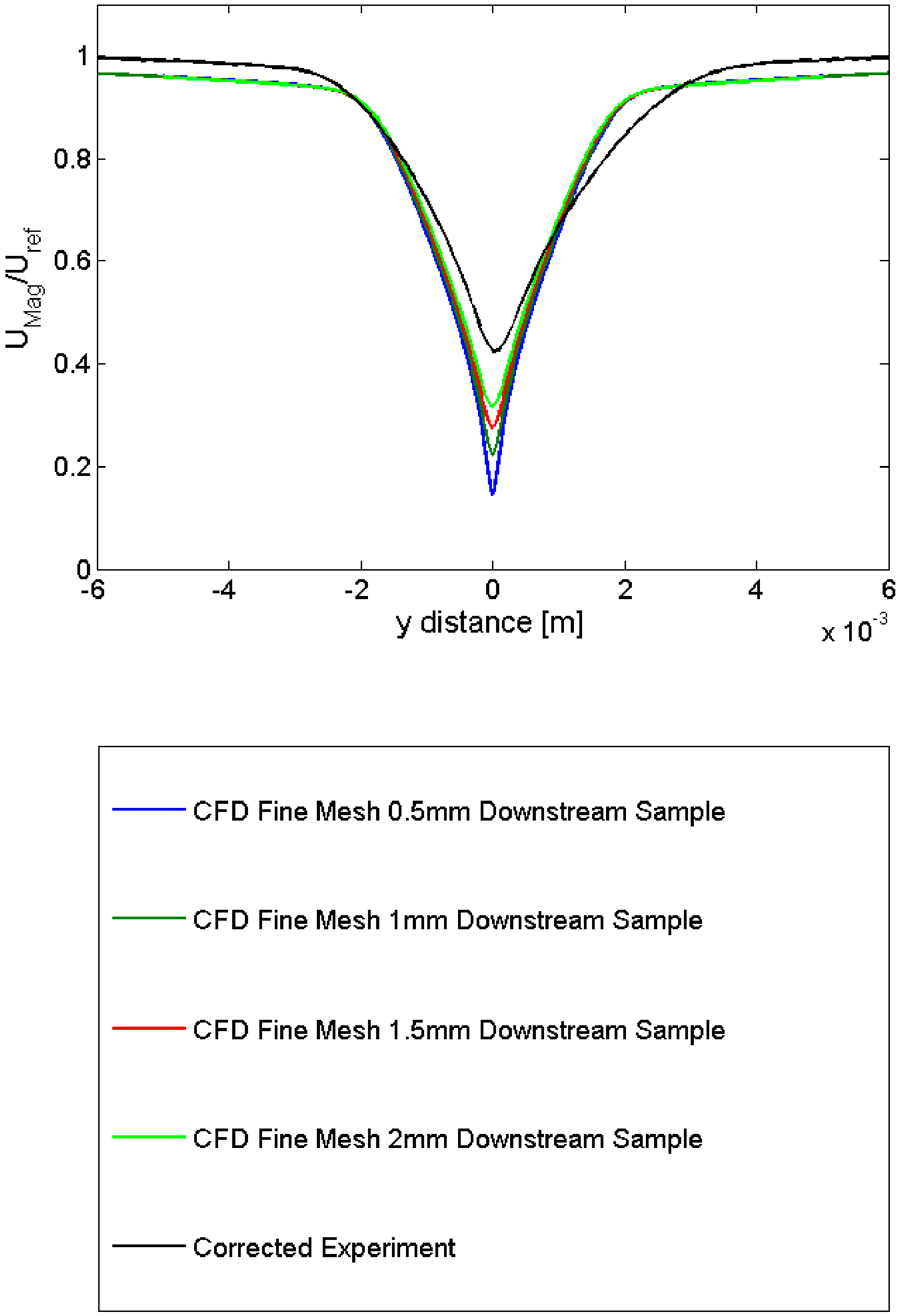

Figure 6.30: University of Adelaide anechoic wind tunnel case 39mm plane velocity sample downstream distance dependence plot

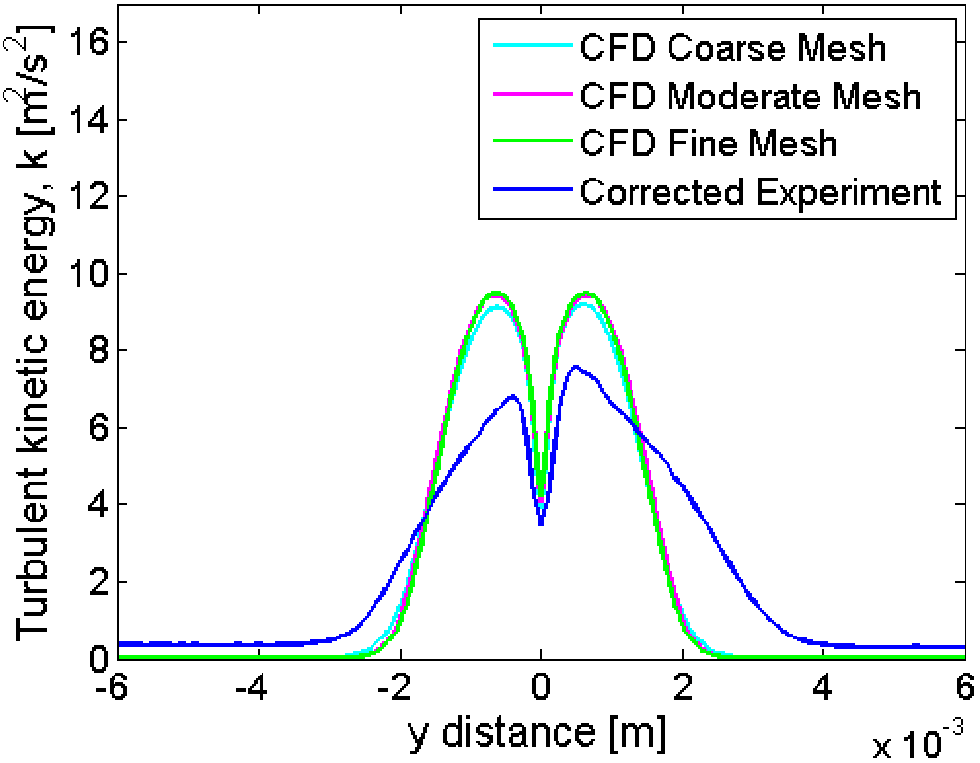

Figure 6.31: University of Adelaide anechoic wind tunnel case 39mm plane turbulence intensity profile comparison

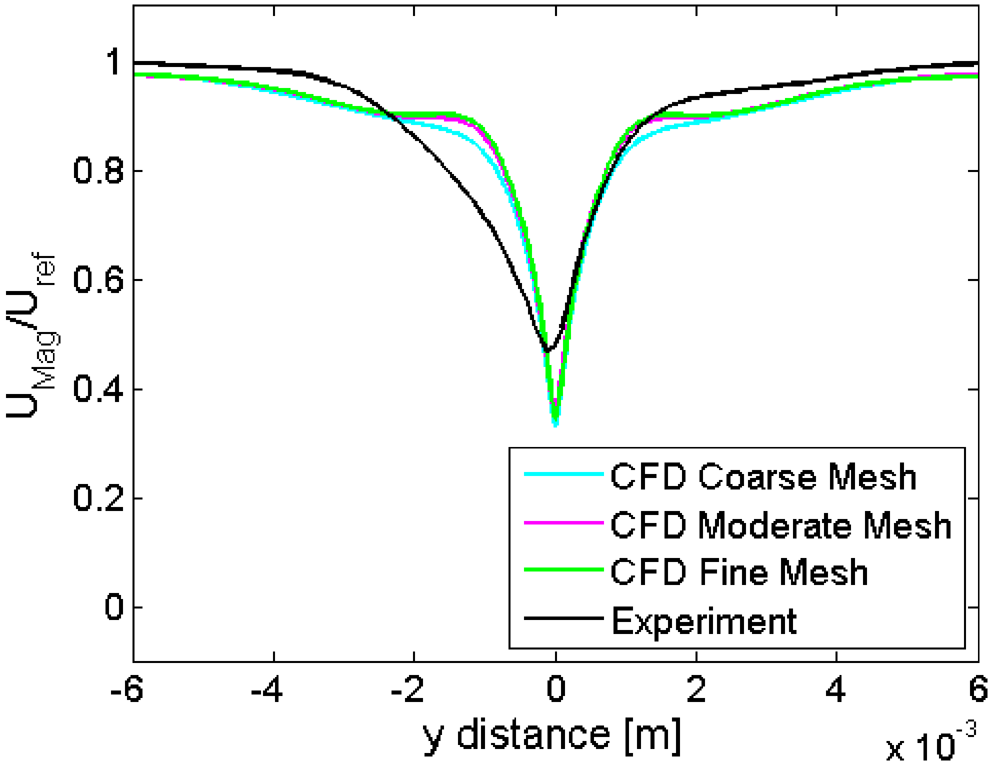

Figure 6.32: University of Adelaide anechoic wind tunnel case 64mm plane velocity profile comparison

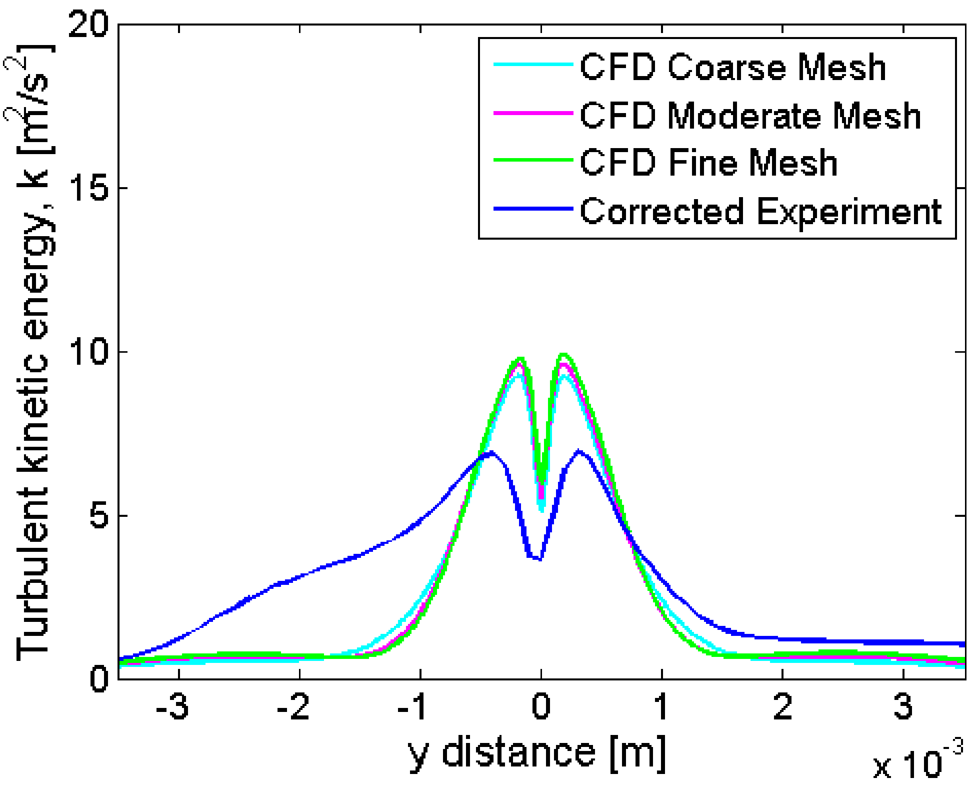

Figure 6.33: University of Adelaide anechoic wind tunnel case 64mm plane turbulence intensity profile comparison

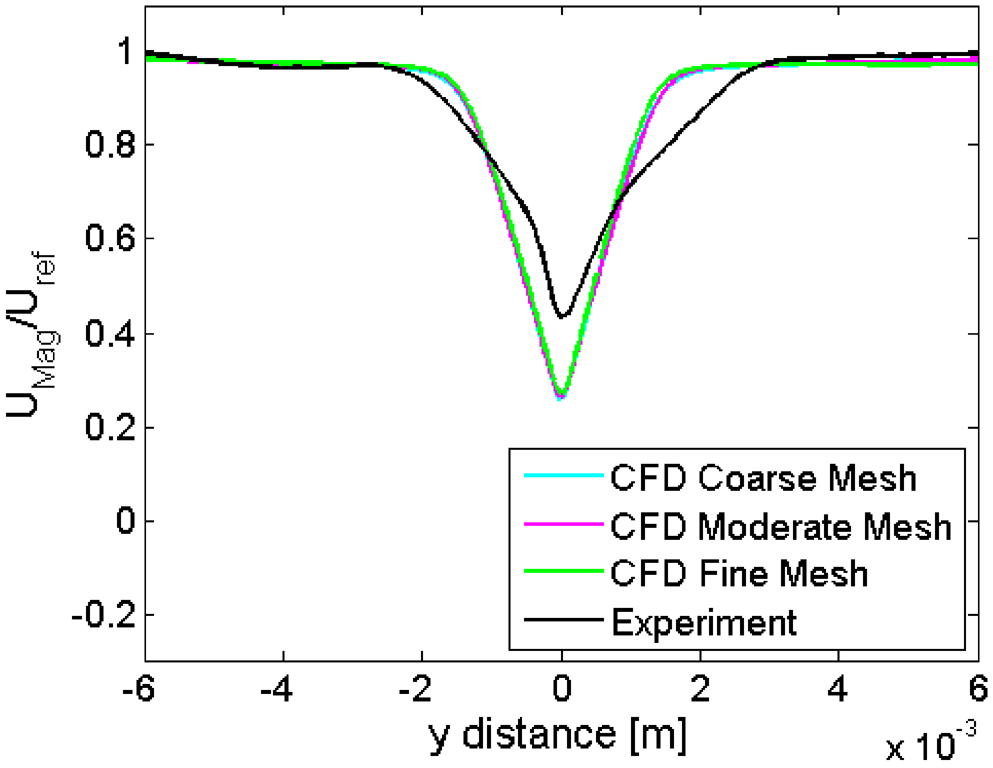

Figure 6.34: 69mm plane velocity profile comparison

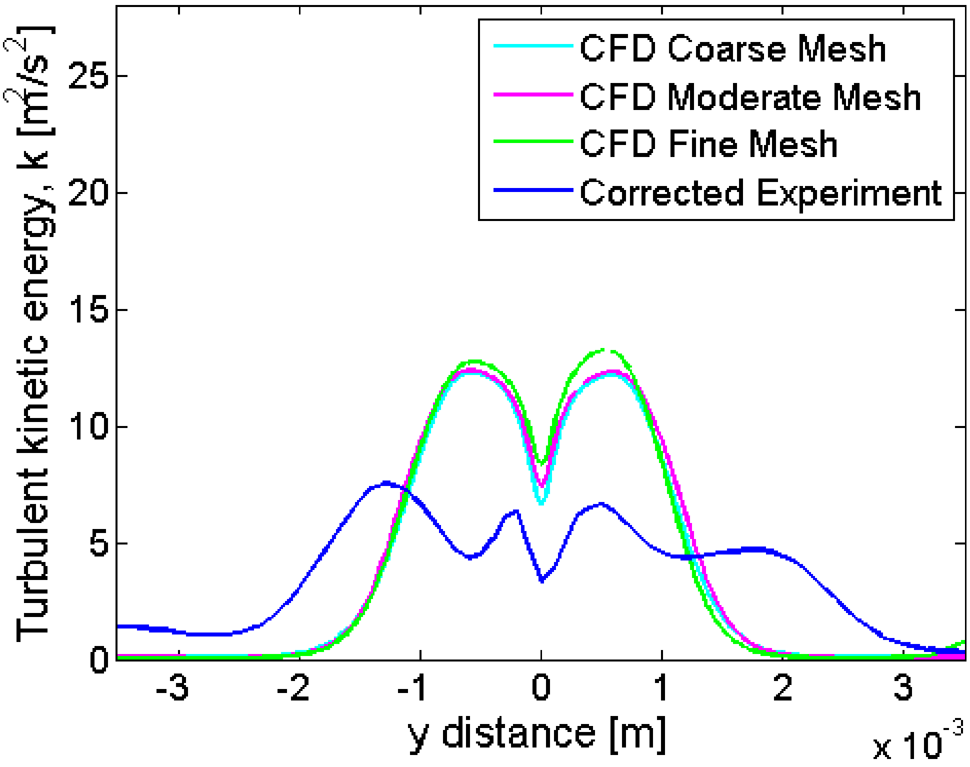

Figure 6.35: University of Adelaide anechoic wind tunnel case 69mm plane turbulence intensity profile comparison

6.4.6 3D RSNM TE Specifications and Results

The 3DRSNM computations using the expectation value correction were run over sample regions extending one, two, and three boundary layers upstream, downstream, and across stream from the TE of the plate, and the whole span of the airfoil, to predict the trailing edge noise at the experimental microphone location for comparison purposes. The microphone was located 585 mm above the midspan of the TE of the plate. Firstly the 3D RSNM method was run on the coarse mesh sample extending one boundary layer upstream, downstream and across stream, assuming the same coefficients for the spanwise correlation constant as the planeflow one, namely $C_{l_z} = 0.11$, but this was found to result in a significant underprediction relative to the experimentally measured noise. Visual inspection of results based on variation of the value of C_{l_z} suggest that a value of or about $C_{l_z} = 35$ produces the best agreement with the experimentally measured noise. Figure 6.36 shows the resulting noise prediction using the empirically optimised values of C_{l_z} as well as noise prediction using the BPM method for an airfoil of the same span, but assumed to be in uniform flow at the same freestream velocity as the experiment by Moreau and Doolan (2013). It can be seen that the 3D RSNM method performs well, closely matching the experimentally measured results over frequencies ranging from 3,000-10,000 Hz (less than 2.5 dB difference). At lower frequencies both the 3DRSNM and BPM predictions underpredict that of the experiment. The sample region independence, as well as the independence of the resulting RSNM noise prediction, when using the different resolution meshes was investigated, and the results are given in Figure 6.37. No significant grid dependence is seen. For example, the results change by less than 0.5 dB between all mesh level based noise predictions for the smallest sample region, across the frequency range of 600Hz to 10000Hz. Increasing the sample region is also seen to produce negligible change in the resulting noise prediction, a result which is consistent with previous findings of Doolan et al. (2010). In the work of Doolan et al. (2010) it was seen that extending the RSNM sampling region beyond one boundary layer produced negligible difference to the resulting noise prediction, indicating that the majority of the TE noise is due to the flow within a distance of one boundary layer height from the trailing edge.

6.4.7 Amiet Based LE Noise Model Specifications and Results

The CFD data used for the leading edge sound prediction model was obtained at a location one quarter chord upstream of the leading edge, to ensure the flow was unaffected by the wing and was similar to the flow entering the computational domain. There was very little variation between the predictions made based on the different mesh results, with noise levels changing by less than 0.2 dB between the coarse and moderate, as well as moderate and fine mesh results. Figure 7.38 compares the leading edge noise prediction results for each mesh solution with the experimental noise result. The results suggest that LE noise is not a significant noise source in this case except at low frequencies ($<$1kHz).

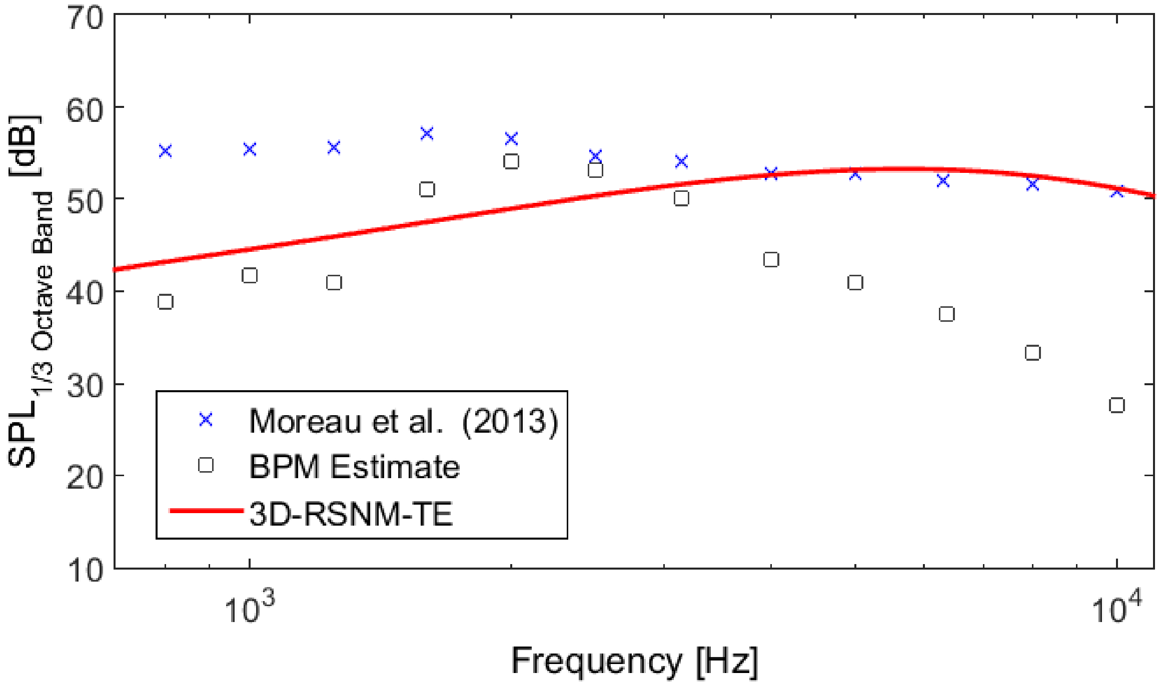

Figure 6.36: University of Adelaide Anechoic Wind Tunnel Case 3DRSNM-TE coarse mesh smallest sample region optimisation of C_{l_z} value comparison against BPM prediction

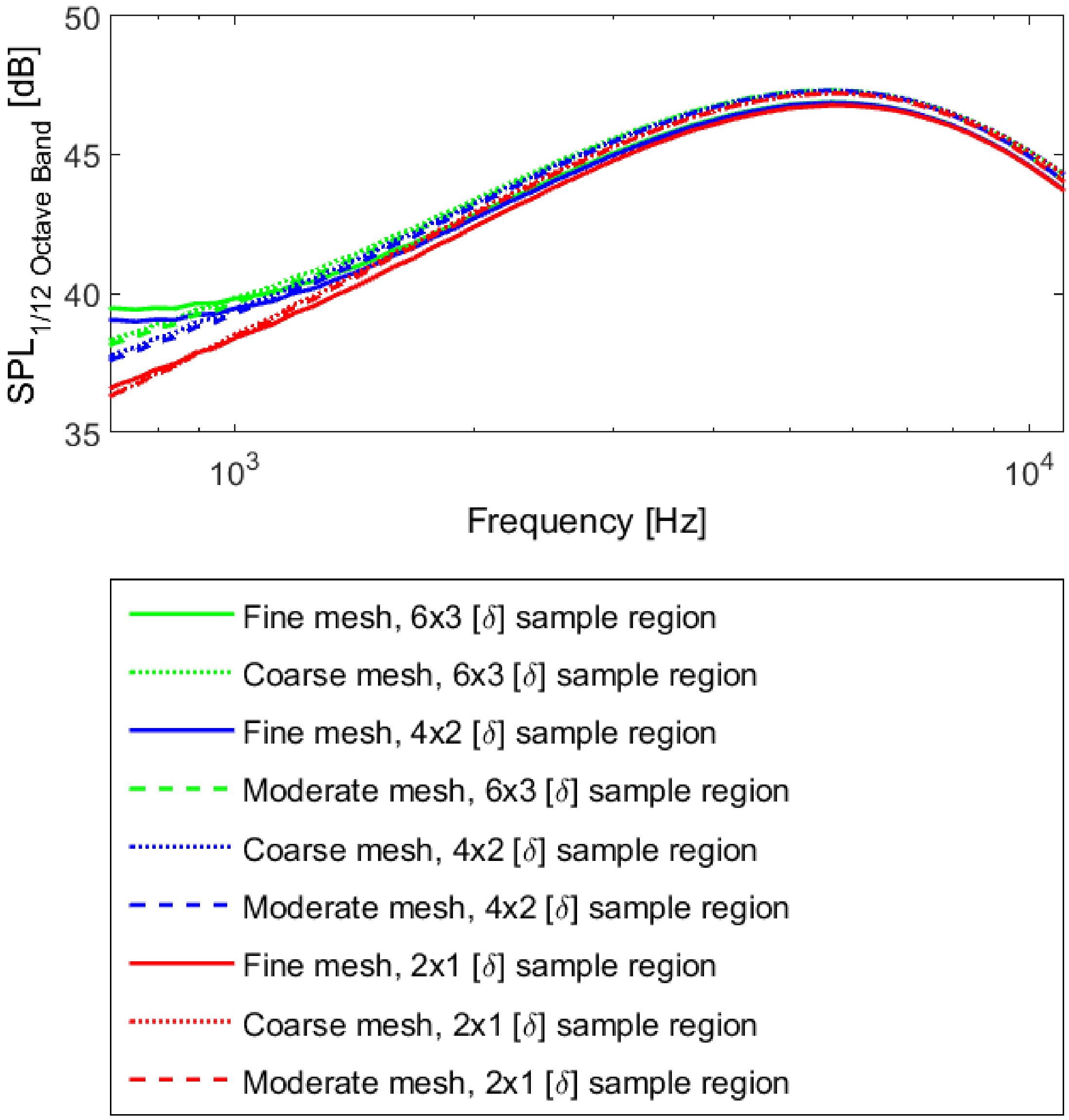

Figure 6.37: University of Adelaide Anechoic Wind Tunnel Case 3DRSNM-TE mesh and sample region dependence and comparison

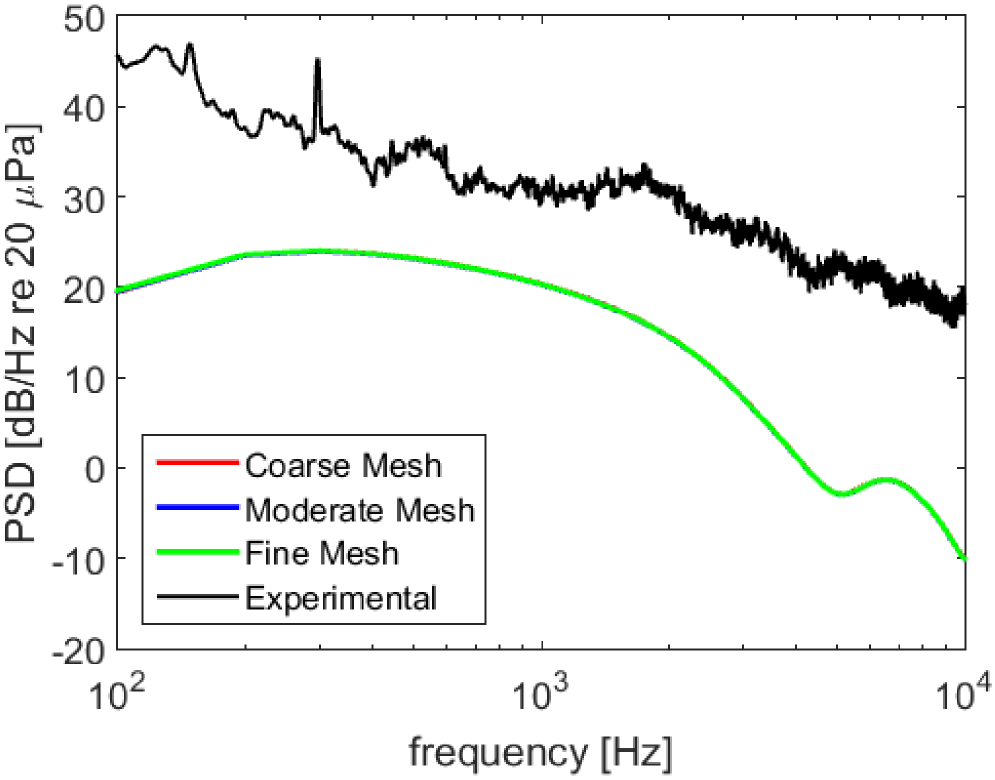

Figure 6.38: University of Adelaide anechoic wind tunnel case leading edge noise predition

6.5 Conclusions and Summary

The 3DRSNM and Amiet based leading edge noise prediction methods were applied to the case of a flat topped finite span wall-mounted wing which involves 3D flow features. The trailing edge noise predictions agree well with the experimentally measured noise after emprical optimisation of the C_{l_z} parameter. The value of C_{l_z} identified to provide the best agreement with the experimental results was found to be 35, which the significantly larger than that required to optimise the cases investigated in Chapter 5. This once again highlights the need to correctly set all the RSNM semi-empirical parameter values, and that investigating means to do so is proposed as an avenue for future work. Additionally, the tip flow structure for flat ended wing in junction flows at zero angle of attack was investigated, and a model for the flow topology developed. The results from the developed model are consistent with near-wake results from the literature (Giuni and Green, 2013), and extend understanding beyond the wake region into the tip region, illuminating the vortex formation process.

7 Virginia Tech Cases

7.1 Introduction

This chapter uses the developed extended RSNM to predict the noise from a wing in junction experiment of Moreau et al. (2015). Further testing the 3DRSNM-TE method, beyond that presented in Chapter 6 is undertaken, by predicting the noise for a series of cases in which airfoil angle of attack and aspect ratio are varied. Moreau et al. (2015) obtained beamforming measurements of wall mounted NACA0012 profile wings of aspect ratio 1, 2, and 3, at chord based Reynolds numbers of $Re_c = 8 \times 10^5$-1.6×10^6. The beamforming maps of Moreau et al. (2015) present not only the total noise, but also the noise when segregated into different regions such as the airfoil leading edge, trailing edge, tip and junction. This makes the Moreau et al. (2015) data set attractive, as it may be used for comparisons between noise models attempting to predict these individual noise components, as well as the total noise in agregate. Therefore, the work of Moreau et al. (2015) provides a suitable experimental data set against which to compare the noise predictions of this study. This directly addresses the third thesis aim (see Section 2.7), which is to apply the developed noise modelling techniques to recent wing in junction experiments.

7.2 Methodology

Low Reynolds number turbulence modelling RANS simulations were performed, details of the set-up of these are described in Section 7.3. CFD flow data, as well as trailing and leading edge noise predictions made from the CFD flow data using the 3DRSNM-TE and Amiet based leading edge noise prediction methods, detailed in Sections 3.8 and 3.7, are compared with noise measurements in Sections 7.4.4 and 7.4.5, respectively.

7.2.1 Experimental Details

The experimental data against which comparisons will be made was gathered in the Stability Wind Tunnel at Virginia Tech and details of the experimental results and procedure can be found in Moreau et al. (2015). The present work compares the highest Reynolds number cases of those from Moreau et al. (2015), for a chord based Reynolds numbers of $Re_c = 1.6 \times 10^6$. Moreau et al. (2015) obtained noise measurements using a 9-armed spiral beamforming array composed of 117 Panasonic model WM-64PNT Electret microphones. This was used to conduct frequency domain beamforming and produce sound maps. The sound maps were integrated over regions of interest, such as the leading and trailing edge, to segregate the total noise into components, with results presented as one-twelfth-octave band acoustic spectra.

The geometry is a flat ended finite NACA 0012 wing at angles of attack of 0, 6 and 12 degrees attached to a flat plate wall as shown in Figure 7.1, with cartesian coordinate system with origin at the wing-leading-edge-junction interface. For all three aspect ratios the wing chord (C) is 0.4 m, and there are three aspect ratios of 1, 2 and 3, corresponding to wing spans (S) of 0.4, 0.8 and 1.2 m. The experiments of Moreau et al. (2015) used unmodified NACA0012 profiles, which have blunt trailing edges. The trailing edges in the simulations have, however, been modified to be sharp. The only significant effect on flow and noise results expected to result from this difference is that no bluntness vortex shedding noise will be present in the CFD results, but will be observable in the experimental results.

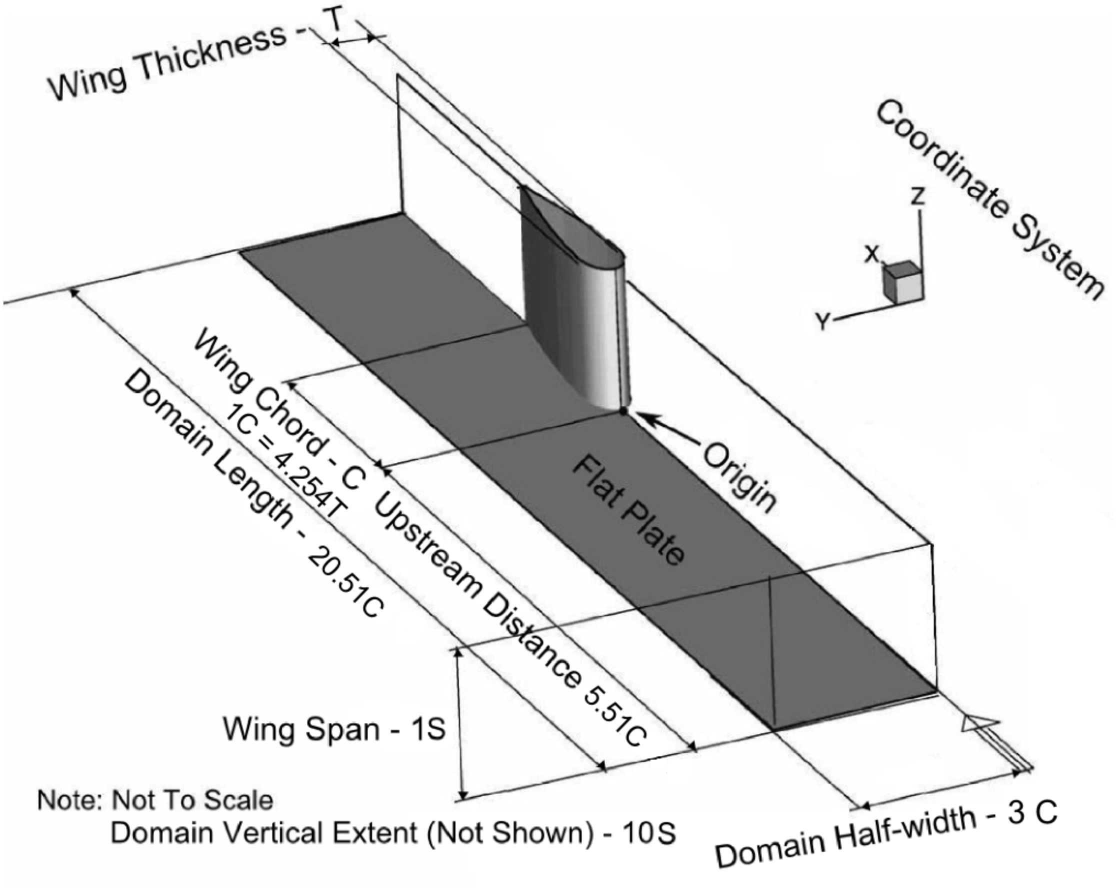

Figure 7.1: Virginia Tech cases computational domain

7.3 Modelling Details

The flow was treated as incompressible and solved using the OpenFOAM$^{\text{TM}}$code using the Semi-Implicit Method for Pressure-Linked Equations algorithm. The RANS equations were solved using, for closure, the k-ω-SST model, detailed in Appendix C. Wall functions for turbulence properties (turbulent eddy viscocity, ν_T, specific dissipation, ω, and turbulent kinetic energy, k) were used thoughout, and are detailed in Appendix D.

7.3.1 Inlet Boundary Positions and Conditions

The computational boundaries were considered as five surfaces, the upstream plane, the downstream plane, the port-side plane, the starboard-side plane, the top plane, as well as the solid surface formed by the wing-plate, and these are shown in Figure 7.2. Experimentally the boundary layer height on the flat plate, in the absence of the airfoil, for freestream wind tunnel velocity of 60 m/s, was measured at a location 130 mm upstream of the airfoil leading edge location (though with the airfoil removed from the wind tunnel at the time), and found to be δ = 68 mm (Moreau et al., 2015). The inlet position for the simulation was set based on turbulent simple flat plate boundary layer theory so that the uniform inlet boundary conditions would develop to match this boundary layer measurement, and results in the upstream plane being located at X = -5.511 in the Y-Z plane. The top plane is located at Z=10 S in the X-Y plane. The post-side and starboard-side X-Z planes are located at Y = 3 C and Y = -3 C respectively. The downstream Y-Z plane was placed at X=15 C.

7.3.2 Zero Angle of Attack Boundary Conditions

For the zero angle of attack cases, the upstream plane was set to have uniform velocity of $(U_x, U_y, U_z) = (35, 0, 0) ms^{-1}$, while the turbulence properties were estimated using the eddy viscosity ratio method with an assumed eddy viscosity ratio of unity, and turbulence intensity set to 0.03%, matching the level of the Virginia Tech facility (Moreau et al., 2015), resulting in values of $k{=}4.86{\times}10^{-4}$ m^{2}s^{-2}, and specific turbulence dissipation, ω = 32.4 s^{-1}. For pressure, a zero gradient boundary condition was applied on the upstream plane. The eddy viscosity on the upstream plane was calculated from the other flow properties. The airfoil and plate were treated as no-slip surfaces and so have a fixed value of zero velocity applied. Low-RE wall functions were used for the turbulence properties, and a zero gradient boundary condition was applied for pressure. For the zero angle of attack cases, the port and starboard side planes, as well as the top plane, receive the same treatment, with Neumann type boundary conditions, specifying zero gradient in the plane-normal directions for each plane for each property, except for the turbulent viscosity which was calculated from the other flow properties. The downsteam plane has a Neumann type boundary condition specifying zero gradient applied in the plane-normal directions for all variables, except for pressure, for which a Dirichlet type boundary condition is applied, which takes a value of zero as the simulation is conducted in terms of relative pressure.

7.3.3 Non-Zero Angle of Attack Boundary Conditions

For the non-zero angle of attack cases, boundaries were set in the same fashion as for the zero angle of attack cases for the upstream plane, the downstream plane, the top plane as well as the solid surface formed by the wing-plate pair, except that the uniform velocity on the upstream plane was set so as to generate the angle of attack desired, namely for 6 degrees angle of attack the velocity is set to $(U_x, U_y, U_z) = (59.67, 6.27, 0)$ ms^{-1} and for 12 degrees angle of attack the velocity is set to $(x, y, z) = (58.6912.470)$ ms^{-1}. The starboard-side plane was set to have identical conditions as the downstream plane, while the port-side plane was set to have identical conditions as the upstream plane.

7.3.4 Grid Generation

The grids used in this investigation have a structured CH near wing mesh topology and far-field region, with a connecting unstructured region, an example of which is shown in Figure 7.3. Grid independence was investigated using the zero angle of attack case with aspect ratio of one, and three meshes, with 2.26×10^7, 3.58×10^7 and 5.96×10^7 total cells for the coarse, moderate and fine meshes respectively. These results will be discussed further in Section 7.4.2. The coarse mesh is then used for all other angle of attack and aspect ratio combinations. The minimum, maximum and average y^+ values for each aspect ratio and angle of attack combination on the wing and plate surfaces are given in Table 7.1.

7.3.5 Residual Control and Numerical Methods

The simulations on the standard coarse mesh and moderate meshes were run until all residuals reached 10^{-5} or less, and on the fine mesh until all residuals reached 2×10^{-5} or less. Linear interpolation schemes were used throughout, as was a second order accurate linear scheme for the

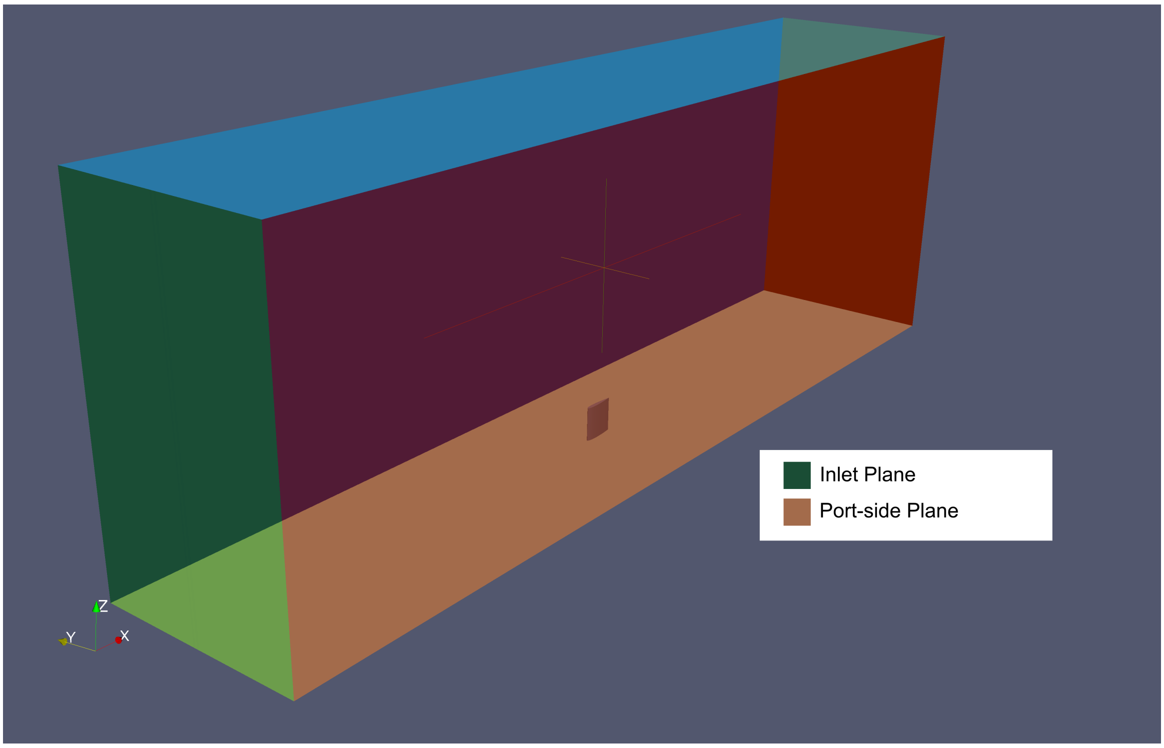

(a) Virginia Tech cases foreground boundaries

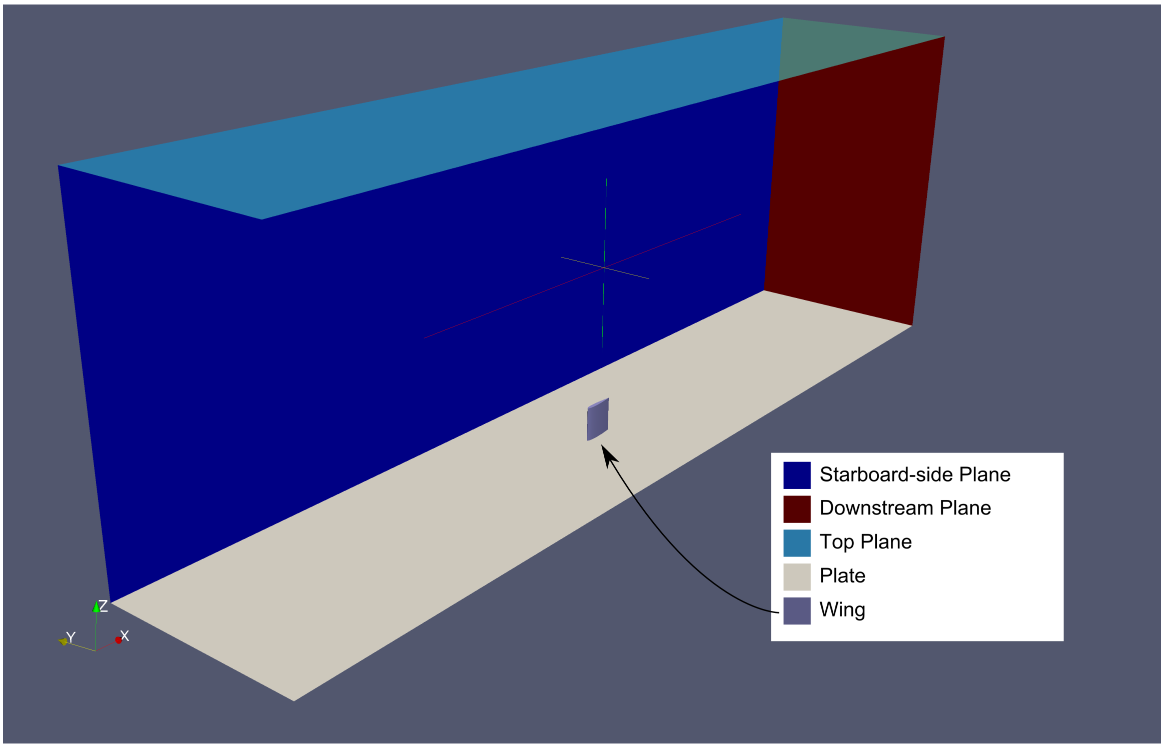

(b) Virginia Tech cases background boundaries

Figure 7.2: Virginia Tech cases computational boundaries diagram

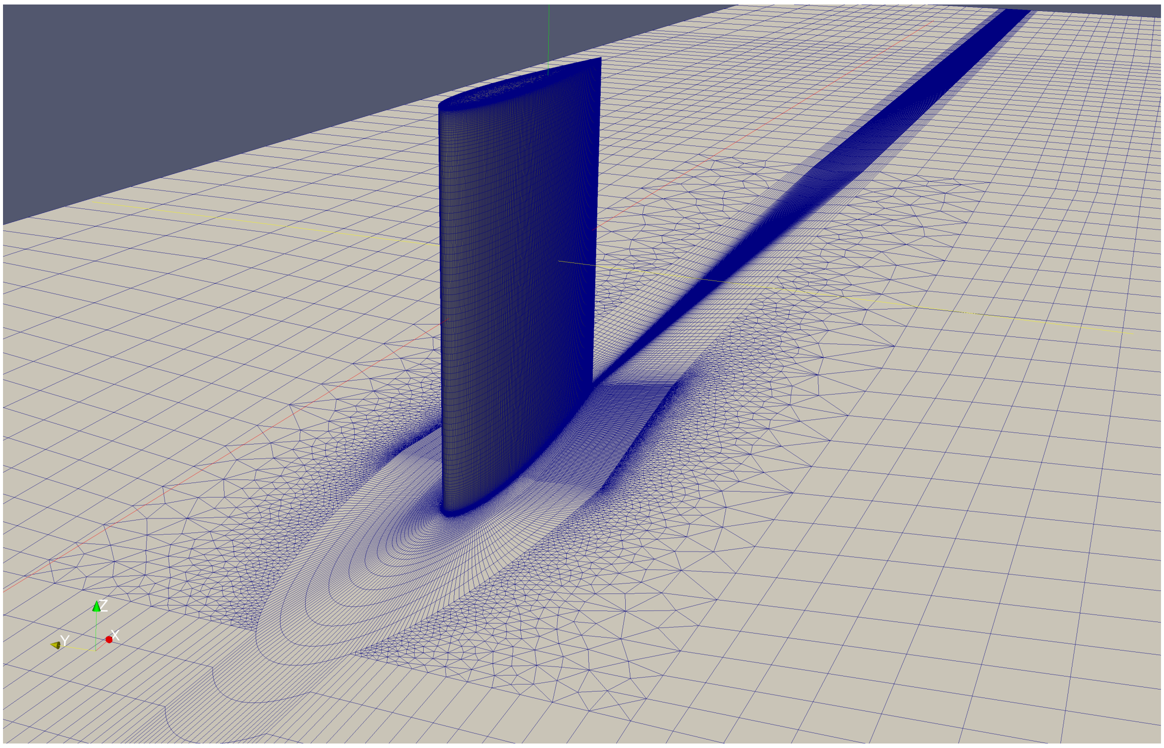

Figure 7.3: Virginia Tech case aspect ratio = 1 coarse mesh visualisation

Table 7.1: Mesh y^+ statistics

Wing (Plate)	AOA	Min. y^+	Max. y^+	Av. y^+
AR=1	0	1.36E-3 (3.33E-3)	3.00 (1.75)	0.367 (0.786)
	6	2.20E-3 (2.62E-3)	3.10 (2.53)	0.365 (0.835)
	12	1.60E-3 (3.52E-3)	2.79 (2.24)	0.328 (0.750)
AR=2	0	1.73E-3 (5.20E-3)	5.69 (3.65)	0.477 (1.59)
	6	3.33E-3 (8.62E-3)	5.87 (5.61)	0.486 (1.61)
	12	1.27E-3 (7.87E-3)	6.46 (6.03)	0.514 (1.55)
AR=3	0	1.71E-3 (6.32E-3)	7.66 (5.51)	0.612 (2.32)
	6	7.18E-3 (3.00E-2)	8.02 (8.26)	0.616 (2.44)
	12	1.13E-3 (4.24E-3)	8.96 (8.57)	0.656 (2.35)

discretisation of gradient terms. The divergence terms for the velocity, turbulent kinetic energy and dissipation fields were discretised using a first order accurate upwind scheme. All Laplacian terms were discretised with a second order accurate linear scheme with explicit non-orthogonal correction. Finally, explicit non-orthogonal correction was performed when calculating surface normal gradient terms.

7.4 Results and Analysis

7.4.1 Discussion and Analysis of the Moreau et al. (2015) Results

What follows is a discussion and analysis of the noise isolation techniques and results of Moreau et al. (2015). The results of Moreau et al. (2015) include sound maps, such as those shown in Figure 7.4. Note that the Moreau et al. (2015) results have a coordinate system with an origin which is offset from that defined in Figure 7.2, such that the origin occurs at the center of the wind tunnel test section. These sound maps were then integrated over regions of interest, producing one-twelfth-octave band acoustic spectra estimates for the noise originating from those regions, such as that shown in Figure 7.5. These regions have different extents when considering the different aspect ratio airfoils, and full details of the extents for each aspect ratio may be found in Moreau et al. (2015). For example, the different regions defined for the aspect ratio 3 airfoil, are shown in Figure 7.6, namely the total airfoil noise (Figure 7.6a), leading and trailing edge components (Figure 7.6b), and junction and tip components (Figure 7.6c).

The integration regions defined by Moreau et al. (2015), although useful for segregating the noise generated in the various regions, should not be considered to represent solely noise resulting from the mechanism associated with the region names. For example, consider the tip region as defined for the aspect ratio 3 wing, given in Figure 7.6c, and the sound map results for aspect ratio 3, $U_{ref} = 60$ m/s, zero AOA wing, given in Figure 7.4. At the higher frequencies of those considered, $f = 2.8$ kHz, $f = 3.75$ kHz, and $f = 4.5$ kHz (given in Figures 7.4c, 7.4d and 7.4e respectively), strong isolated sources can be seen to occur at the wing tip trailing edge, which can be attributed to a tip noise mechanism. However, at the lower frequencies of those considered, $f = 1$ kHz, and $f = 2.24$ kHz (given in Figures 7.4a and 7.4b respectively), the noise sources are not concentrated at the tip, but relatively evenly distributed along the length of the airfoil trailing edge, and may be attributed to trailing edge noise mechanisms. Although being attributed to the trailing edge noise mechanism, as they occur within the tip integration region, they will contribute to the resulting tip region spectra. Conversely, the TE region as defined by Moreau et al. (2015) will not only capture the lower frequency distributed TE noise, but will also include the strong isolated tip noise sources which occur at the higher frequencies considered (again $f = 2.8$, $f = 3.75$, $f = 4.5$ kHz as given in Figures 7.4c, 7.4d and 7.4e respectively).

The previous examples highlight that when comparing the Moreau et al. (2015) region spectra estimates against those resulting from the noise models which will be presented in Sections 7.4.3-7.4.5, that in every instance, care must be taken to consider across which frequency ranges the Moreau et al. (2015) integration regions are dominated by which noise source mechanisms, and if these correspond to that being considered at the time.

7.4.2 Grid Independence Results

The boundary layer heights were determined for each mesh solution at a location 130 mm upstream of the airfoil leading edge location, matching the location at which experimental measurements were taken by Moreau et al. (2015), as the location in the outer boundary layer where

$$\frac{\partial Ti}{\partial y} \geq -0.2 \tag{7.1}$$

where Ti is the turbulence intensity and y is the wall distance normalised by chord, and the results are given along with that measured experimentally by Moreau et al. (2015) in Table 7.2. The simulated results, vary by less than 5% from the value in the experimental setup, and so are consider to be sufficiently close for the purpose of the present work.

The total force components (pressure and viscous) on the wing were extracted from each simulation. The results are given in Table 7.3. The symmetry of the case should result in $Fy = 0$, and the results were found to be sufficiently close to this value. The drag (Fx) and spanwise

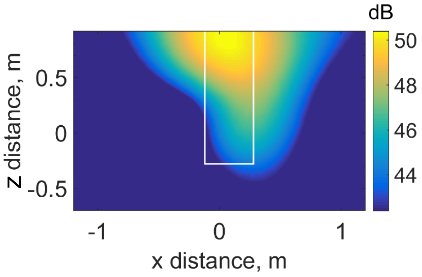

(a) $f = 1$ kHz (adapted from Moreau et al. (2015))

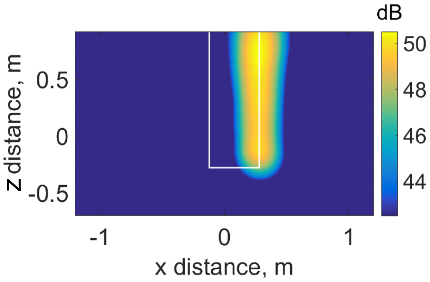

(b) $f = 2.2$ kHz (adapted from Moreau et al. (2015))

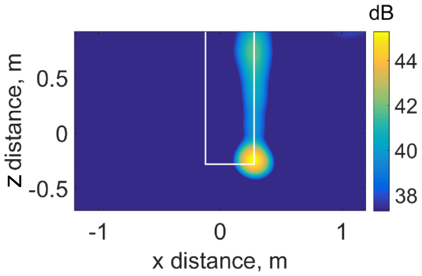

(c) $f = 2.8$ kHz (adapted from Moreau et al. (2015))

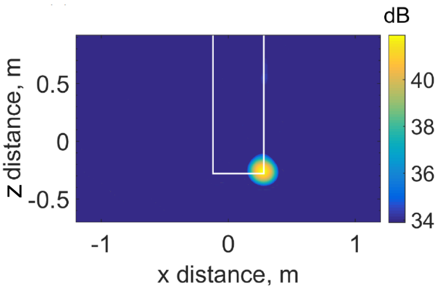

(d) $f = 3.75$ kHz (adapted from Moreau et al. (2015))

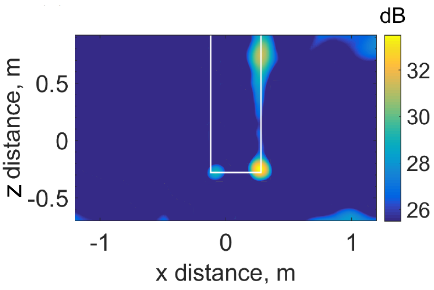

(e) $f = 4.5$ kHz (adapted from Moreau et al. (2015))

Figure 7.4: Moreau et al. (2015) sound map results for aspect ratio 3, $U_{ref} = 60$ m/s, zero AOA wing (adapted from Moreau et al. (2015))

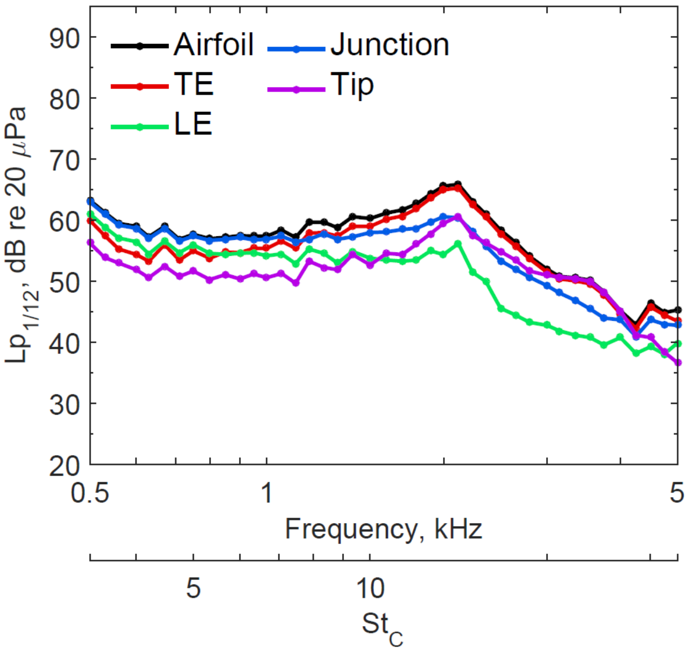

Figure 7.5: Integrated one-twelfth-octave band total airfoil, as well as isolated trailing edge, leading edge, junction and tip spectra for the wall-mounted airfoil with aspect ratio 3 at $U_{ref} = 60$ m/s and zero AOA (taken from Moreau et al. (2015))

(Fz) forces show good convergence, with changes of less than 1.67% and 0.46% respectively between the moderate and fine mesh solutions.

The sizing of the vortex tip vortex at the trailing edge for each of the present cases was evaluated in terms of crossflow velocities. Specifically, in the plane defined by $X = C$ the minimum of the swirl velocity $(U_{swirl} = \sqrt{U_y^2 + U_z^2})$ was used to determine the location of the tip vortex core. Velocity profiles were taken cutting through this, along lines of constant y. Figure 7.7 gives the swirl velocities along these profiles. The size of the vortex was determined from the peak to peak distance of the swirl velocity maxima and these are given for each case in Table 7.4. The effect of considering the inclination of the vortex on this measure was also investigated and found to be negligible. For example, for the $AR = 1$, $AOA = 12$ degrees case, sample planes taken $\frac{1}{20}C$ upstream and downstream of the trailing edge were used to determine that the tip vortex has a 9.44 degree inclination in the positive y direction from the x-axis. When velocity profiles were taken at the trailing edge location, accounting for this, the resulting measure of vortex size changed from $0.1248[C]$ to $0.1242[C]$; a change of less than 0.5%.

Table 7.2: Virginia Tech aspect ratio 1, zero angle of attack case, boundary layer heights comparison

	Coarse Mesh	Moderate Mesh	Fine Mesh	Experimental Value
δ (mm)	70.5	69.6	70.8	68

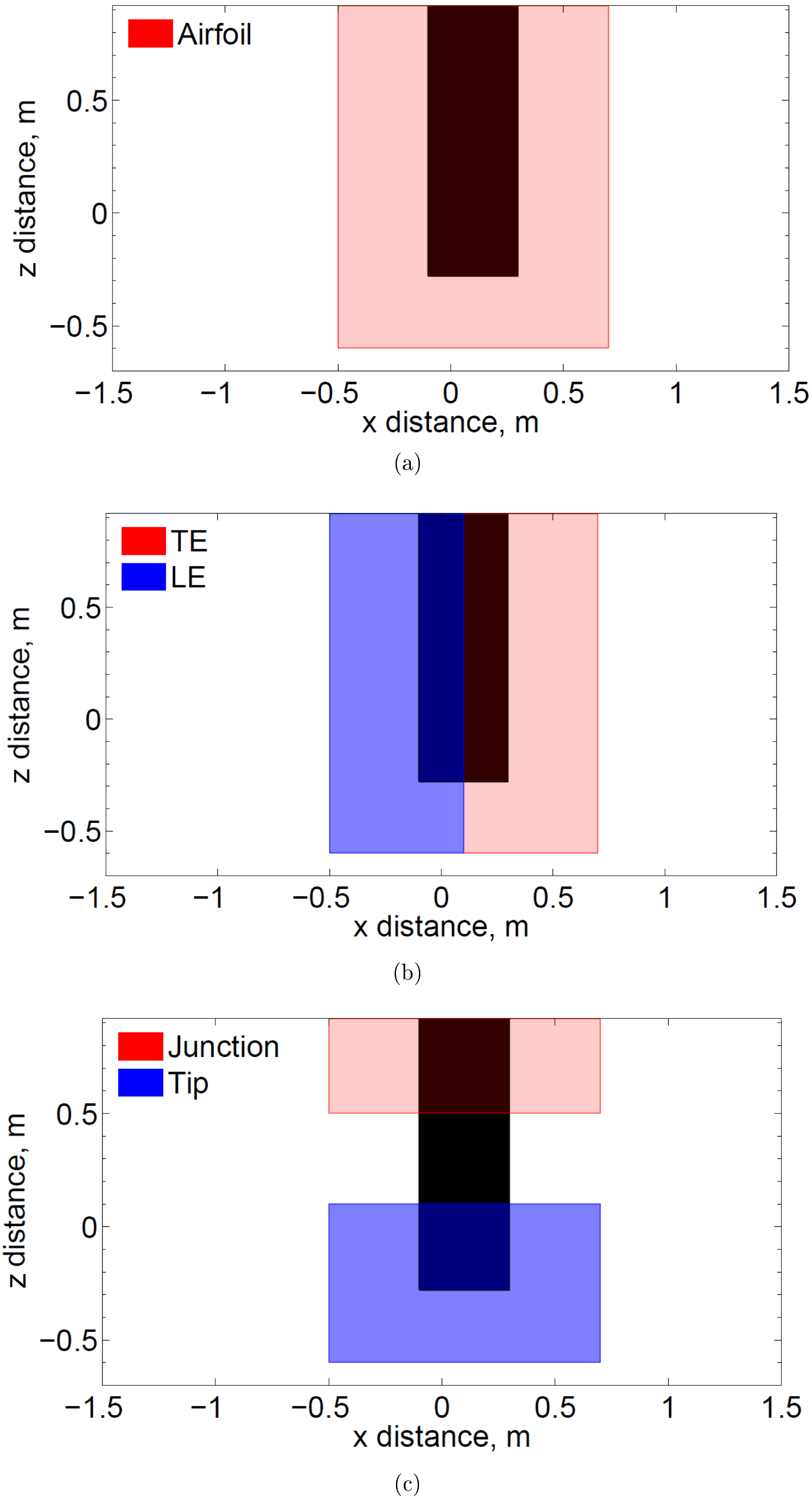

(a)

(b)

(c)

Figure 7.6: Integration regions a) Airfoil, b) Trailing and leading edges, c) Junction and tip, adapted from Moreau et al. (2015)

Table 7.3: Virginia Tech aspect ratio 1, zero angle of attack case, forces on the wing

Parameter	Coarse Mesh	Moderate Mesh	Fine Mesh
Fx [N]	4.3723	4.5446	4.4690
Fy [N]	0.0372	-0.0012	-0.0167
Fz [N]	2.7136	2.7288	2.7165

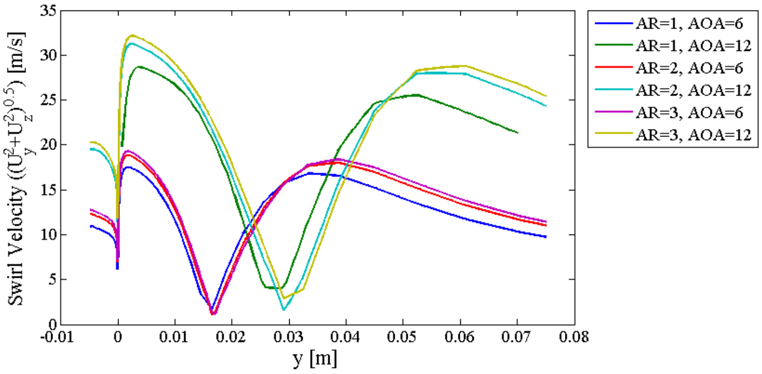

Figure 7.7: Virginia Tech cases trailing edge tip vortex swirl velocity profiles

Table 7.4: Virginia Tech cases trailing edge tip vortex size

AR	AOA [Degrees]	Core Size [C]
1	6	0.0796
1	12	0.1248
2	6	0.0924
2	12	0.1369
3	6	0.0924
3	12	0.1460

7.4.3 Vortex Size Based Isolated Tip Noise Model

Applying a linear fit on the vortex sizing measurements from Table 7.4 produces a model for tip vortex size (L_v) at the trailing edge given by

$$\frac{L_v}{C} = A * AOA + B; \tag{7.2}$$

where $A = 0.0080$ and $B = 0.0404$ for angles of attack in degrees $6 \leq AOA \leq 12$. These values may be compared to the model which was proposed with ‘no experimental confirmation’ by Brooks et al. (1989) which is of the same form but with $A = 0.0095$ and $B = 0.0378$ (recall Equation 3.28). This was used as the scaling parameter for a new empirical flat tip noise model. This is a model based on that originally proposed by Brooks et al. (1989), calibrated against the isolated tip noise identified in Moreau et al. (2015), returns the one-third octave band sound pressure levels in dB with reference to 20 micro-Pascals, and is given by

$$SPL_{1/3TIP} = 10\log_{10}\left(\frac{M^{7.5}L_v^5\overline{D}_h}{r_e^2}\right) + 10\log_{10}(\exp(-(\frac{St_C - A1}{A2})^2)) + A3, \tag{7.3}$$

where $St_C = \frac{fC}{U_{ref}}$, $A1 = 22$, $A2 = 3.2$, $A3 = 254$, M is the Mach number, L_v is the tip vortex size in metres, and r_e is the distance in metres from the midspan of the TE to the observation point at which the noise level is being calculated. This proposed tip noise model employs a Gaussian fit about the peak Strouhal number of $St_C = 22$, for the isolated tip noise component identified by Moreau et al. (2015). The constants $A1$, $A2$, and $A3$ were selected so as to minimise the error between the predicted spectra and experimental data. Figures 7.8, 7.9 and 7.10, give the noise prediction which results from the model along with the experimental data at the highest angle of attack and Reynolds number at each aspect ratio. Figures 7.11 and 7.12 give the noise prediction at the 8 and 12 degrees angle of attack at the lowest Reynolds number investigated by Moreau et al. (2015), showing the models effectiveness across a range of Reynolds numbers and angles of attack. The model can be seen to capture the high frequency peak in each case. It does not capture the broadband noise seen at the lower frequencies of the Moreau et al. (2015) results, because, the noise at the lower frequencies is dominated by trailing edge noise, as discussed in detail in Section 7.4.1.

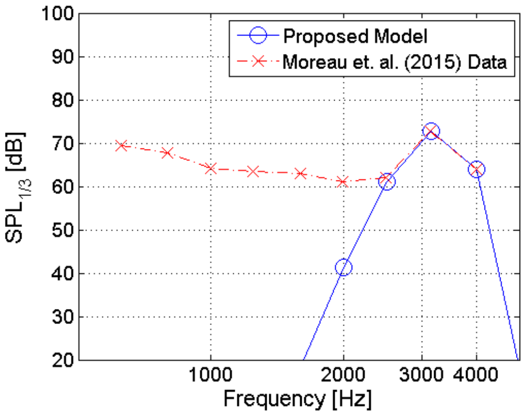

Figure 7.8: Isolated tip noise model compared against experimental levels for $AR = 3$, $AOA = 12$ degrees, $U = 60[m/s]$ case

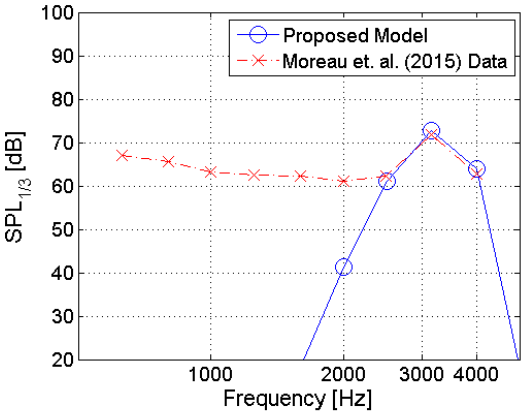

Figure 7.9: Isolated tip noise model compared against experimental levels for $AR = 2$, $AOA = 12$ degrees, $U = 60[m/s]$ case

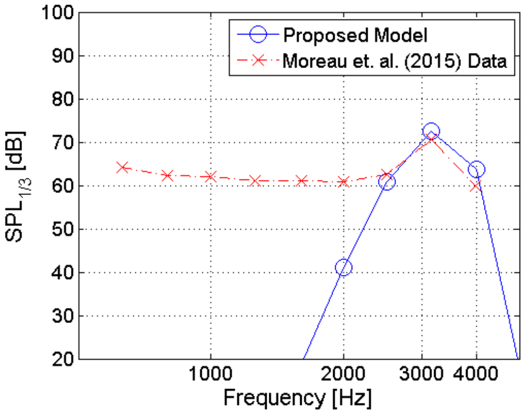

Figure 7.10: Isolated tip noise model compared against experimental levels for $AR = 1$, $AOA = 12$ degrees, $U = 60[m/s]$ case

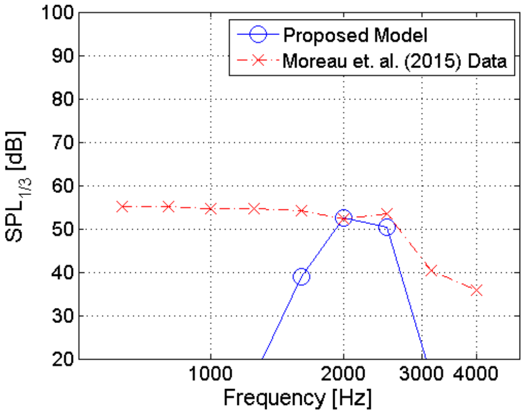

Figure 7.11: Isolated tip noise model compared against experimental levels for $AR = 3$, $AOA = 8$ degrees, $U = 40[m/s]$ case

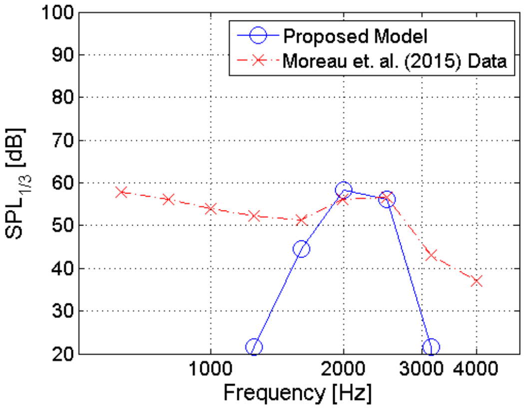

Figure 7.12: Isolated tip noise model compared against experimental levels for $AR = 3$, $AOA = 12$, $U = 40[m/s]$ case

7.4.4 3D RSNM TE Specifications and Results

Spanwise 3D RSNM

Starting with the AR=1 zero angle of attack case, 3D RSNM TE computations using the spanwise adaptation (Equation 3.70) were run over sample regions extending one, two, and three boundary layers upstream, downstream, and across stream from the TE of the plate and the whole span of the airfoil, to predict the trailing edge noise at the location matching that of the experimental microphone location for comparison purposes (Moreau et al., 2015). The 3D RSNM TE method was used on the AR=1 and zero angle of attack case, initially assuming the same coefficient for the spanwise correlation constant as the planeflow one, namely $C_{l_z} = 0.11$; however this was found to result in a significant underprediction relative to the experimentally measured noise. Visual inspection of results based on variation of the value of C_{l_z} suggest that a value of or about $C_{l_z} = 5$ produces good agreement with the experimentally measured noise. A value which is consistent with the results of Chapter 5 in which a value of $C_{l_z} \approx 5$ was found to produce good results when applying the method to the semi-infinite, flat plate-strut, and NACA0012 airfoils. Figure 7.13 shows the resulting noise prediction using the classical and empirically optimised values of C_{l_z}. Results for increasingly large sample regions were then obtained using the optimised value of C_{l_z} on sample regions for each mesh level, the results of which are given in Figures 7.14-7.16 and which are consistent with previous findings (Doolan et al., 2010) as well as those of Chapter 5 and Section 6.4.6, in that extending the sampling region beyond one boundary layer produced negligible difference to the resulting noise prediction. Results are not strongly dependent on the CFD solution detail; differences between resulting noise prediction based on the smallest sample region from the coarse and moderate mesh based predictions, and also the moderate and fine mesh based predictions, differing by less than 0.6 dB thoughout. It can be seen that when C_{l_z} is suitably set the 3D RSNM method performs well, providing reasonable agreement with the experimentally measured results over frequencies ranging from 500-5,000 Hz.

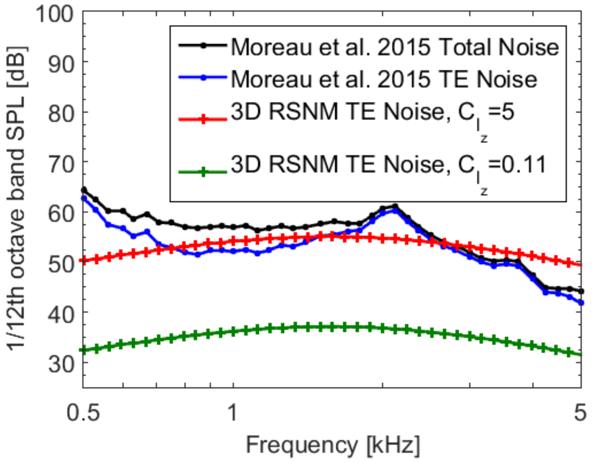

Figure 7.13: Virginia Tech aspect ratio 1, zero angle of attack case, 3DRSNM-TE resulting noise prediction variation of C_{l_z} value effect comparison

For the remaining angle of attack and aspect ratio combinations, the noise prediction results using $C_{l_z} = 5$ are given in Figures 7.17-7.24. It can be seen that although the overall levels are well predicted for each angle of attack and aspect ratio combination, the peaks occurring at higher frequency (around 3.5 kHz), which increase in sound level with increasing angle of

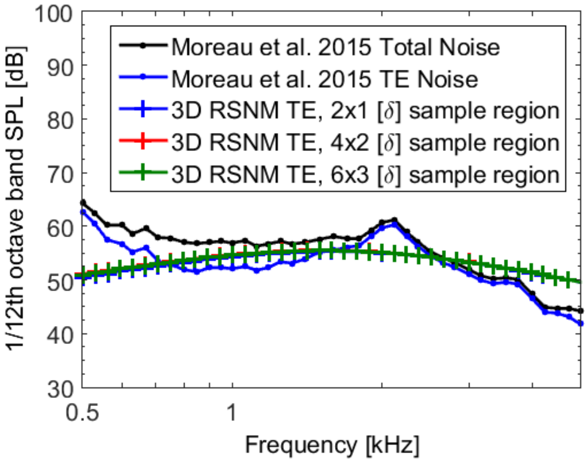

Figure 7.14: Virginia Tech aspect ratio 1, zero angle of attack case, 3DRSNM-TE coarse mesh and sample region dependence and comparison

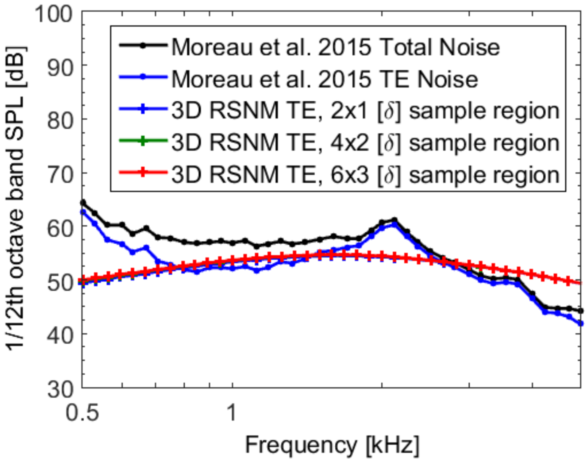

Figure 7.15: Virginia Tech aspect ratio 1, zero angle of attack case, 3DRSNM-TE moderate mesh and sample region dependence and comparison

attack, are not captured by the spanwise 3D RSNM TE model. As discussed in detail in Section 7.4.1, this is because the noise at these frequencies is dominated by tip noise sources. These peaks may be predicted using the developed isolated tip noise model. Similarly, the peaks occuring at around 2 kHz, which can be seen in the cases where angle of attack is less than 6 degrees (at higher angles of attack the tip noise component obscures this feature, due to its dominating sound level), is not predicted by the 3D RSNM TE model. This peak is attributed to bluntness vortex shedding.

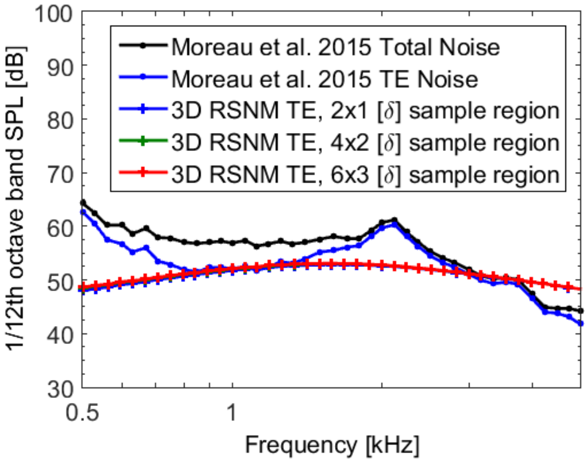

Figure 7.16: Virginia Tech aspect ratio 1, zero angle of attack case, 3DRSNM-TE fine mesh and sample region dependence and comparison

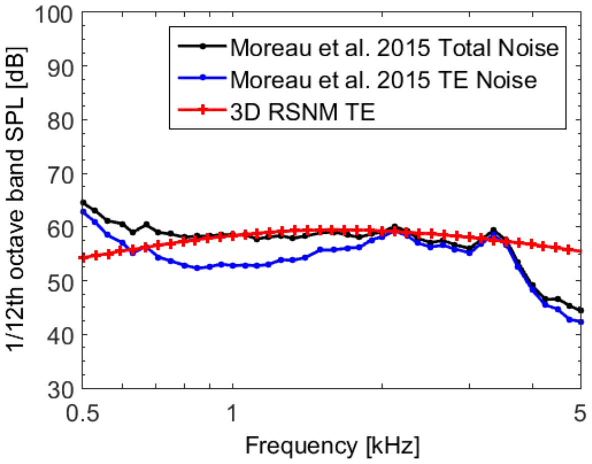

Figure 7.17: Virginia Tech aspect ratio 1, 6 degree angle of attack case, 3DRSNM-TE resulting noise prediction

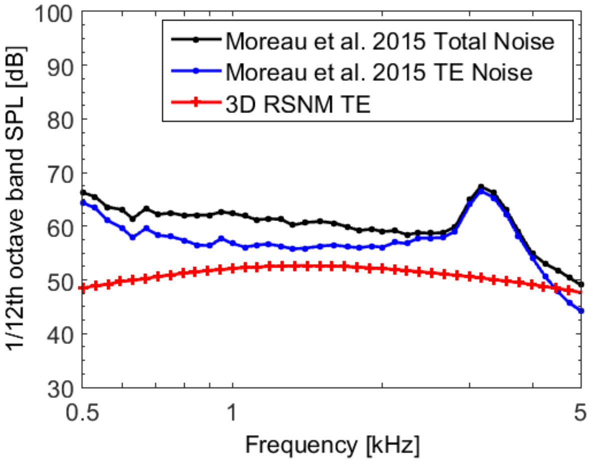

Figure 7.18: Virginia Tech aspect ratio 1, 12 degree angle of attack case, 3DRSNM-TE resulting noise prediction

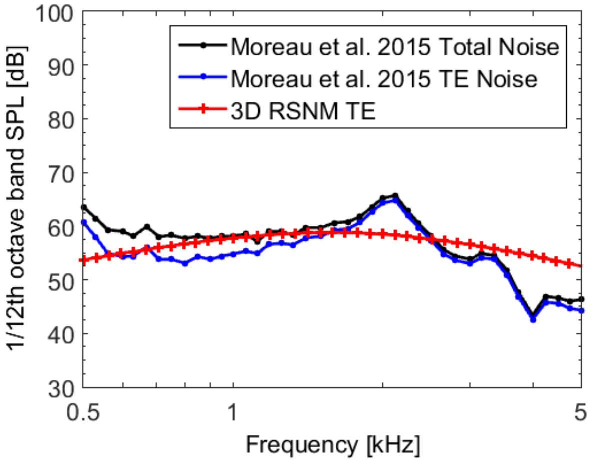

Figure 7.19: Virginia Tech aspect ratio 2, 0 degree angle of attack case, 3DRSNM-TE resulting noise prediction

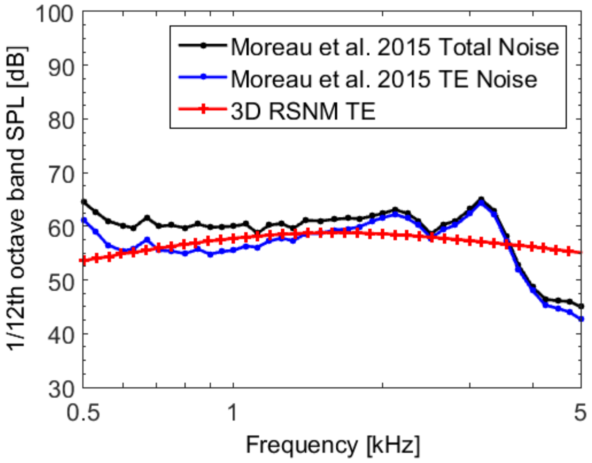

Figure 7.20: Virginia Tech aspect ratio 2, 6 degree angle of attack case, 3DRSNM-TE resulting noise prediction

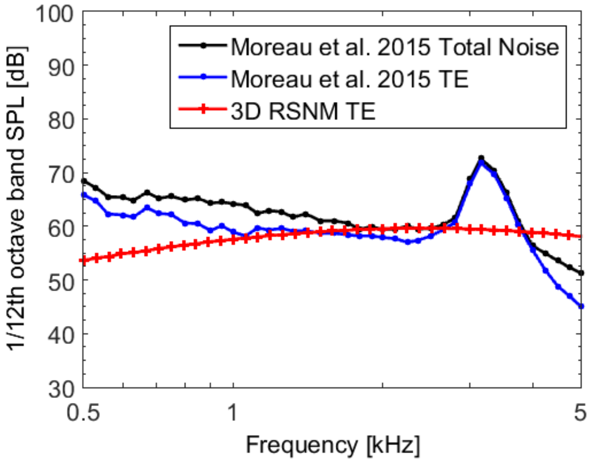

Figure 7.21: Virginia Tech aspect ratio 2, 12 degree angle of attack case, 3DRSNM-TE resulting noise prediction

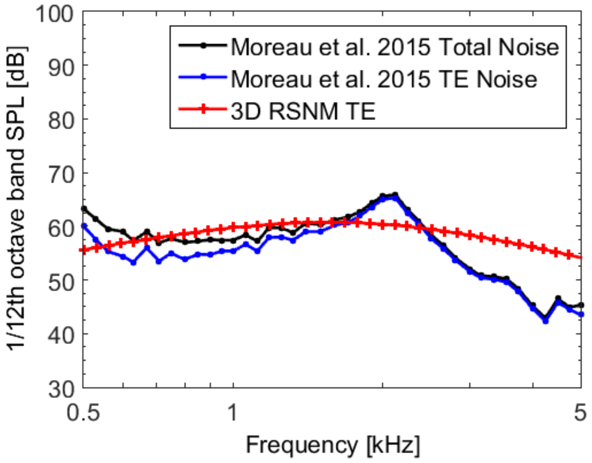

Figure 7.22: Virginia Tech aspect ratio 3, 0 degree angle of attack case, 3DRSNM-TE resulting noise prediction

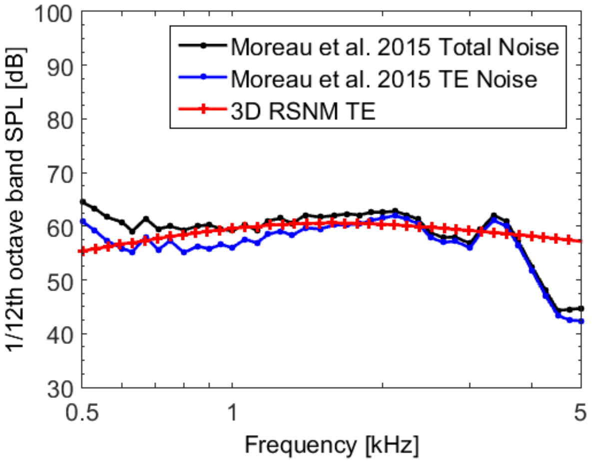

Figure 7.23: Virginia Tech aspect ratio 3, 6 degree angle of attack case, 3DRSNM-TE resulting noise prediction

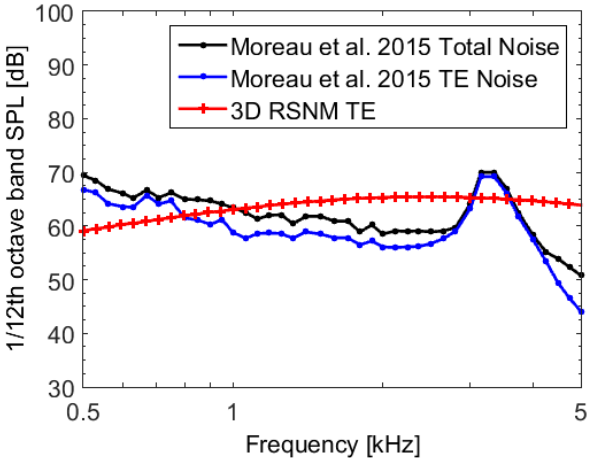

Figure 7.24: Virginia Tech aspect ratio 3, 12 degree angle of attack case, 3DRSNM-TE resulting noise prediction

Complete 3D RSNM

Using the same conditions as for the spanwise adaptation described in the previous section, noise predictions were made using the 3D RSNM TE computations using the complete extension that incorporates expectation value corrections for all three directional components (Equation 3.71). As was found for the spanwise extension, a C_{l_z} value of or about $C_{l_z} = 5$ produces good agreement with the experimentally measured noise. Figure 7.25 shows the resulting noise prediction using the classical and empirically optimised values of C_{l_z} for the $AR = 1$, $AOA = 0$ case coarse mesh sample. Results for increasingly large sample regions were then obtained using the optimised value of C_{l_z} on the coarse mesh solution, the results of which are given in Figure 7.26 and which are consistent with previous findings (Doolan et al., 2010) as well as those of Section 5 and Section 6.4.6, and earlier in this section, in that extending the sampling region beyond one boundary layer produced negligible difference to the resulting noise prediction. Results are not strongly dependent on the CFD solution detail; differences between the resulting noise predictions based on the smallest sample region from the coarse and moderate mesh based predictions and also the moderate and fine mesh based predictions are shown in Figure 7.27.

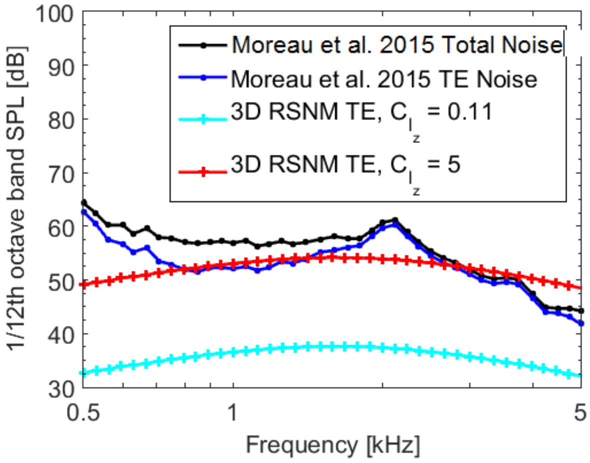

Figure 7.25: Virginia Tech aspect ratio 1, zero angle of attack case, 3DRSNM-TE resulting noise prediction variation of C_{l_z} value effect comparison

For the remaining angle of attack and aspect ratio combinations, the noise prediction results using $C_{l_z} = 5$ are given in Figures 7.28-7.35. It can be seen that although the overall levels are well predicted for each angle of attack and aspect ratio combination, the peaks occurring at higher frequency (around 4kHz), which increase with increasing angle of attack, are not captured by the complete 3D RSNM TE model. The beamform mapping of Moreau et al. (2015) shows that this peak may be attributed to tip noise, and so it is unsurprising that the trailing edge noise model does not account for the increase in noise due to that mechanism. Similarly at the lowest frequencies the beamform mapping results of Moreau et al. (2015) show that at the lowest frequencies considered, the dominant noise sources are not centred about the trailing edge but rather are concentrated at the wing-junction mid-chord, and so it is unsurprising that the trailing edge noise model underpredicts the experimentally measured total noise at these frequencies where trailing edge noise is not the dominant source.

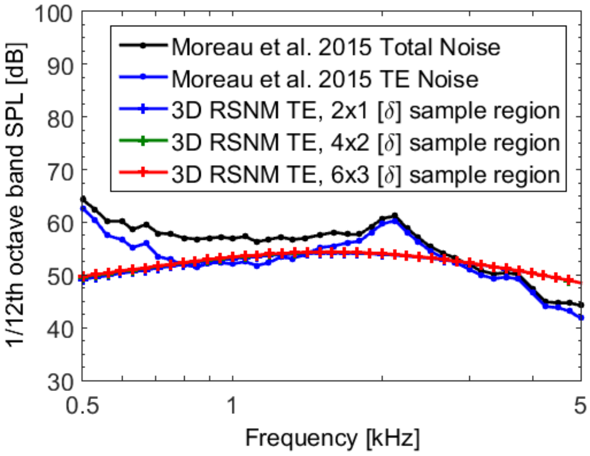

Figure 7.26: Virginia Tech aspect ratio 1, zero angle of attack case, 3DRSNM-TE coarse mesh and sample region dependence and comparison

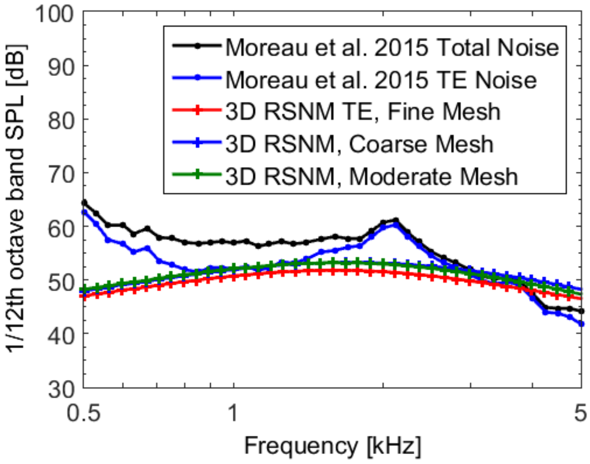

Figure 7.27: Virginia Tech aspect ratio 1, zero angle of attack case, 3DRSNM-TE coarse mesh and sample region dependence and comparison

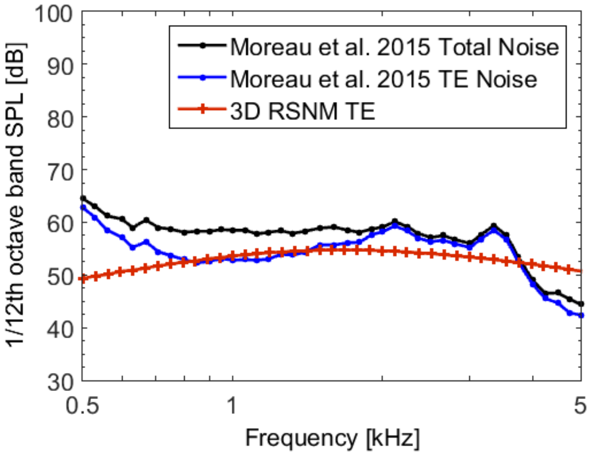

Figure 7.28: Virginia Tech aspect ratio 1, 6 degree angle of attack case, 3DRSNM-TE resulting noise prediction

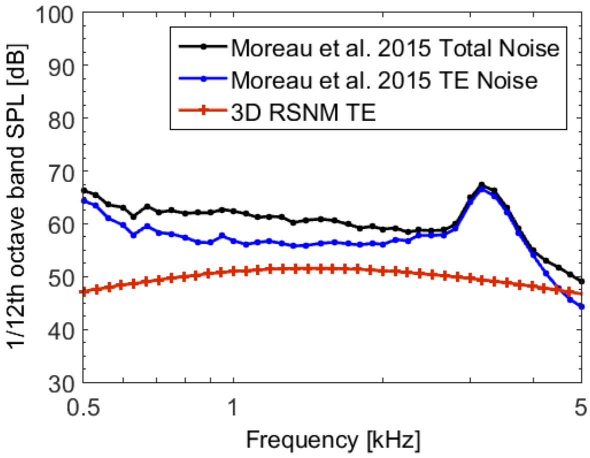

Figure 7.29: Virginia Tech aspect ratio 1, 12 degree angle of attack case, 3DRSNM-TE resulting noise prediction

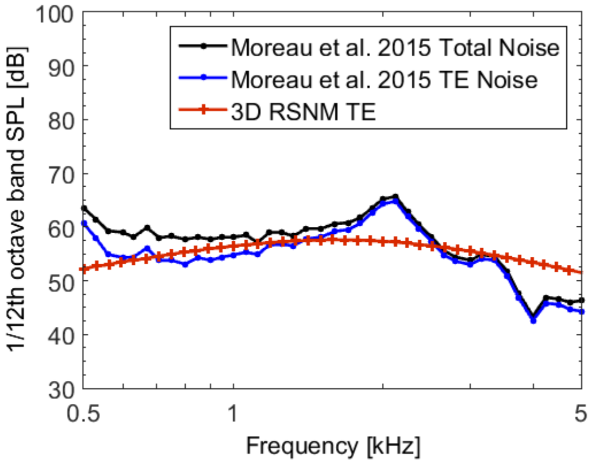

Figure 7.30: Virginia Tech aspect ratio 2, 0 degree angle of attack case, 3DRSNM-TE resulting noise prediction

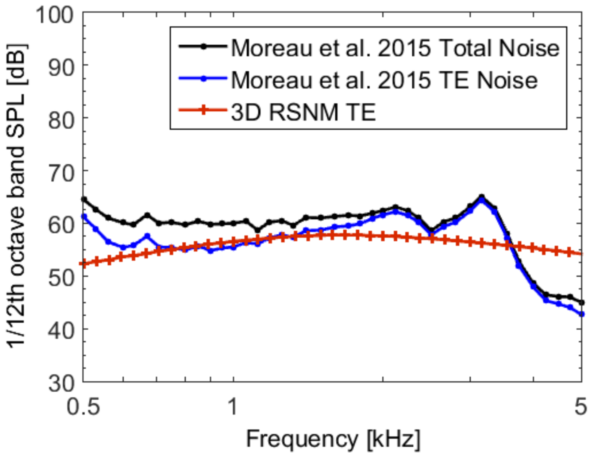

Figure 7.31: Virginia Tech aspect ratio 2, 6 degree angle of attack case, 3DRSNM-TE resulting noise prediction

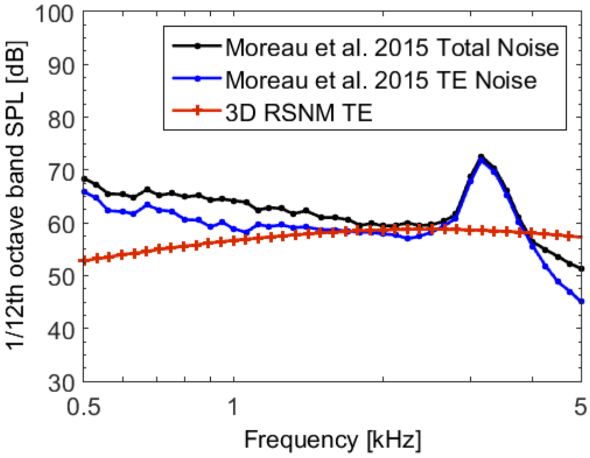

Figure 7.32: Virginia Tech aspect ratio 2, 12 degree angle of attack case, 3DRSNM-TE resulting noise prediction

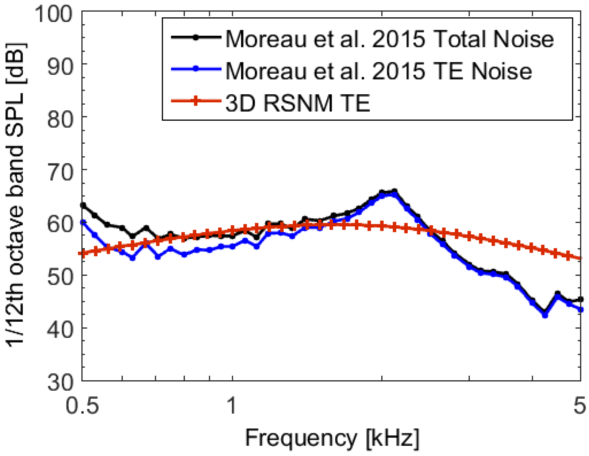

Figure 7.33: Virginia Tech aspect ratio 3, 0 degree angle of attack case, 3DRSNM-TE resulting noise prediction

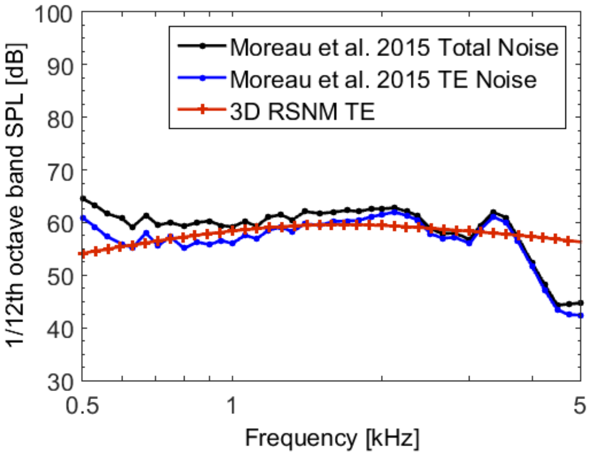

Figure 7.34: Virginia Tech aspect ratio 3, 6 degree angle of attack case, 3DRSNM-TE resulting noise prediction

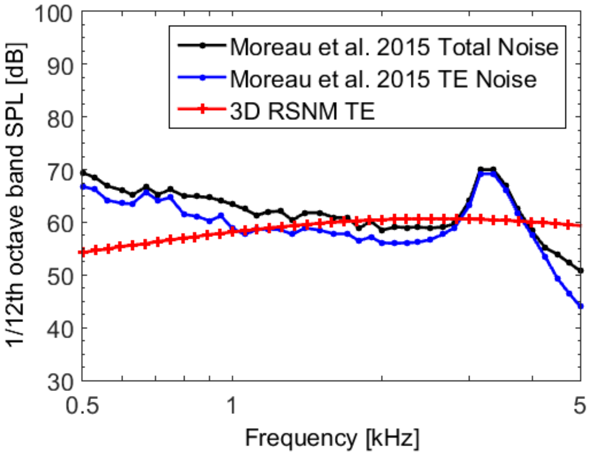

Figure 7.35: Virginia Tech aspect ratio 3, 12 degree angle of attack case, 3DRSNM-TE resulting noise prediction

7.4.5 Amiet Based LE Noise Model Specifications and Results

The leading edge noise model detailed in Section 3.7 was used to predict the leading edge noise from CFD data obtained at a location one quarter chord upstream of the leading edge for the $AR = 1$, $AOA = 0$ case. As in Doolan et al. (2012), unrealistically small turbulent length scale estimates were obtained when using the Wilcox (2006) suggested value of $C = 0.09$. A value of $C = 0.5$ is used in the present work to generate turbulent length scales from the CFD based turbulent dissipation and kinetic energy. The number of sectional elements, N, was varied according to $N = J^2$, $J = 0, 1, 2, 3, ...$ and selected results for varying numbers of sectional elements used in the noise prediction using the coarse mesh CFD data are given in Figure 7.36 where they are compared against the isolated LE noise as measured experimentally by Moreau et al. (2015). It can be seen that this result quickly converges as the number of elements considered is increased. The one-twelfth-octave band levels change by less than 0.3 dB on average between the N=16 and N=32 noise predictions. Best agreement is seen at higher frequencies while at lower frequencies the LE noise model underpredicts the absolute levels measured experimentally. Consideration of Figure 7.37, which gives the noise components measured experimentally, reveals that the majority of the noise at frequencies lower than 2 kHz comes from the junction region. This suggests that the LE noise model is not fully capturing the increase in LE noise generated at the more turbulent junction flow region over that generated by the rest of the airfoil span. This could be attributed to the flow features at the junction enhancing the standard noise generation mechanism, or being themselves the cause of separate noise mechanisms. There was very little variation between the predictions made based on the different mesh results, with noise levels changing by less than 0.2 dB between the coarse and fine $N = 32$ results, as shown in Figure 7.38. Similarly the leading edge noise was determined for the $AOA = 0$ degree, $AR = [2, 3]$ cases and results are shown for $N = 512$ along with the experimental results of Moreau et al. (2015) in Figures 7.39 and 7.40. Trends are similar to the $AR = 1$, $AOA = 0$ case, namely the best agreement is seen at higher frequencies while at lower frequencies the LE noise model underpredicts the absolute levels measured experimentally. The results suggest that LE noise is not a significant noise source in this case except at low frequencies (<1kHz). Angle of attack will not produce significant differences for the spectra predicted using this method as the turbulence sampled upstream will be almost identical.

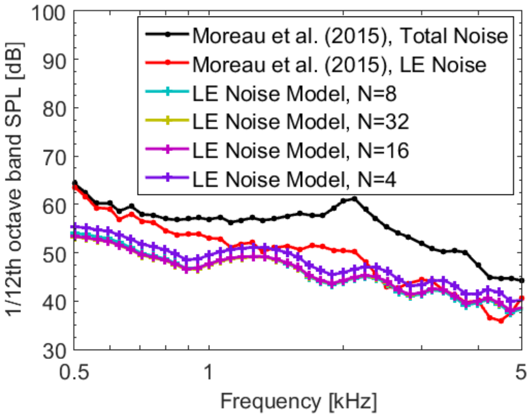

Figure 7.36: Virginia Tech $AR = 1$, $AOA = 0$ case leading edge noise prediction

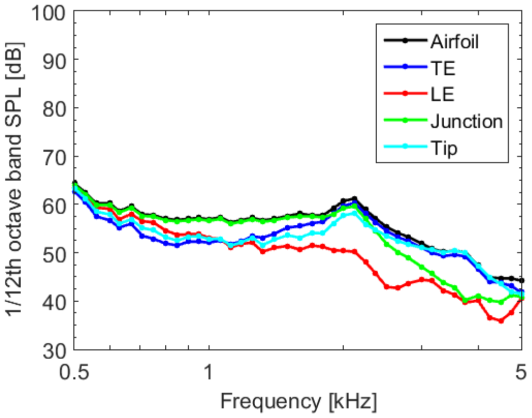

Figure 7.37: Virginia Tech $AR = 1$, $AOA = 0$ case experimentally measured noise components and total noise

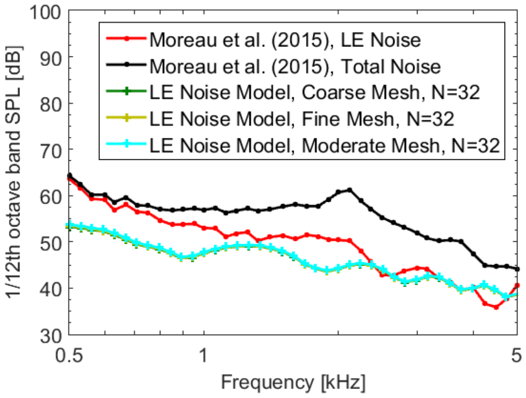

Figure 7.38: Virginia Tech $AR = 1$, $AOA = 0$ case leading edge noise prediction

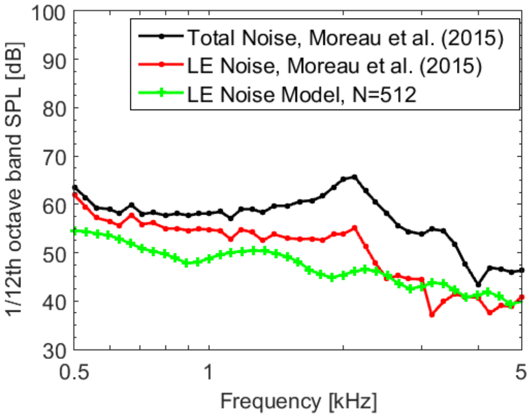

Figure 7.39: Virginia Tech $AR = 2$, $AOA = 0$ case leading edge noise prediction

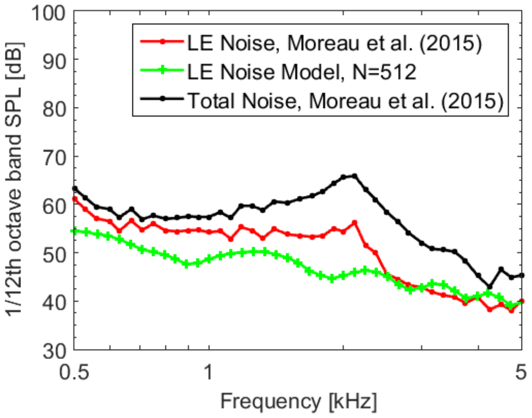

Figure 7.40: Virginia Tech $AR = 2$, $AOA = 0$ case leading edge noise prediction

7.4.6 Noise Modelling Comparison

For the purposes of comparison of the noise modelling techniques to those originally available in the literature, Figure 7.41 compares trailing edge noise modelled using the 3D RSNM method, the BPM method, the trailing edge noise modelled using the developed isolated tip noise model, and the BPM TIP noise model, as well as the leading edge noise predicted using the Amiet based LE noise model, to each other, as well as the experimentally measured total noise. For comparison purposes, results from models which output in one-third octave band levels have been interpolated onto one-twelfth octave band frequencies, and level adjusted assuming the sound distributes evenly over the larger number of bands, by addition of a factor of $10log_{10}(\frac{1}{4})$, to produce levels equivalent to the one-twelfth octave band level results. It can be seen that the TE noise estimate based on the 3D RSNM method exceeds that of the BPM method at all but the lowest ($<$600Hz) frequencies considered, at which frequencies both the 3D RSNM and BPM significantly underpredict the experimental noise levels.The Amiet based LE noise, developed isolated tip noise model and 3D RSNM TE noise predictions are then considered to be independent sources, and added together, to predict the total noise. This total noise estimate is compared to the total noise predicted when combining the BPM TE and tip noise models, again added together as though independent sources, in Figure 7.42. As a measure of the increased accuracy of the developed noise models over those of the literature, the smallest, largest and average level difference between the developed models aggregate and the experimental results were compared, yielding results of [5.40, -11.55, -3.37] dB while doing the same for the BPM aggregate gives [-9.95, -30.82, -15.05] dB, for an average increase in accuracy of 11.69 dB.

7.5 Conclusions and Summary

Leading edge, tip, and trailing edge noise models were applied to an array of test cases spanning aspect ratios from 1 to 3 and angles of attack from 0 to 12 degrees. The trailing edge noise model, and the 3DRSNM model, required variation of the spanwise correlation constant C_{l_z} from the originally proposed value of 0.11, to prevent significant underestimation of the predicted noise levels, as was also observed in Sections 5 and 6. This reinforces the conclusion that accurate setting the RSNM semi-empirical model term is instrumental to the accuracy of the 3D-RSNM-TE model. Again highlighting the need to investigate a rigorous method of determing these quantities as a worthwhile avenue for future work. The spanwise and complete model both achieved good prediction of overall noise levels when compared to the experimental results across frequency ranges where trailing edge noise had been found to be the dominant noise source. The model was found to underpredict the experimentally measured noise levels from the literature both at the lowest frequencies considered, where the dominant noise sources are not from the trailing edge, but centred about the wing-junction mid-span, and at the peaks occurring at around 3150 Hz when at angles of attack, whereat tip noise is the dominant mechanism. When compared to the original RSNM model, the spanwise as well as complete 3D-RSNM-TE are expected to be of immediate practical interest on the basis of allowing significant reductions in the required acoustic grid resolution, greatly reducing the computational effort involved, and so increasing the practicability of the method for industrial applications.

The Amiet based LE noise model was applied and found to best agree with the experimentally measured LE noise component at higher frequencies, while at lower frequencies the LE noise model underpredicts the absolute levels measured experimentally. This is attributed in part to the model failing to capture all of the noise in the junction region, due to reflections from the solid surface. Additionally it is expected that additional noise production mechanisms will occur in this region, and they that would not be captured by this model, and so account for

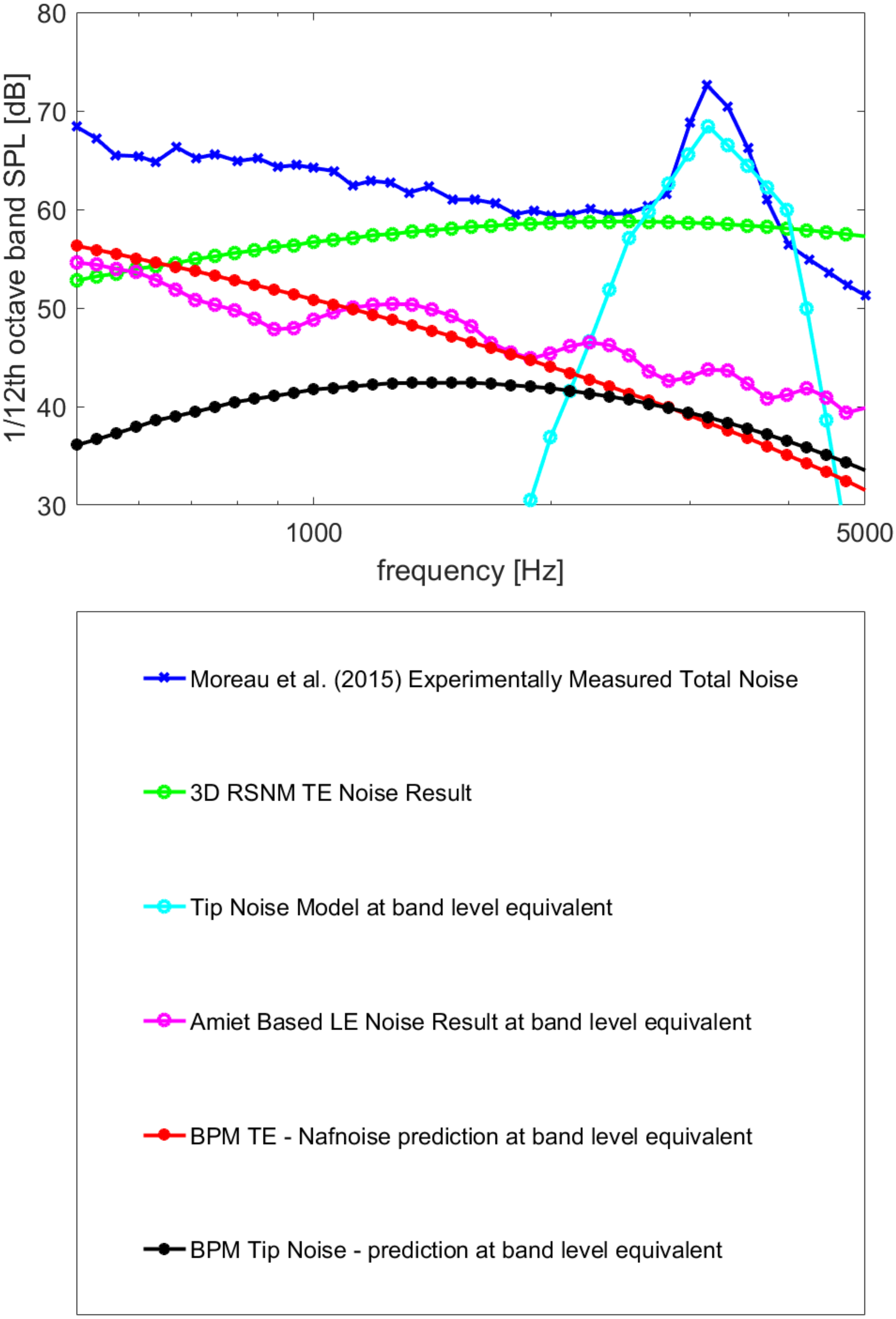

Figure 7.41: Virginia Tech cases AR = 2, AOA =12, developed noise models compared against those of literature

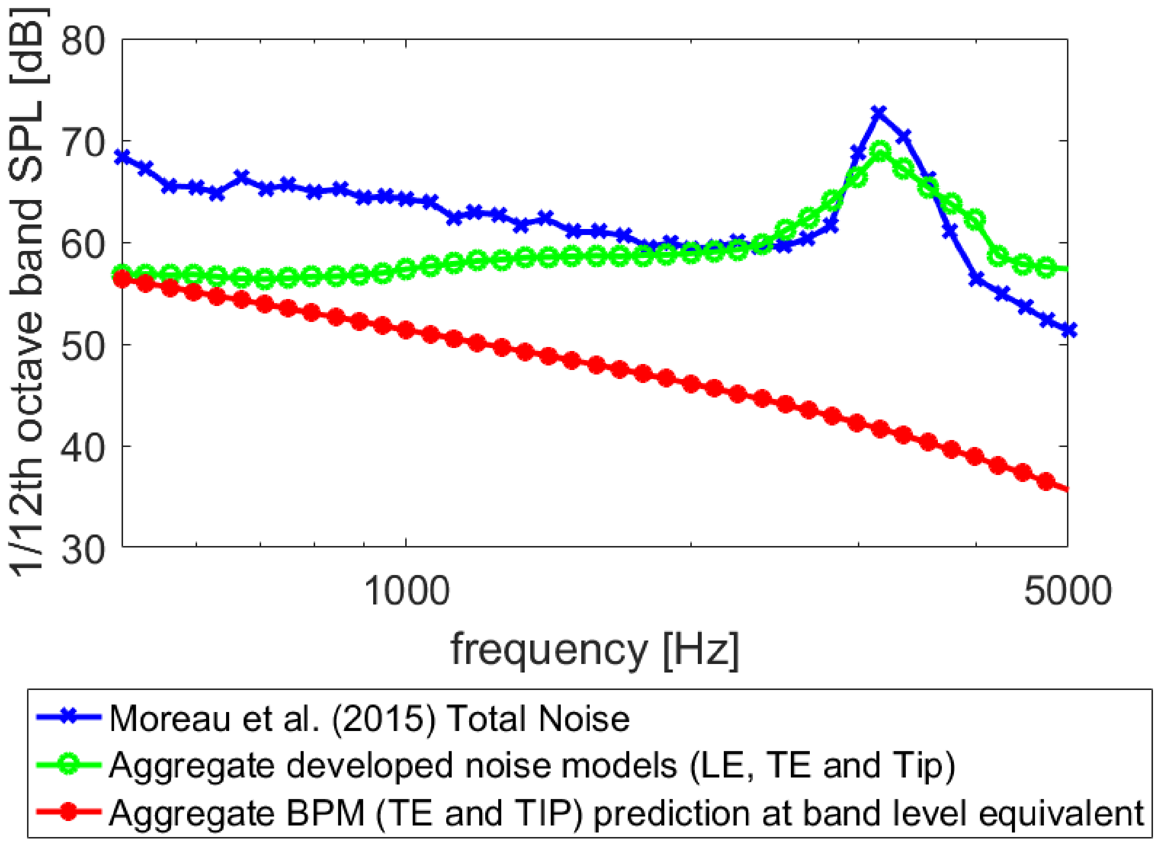

Figure 7.42: Virginia Tech cases AR = 2, AOA =12, combined developed noise models compared against those of literature

the remainder of the deficit.

The trailing edge vortex size for flat ended airfoils was investigated for moderate to high angles of attack. A model describing this vortex sizing was developed and found to be in reasonable agreement with that of Brooks et al. (1989) which was proposed with 'no experimental confirmation'. It is conjectured that at sufficiently low angles of attack, there may be an additional or transitional regime, between the zero angle of attack and high angle of attack tip flow topologies. Experimental observations, or time dependent flow simulations would be required to investigate this possibility. In any case, characterising the vortex sizing for flat-ended airfoils at low angles of attack is identified as potential future work, as is investigating the effectiveness of the proposed vortex sizing model under these conditions.

A model for predicting tip noise was developed which used the trailing edge vortex size as the fundamental scaling parameter. The developed model was seen to be effective at the extremes of the ranges of aspect ratios and Reynolds numbers investigated by Moreau et al. (2015), at moderate to high angles of attack. At low angles of attack, isolated tip noise was not readily separable from other noise sources in the Moreau et al. (2015) data, so identifying the effectiveness of the models at low angles of attack remains to be investigated.

8 Summary of Conclusions, and Recommendations for Future Work

8.1 Summary of Conclusions

The junction region of a wing in junction flow was investigated using RANS simulations and eight turbulence models, replicating the experiments of Devenport and Simpson (1990) and Devenport and Simpson (1992). The results for the turbulence models which had been previously used to investigate the case numerically in the literature (summarised in Table 2.3), namely the k-ϵ, k-ω, k-ω SST and Spalart Allmaras models, were compared with those obtained herein, as well as experimental measurements (Devenport and Simpson, 1990) and (Devenport and Simpson, 1992). The models which had not been used to previously investigate this case, namely the RNG k-ϵ, Realisable k-ϵ, LRR and Launder Gibson RSTM models, were also compared with the experimental data, and it was found that of the turbulence models used, that the Realisable $k-\epsilon$ model and the Reynolds stress transport models produced the most accurate flow predictions. This directly addressed the first thesis aim, to investigate the strengths and limitations of RANS based turbulence models for predicting wall-mounted finite span wing flows.

Flow simulations were conducted to predict flow of a number of wall-mounted finite span wing experiments, namely those of Moreau and Doolan (2013) and Moreau et al. (2015). These were used to provide insight into the tip vortex and its formation process for flat ended airfoils, addressing the fourth thesis aim, to characterise the tip vortex formation process for flat ended airfoils at zero angle of attack. The proposed tip vortex formation process and topology is given in detail in Section 6.4.3.

The simulated flow results were also used with a number of developed noise models to predict some of the most significant noise mechanisms present in wall-mounted finite span wing flows, and these predictions were also compared to experimental measurements. The RSNM method, which had previously been used to predict trailing edge noise for a number of two dimensional flow cases, was extended to account for spanwise variations in wing geometric or flow properties, allowing it to be used on junction flows. This was achieved using a newly proposed velocity cross-spectrum model, as well as improved implementation, which more accurately accounts for the average correlation of the volumes being used in the noise computation with themselves. The developed 3D RSNM approach was found to be effective at capturing the trailing edge noise spectral shape, but using the semi-empirical model values proposed by (Albarracin et al., 2012a), can result in underestimation of the predicted noise levels relative to those measured experimentally. The capacity of the model to be tuned to achieve accurate noise levels was shown by variational parametric investigation on the spanwise correlation constant Cl_z, allowing it to vary from the same as that originally proposed for the flow plane (C_{l_x}=C_{l_y}=0.11), which, when increased, resulted in improved noise level predictions for a number of airfoils and flow conditions. The leading edge noise model of Amiet (1975), which had been developed for two dimensional airfoil geometry-flow conditions, was also extended for use in situations with spanwise variation in airfoil geometry and/or flow properties. The extended model was applied to predict the leading edge noise for a number of wall-mounted finite span wing flow cases. Resulting noise predictions were found to best agree with the experimentally measured LE noise component at higher frequencies, while at lower frequencies the LE noise model underpredicts the absolute levels measured experimentally. This is currently attributed in part to the model failing to capture all of the noise in the junction region, due to reflections from the solid surfaces, as well as additional noise production mechanisms that may well be occurring in this region. One simple approximation to account for reflections from the wall mounting would be to increase the predicted levels by 3 dB. However, even accounting for this, there is still a deficit. It is proposed that intense flows around the wing tip and root, are sufficiently different from the free turbulence upon which the model is based, and that additional noise mechanisms may also be present in these locations, resulting in enhanced noise production above that predicted by the model. It is worth considering that the wings investigated have all been of relatively low aspect ratio. For wings of larger aspect ratio the relative contribution of these enhanced regions when compared to that of the span would be expected to be reduced, and as such the method would be expected to be more effective in such cases. Finally a noise model for predicting the isolated tip noise was developed which used the trailing edge vortex size as the fundamental scaling parameter. The developed model was seen to be effective at the extremes of the ranges of aspect ratios and Reynolds numbers investigated. In totality, these models represent a significant increase in the ability to predict the most significant noise sources present in wing in junction flows. This capacity directly addresses the second and third thesis aims, to develop and extend the semi-analytical and RSNM techniques so as to take into account spanwise variations in wing geometry and flow properties, allowing them to be used to predict wing-in-junction flow noise, and to use the developed noise models to predict the flow and noise from a number of recent wing-in-junction experiments. For example, the results presented in Section 7.4.6 show that the aggregate developed noise models on average 11.69 dB more accurate than the literature models against which they were compared.

8.2 Future Work

Chapter 6 presented flow simulations for the wall-mounted finite span wing experiments of Moreau and Doolan (2013), and these were used to provide insight into the tip vortex and its formation process for flat ended airfoils. Significantly different tip vortex topologies are observed at zero angle of attack when compared to those observed at moderate to high angles of attack. It is suspected that at sufficiently low angles of attack there may be an additional or transitional regime between the zero angle of attack and high angle of attack tip flow topology. Experimental observations or time dependent flow simulations would be required to investigate this possibility, and this is nominated as a potential avenue for future work. The wall-mounted finite span wing flow simulations presented in Chapter 6 and Chapter 7 do not exhibit significant interaction between the vortices of the junction and tip regions. At lower aspect ratios, the horseshoe and tip vortices are expected to interact more directly, and investigation of the flow topology and associated noise produced under such conditions, is also flagged as an avenue for future work.

The Amiet based leading edge noise model, developed in Section 3.7, has been seen to produce underpredictions for the LE when applied in Chapters 6 and 7. This is partly attributed to the model not taking into account reflections from the wall mounting. It is proposed that intense flows around the wing tip and root, are sufficiently different from the free turbulence upon which the model is based, and that additional noise mechanisms may also be present in these locations. Investigating the enhanced noise produced in, as well as determining a more effective method to predict the LE noise from these regions, is identified as an avenue of future work.

Chapters 5, 6 and 7 found 3D RSNM to be effective at capturing the trailing edge noise spectral shape, however using the same value for the spanwise correlation constant Cl_z as that originally proposed for the flow plane (C_{l_x}=C_{l_y}=0.11) was seen to result in underestimation of the predicted noise levels relative to those measured experimentally. This has been attributed to the semi-empirical model values inherited from 2D RSNM. Initially, the spanwise correlation lengthscale coefficient, was taken to have the same value as that of the flow-plane. Using a value for the spanwise correlation constant $Cl_z = 5$ was found to produce sound pressure levels which more accurately reflect those measured, for NACA0012 profile wings for the range of Reynolds numbers ($Re_C = 1.61 \times 10^5 \leq Re_c \leq 4.02 \times 10^6$) and angles of attack ($0 \leq AOA \leq 12$) considered (note that variation of angles of attack were all investigated at a single Reynolds number of $Re_C = 1.61 \times 10^6$). This value of the spanwise correlation constant may not prove to be effective for accurate predictions at Reynolds numbers outside of this range, as well as for differing airfoil geometries. Accurate setting of the model semi-empirical constants is thus found to be instrumental to the accuracy of the 3D-RSNM-TE model, and determining if these terms are a function of other flow or geometric properties is identified as an avenue of future work. Study of how to set the semi-empirical length and timescale constants, could be undertaken numerically using time resolved CFD methods, or experimentally. Such experimental investigations were being undertaken concurrently with the present work by Albarracin (2016) at the School of Mechanical Engineering at the University of Adelaide. The work presented extended the RSNM method, from what was previously a 2D only method, so as to be readily applicable when wing geometry, or flow conditions vary as along the span of the wing. However, it has still only been used for cases where the airfoil had uniform profile along that span while the flow was varied. Therefore, applying 3D RSNM to cases involving wings with taper, sweep, and other variations in profile is identified as an avenue for future work, and one which would further increase the applicability of the method for the non-simplified airfoils typically utilised in industrial applications.

References

Ahmed, A. and Khan, M.J. ‘Effect of sweep on wing-body juncture flow.’ *AIAA Paper*, pages 95–0868, 1995.

Albarracin, C. ‘Email correspondence.’ Email Correspondence, 2014.

Albarracin, C. ‘Email correspondence.’ Email Correspondence, 2016.

Albarracin, C., Doolan, C., Jones, R., Hansen, C., Brooks, L., and Teubner, M. ‘A RANS-Based Statistical Noise Model for Trailing Edge Noise.’ In ‘Proceedings of the 18th AIAA CEAS Aeroacoustics Conference, AIAA Paper,’ volume 2181. 2012a.

Albarracin, C.A., Doolan, C.J., Hansen, C.H., and Brooks, L.A. ‘Turbulent trailing edge noise estimation using a RANS-based statistical noise model.’ *Proceedings of ACOUSTICS 2011, 2-4 November, Gold Coast, Australia*, 2011.

Albarracin, C.A., Marshallsay, P., Brooks, L.A., Cederholm, A., Chen, L., and Doolan, C.J. ‘Comparison of aeroacoustic predictions of turbulent trailing edge noise using three different flow solutions.’ In ‘Proceedings of the 18th Australasian Fluid Mechanics Conference,’ pages 3–7. Launceston, Australia, 2012b.

Alsayed, O.A., Asrar, W., and Omar, A.A. ‘Evaluation of aircraft wing-tip vortex using piv.’ In ‘The 10th Asian International Conference on Fluid Machinery,’ volume 1225, pages 382–390. AIP Publishing, 2010.

Amiet, R.K. ‘Acoustic radiation from an airfoil in a turbulent stream.’ *Journal of Sound and Vibration*, volume 41(4), pages 407–420, 1975.

Amiet, R. ‘Noise due to turbulent flow past a trailing edge.’ *Journal of sound and vibration*, volume 47, no. 3, pages 387–393, 1976.

Anderson, E.A., Wright, C.T., and Lawton, T. ‘Experimental study of the structure of the wingtip vortex.’ *AIAA paper*, volume 269, 2000.

Apsley, D.D. and Leschziner, M.A. ‘Investigation of advanced turbulence models for the flow in a generic wing-body junction.’ *Flow, Turbulence and Combustion*, volume 67, pages 25–55, 2001.

Bailey, S.C., Tavoularis, S., and Lee, B.H. ‘Effects of freestream turbulence on wing-tip vortex formation and near field.’ *Journal of Aircraft*, volume 43(5), pages 1282–1291, 2006.

Barber, T. ‘An investigation of strut-wall intersection losses.’ *Journal of Aircraft*, volume 15, no. 10, pages 676–681, 1987.

Bonnin, J.C., Buchel, T., and Rodi, W. ‘Databases and testing of calculation methods for turbulent flows.’ *Ercoftac Bulletin*, volume 28, pages 49–54, 1996.

Bordji, M., Gand, F., Brunet, V., and Deck, S. ‘Comparative study of linear and non-linear rans closures for corner flows.’ In ‘32nd AIAA Applied Aerodynamics Conference, AIAA Aviation and Aeronautics Forum and Exposition 2014,’ 2014.

Boussinesq, J. *Essai sur la théorie des eaux courantes*. Imprimerie nationale, 1877.

Bradshaw, P. 'Turbulent secondary flows.' *Annual review of fluid mechanics*, volume 19(1), pages 53–74, 1987.

Bragg, G. 'The turbulent boundary layer in a corner (turbulent boundary layer in corner, measuring velocities, wall shear and turbulent normal stresses by employing momentum integral and similarity analyses).' *Journal of Fluid Mechanics*, volume 36(3), pages 485–503, 1969.

Bronzaft, A.L., Ahern, K.D., McGinn, R., O'Connor, J., and Savino, B. 'Aircraft noise: A potential health hazard.' *Environment and Behavior*, volume 30, pages 101–113, 1998.

Brooks, T.F. and Hodgson, T.H. 'Trailing edge noise prediction from measured surface pressures.' *Journal of Sound and Vibration*, volume 78(1), pages 69–117, 1981.

Brooks, T.F. and Marcolini, M.A. 'Airfoil tip vortex formation noise.' *AIAA journal*, volume 24(2), no. 2, pages 246–252, 1986.

Brooks, T.F., Pope, D.S., and Marcolini, M.A. 'Airfoil self-noise and prediction.' Technical report, NASA, 1989.

Cebeci, T. and Bradshaw, P. *Momentum transfer in boundary layers.* Hemisphere Publishing Corp, 1977.

Chandiramani, K.L. 'Diffraction of evanescent waves with applications to aerodynamically scattered sound and radiation from unbaffled plates.' *The Journal of the Acoustical Society of America*, volume 55, no. 1, pages 19–29, 1974.

Chapman, C. 'High-speed leading-edge noise.' In 'Proceedings of the Royal Society of London A: Mathematical, Physical and Engineering Sciences,' volume 459, pages 2131–2151. The Royal Society, 2003.

Chase, D. 'The character of the turbulent wall pressure spectrum at subconvective wavenumbers and a suggested comprehensive model.' *Journal of Sound and Vibration*, volume 112(1), pages 125–147, 1987.

Chen, H.C. 'Assessment of a Reynolds stress closure model for appendage-hull junction flows.' *Journal of Fluids Engineering*, volume 117, pages 557–563, 1995.

Chow, J.S., Zilliac, G.G., and Bradshaw, P. 'Mean and turbulence measurements in the near field of a wingtip vortex.' *AIAA Journal*, volume 35(10), pages 1561–1567, 1997.

Churchfield, M.J. and Blaisdell, G.A. 'Reynolds stress relaxation turbulence modeling applied to a wingtip vortex flow.' *AIAA Journal*, volume 51(11), pages 2643–2655, 2013.

Coles, D. 'The law of the wake in the turbulent boundary layer.' *Journal of Fluid Mechanics*, volume 1(2), pages 191–226, 1956.

Corcos, G.M. 'The structure of the turbulent pressure field in boundary-layer flows.' *Journal of Fluid Mechanics*, volume 18(3), pages 353–378, 1964.

Dacles-Mariani, J., Kwak, D., and Zilliac, G. 'Accuracy assessment of a wingtip vortex flowfield in the near-field region.' *AIAA Paper*, volume 208, 1996.

Dacles-Mariani, J., Rogers, S., Kwak, D., Zilliac, G., and Chow, J. 'A computational study of wingtip vortex flowfield. aiaa 93-3010.' In '24th Fluid Dynamics Conference, Orlando FL, July,' pages 6–9. 1993.

Dacles-Mariani, J., Zilliac, G.G., Chow, J.S., and Bradshaw, P. 'Numerical/experimental study of a wingtip vortex in the near field.' *AIAA Journal*, volume 33(9), pages 1561–1568, 1995.

Dandois, J. 'Improvement of corner flow prediction using the quadratic constitutive relation.' *AIAA Journal*, pages 1–12, 2014.

de Villiers, E. *The Potential of Large Eddy Simulation for the Modeling of Wall Bounded Flows.* Ph.D. thesis, Department of Mechanical Engineering, Imperial College of Science, Technology and Medicine, 2006.

Defence Science and Technology Organisation. 'Some aspects of submarine design part 1. hydrodynamics.' Technical report, Defence Science and Technology Organisation, 2004.

Devenport, W., Burdisso, R., Camargo, H., Crede, E., Remilleux, M., Rasnik, M., and Seeters, P.V. 'Aeroacoustic testing of wind turbine airfoils.' Technical report, National Renewable Energy Laboratories, Virginia Polytechnic Institute and State University Blacksburg, Virginia, 2010a.

Devenport, W.J., Rife, M.C., Liapis, S.I., and Follin, G.J. 'The structure and development of a wing-tip vortex.' *Journal of Fluid Mechanics*, volume 312, pages 67–106, 1996.

Devenport, W.J. and Simpson, R.L. 'Time-dependent and time-averaged turbulence structure near the nose of a wing-body junction.' *Journal of Fluid Mechanics*, volume 210, pages 23–55, 1990.

Devenport, W.J. and Simpson, R.L. 'Flow past a wing-body junction - experimental evaluation of turbulence models.' *AIAA Journal*, volume 30, no. 4, pages 873–881, 1992.

Devenport, W.J., Staubs, J.K., and Glegg, S.A. 'Sound radiation from real airfoils in turbulence.' *Journal of Sound and Vibration*, volume 329, no. 17, pages 3470–3483, 2010b.

Dixit, S.A. and Ramesh, O. 'Large-scale structures in turbulent and reverse-transitional sink flow boundary layers.' *Journal of Fluid Mechanics*, volume 649, pages 233–273, 2010.

Doolan, C.J., Gonzalez, C.A., and Hansen, C.H. 'Statistical estimation of turbulent trailing edge noise.' In 'Proceedings of 20th International Congress on Acoustics, ICA 2010,' 2010.

Doolan, C.J., Coombs, J.L., Moreau, D.J., Zander, A.C., and Brooks, L.A. 'Prediction of noise from a wing-in-junction flow using computational fluid dynamics.' In 'Proceedings of Acoustics,' 2012.

Duraisamy, K. *Studies in Tip Vortex Formation, Evolution and Control.* Ph.D. thesis, Faculty of the Graduate School of the University of Maryland, College Park, 2005.

Duraisamy, K., Ramasamy, M., Baeder, J.D., and Leishman, J.G. 'High-resolution computational and experimental study of rotary-wing tip vortex formation.' *AIAA Journal*, volume 45(11), pages 2593–2602, 2007.

Ewert, R. 'Broadband slat noise prediction based on caa and stochastic sound sources from a fast random particle-mesh (rpm) method.' *Computers & Fluids*, volume 37(4), pages 369–387, 2008.

Ferziger, J.H. and Peric, M. *Computational Methods for Fluid Dynamics.* Springer-Verlag, 1995.

Ffowcs-Williams, J. and Hall, L. 'Aerodynamic sound generation by turbulent flow in the vicinity of a scattering half plane.' *Journal of Fluid Mechanics*, volume 40, pages 657–670, 1970.

Fink, M.R. 'Noise component method for airframe noise.' *Journal of Aircraft*, volume 16(10), pages 659–665, 1979.

Fleig, O. and Arakawa, C. 'Large-eddy simulation of tip vortex flow at high Reynolds number.' *AIAA Paper*, volume 261, 2004.

Fleming, J.L., Simpson, R.L., Cowling, J.E., and Devenport, W.J. 'An experimental study of a turbulent wing-body junction and wake flow.' *Experiments in Fluids*, volume 14, pages 366–378, 1993.

Fleming, J.L., Simpson, R.L., and Devenport, W.J. 'An experimental study of a turbulent wing-body junction and wake flow.' Technical report, Aerospace and Ocean Engineering Department, 1991.

Franke, M., Wallin, S., and Thiele, F. 'Assessment of explicit algebraic Reynolds-stress turbulence models in aerodynamic computations.' *Aerospace Science and Technology*, volume 9, pages 573–581, 2005.

Freymuth, P. 'Vortex topology of rectangular wings in pictures, sketches, and conjectures.' *Journal of Flow Visualization and Image Processing*, volume 1(1), 1993.

Fu, S., Xiao, Z., Chen, H., Zhang, Y., and Huang, J. 'Simulation of wing-body junction flows with hybrid RANS/LES methods.' *International Journal of Heat and Fluid Flow*, volume 28, pages 1379–1390, 2007.

Gand, F., Monnier, J.C., Deluc, J.M., and Choffat, A. 'Experimental study of the corner flow separation on a simplified junction.' *AIAA Journal*, pages 1–9, 2015.

Gand, F., Brunet, V., and Deck, S. 'A combined experimental, RANS and LES investigation of a wing body junction flow.' In '40th Fluid Dynamics Conference and Exhibit,' 2010a.

Gand, F., Deck, S., Brunet, V., and Sagaut, P. 'Flow dynamics past a simplified wing body junction.' *Physics of Fluids*, volume 22, 2010b.

George, A.R. and Chou, S.T. 'Broadband rotor noise analysis.' Technical report, NASA (CR-3797), 1984.

George, A.R., Najjar, F.E., and Kim, Y.N. 'Noise due to tip vortex formation on lifting rotors.' In 'Proceedings of the 6th Aeroacoustics Conference on American Institute of Aeronautics and Astronautics, Hartford, CT, USA,' volume 46. 1980.

Gessner, F. 'The origin of secondary flow in turbulent flow along a corner.' *Journal of Fluid Mechanics*, volume 58(1), pages 1–25, 1973.

Geyer, T., Sarradj, E., and Giesler, J. 'Application of a beamforming technique to the measurement of airfoil leading edge noise.' *Advances in Acoustics and Vibration*, volume 2012, 2012.

Gibson, M.M. and Launder, B.E. 'Ground effects on pressure fluctuations in the atmospheric boundary layer.' *Journal of Fluid Mechanics*, volume 86, pages 491–511, 1978.

Giuni, M. *Vortex formation on squared and rounded tip.* Ph.D. thesis, University of Glasgow School of Engineering, 2013.

Giuni, M. and Green, R.B. 'Vortex formation on squared and rounded tip.' *Aerospace Sc*, volume 29(1), pages 191–199, 2013.

Glegg, S., Morin, B., Atassi, O., and Reba, R. 'Using RANS calculations of turbulent kinetic energy to provide predictions of trailing edge noise.' *AIAA Paper*, volume 2993, no. 2008, page 582, 2008.

Goody, M. 'Empirical spectral model of surface pressure fluctuations.' *AIAA Journal*, volume 42(9), pages 1788–1794, 2004.

Hardin, J.C. and Martin, J.E. 'Flap side-edge noise: Acoustic analysis of Sen's model.' *AIAA Journal*, volume 35, no. 5, pages 810–815, 1997.

Harun, Z. *The structure of adverse and favourable pressure gradient turbulent boundary layers.* Ph.D. thesis, University of Melbourne, Department of Mechanical Engineering, 2012.

Herr, M., Appel, C., Dierke, J., and Ewert, R. 'Trailing-edge noise data quality assessment for CAA validation.' *AIAA Paper*, volume 3877, 2010.

Howe, M. 'A review of the theory of trailing edge noise.' *Journal of Sound and Vibration*, volume 61(3), pages 437–465, 1978.

Howe, M. 'Trailing edge noise at low mach numbers.' *Journal of Sound and Vibration*, volume 225, no. 2, pages 211–238, 1999.

Ikeda, T., Atobe, T., and Takagi, S. 'Direct simulations of trailing-edge noise generation from two-dimensional airfoils at low Reynolds numbers.' *Journal of Sound and Vibration*, volume 311, pages 556–574, 2012.

Jasak, H. *Error Analysis and Estimation for the Finite Volume Method with Applications to Fluid Flows.* Ph.D. thesis, Department of Mechanical Engineering, Imperial College of Science, Technology and Medicine, 1996.

Jiang, L., Cai, J., and Liu, C. 'Large-eddy simulation of wing tip vortex in the near field.' *International Journal of Computational Fluid Dynamics*, volume 22(5), pages 289–330, 2008.

Jones, L. and Sandberg, R. 'Numerical investigation of airfoil self-noise reduction by addition of trailing-edge serrations.' In '16th AIAA/CEAS Aeroacoustics Conference Proceedings,' volume 3703. 2010.

Kaltenbach, M., Maschke, C., and Klinke, R. 'Health consequences of aircraft noise.' *Deutsches Arzteblatt International*, volume 105, pages 548–556, 2008.

Kamruzzaman, M., Herrig, A., Lutz, T., Würz, W., Krämer, E., and Wagner, S. 'Comprehensive evaluation and assessment of trailing edge noise prediction based on dedicated measurements.' *Noise Control Engineering Journal*, volume 59(1), pages 54–67, 2011.

Kendall, J.M. 'Measurements of noise produced by flow past lifting surfaces.' In 'AIAA, Aerospace Sciences Meeting,' 1978.

Khan, J. and Ahmed, A. 'On the juncture vortex in the transverse planes.' In '40th AIAA Aerospace Sciences Meeting & Exhibit,' 2002.

Khan, M.J., Ahmed, A., and Trosper, J.R. ‘Dynamics of the juncture vortex.’ *AIAA Journal*, volume 33, no. 7, pages 1273–1278, 1995.

Kolmogorov, A.N. ‘Equations of turbulent motion of an incompressible fluid.’ *Izvestia Academy of Sciences, USSR; Physics*, volume 40, No. 5, pages 927–936, 1942.

Kornilov, V. and Kharitonov, A. ‘Investigation of the structure of turbulent flows in streamwise asymmetric corner configurations.’ *Experiments in Fluids*, volume 2(4), pages 205–212, 1984.

Kraichman, R.H. ‘Diffusion by random velocity field.’ *Journal of Fluid Mechanics*, volume 12, pages 22–31, 1970.

Krogstad, P.Å. and Skåre, P.E. ‘Influence of a strong adverse pressure gradient on the turbulent structure in a boundary layer.’ *Physics of Fluids*, volume 7(8), pages 2014–2024, 1995.

Laflin, K.R., Klausmeyer, S.M., Zickuhr, T., Vassberg, J.C., Wahls, R.A., Morrison, J.H., Brodersen, O.P., Rakowitz, M.E., Tinoco, E.N., and Godard, J.L. ‘Data summary from second AIAA computational fluid dynamics drag prediction workshop.’ *Journal of Aircraft*, volume 42(5), pages 1165–1178, 2005.

Launder, B.E., Reece, G.J., and Rodi, W. ‘Progress in the development of a Reynolds-stress turbulence closure.’ *Journal of Fluid Mechanics*, volume 68(3), pages 537–566, 1975.

Launder, B.E. and Sharma, B.I. ‘Application of the energy-dissipation model of turbulence to the calculation of flow near a spinning disc.’ *Letters in Heat and Mass Transfer*, volume 1, pages 131–138, 1974.

Laurence, D. and Rodi, W. *Engineering Turbulence Modelling and Experiments-4*. Elsevier, 1999.

Lee, Y.T., Blake, W.K., and Farabee, T.M. ‘Modeling of wall pressure fluctuations based on time mean flow field.’ *Journal of Fluids Engineering*, volume 127, no. 2, pages 223–240, 2005.

Leloudas, G., Zhu, W.J., Sørensen, J.N., Shen, W.Z., and Hjort, S. ‘Prediction and reduction of noise from a 2.3 MW wind turbine.’ In ‘Journal of Physics: Conference Series,’ volume 75. 2007.

Lighthill, M.J. ‘On sound generated aerodynamically. i. general theory.’ In ‘Proceedings of the Royal Society of London A: Mathematical, Physical and Engineering Sciences,’ volume 211, pages 564–587. The Royal Society, 1952.

Lockard, D. and Lilley, G. ‘The airframe noise reduction challenge.’ Technical report, National Aeronautics and Space Administration, 2004.

Lombard, J.E.W., Moxey, D., Hoessler, J.F., Dhandapani, S., Taylor, M.J., and Sherwin, S.J. ‘Implicit large eddy simulation of a wingtip vortex at $Re_c = 1.2 \times 10^6$.’ *arXiv preprint arXiv:1507.06012*, volume 1, pages 1–22, 2015.

Macdonald, H.M. ‘A class of difraction problems.’ In ‘Proc. Lond. Math. Soc.’, volume 14, pages 410–427. 1915.

Malik, A. *Suppression of junction flow effects in half model wind tunnel testing*. Ph.D. thesis, Loughborough University, 2013.

Mansour, N. ‘Numerical simulation of the tip vortex of a low-aspect ratio wing at transonic speed.’ *AIAA Journal*, volume 23, pages 1143–1149, 1985.

Marsden, A.L., Wang, M., Dennis, J., and Moin, P. 'Trailing-edge noise reduction using derivative-free optimization and large-eddy simulation.' *Journal of Fluid Mechanics*, volume 572, pages 13–36, 2007.

Martin, P.B., Pugliese, G.J., and Leishman, J.G. 'High resolution trailing vortex measurements in the wake of a hovering rotor.' *Journal of the American Helicopter Society*, volume 48(1), pages 39–52, 2003.

Martinez, R. and Widnall, S.E. 'Unified aerodynamic-acoustic theory for a thin rectangular wing encountering a gust.' *AIAA Journal*, volume 18, no. 6, pages 636–645, 1980.

Mehta, R. 'Effect of wing nose shape on the flow in a wing body junction.' *Aeronautical Journal*, volume 88, page 456, 1984.

Menter, F.R. 'Two-equation eddy-viscosity turbulence models for engineering applications.' *AIAA Journal*, volume 32, no. 8, pages 1598–1605, 1994.

Metner, F. and Esch, T. 'Elements of industrial heat transfer prediction.' In 'Proceeding of the 16th Brazilian Congress of Mechanical Engineering (COBEM),' pages 26–30. 2001.

Moreau, D. and Doolan, C. 'An experimental study of the sound produced by junction flows.' In 'Proceedings of the 20th International Congress on Sound and Vibration,' 2013.

Moreau, D.J., Brooks, L.A., and Doolan, C.J. 'Broadband trailing edge noise from a sharp-edged strut.' *Journal of the Acoustical Society of America*, volume 129(5), pages 2820–2829, 2011.

Moreau, D.J., Doolan, C., Alexander, W.N., Meyers, T.W., and Devenport, W.J. 'Wall-mounted finite airfoil noise production and prediction.' In '21st AIAA/CEAS Aeroacoustics Conference,' page 2831. 2015.

Moreau, D.J., Prime, Z., Porteous, R., Doolan, C.J., and Valeau, V. 'Flow-induced noise of a wall-mounted finite airfoil at low-to-moderate Reynolds number.' *Journal of Sound and Vibration*, volume 333, no. 25, pages 6924–6914, 2014.

Morris, P. and Farassat, F. 'Acoustic analogy and alternative theories for jet noise prediction.' *AIAA Journal*, volume 40(5), pages 671–680, 2002.

Nakayama, A. and Rahai, H. 'Measurements of turbulent flow behind a flat plate mounted normal to the wall.' *AIAA Journal*, volume 22(12), pages 1817–1819, 1984.

Olcmen, S.M. and Simpson, R.L. 'An experimental study of a three-dimensional pressure-driven turbulent boundary layer.' *Journal of Fluid Mechanics*, volume 290, pages 225–262, 1995a.

Olcmen, S.M. and Simpson, R.L. 'A five-velocity-component laser-Doppler velocimeter for measurements of a three-dimensional turbulent boundary layer.' *Measurement Science and Technology*, volume 6, pages 702–716, 1995b.

Olcmen, S.M. and Simpson, R.L. 'Some features of a turbulent wing-body junction vortical flow.' *International Journal of Heat and Fluid Flow*, volume 27, pages 980–993, 2006.

O'Regan, M.S., Griffin, P.C., and Young, T.M. 'Numerical and experimental investigation of the mean and turbulent characteristics of a wing-tip vortex in the near-field.' In 'Proceedings of the Institution of Mechanical Engineers, Part G: Journal of Aerospace Engineering,' SAGE Publications, 2014.

Paciorri, R., Figlioli, A., Mascio, A.D., and Favini, B. ‘RANS simulations of a junction flow.’ *International Journal of Computational Fluid Dynamics*, volume 19(2), pages 179–189, 2005.

Paik, J., Escauriaza, C., and Sotiropoulos, F. ‘On the bimodal dynamics of the turbulent horseshoe vortex system in a wing-body junction.’ *Physics of Fluids*, volume 19, pages 1–20, 2007.

Parchen, R.R. and TNO-TH, T.P.D. *Progress report DRAW: A prediction scheme for trailing edge noise based on detailed boundary layer characteristics.* TNO Institute of Applied Physics, 1998.

Parniex, S., Durbin, P.A., and Behnia, M. ‘Computation of 3-D turbulent boundary layers using the V2F model.’ *Flow, Turbulence and Combustion*, volume 60, pages 19–46, 1998.

Patankar, S.V. ‘A calculation procedure for two-dimensional elliptic situations.’ *Numerical Heat Transfer*, volume 4(4), pages 409–425, 1981.

Paterson, R. and Amiet, R. ‘Noise and surface pressure response of an airfoil to incident turbulence.’ *J. Aircraft*, volume 14(8), pages 729–736, 1977.

Peltier, L. and Hambric, S. ‘Estimating turbulent-boundary-layer wall-pressure spectra from CFD RANS solutions.’ *Journal of Fluids and Structures*, volume 23(6), pages 920–937, 2007.

Pope, S.B. *Turbulent Flows.* Cambridge University Press, 2000.

Prats, X., Puig, V., and Quevedo, J. ‘A multi-objective optimization strategy for designing aircraft noise abatement procedures. Case study at Girona airport.’ *Transportation Research Part D*, volume 1, pages 31–41, 2011.

Remmler, S., Christophe, J., Anthoine, J., and Moreau, S. ‘Computation of wall pressure spectra from steady flow data for noise prediction.’ *AIAA Journal*, volume 48(9), pages 1997–2007, 2010.

Roache, P.J. *Verification and Validation in Computational Science and Engineering.* Hermosa Publishers, 1998.

Rogers, A.L., Manwell, J.F., and Wright, S. ‘Wind turbine acoustic noise.’ *Renewable Energy Research Laboratory, Amherst: University of Massachusetts*, 2006.

Rood, E.P. and Anthony, D.G. ‘Tail profile effects on unsteady large scale flow structure in the wing and plate junction.’ In ‘Forum on unsteady flow-1985; Proceedings of the Winter Annual Meeting, Miami Beach, FL, November 17-22, 1985 (A86-28664 12-34). New York, American Society of Mechanical Engineers, 1985, p. 30-32. Navy-sponsored research.’, 1985.

Rozenberg, Y. *Modélisation analytique du bruit aérodynamique à large bande des machines tournantes: utilisation de calculs moyennés de mécanique des fluides.* Ph.D. thesis, Ecole Centrale de Lyon, 2007.

Sandberg, R.D., Jones, L.E., and Sandham, N.D. ‘Investigation and prediction of transitional airfoil self-noise.’ In ‘Proceedings of the 15th AIAA/CEAS Aeroacoustics Conference, AIAA Paper,’ 2009.

Schlinker, R.H. and Amiet, R.K. ‘Helicopter rotor trailing edge noise.’ In ‘AIAA, Astrodynamics Specialist Conference,’ volume 1. 1981.

Sen, R. ‘Local dynamics and acoustics in a simple model of airfoil lateral-edge noise.’ *AIAA*, pages 80–1010, 1996.

Shabaka, I.M.M.A. and Bradshaw, P. ‘Turbulent flow measurements in an idealized wing/body junction.’ *AIAA Journal*, volume 19(2), pages 131–132, 1981.

Shekarriz, A., Fu, T., Katz, J., and Huang, T. ‘Near-field behavior of a tip vortex.’ *AIAA journal*, volume 31(1), pages 112–118, 1993.

Shih, T.H., Liou, W.W., Shabbir, A., Yang, Z., and Zhu, J. ‘A new k-ϵ eddy viscosity model for high reynolds number turbulent flows.’ *Computers and Fluids*, volume 24, pages 227–238, 1995.

Simpson, R.L. ‘Junction flows.’ *Annual Review of Fluid Mechanics*, volume 33, pages 415–443, 2001.

Smirnov, A., Shi, S., and Celik, I. ‘Random flow generation technique for large eddy simulations and particle-dynamics modeling.’ *Journal of Fluids Engineering*, volume 123(2), pages 359–371, 2001.

Smol’Yakov, A. and Tkachenko, V. ‘Model of a field of pseudosonic turbulent wall pressures and experimental data.’ *Soviet physics. Acoustics*, volume 37(6), pages 627–631, 1991.

Spalart, P.R. and Allmaras, S.R. ‘A one-equation turbulence model for aerodynamic flows.’ *Recherche Aerospatiale*, volume 1, pages 5–21, 1994.

Spalart, P. ‘Strategies for turbulence modelling and simulations.’ *International Journal of Heat and Fluid Flow*, volume 21(3), pages 252–263, 2000.

Speziale, C.G. ‘On nonlinear k-l and k-ε models of turbulence.’ *Journal of Fluid Mechanics*, volume 178, pages 459–475, 1987.

Srinivasan, G., McCroskey, W., Baeder, J., and Edwards, T. ‘Numerical simulation of tip vortices of wings in subsonic and transonic flows.’ *AIAA Journal*, volume 26(10), pages 1153–1162, 1988.

Tam, C.K.W. and Auriault, L. ‘Jet mixing noise from fine-scale turbulence.’ *AIAA Journal*, volume 37, no. 2, pages 145–153, 1999.

Terracol, M. ‘A zonal RANS/LES approach for airframe trailing-edge noise prediction.’ *ONERA: Tire a Part*, page 1, 2005.

Togiti, V., Eisfeld, B., and Brodersen, O. ‘Turbulence model study for the flow around the NASA common research model.’ *Journal of Aircraft*, pages 1–13, 2014.

U.S. Department of Transportation Federal Aviation Administration Aviation Policy and Plans. ‘FAA aerospace forecast fiscal years 2011-2031.’ Technical report, Federal Aviation Administration, 2011.

Uzun, A. and Hussauni, M.Y. ‘Large-eddy simulation of a wing tip vortex on overset grids.’ *AIAA Journal*, volume 44(6), 2006.

Vassberg, J.C., Tinoco, E.N., Mani, M., Levy, D., Zickuhr, T., Mavriplis, D.J., Wahls, R.A., Morrison, J.H., Brodersen, O.P., Eisfeld, B., and Murayama, M. ‘Comparison of NTF experimental data with CFD predictions from the third AIAA CFD drag prediction workshop.’ *AIAA Paper*, volume 6918, 2008.

Versteeg, H.K. and Malalasekera, W. *An Introduction to Computation Fluid Dynamics The Finite Volume Method.* Prentice Hall, 2007.

Viswanathan, K., Krothapalli, A., Seiner, J.M., Czech, M.J., Greska, B., and Jansen, B.J. 'Assessment of low-noise nozzle designs for fighter aircraft applications.' *Journal of Aircraft*, volume 48, pages 412–423, 2011.

Von Karman, T. 'Mechanical similitude and turbulence.' Technical report, NACA, 1931.

Wang, H., Zhou, Y., Chan, C., and Lam, K. 'Effect of initial conditions on interaction between a boundary layer and a wall-mounted finite-length-cylinder wake.' *Physics of Fluids*, volume 18(6), page 065106, 2006.

Wang, M. and Moin, P. 'Computation of trailing-edge flow and noise using large-eddy simulation.' *AIAA Journal*, volume 38, no. 12, pages 2201–2209, 2000.

Wenzel, S., Kölker, K., Bießlich, P., and Lütjens, K. 'Approach to forecast air-traffic movements at capacity-constrained airports.' *Journal of Aircraft*, volume 52, no. 5, pages 1710–1715, 2015.

Wilcox, D. *Turbulence Modeling for CFD.* DCW Industries Inc., California, USA., 1998.

Wilcox, D. *Turbulence Modeling for CFD.* DCW Industries Inc., California, USA., 2006.

Wilcox, D.C. 'Reassessment of the scale-determining equation for advanced turbulence models.' *AIAA Journal*, volume 26, pages 1299–1310, 1988.

Wilcox, D.C. 'Formulation of the k-omega turbulence model revisited.' *AIAA Journal*, volume 46, no. 11, pages 2823–2838, 2008.

Winkler, J., Moreau, S., and Carolus, T. 'Airfoil trailing-edge blowing: Broadband noise prediction from large-eddy simulation.' *AIAA Journal*, volume 50, no. 2, pages 294–303, 2012.

Wolf, W.R. and Lele, S.K. 'Trailing-edge noise predictions using compressible large-eddy simulation and acoustic analogy.' *AIAA Journal*, volume 50, no. 11, pages 2423–2434, 2012.

Wong, J. and Png, E. 'Numerical investigation of the wing body junction vortex using various large eddy simulation models.' In '39th AIAA Fluid Dynamics Conference,' 2009.

Yakhot, V., Orszag, S.A., Thangam, S., Gatski, T.B., and Speziale, C.G. 'Development of turbulence models for shear flows by a double expansion technique.' *Physics of Fluids*, volume 4, pages 1510–1520, 1992.

Yamamoto, K., Tanaka, K., and Murayama, M. 'Effect of a nonlinear constitutive relation for turbulence modeling on predicting flow separation at wing–body juncture of transonic commercial aircraft.' *AIAA Paper*, volume 2895, 2012.

A Turbulence Model Validation and Comparison Results Figures

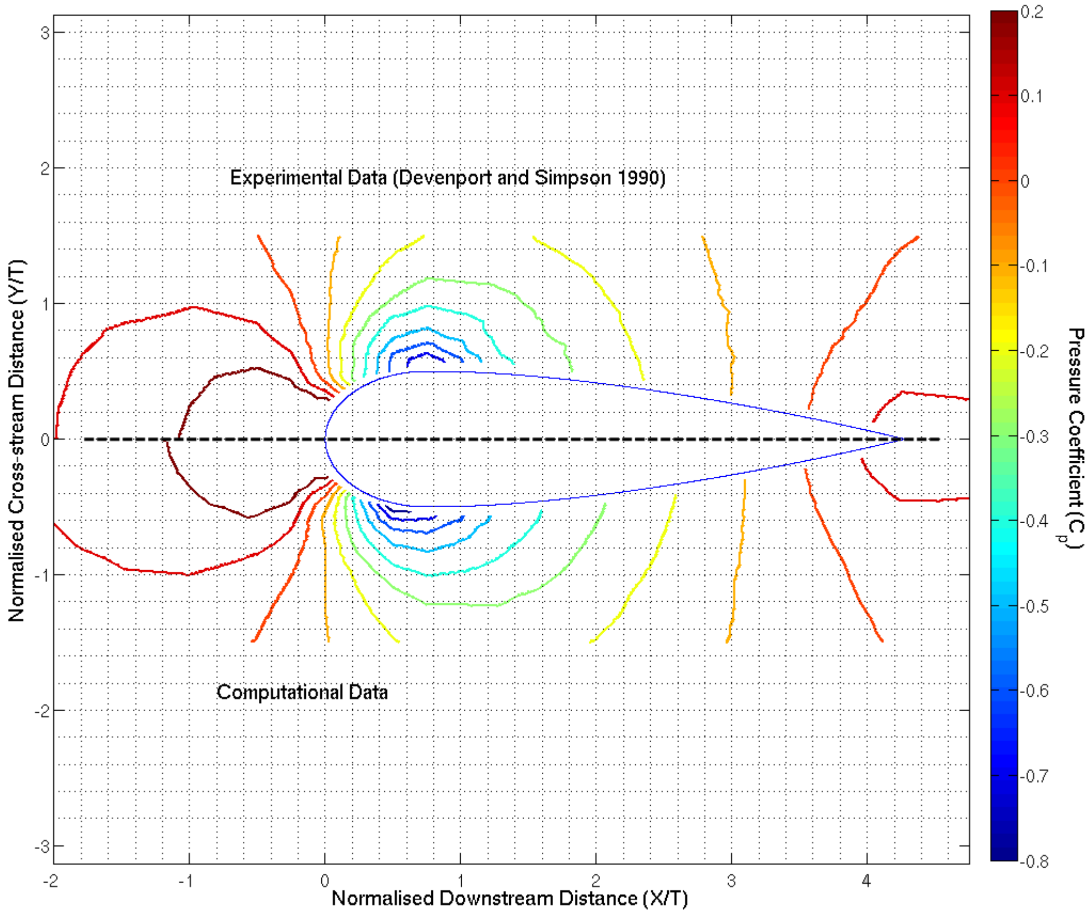

Figure A.1: RNG $k - \epsilon$ model very-fine grid flat plate pressure coefficient plot.

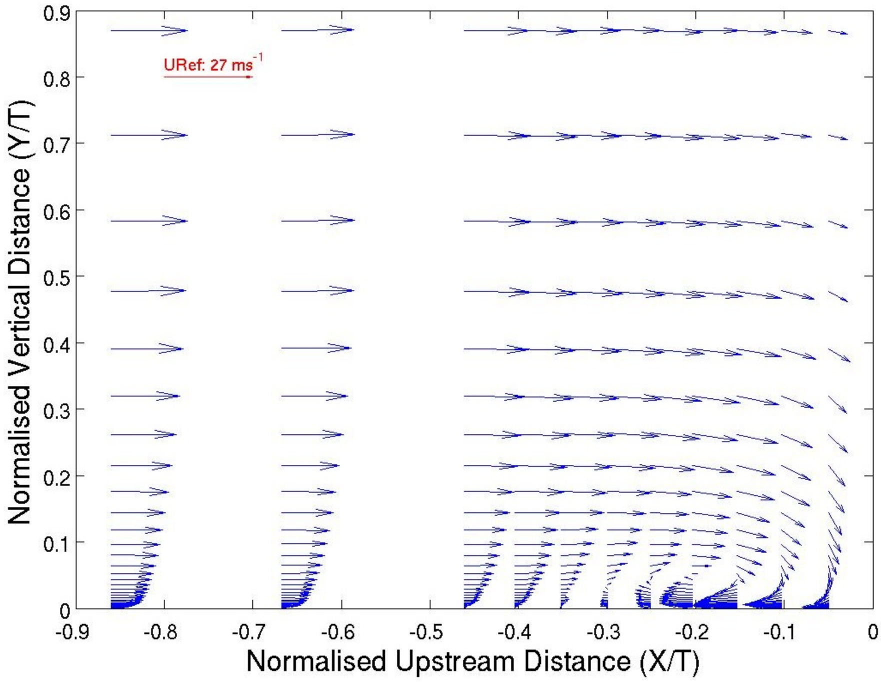

(a) Devenport and Simpson (1990) upwind symmetry plane velocity vector plot.

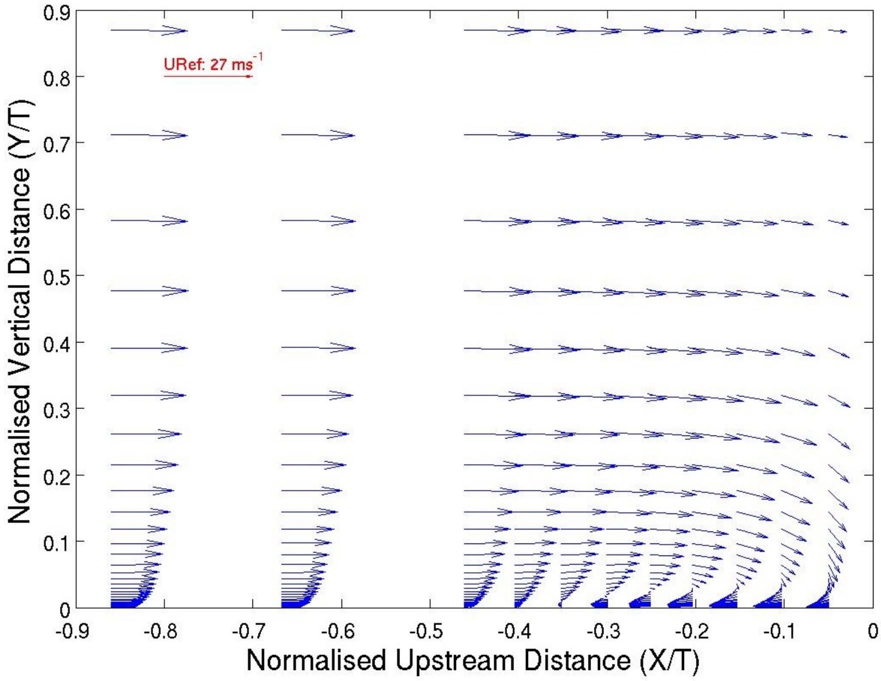

(b) RNG $k-\epsilon$ model upwind symmetry plane velocity vector plot.

Figure A.2: RNG $k-\epsilon$ model upwind symmetry plane velocity vector plot compared with Devenport and Simpson (1990) experiment.

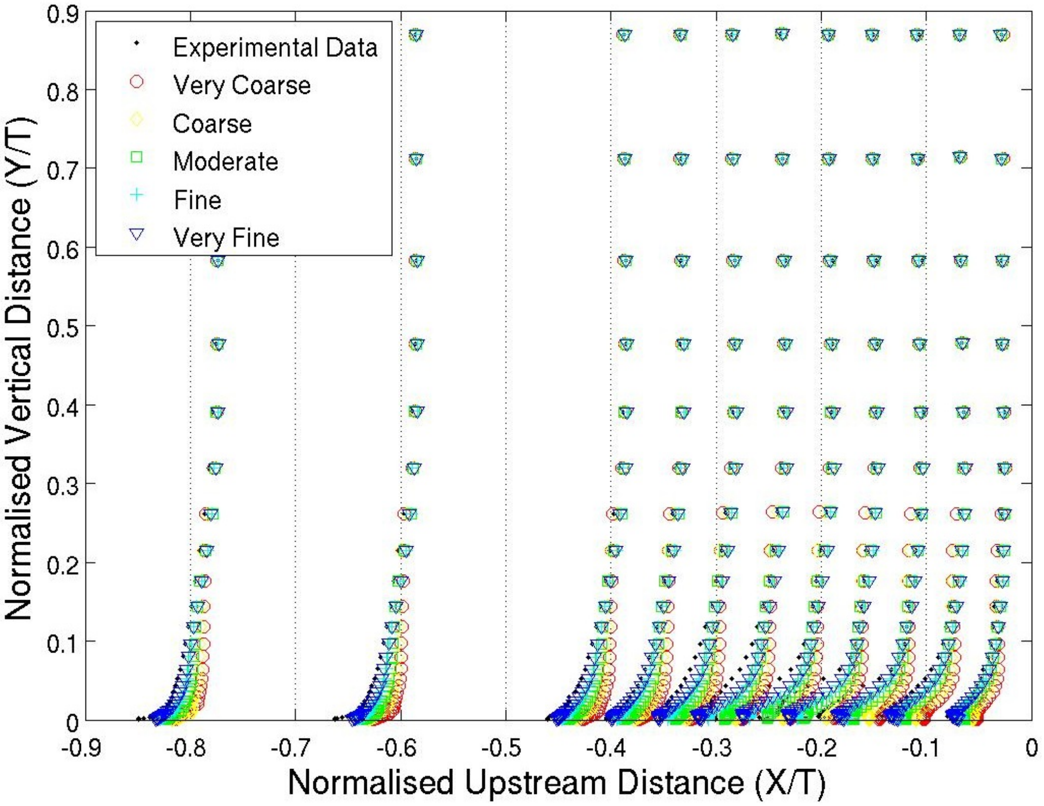

Figure A.3: RNG $k-\epsilon$ model grid dependence of upstream symmetry plane velocity profiles.

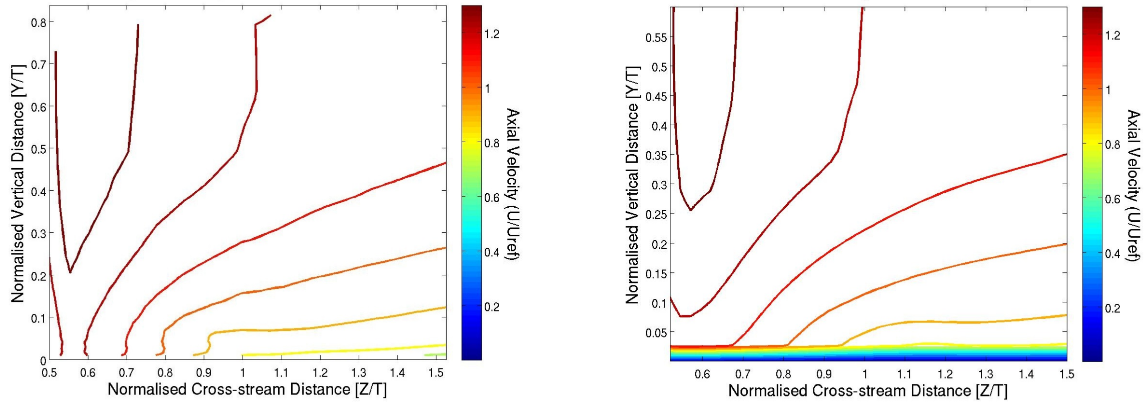

(a) Devenport and Simpson (1990) experiment plane 05 axial velocity contour plot.

(b) RNG $k - \epsilon$ model plane 05 axial velocity contour plot.

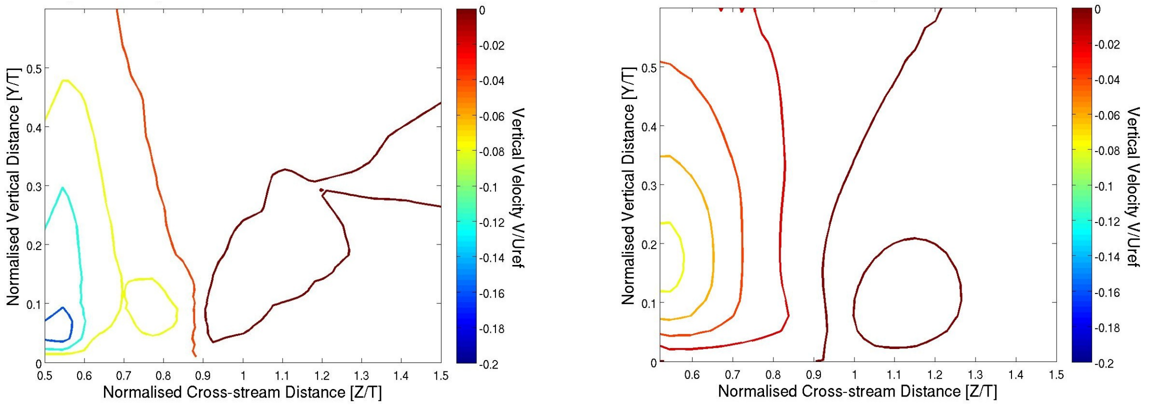

(c) Devenport and Simpson (1990) experiment plane 05 vertical velocity contour plot.

(d) RNG $k - \epsilon$ model plane 05 vertical velocity contour plot.

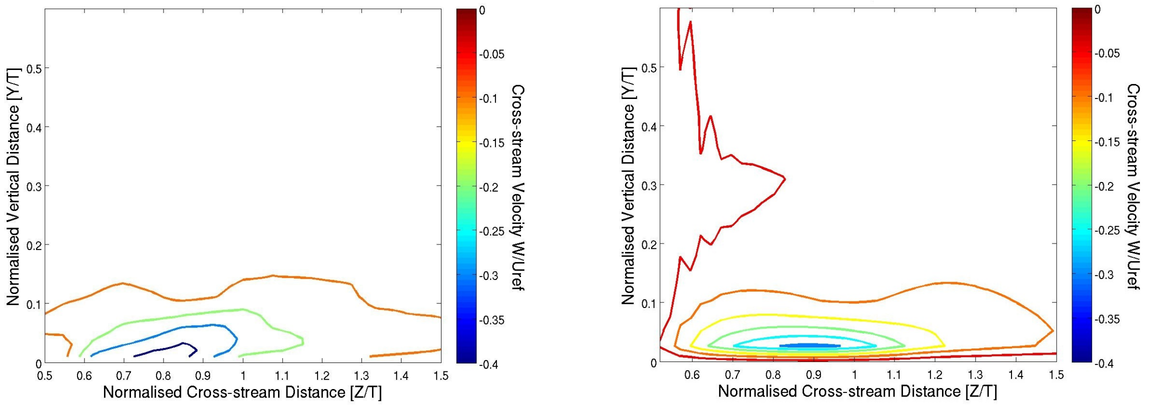

(e) Devenport and Simpson (1990) experiment plane 05 cross-stream velocity contour plot.

(f) RNG $k - \epsilon$ model plane 05 cross-stream velocity contour plot.

Figure A.4: RNG $k - \epsilon$ model plane 05 velocity contour plots compared with Devenport and Simpson (1990) experiment.

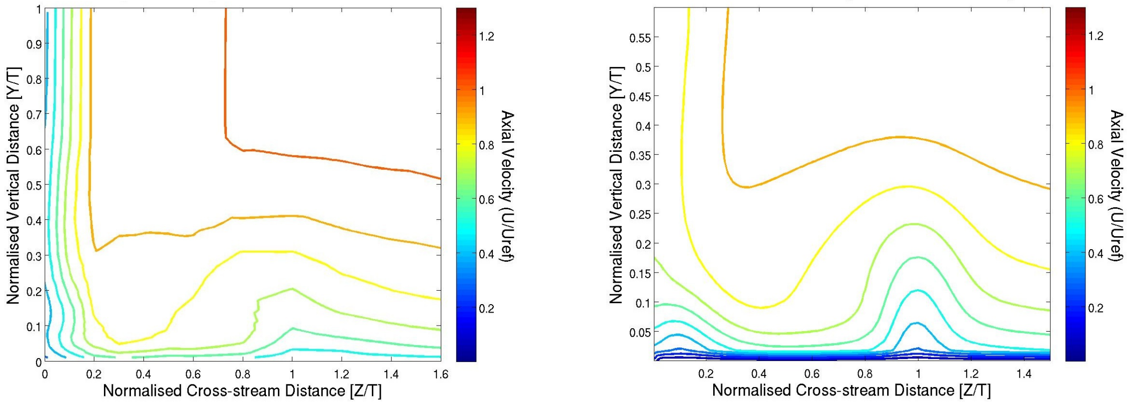

(a) Devenport and Simpson (1990) experiment plane 10 axial velocity contour plot.

(b) RNG $k-\epsilon$ model plane 10 axial velocity contour plot.

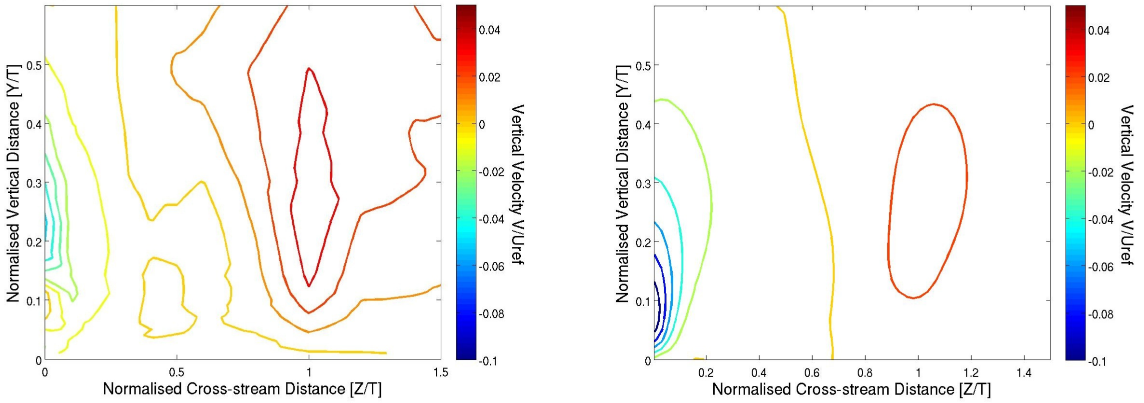

(c) Devenport and Simpson (1990) experiment plane 10 vertical velocity contour plot.

(d) RNG $k-\epsilon$ model plane 10 vertical velocity contour plot.

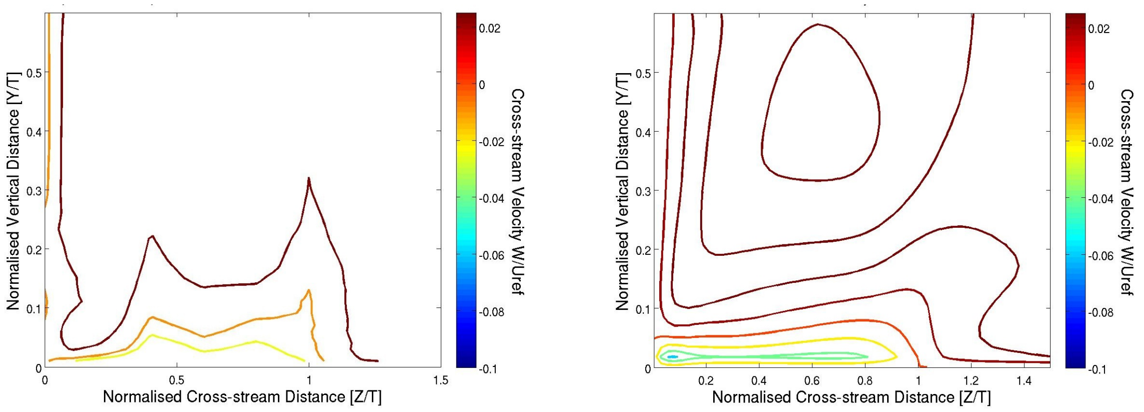

(e) Devenport and Simpson (1990) experiment plane 10 cross-stream velocity contour plot.

(f) RNG $k-\epsilon$ model plane 10 cross-stream velocity contour plot.

Figure A.5: RNG $k-\epsilon$ model plane 10 velocity contour plots compared with Devenport and Simpson (1990) experiment.

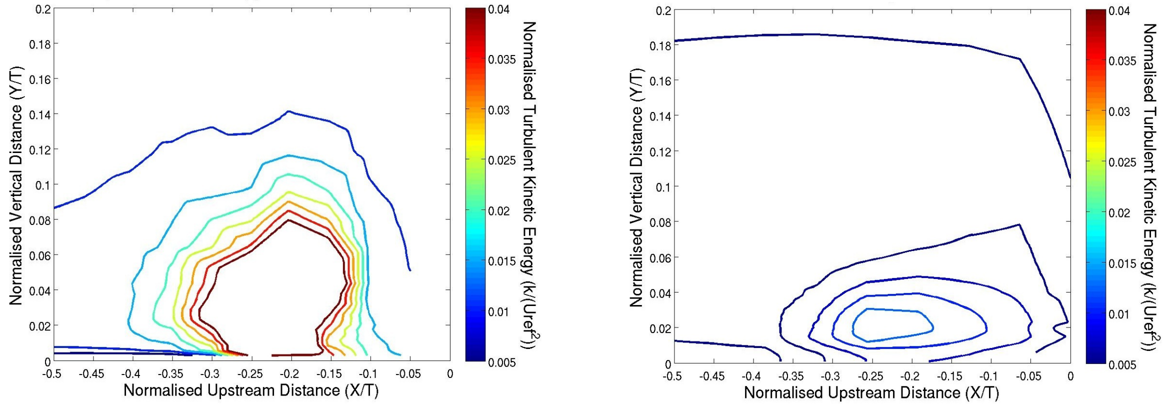

(a) Devenport and Simpson (1990) experiment upstream symmetry plane turbulent kinetic energy contour plot.

(b) RNG $k - \epsilon$ model upstream symmetry plane turbulent kinetic energy contour plot.

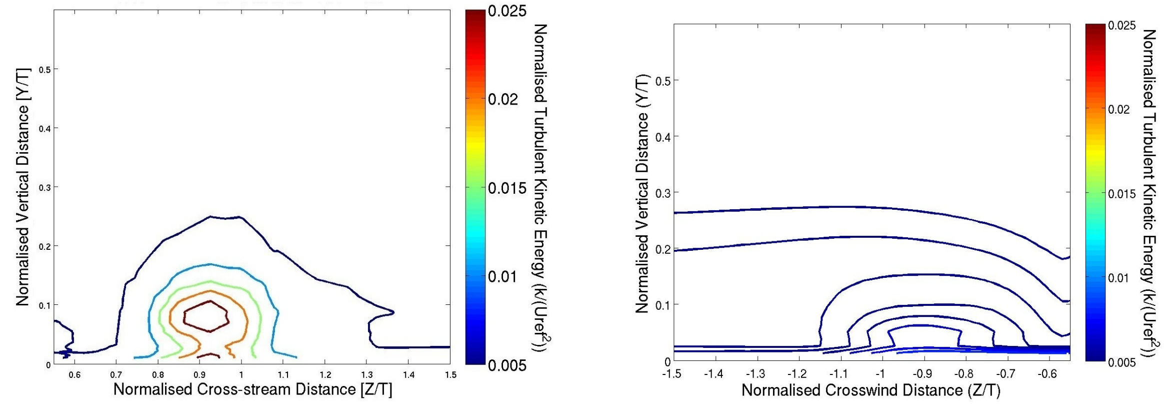

(c) Devenport and Simpson (1990) experiment plane 05 turbulent kinetic energy contour plot.

(d) RNG $k - \epsilon$ model plane 05 turbulent kinetic energy contour plot.

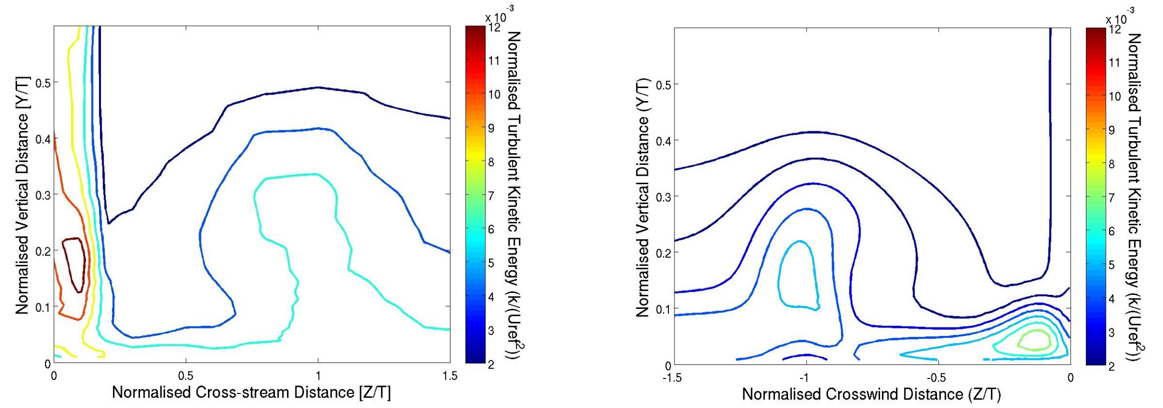

(e) Devenport and Simpson (1990) experiment plane 10 turbulent kinetic energy contour plot.

(f) RNG $k - \epsilon$ model plane 10 turbulent kinetic energy contour plot.

Figure A.6: RNG $k - \epsilon$ model turbulent kinetic energy contour plots compared with Devenport and Simpson (1990) experiment.

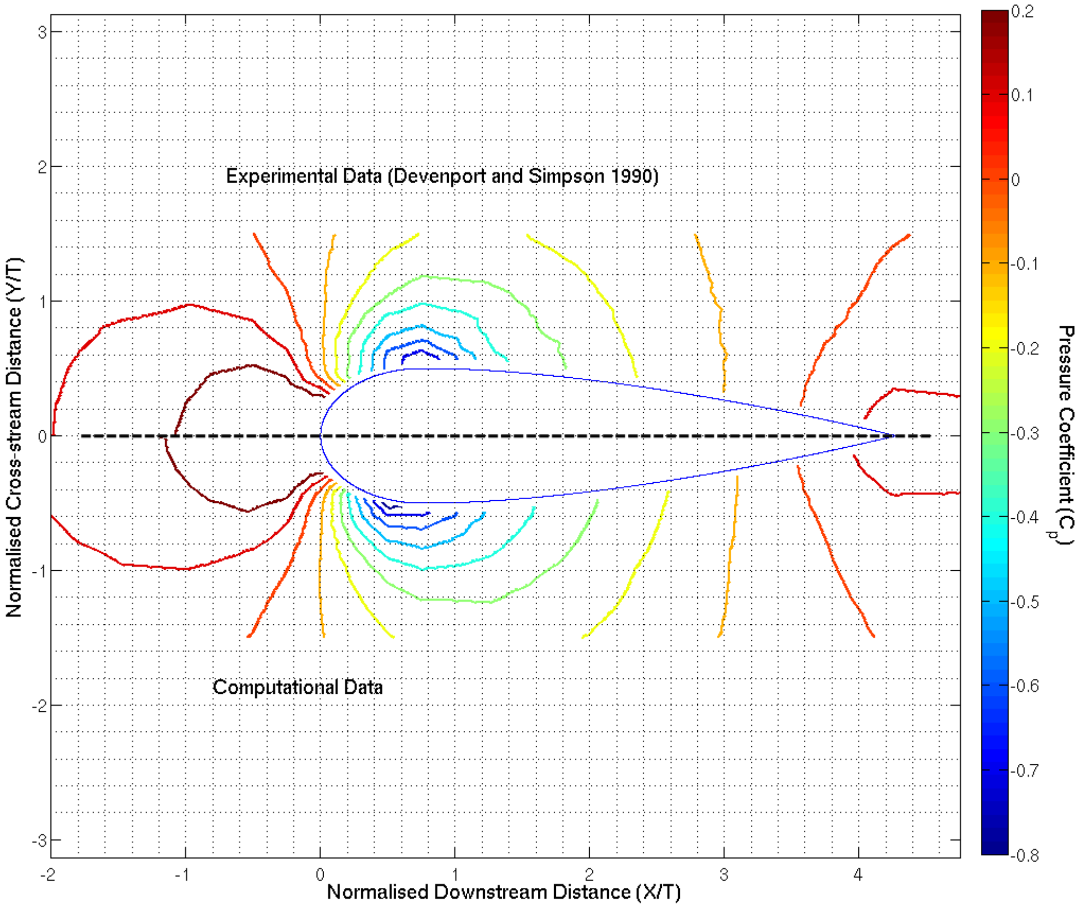

Figure A.7: Realisable $k - \epsilon$ model very-fine grid flat plate pressure coefficient plot.

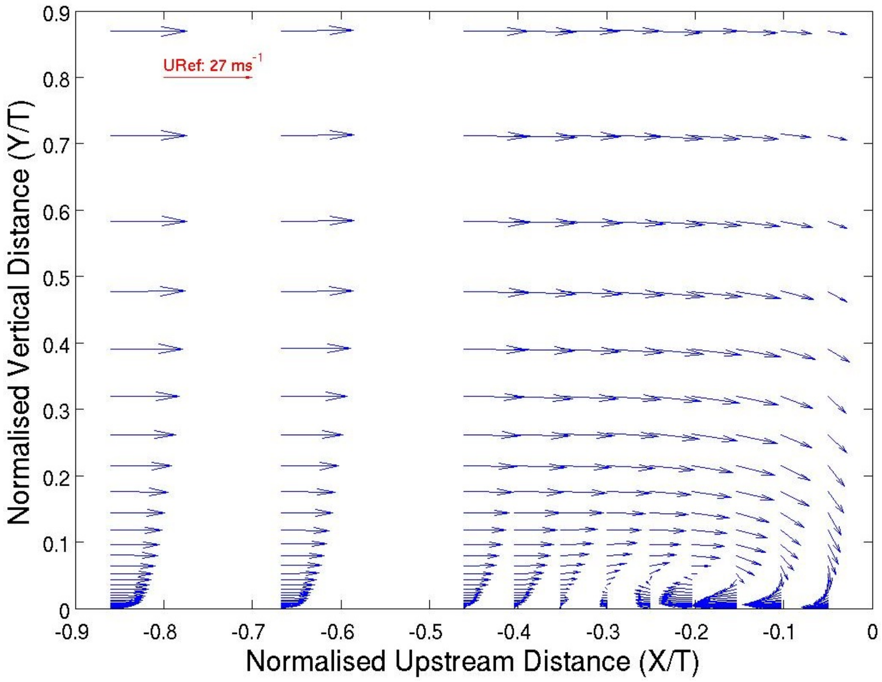

(a) Devenport and Simpson (1990) upwind symmetry plane velocity vector plot.

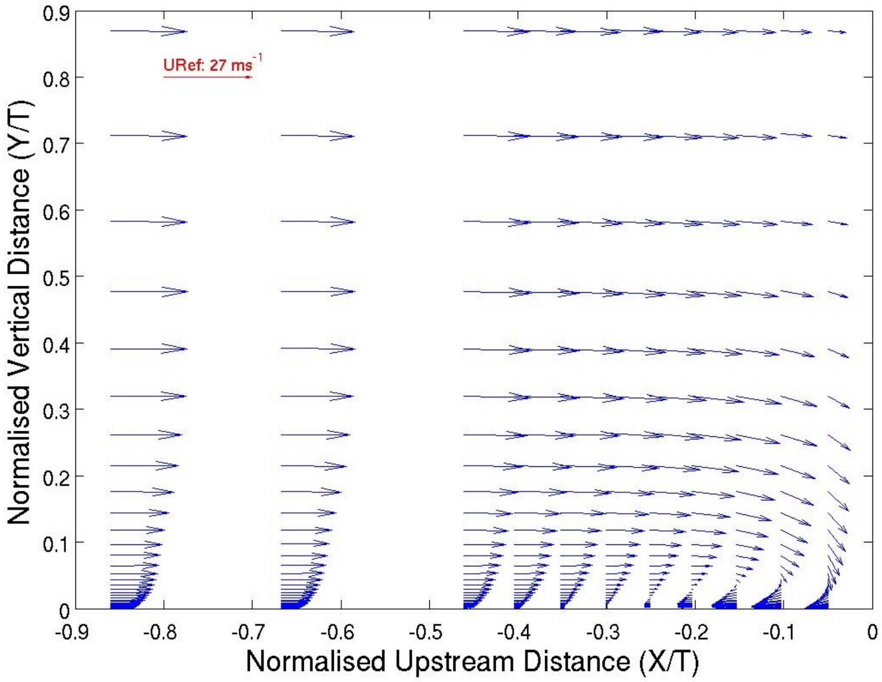

(b) Realisable $k - \epsilon$ model upwind symmetry plane velocity vector plot.

Figure A.8: Realisable $k - \epsilon$ model upwind symmetry plane velocity vector plot compared with Devenport and Simpson (1990) experiment.

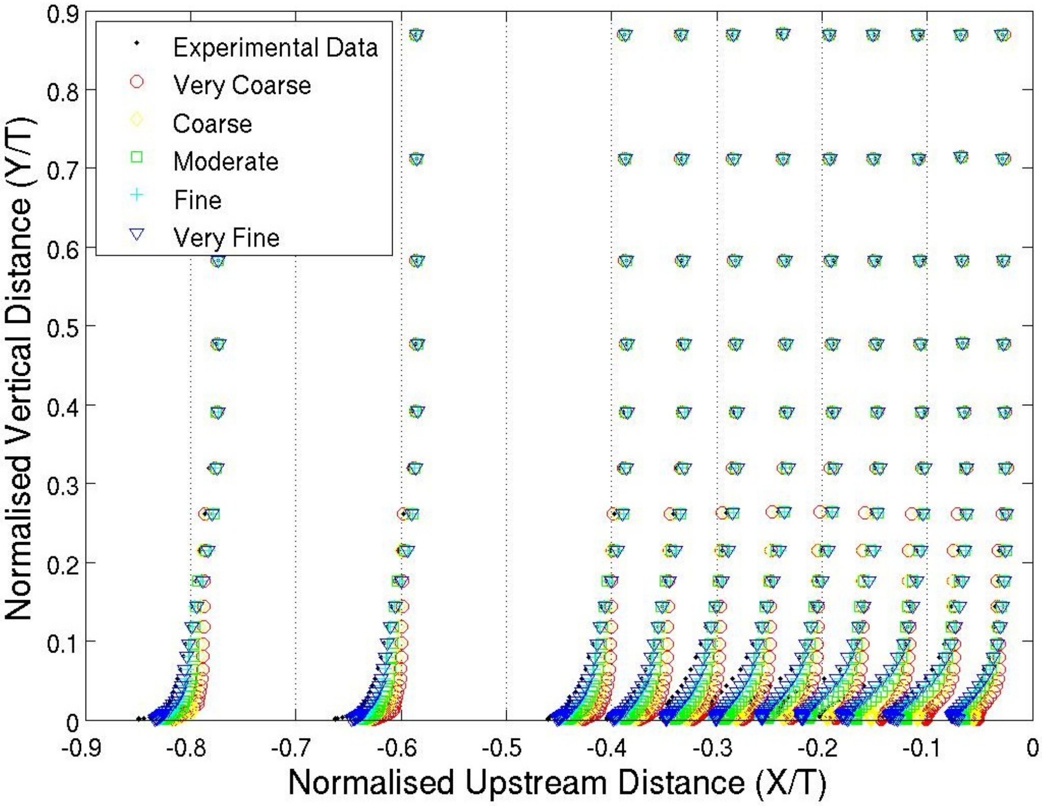

Figure A.9: Realisable $k-\epsilon$ model grid dependence of upstream symmetry plane velocity profiles.

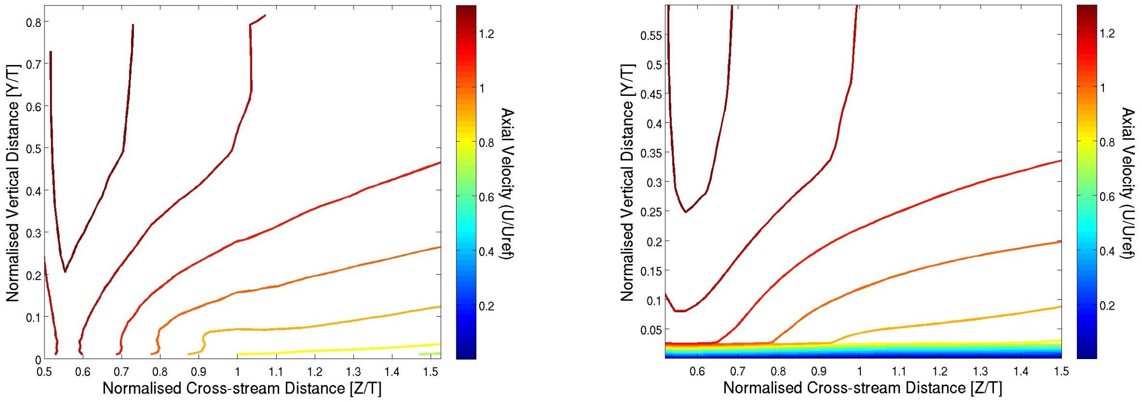

(a) Devenport and Simpson (1990) experiment plane 05 axial velocity contour plot.

(b) Realisable $k-\epsilon$ model plane 05 axial velocity contour plot.

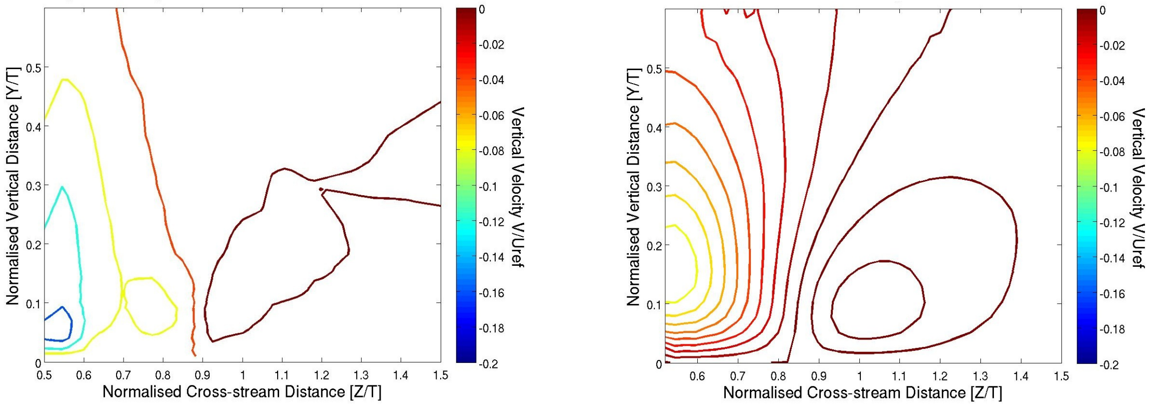

(c) Devenport and Simpson (1990) experiment plane 05 vertical velocity contour plot.

(d) Realisable $k-\epsilon$ model plane 05 vertical velocity contour plot.

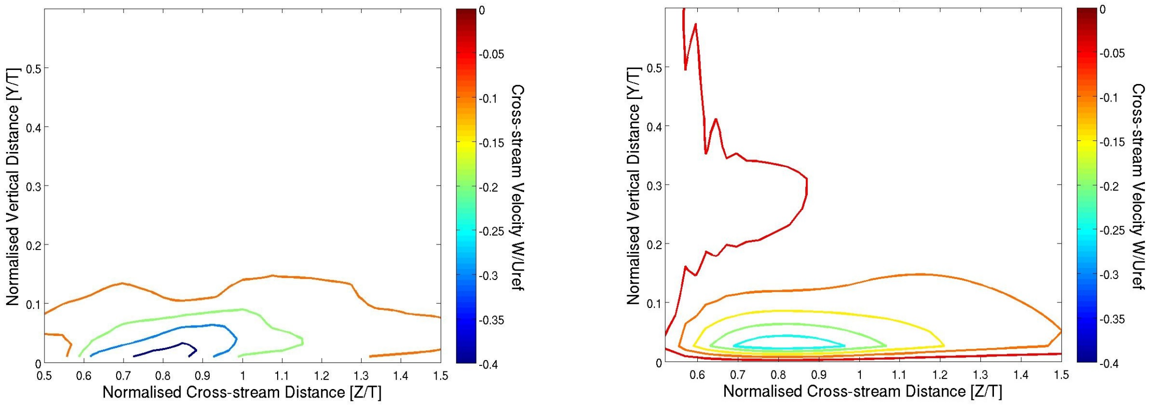

(e) Devenport and Simpson (1990) experiment plane 05 cross-stream velocity contour plot.

(f) Realisable $k-\epsilon$ model plane 05 cross-stream velocity contour plot.

Figure A.10: Realisable $k-\epsilon$ model plane 05 velocity contour plots compared with Devenport and Simpson (1990) experiment.

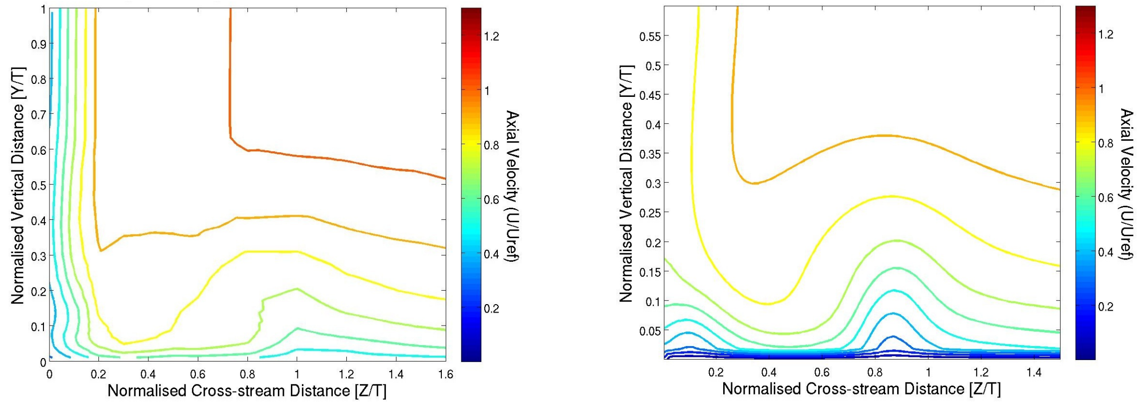

(a) Devenport and Simpson (1990) experiment plane 10 axial velocity contour plot.

(b) Realisable $k-\epsilon$ model plane 10 axial velocity contour plot.

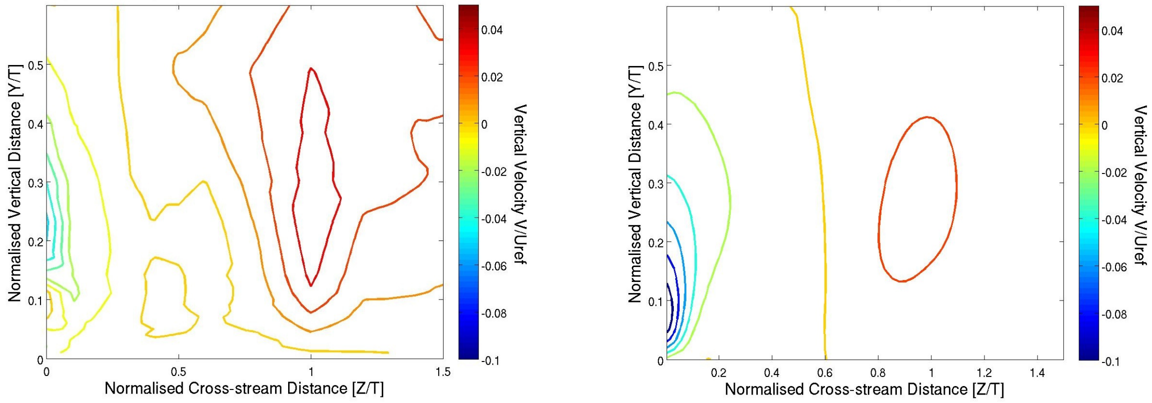

(c) Devenport and Simpson (1990) experiment plane 10 vertical velocity contour plot.

(d) Realisable $k-\epsilon$ model plane 10 vertical velocity contour plot.

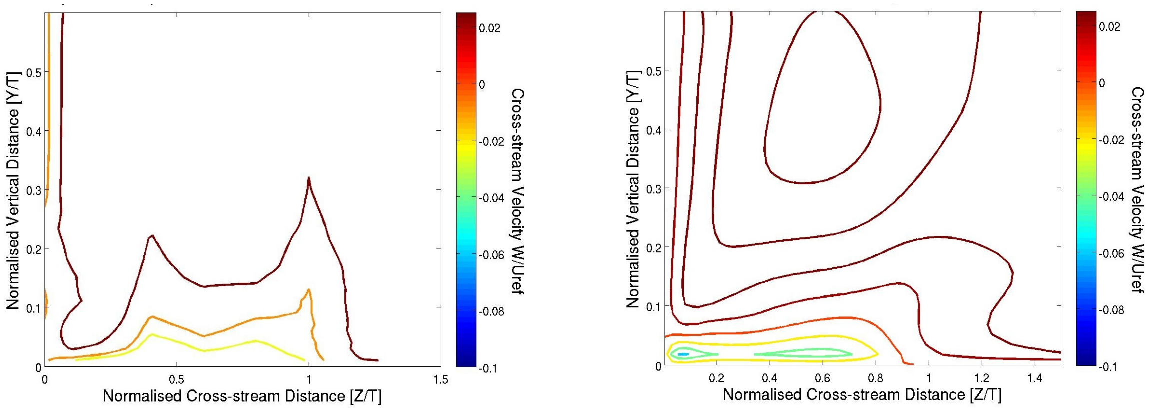

(e) Devenport and Simpson (1990) experiment plane 10 cross-stream velocity contour plot.

(f) Realisable $k-\epsilon$ model plane 10 cross-stream velocity contour plot.

Figure A.11: Realisable $k-\epsilon$ model plane 10 velocity contour plots compared with Devenport and Simpson (1990) experiment.

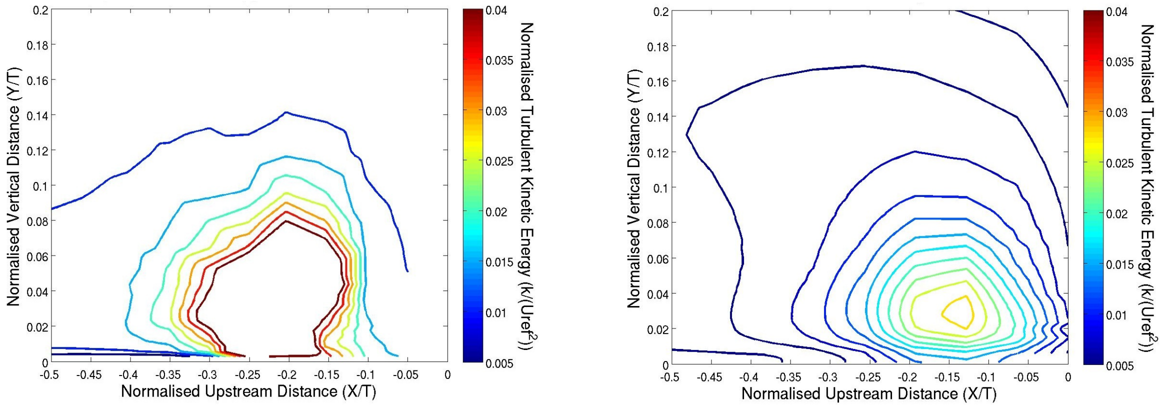

(a) Devenport and Simpson (1990) experiment upstream symmetry plane turbulent kinetic energy contour plot.

(b) Realisable $k-\epsilon$ model upstream symmetry plane turbulent kinetic energy contour plot.

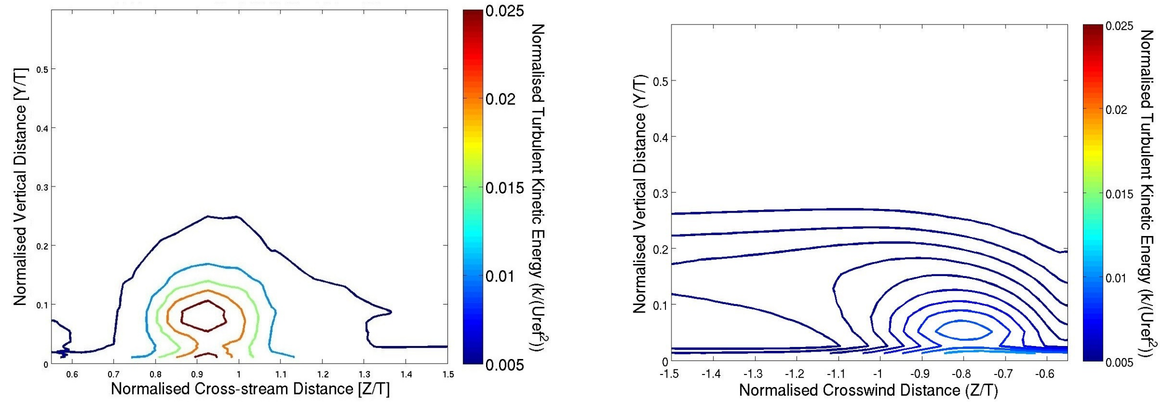

(c) Devenport and Simpson (1990) experiment plane 05 turbulent kinetic energy contour plot.

(d) Realisable $k-\epsilon$ model plane 05 turbulent kinetic energy contour plot.

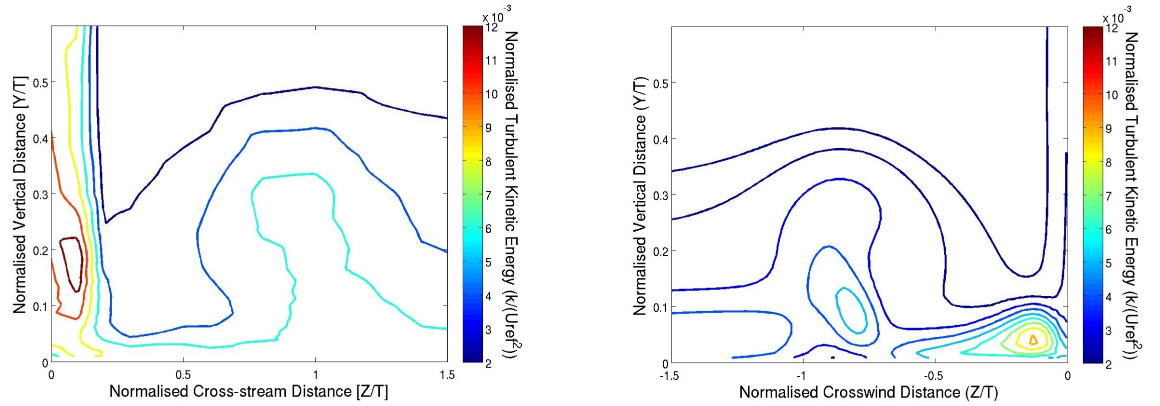

(e) Devenport and Simpson (1990) experiment plane 10 turbulent kinetic energy contour plot.

(f) Realisable $k-\epsilon$ model plane 10 turbulent kinetic energy contour plot.

Figure A.12: Realisable $k-\epsilon$ model turbulent kinetic energy contour plots compared with Devenport and Simpson (1990) experiment.

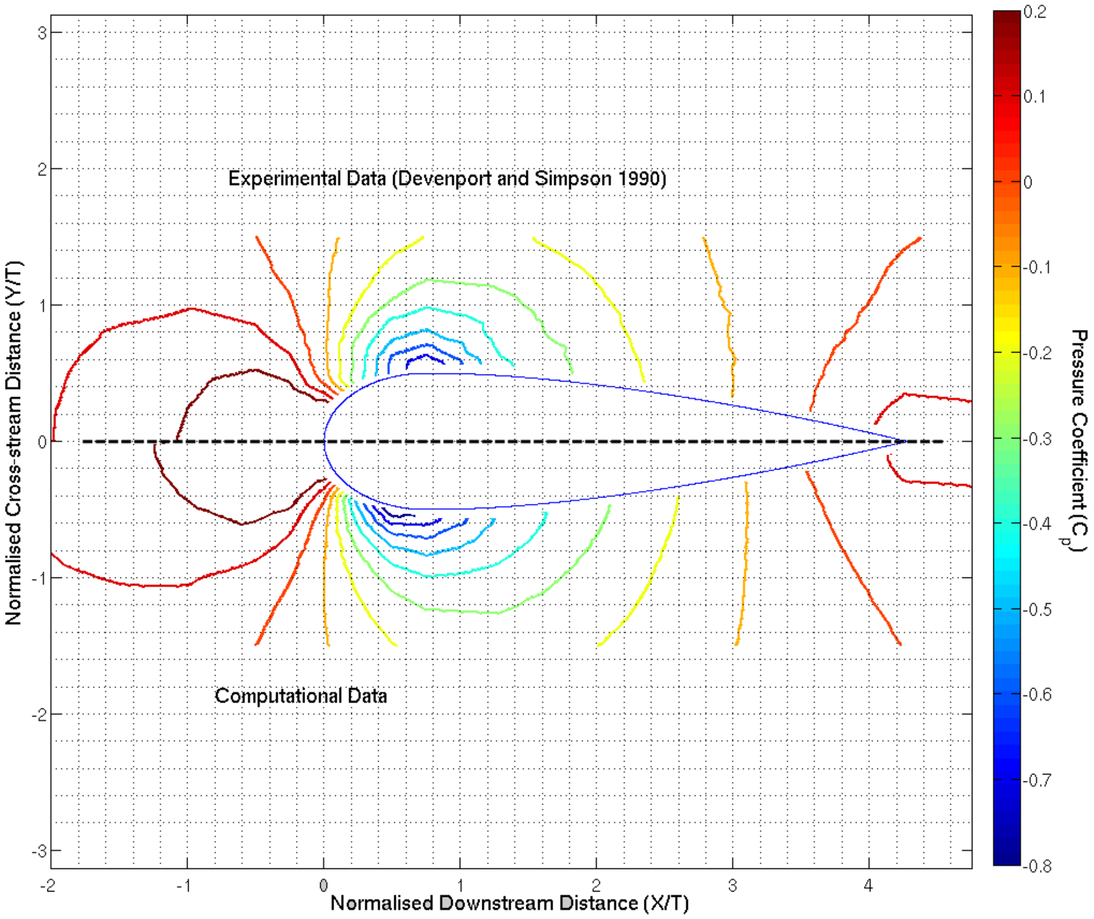

Figure A.13: $k-\omega$ model very-fine grid flat plate pressure coefficient plot.

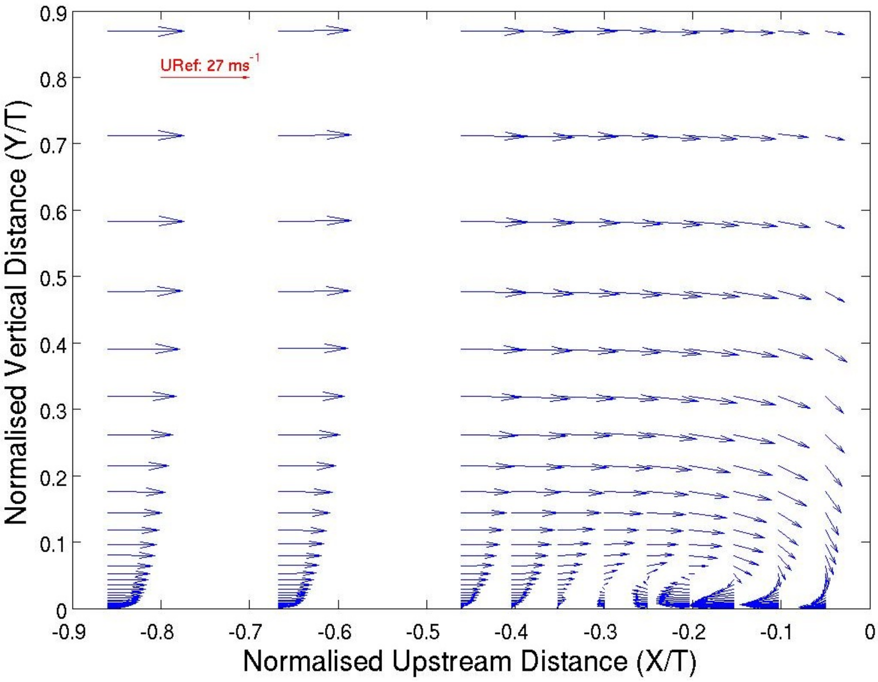

(a) Devenport and Simpson (1990) upwind symmetry plane velocity vector plot.

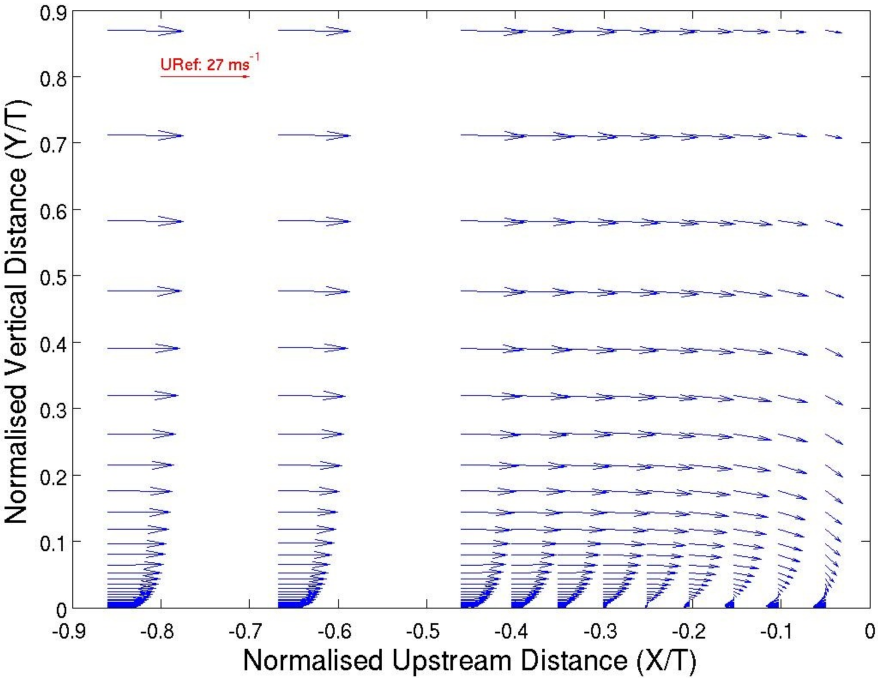

(b) $k-\omega$ model upwind symmetry plane velocity vector plot.

Figure A.14: $k-\omega$ model upwind symmetry plane velocity vector plot compared with Devenport and Simpson (1990) experiment.

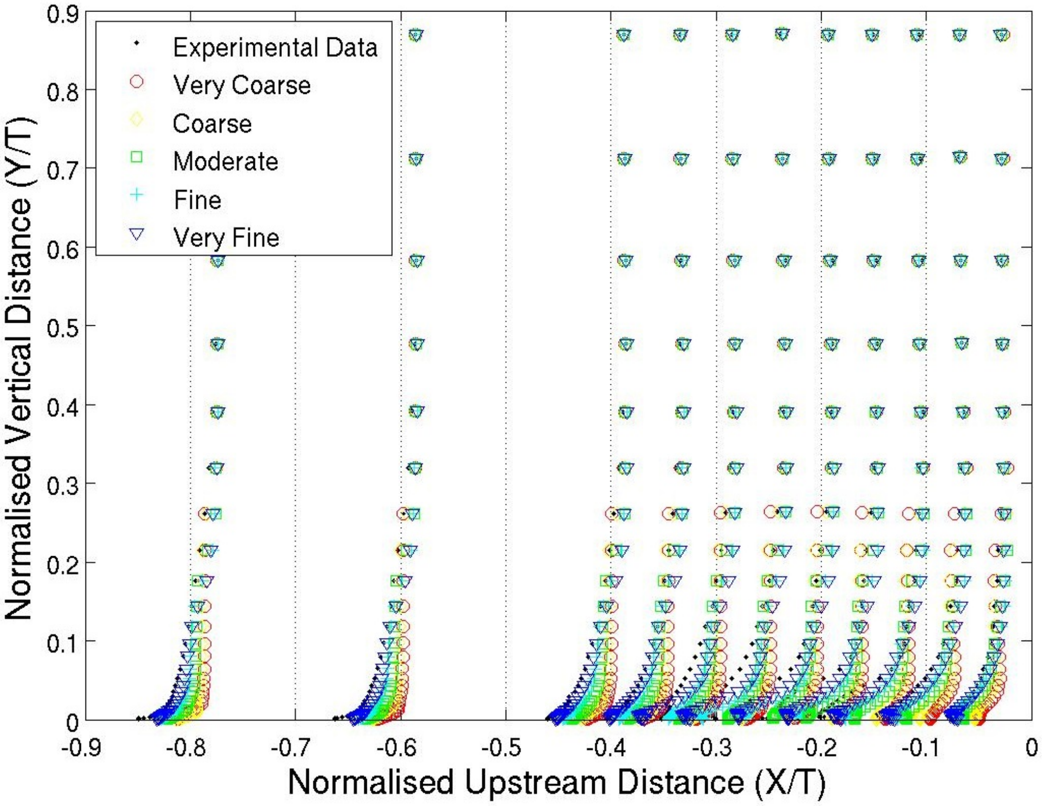

Figure A.15: $k - \omega$ model grid dependence of upstream symmetry plane velocity profiles.

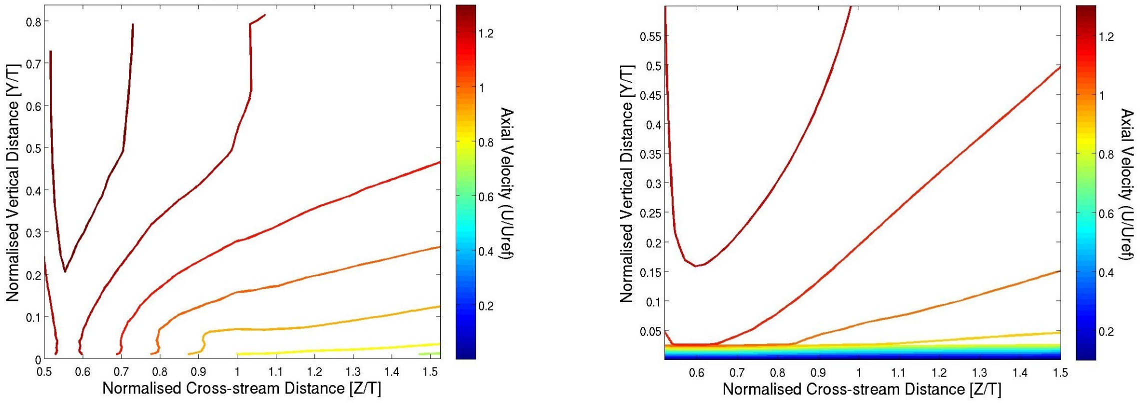

(a) Devenport and Simpson (1990) experiment plane 05 axial velocity contour plot.

(b) $k - \omega$ model plane 05 axial velocity contour plot.

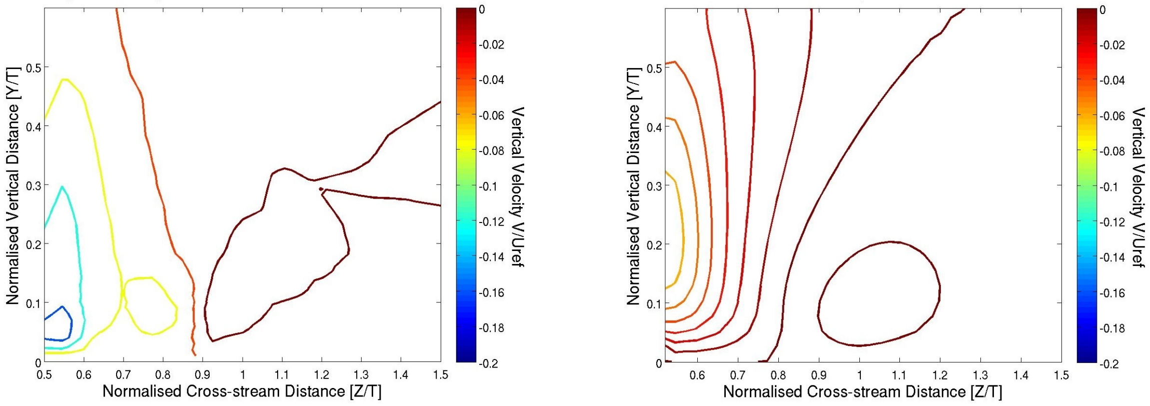

(c) Devenport and Simpson (1990) experiment plane 05 vertical velocity contour plot.

(d) $k - \omega$ model plane 05 vertical velocity contour plot.

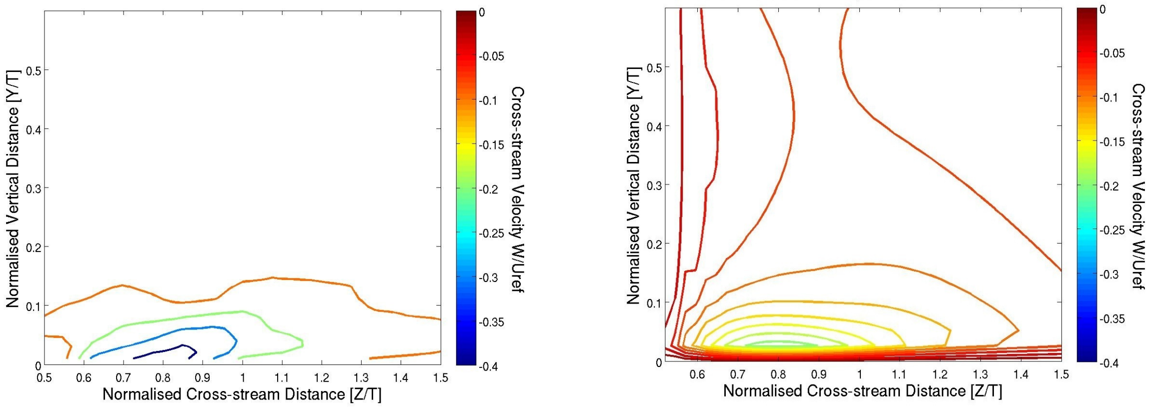

(e) Devenport and Simpson (1990) experiment plane 05 cross-stream velocity contour plot.

(f) $k - \omega$ model plane 05 cross-stream velocity contour plot.

Figure A.16: $k - \omega$ model plane 05 velocity contour plots compared with Devenport and Simpson (1990) experiment.

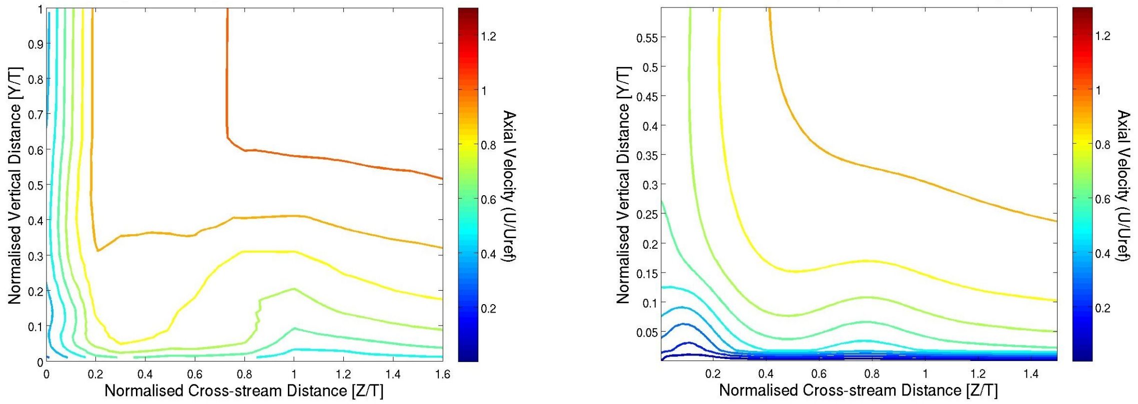

(a) Devenport and Simpson (1990) experiment plane 10 axial velocity contour plot.

(b) $k-\omega$ model plane 10 axial velocity contour plot.

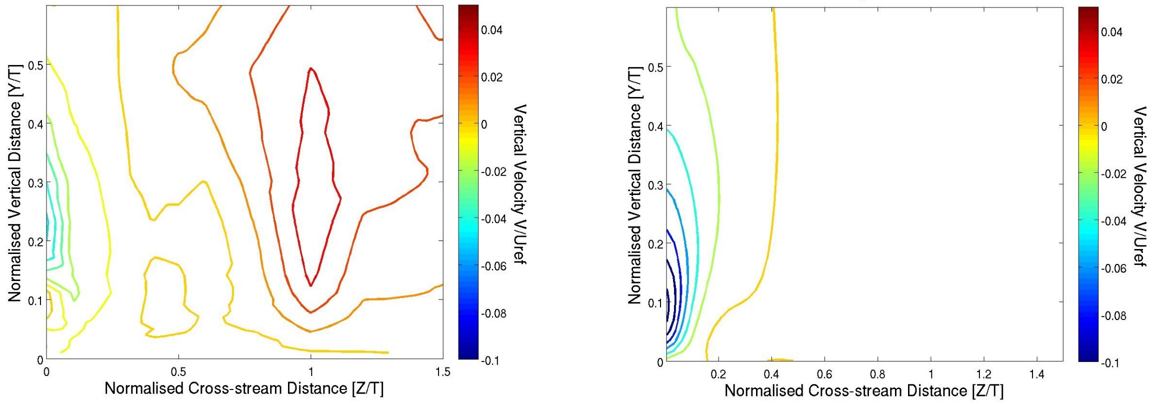

(c) Devenport and Simpson (1990) experiment plane 10 vertical velocity contour plot.

(d) $k-\omega$ model plane 10 vertical velocity contour plot.

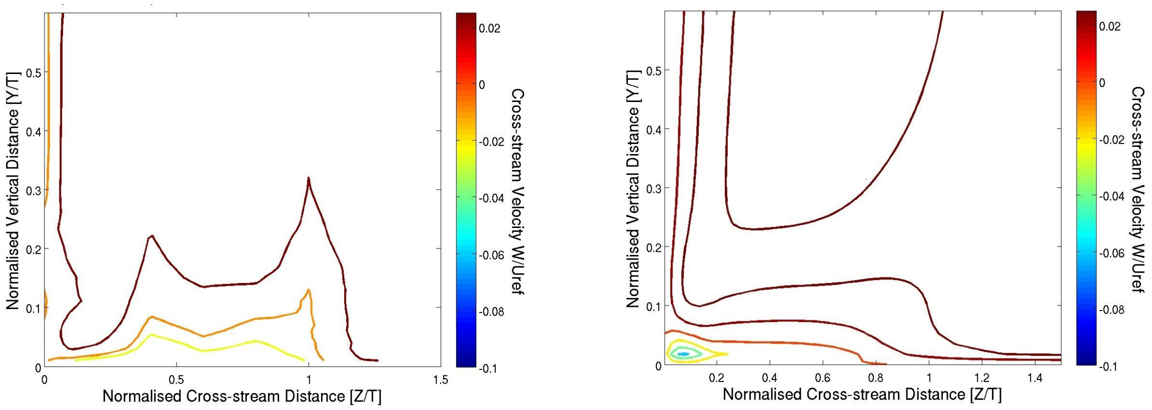

(e) Devenport and Simpson (1990) experiment plane 10 cross-stream velocity contour plot.

(f) $k-\omega$ model plane 10 cross-stream velocity contour plot.

Figure A.17: $k-\omega$ model plane 10 velocity contour plots compared with Devenport and Simpson (1990) experiment.

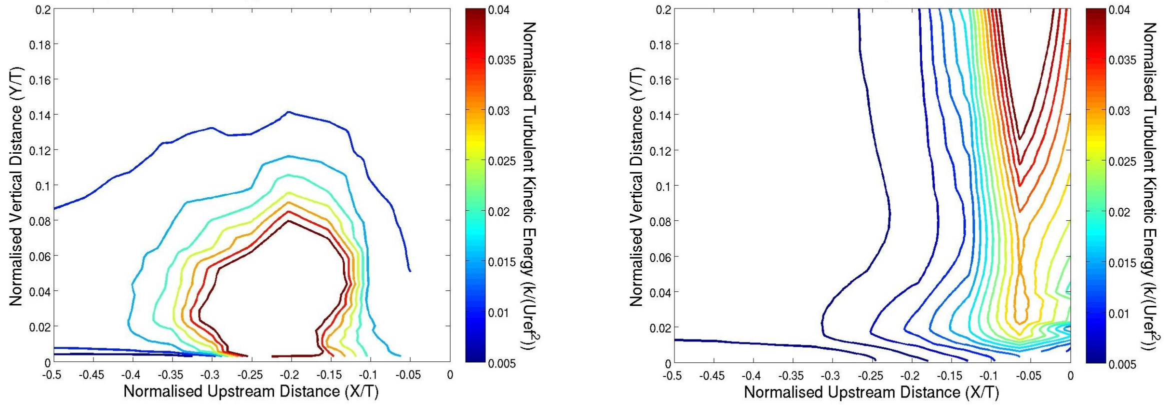

(a) Devenport and Simpson (1990) experiment upstream symmetry plane turbulent kinetic energy contour plot.

(b) $k-\omega$ model upstream symmetry plane turbulent kinetic energy contour plot.

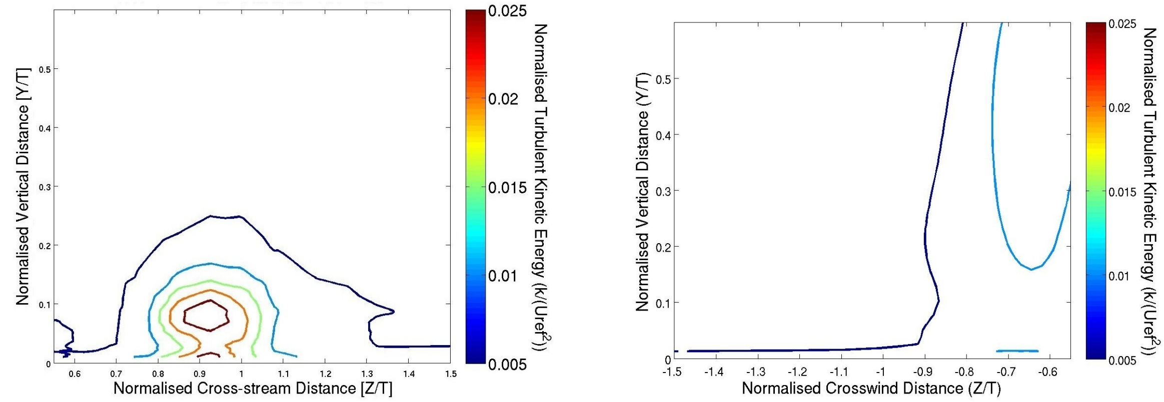

(c) Devenport and Simpson (1990) experiment plane 05 turbulent kinetic energy contour plot.

(d) $k-\omega$ model plane 05 turbulent kinetic energy contour plot.

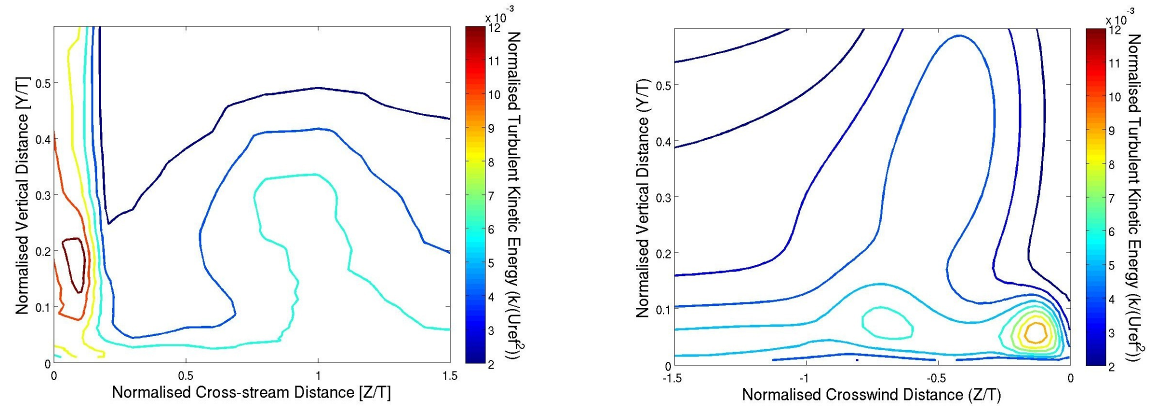

(e) Devenport and Simpson (1990) experiment plane 10 turbulent kinetic energy contour plot.

(f) $k-\omega$ model plane 10 turbulent kinetic energy contour plot.

Figure A.18: $k-\omega$ model turbulent kinetic energy contour plots compared with Devenport and Simpson (1990) experiment.

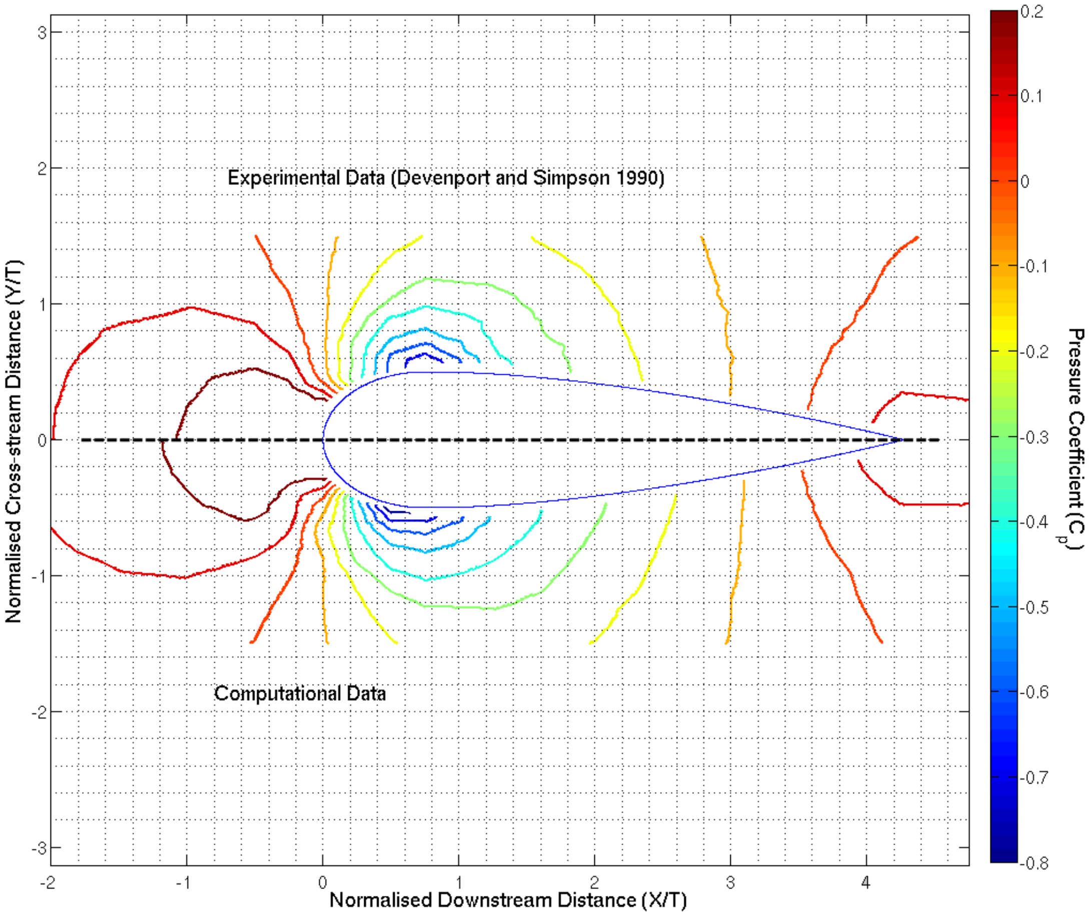

Figure A.19: $k - \omega$ SST model very-fine grid flat plate pressure coefficient plot.

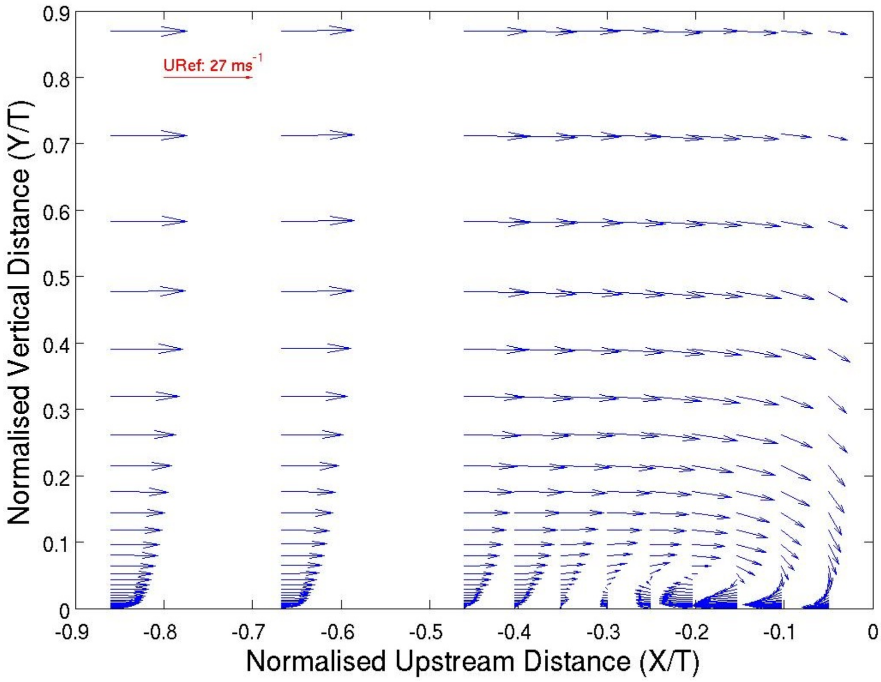

(a) Devenport and Simpson (1990) upwind symmetry plane velocity vector plot.

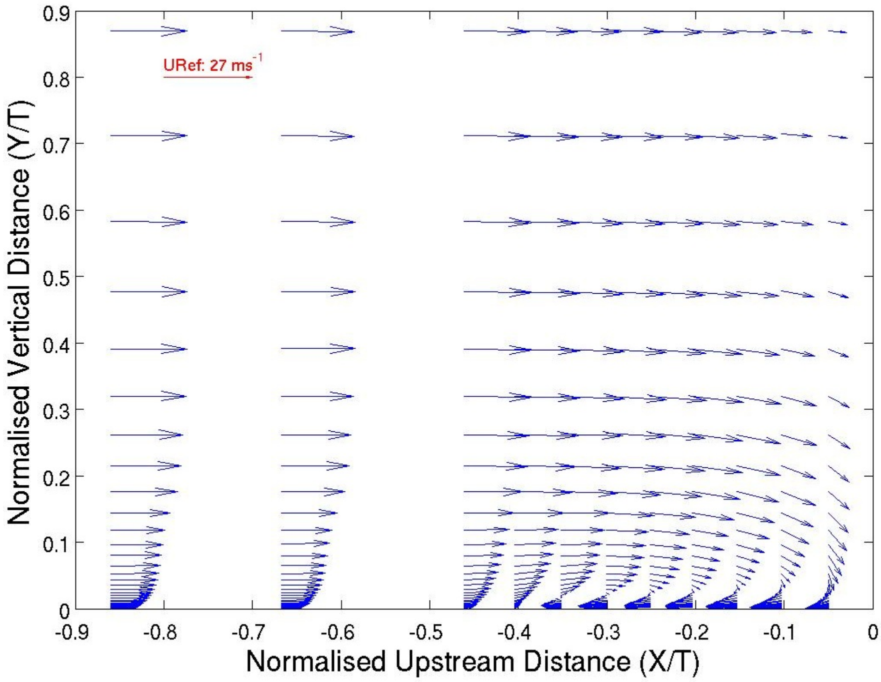

(b) $k-\omega$ SST model upwind symmetry plane velocity vector plot.

Figure A.20: $k-\omega$ SST model upwind symmetry plane velocity vector plot compared with Devenport and Simpson (1990) experiment.

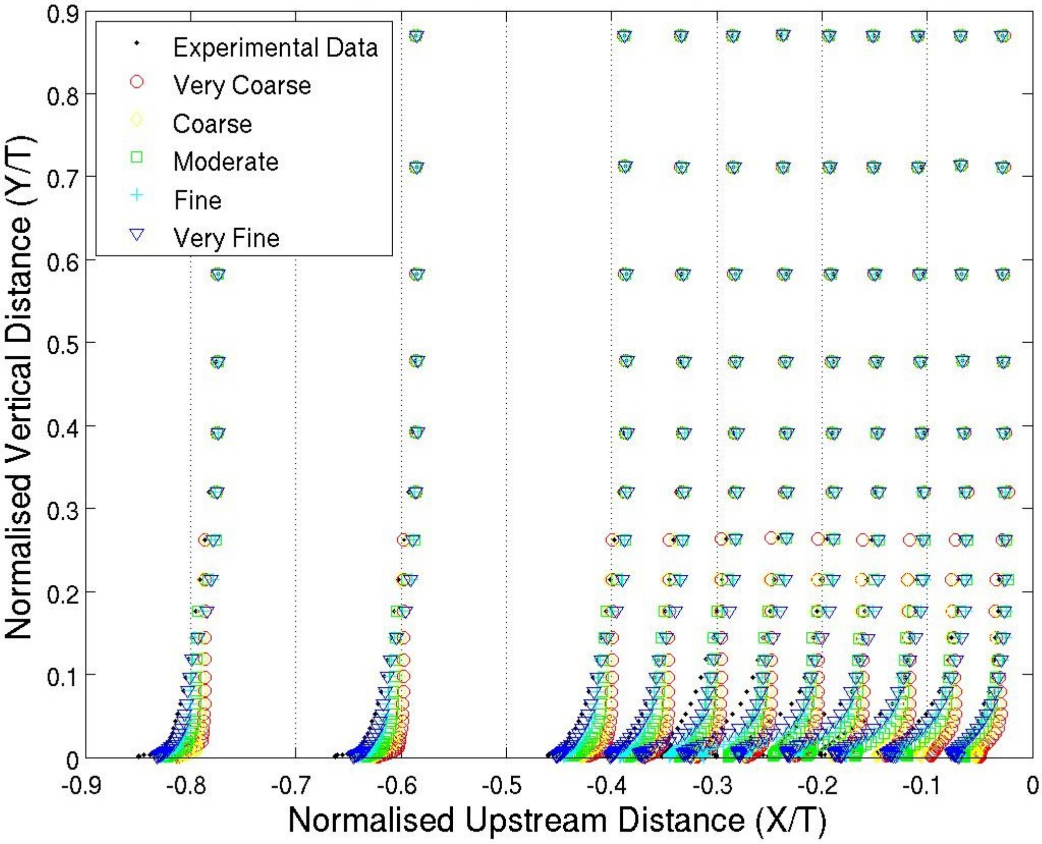

Figure A.21: $k-\omega$ model grid dependence of upstream symmetry plane velocity profiles.

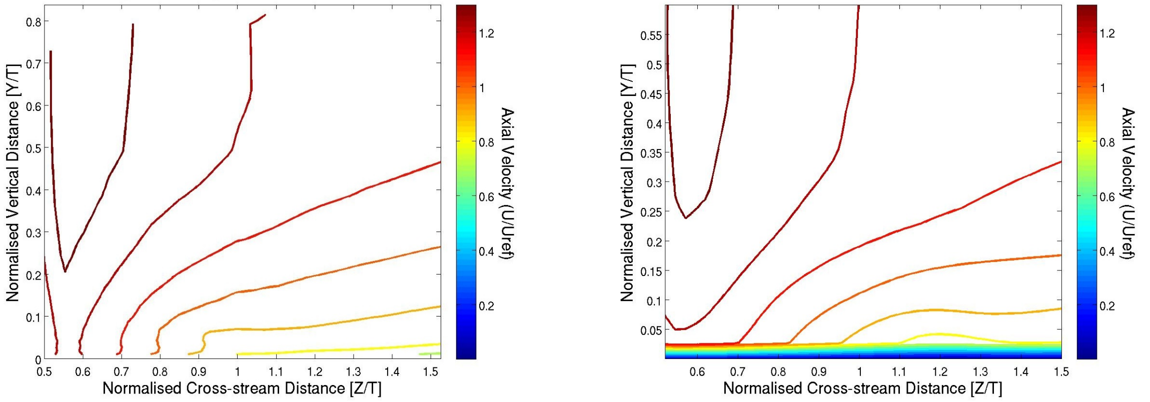

(a) Devenport and Simpson (1990) experiment plane 05 axial velocity contour plot.

(b) $k-\omega$ SST model plane 05 axial velocity contour plot.

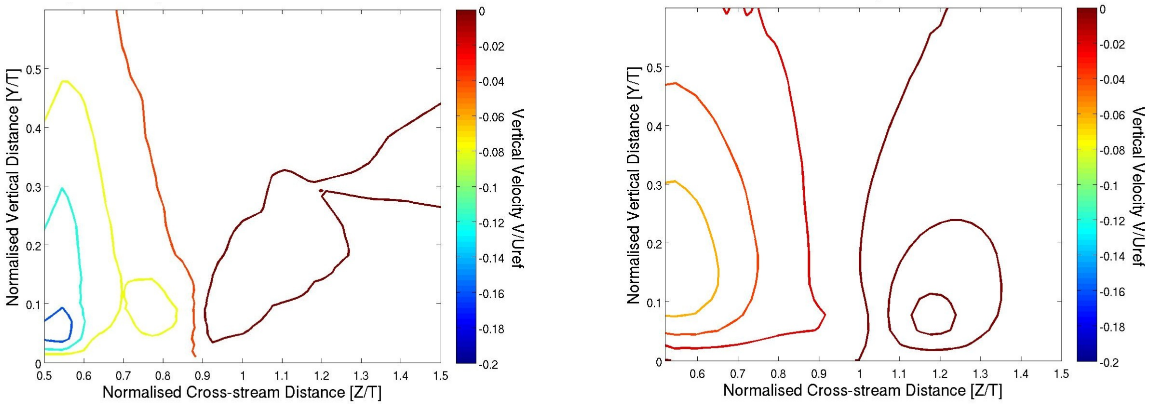

(c) Devenport and Simpson (1990) experiment plane 05 vertical velocity contour plot.

(d) $k-\omega$ SST model plane 05 vertical velocity contour plot.

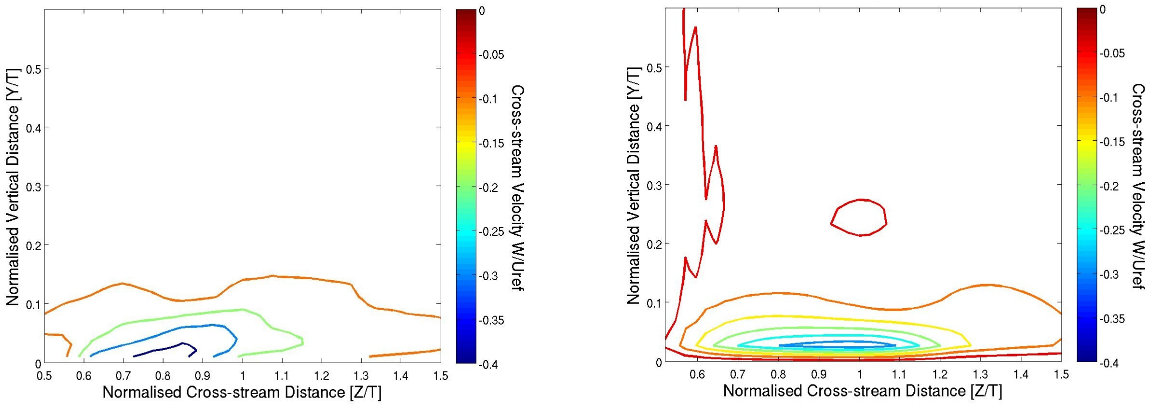

(e) Devenport and Simpson (1990) experiment plane 05 cross-stream velocity contour plot.

(f) $k-\omega$ SST model plane 05 cross-stream velocity contour plot.

Figure A.22: $k-\omega$ SST model plane 05 velocity contour plots compared with Devenport and Simpson (1990) experiment.

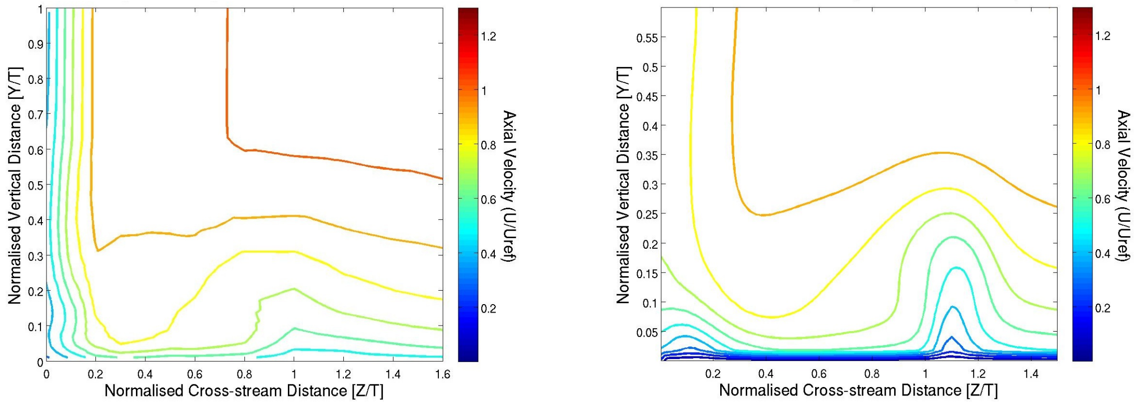

(a) Devenport and Simpson (1990) experiment plane 10 axial velocity contour plot.

(b) $k-\omega$ SST model plane 10 axial velocity contour plot.

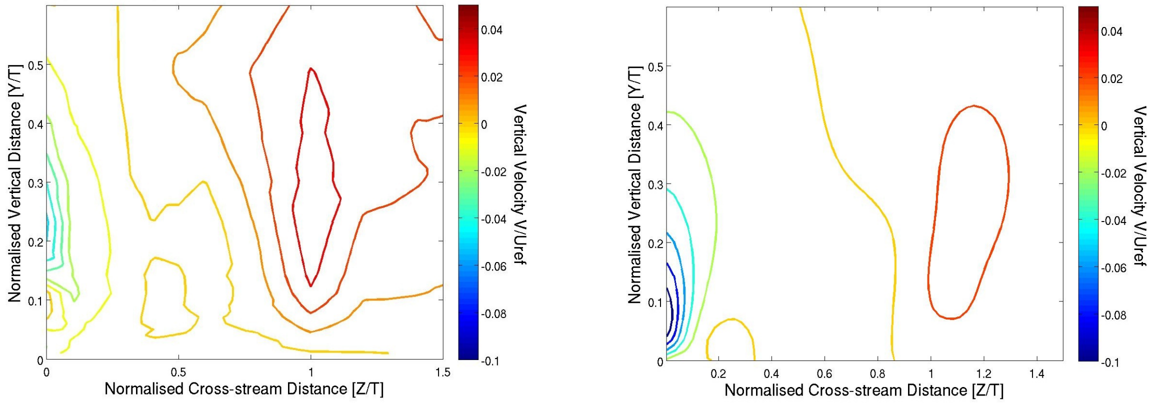

(c) Devenport and Simpson (1990) experiment plane 10 vertical velocity contour plot.

(d) $k-\omega$ SST model plane 10 vertical velocity contour plot.

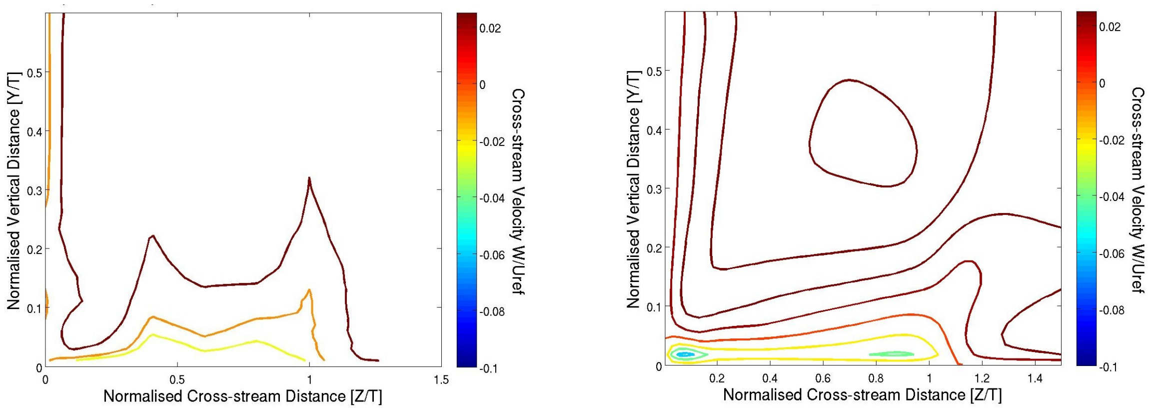

(e) Devenport and Simpson (1990) experiment plane 10 cross-stream velocity contour plot.

(f) $k-\omega$ SST model plane 10 cross-stream velocity contour plot.

Figure A.23: $k-\omega$ SST model plane 10 velocity contour plots compared with Devenport and Simpson (1990) experiment.

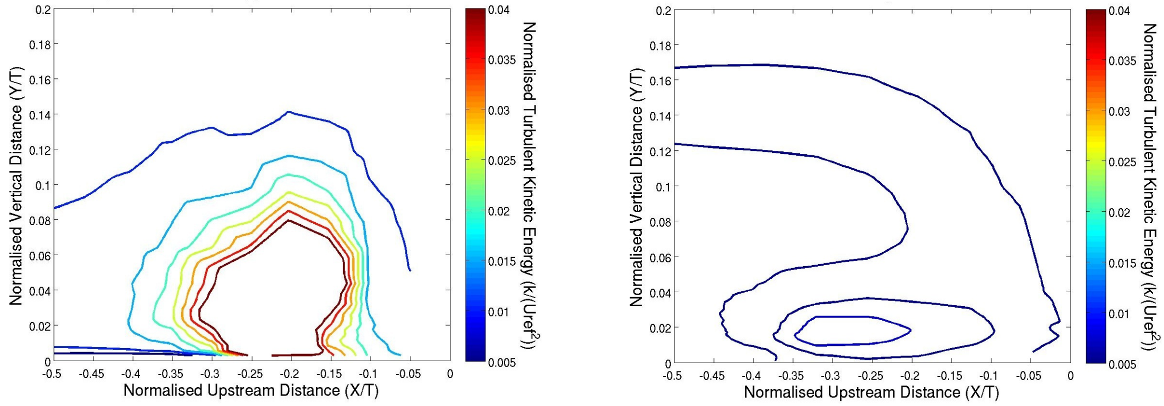

(a) Devenport and Simpson (1990) experiment upstream symmetry plane turbulent kinetic energy contour plot.

(b) $k-\omega$ SST model upstream symmetry plane turbulent kinetic energy contour plot.

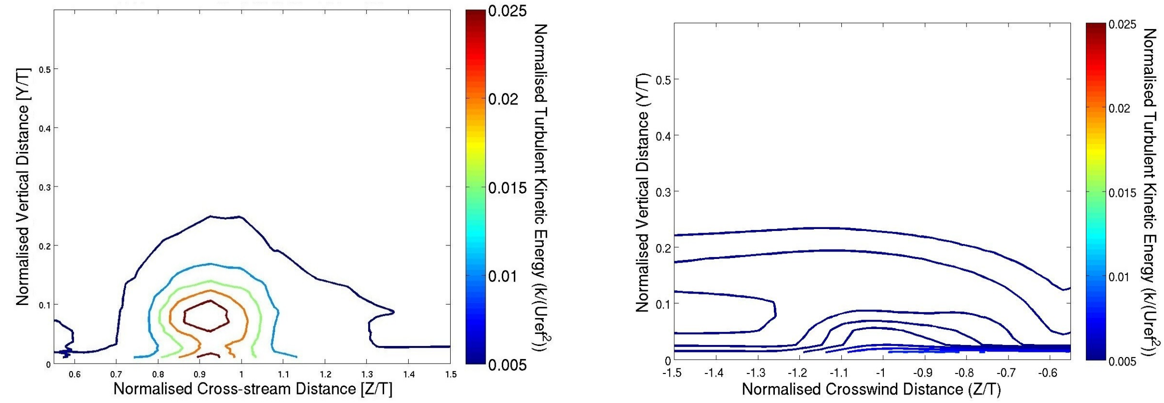

(c) Devenport and Simpson (1990) experiment plane 05 turbulent kinetic energy contour plot.

(d) $k-\omega$ SST model plane 05 turbulent kinetic energy contour plot.

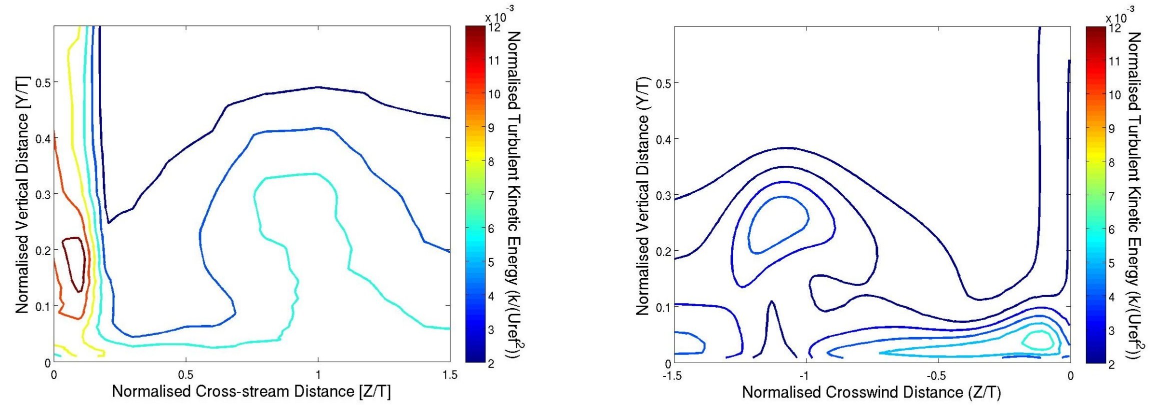

(e) Devenport and Simpson (1990) experiment plane 10 turbulent kinetic energy contour plot.

(f) $k-\omega$ SST model plane 10 turbulent kinetic energy contour plot.

Figure A.24: $k-\omega$ SST model turbulent kinetic energy contour plots compared with Devenport and Simpson (1990) experiment.

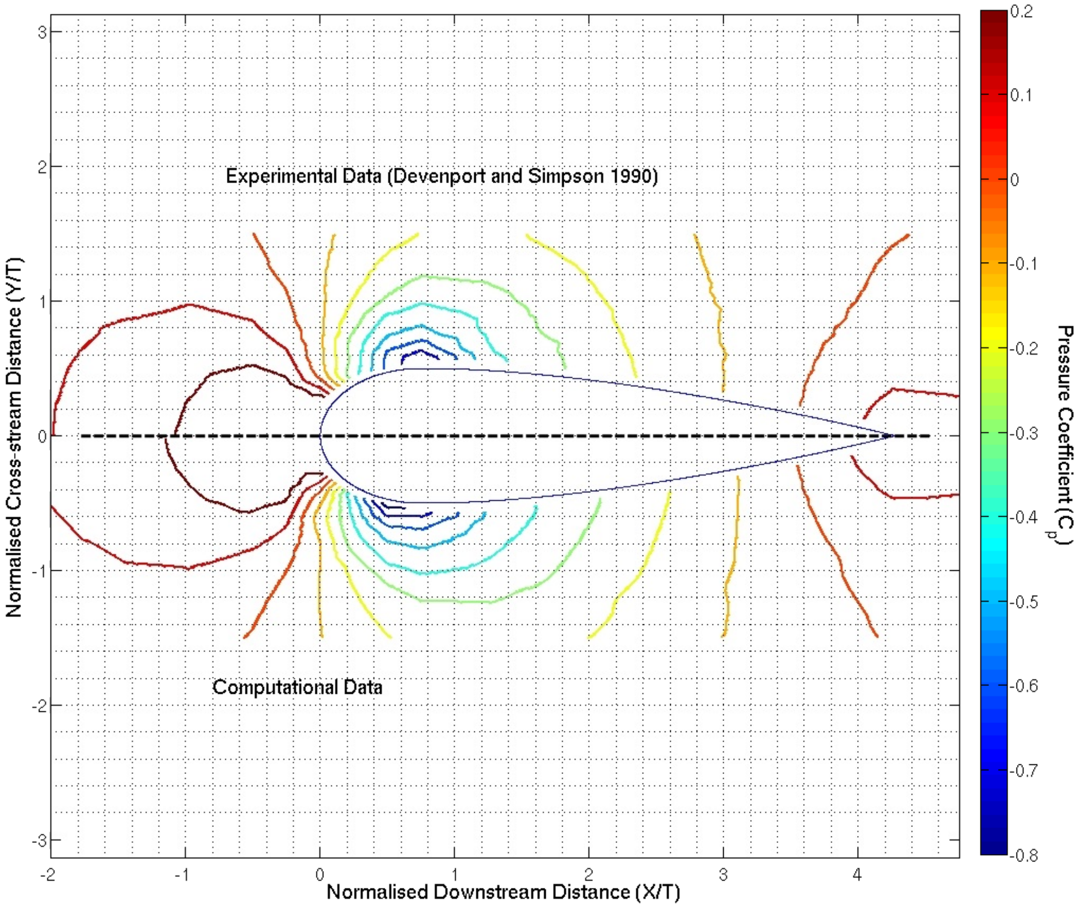

Figure A.25: $k-\omega$ SST model very-fine grid flat plate pressure coefficient plot.

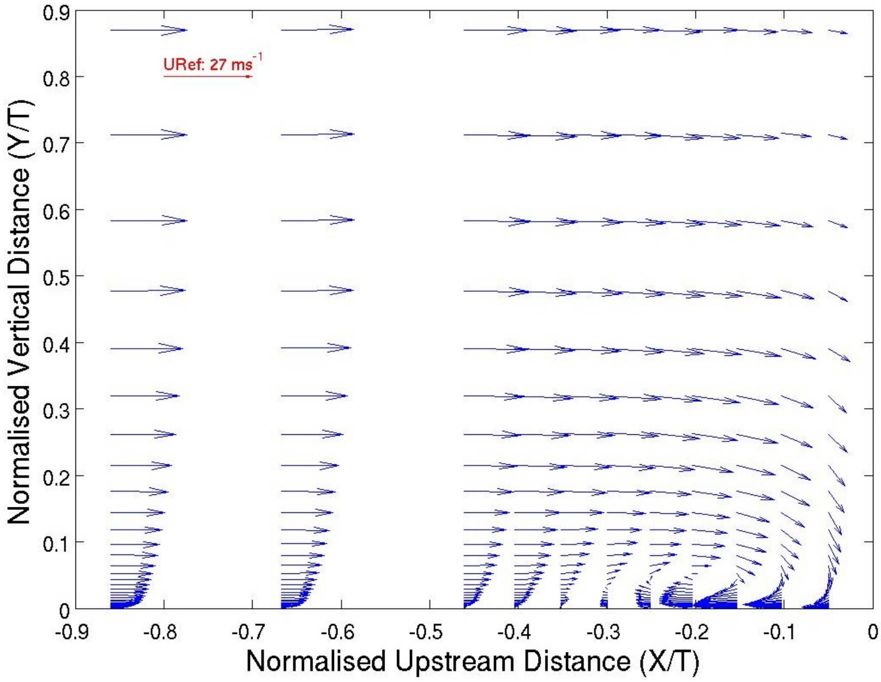

(a) Devenport and Simpson (1990) upwind symmetry plane velocity vector plot.

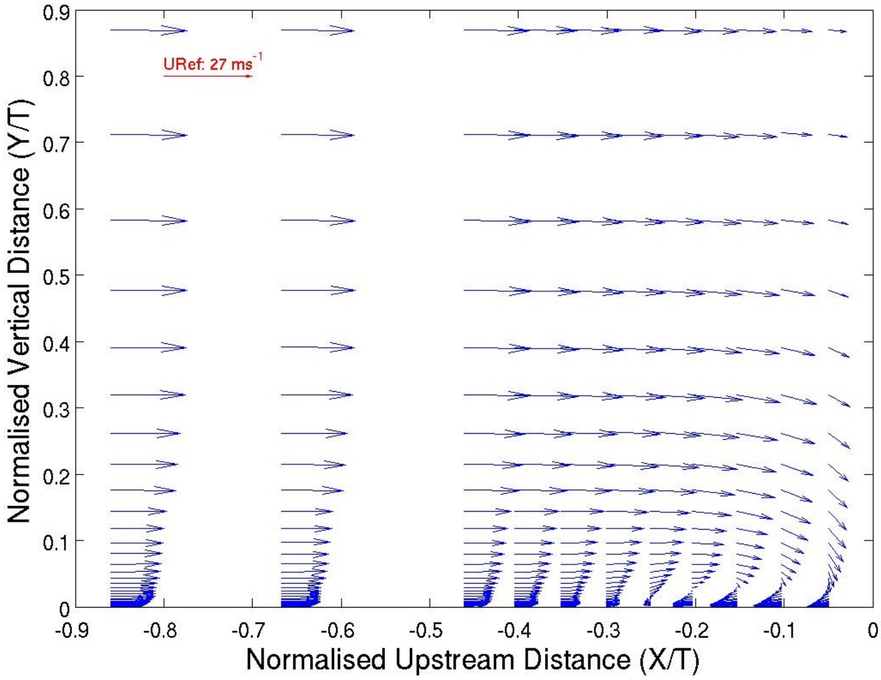

(b) LRR model upwind symmetry plane velocity vector plot.

Figure A.26: LRR model upwind symmetry plane velocity vector plot compared with Devenport and Simpson (1990) experiment.

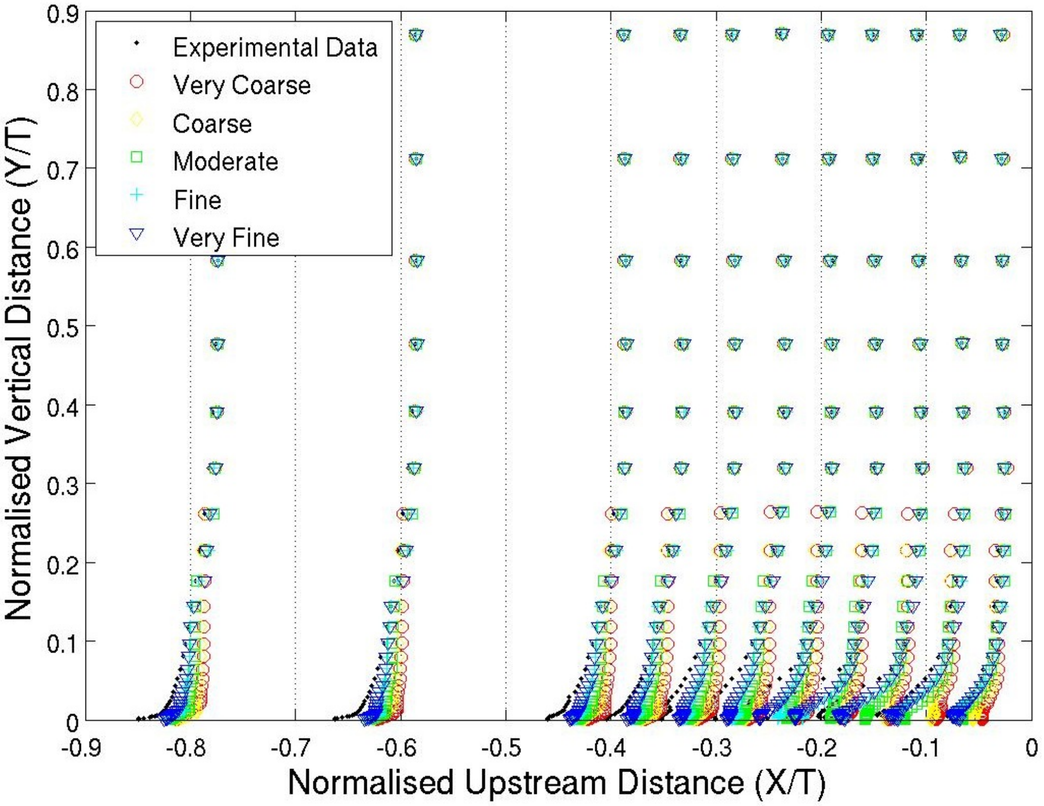

Figure A.27: LRR model grid dependence of upstream symmetry plane velocity profiles.

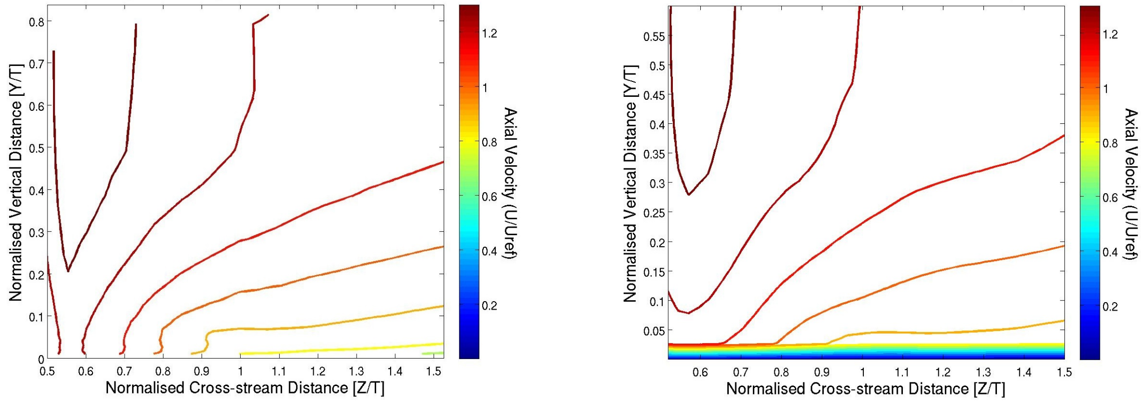

(a) Devenport and Simpson (1990) experiment plane 05 axial velocity contour plot.

(b) LRR model plane 05 axial velocity contour plot.

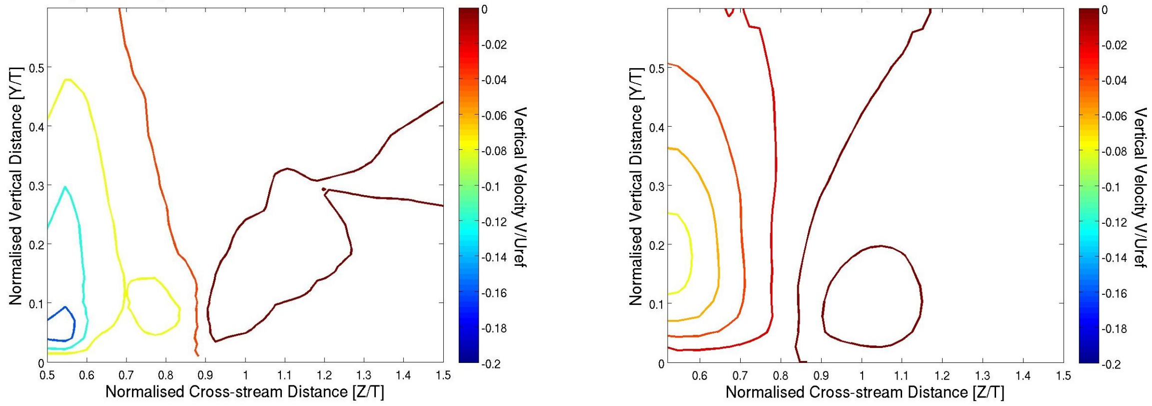

(c) Devenport and Simpson (1990) experiment plane 05 vertical velocity contour plot.

(d) LRR Model model plane 05 vertical velocity contour plot.

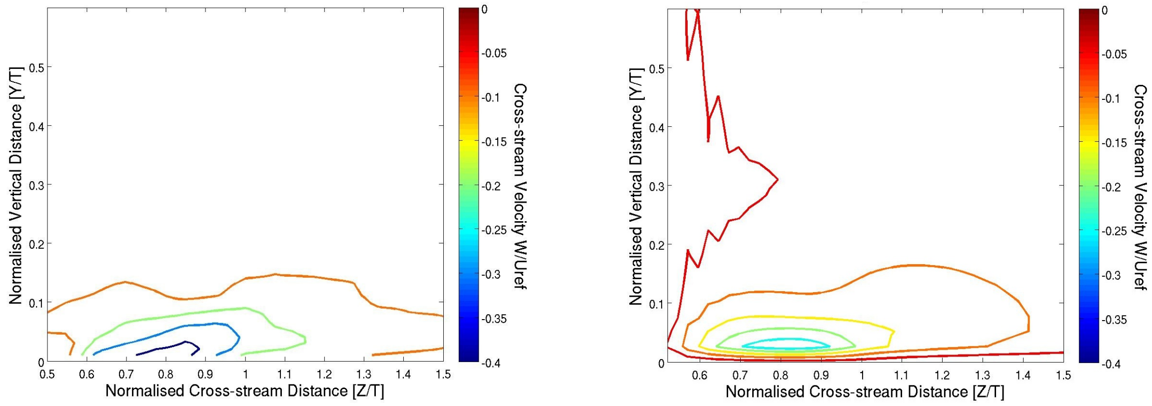

(e) Devenport and Simpson (1990) experiment plane 05 cross-stream velocity contour plot.

(f) LRR Model model plane 05 cross-stream velocity contour plot.

Figure A.28: LRR model plane 05 velocity contour plots compared with Devenport and Simpson (1990) experiment.

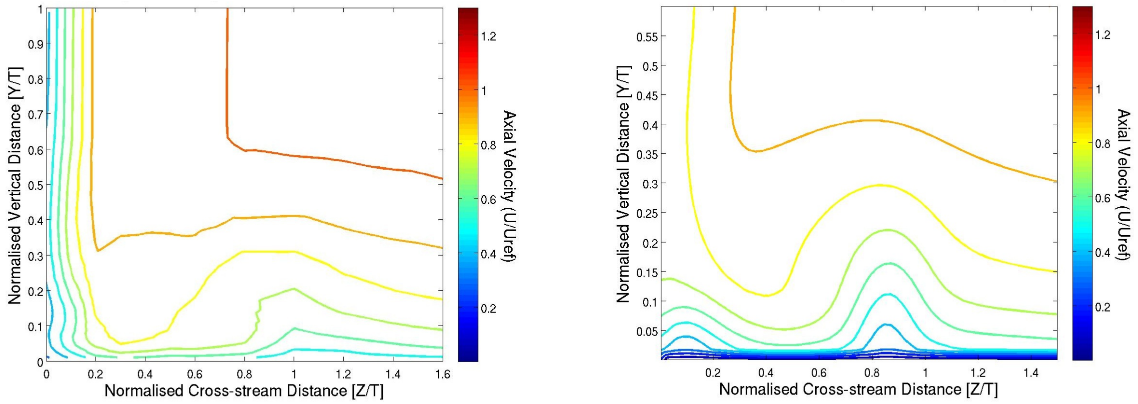

(a) Devenport and Simpson (1990) experiment plane 10 axial velocity contour plot.

(b) LRR model plane 10 axial velocity contour plot.

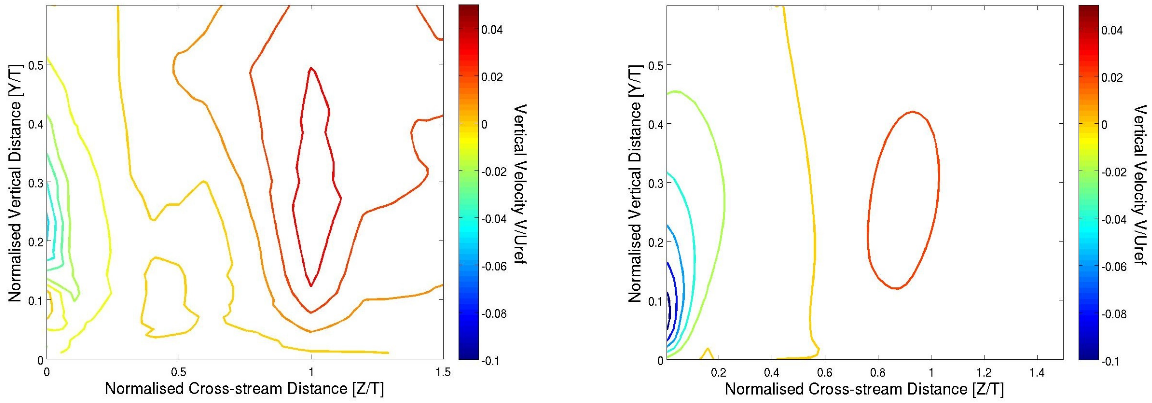

(c) Devenport and Simpson (1990) experiment plane 10 vertical velocity contour plot.

(d) LRR model plane 10 vertical velocity contour plot.

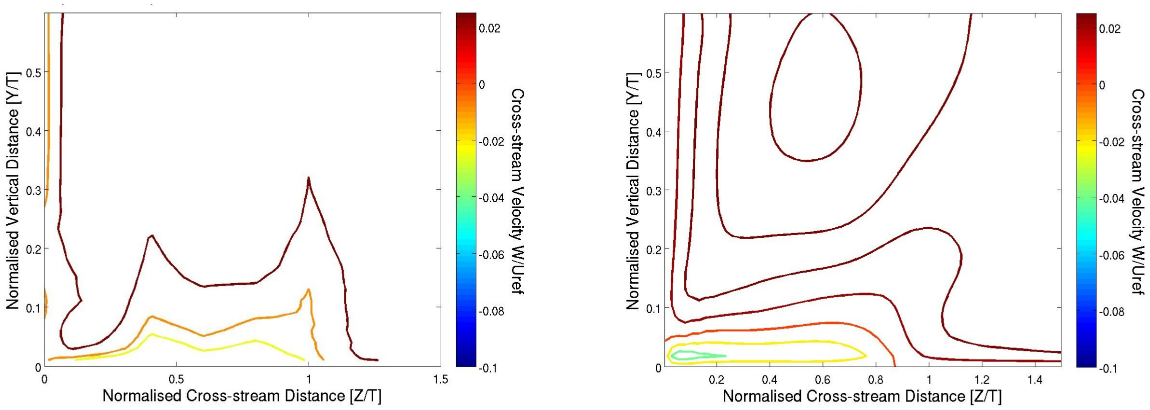

(e) Devenport and Simpson (1990) experiment plane 10 cross-stream velocity contour plot.

(f) LRR model plane 10 cross-stream velocity contour plot.

Figure A.29: LRR model plane 10 velocity contour plots compared with Devenport and Simpson (1990) experiment.

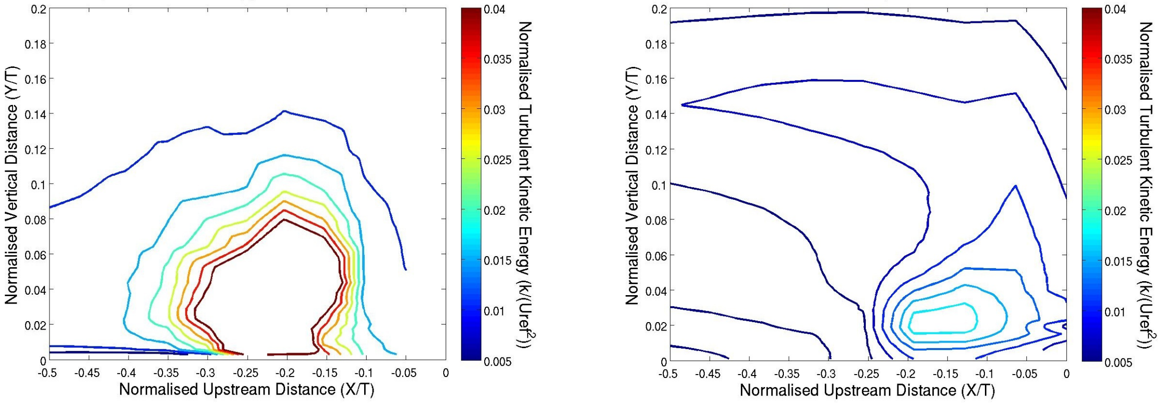

(a) Devenport and Simpson (1990) experiment upstream symmetry plane turbulent kinetic energy contour plot.

(b) LRR model upstream symmetry plane turbulent kinetic energy contour plot.

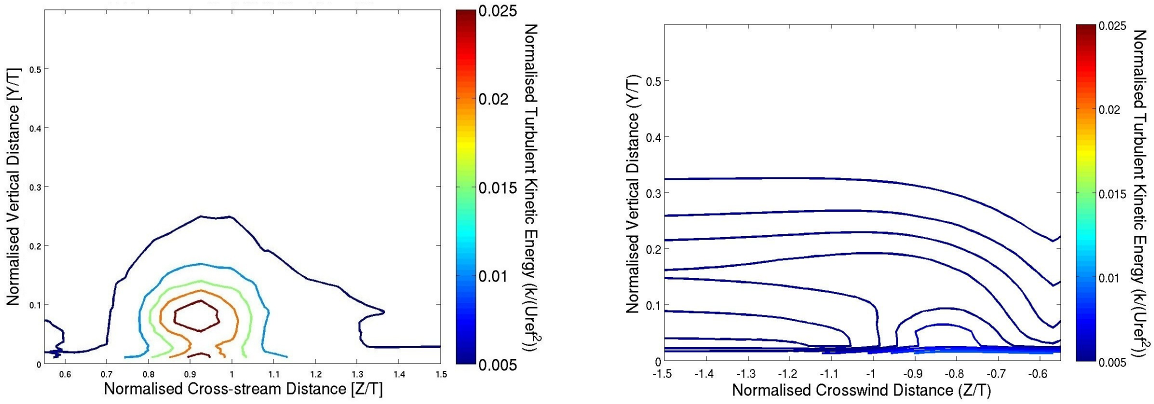

(c) Devenport and Simpson (1990) experiment plane 05 turbulent kinetic energy contour plot.

(d) LRR model plane 05 turbulent kinetic energy contour plot.

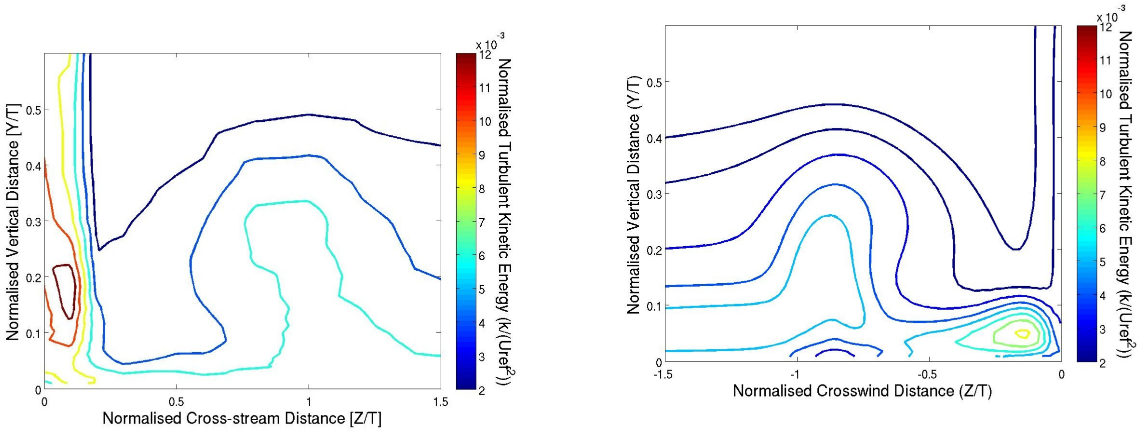

(e) Devenport and Simpson (1990) experiment plane 10 turbulent kinetic energy contour plot.

(f) LRR model plane 10 turbulent kinetic energy contour plot.

Figure A.30: LRR model turbulent kinetic energy contour plots compared with Devenport and Simpson (1990) experiment.

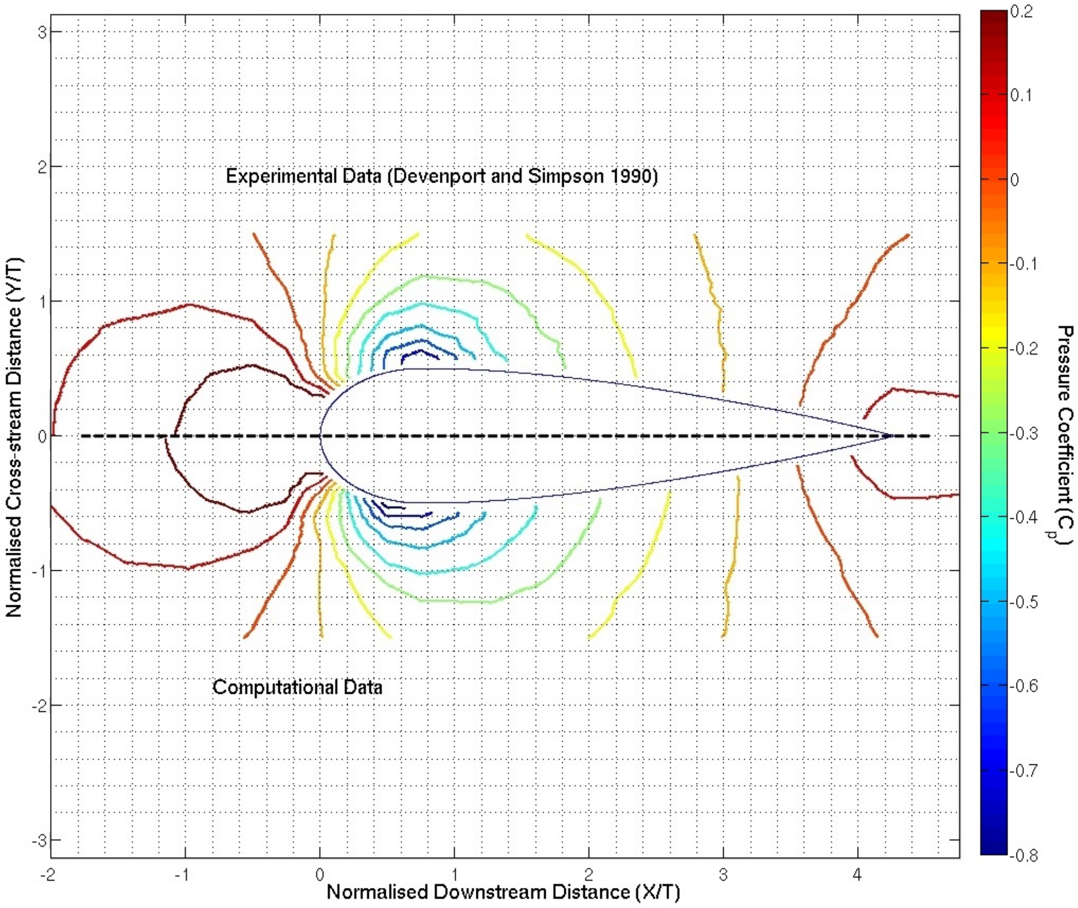

Figure A.31: Launder Gibson model very-fine grid flat plate pressure coefficient plot.

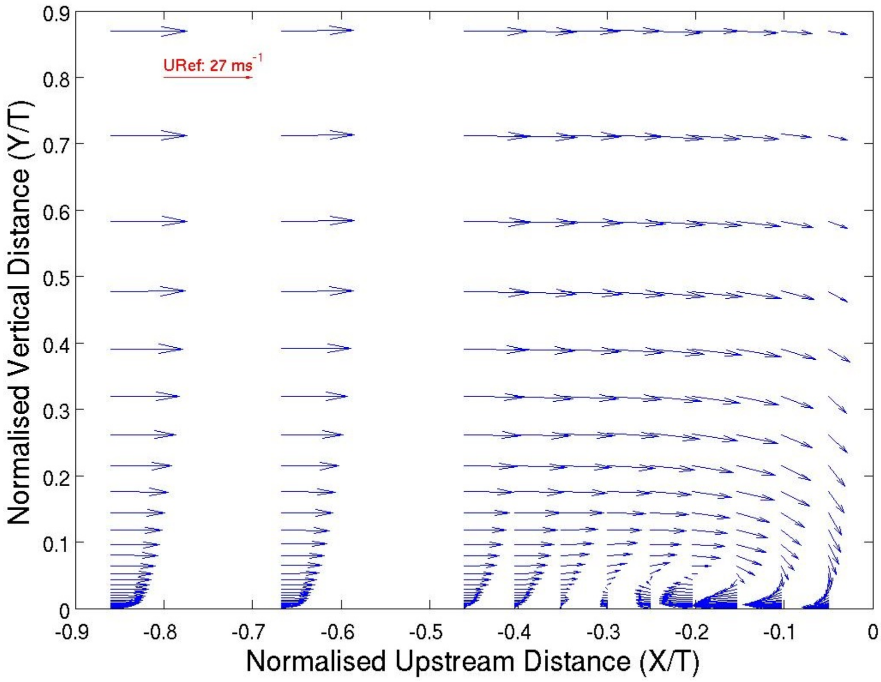

(a) Devenport and Simpson (1990) upwind symmetry plane velocity vector plot.

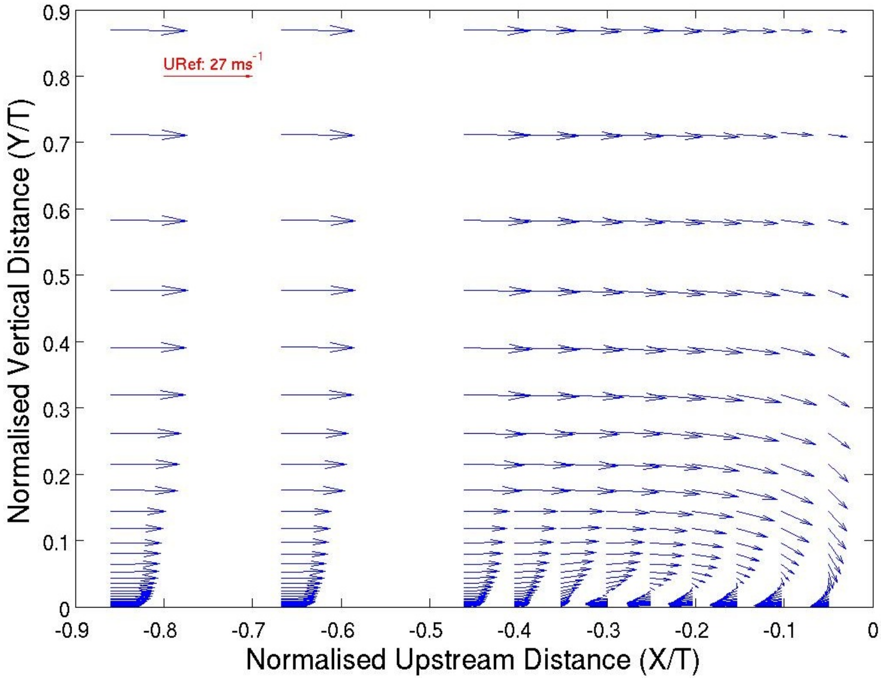

(b) Launder Gibson model upwind symmetry plane velocity vector plot.

Figure A.32: Launder Gibson model upwind symmetry plane velocity vector plot compared with Devenport and Simpson (1990) experiment.

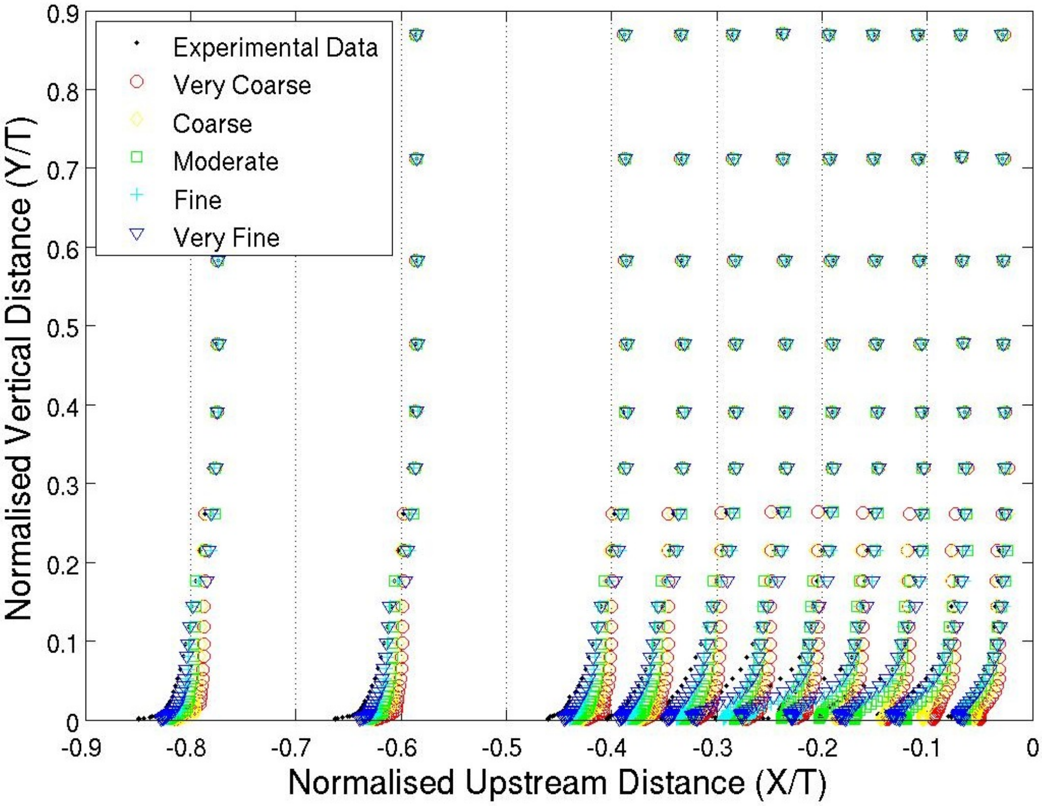

Figure A.33: Launder Gibson model grid dependence of upstream symmetry plane velocity profiles.

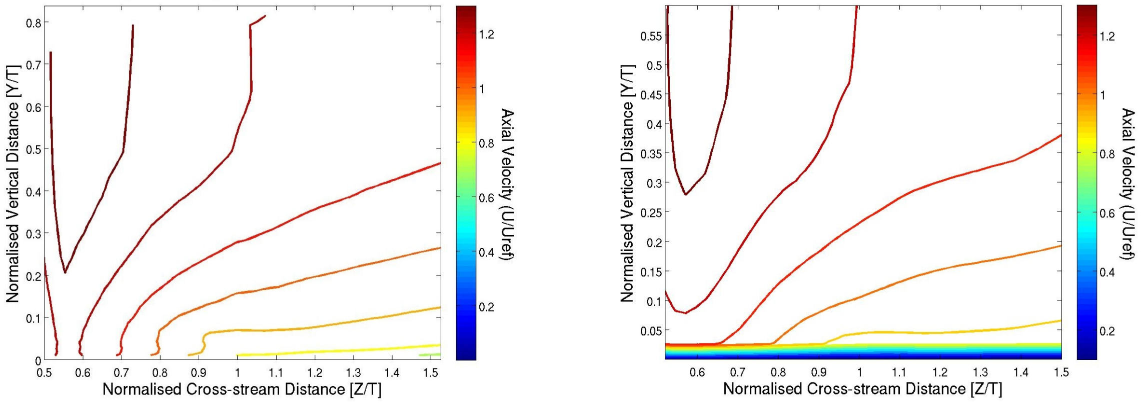

(a) Devenport and Simpson (1990) experiment plane 05 axial velocity contour plot.

(b) Launder Gibson model plane 05 axial velocity contour plot.

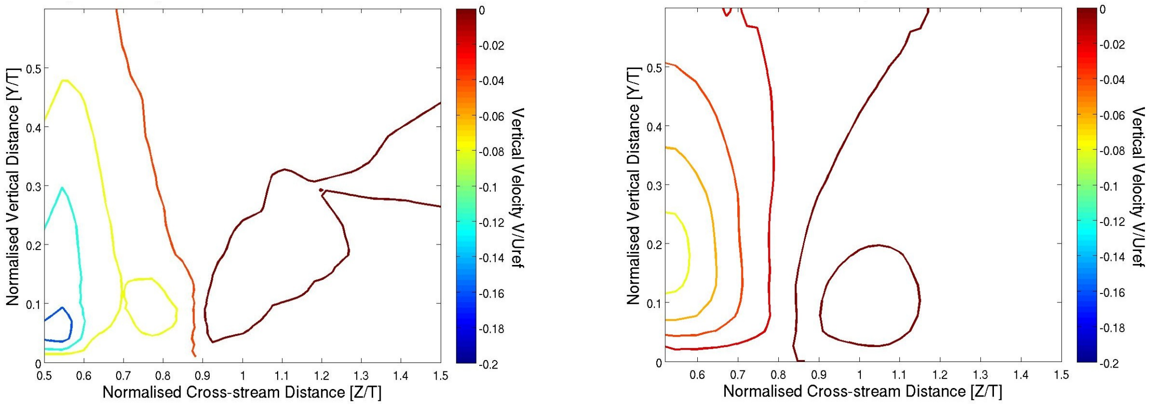

(c) Devenport and Simpson (1990) experiment plane 05 vertical velocity contour plot.

(d) Launder Gibson model plane 05 vertical velocity contour plot.

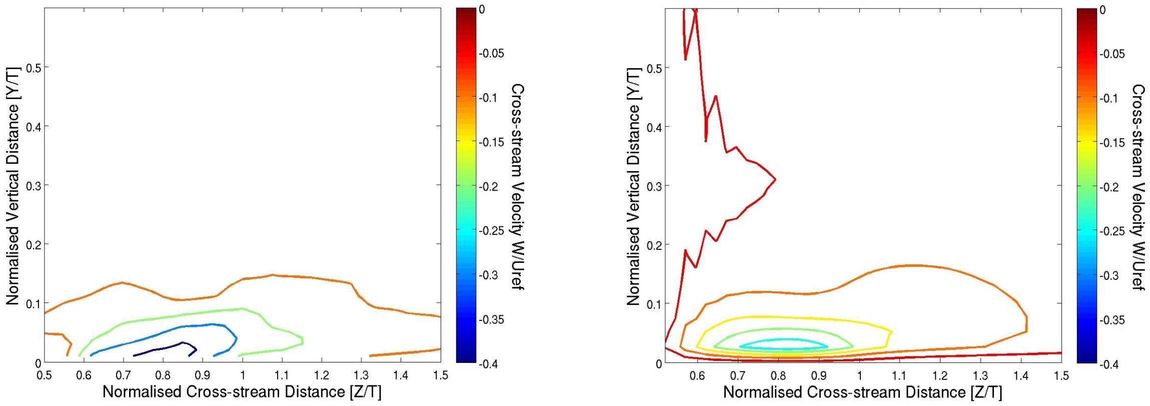

(e) Devenport and Simpson (1990) experiment plane 05 cross-stream velocity contour plot.

(f) Launder Gibson model plane 05 cross-stream velocity contour plot.

Figure A.34: Launder Gibson model plane 05 velocity contour plots compared with Devenport and Simpson (1990) experiment.

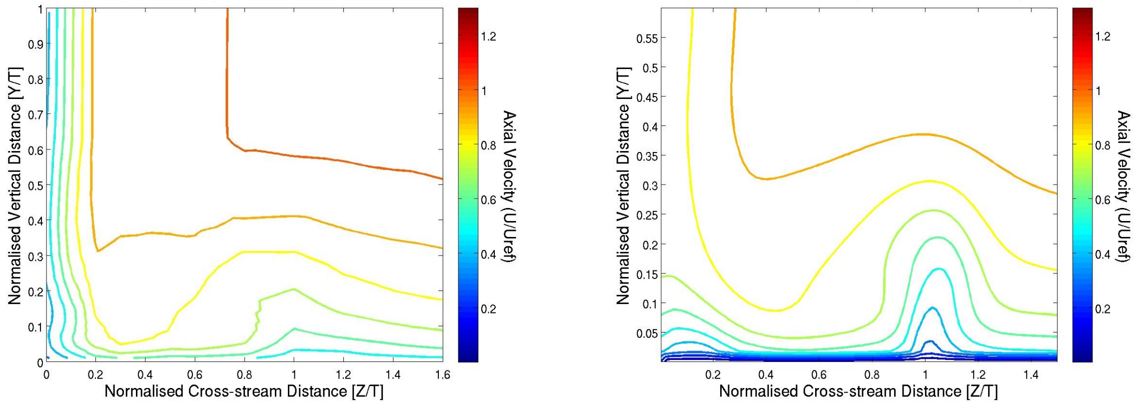

(a) Devenport and Simpson (1990) experiment plane 10 axial velocity contour plot.

(b) Launder Gibson model plane 10 axial velocity contour plot.

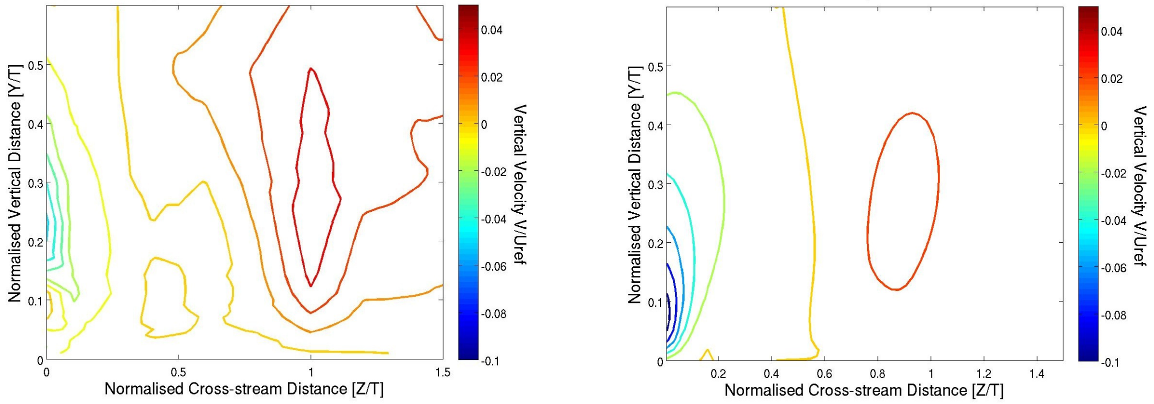

(c) Devenport and Simpson (1990) experiment plane 10 vertical velocity contour plot.

(d) Launder Gibson model plane 10 vertical velocity contour plot.

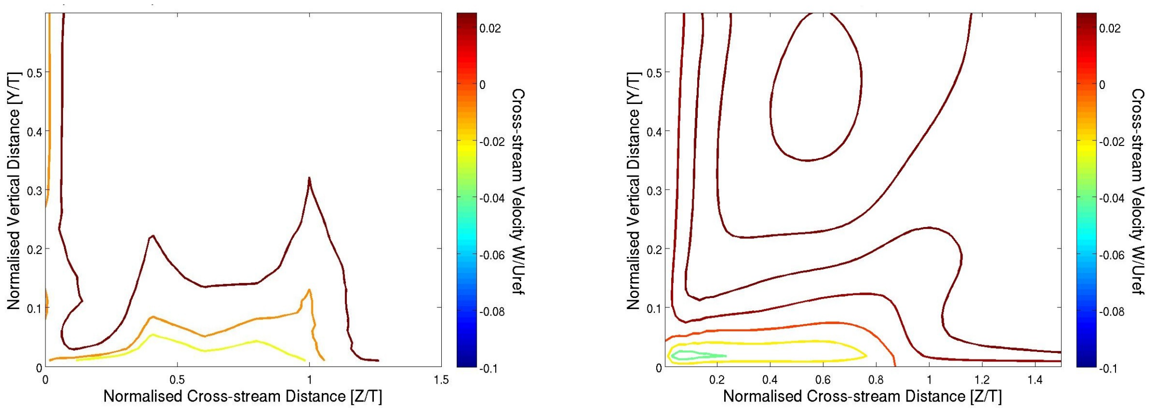

(e) Devenport and Simpson (1990) experiment plane 10 cross-stream velocity contour plot.

(f) Launder Gibson model plane 10 cross-stream velocity contour plot.

Figure A.35: Launder Gibson model plane 10 velocity contour plots compared with Devenport and Simpson (1990) experiment.

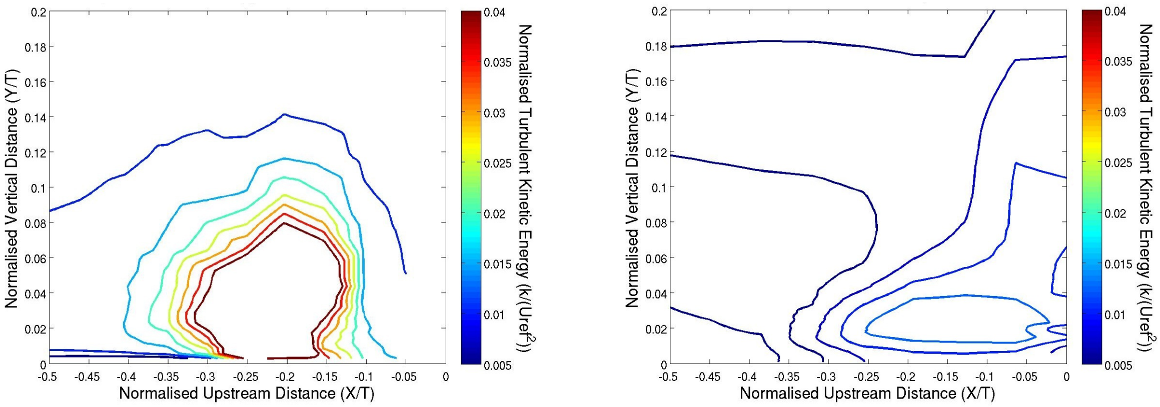

(a) Devenport and Simpson (1990) experiment upstream symmetry plane turbulent kinetic energy contour plot.

(b) Launder Gibson model upstream symmetry plane turbulent kinetic energy contour plot.

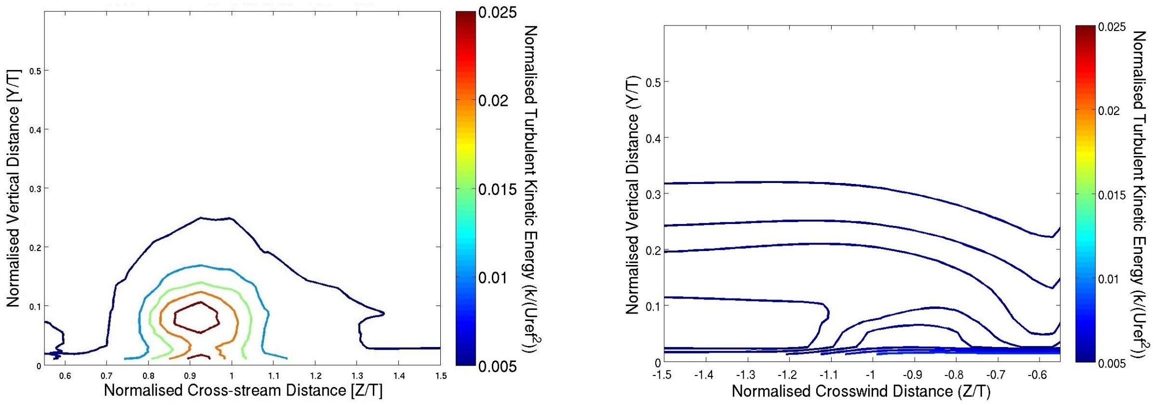

(c) Devenport and Simpson (1990) experiment plane 05 turbulent kinetic energy contour plot.

(d) Launder Gibson model plane 05 turbulent kinetic energy contour plot.

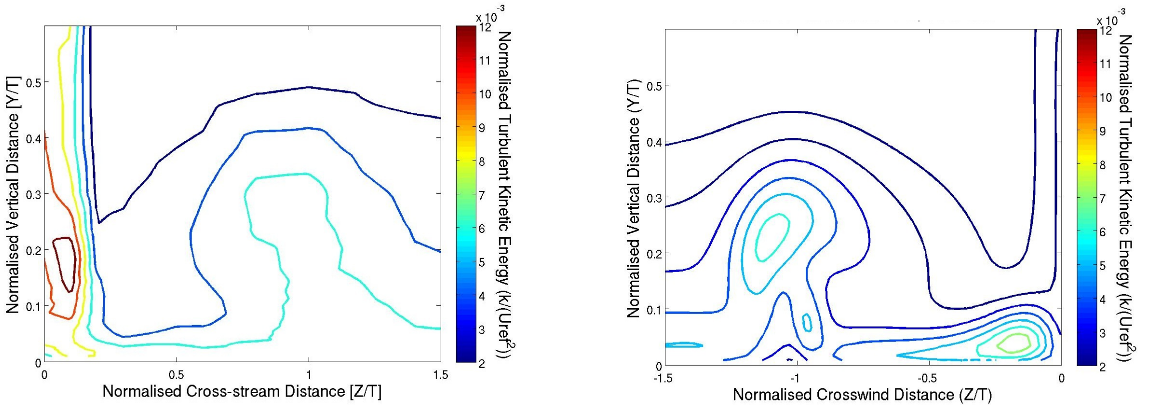

(e) Devenport and Simpson (1990) experiment plane 10 turbulent kinetic energy contour plot.

(f) Launder Gibson model plane 10 turbulent kinetic energy contour plot.

Figure A.36: Launder Gibson model turbulent kinetic energy contour plots compared with Devenport and Simpson (1990) experiment.

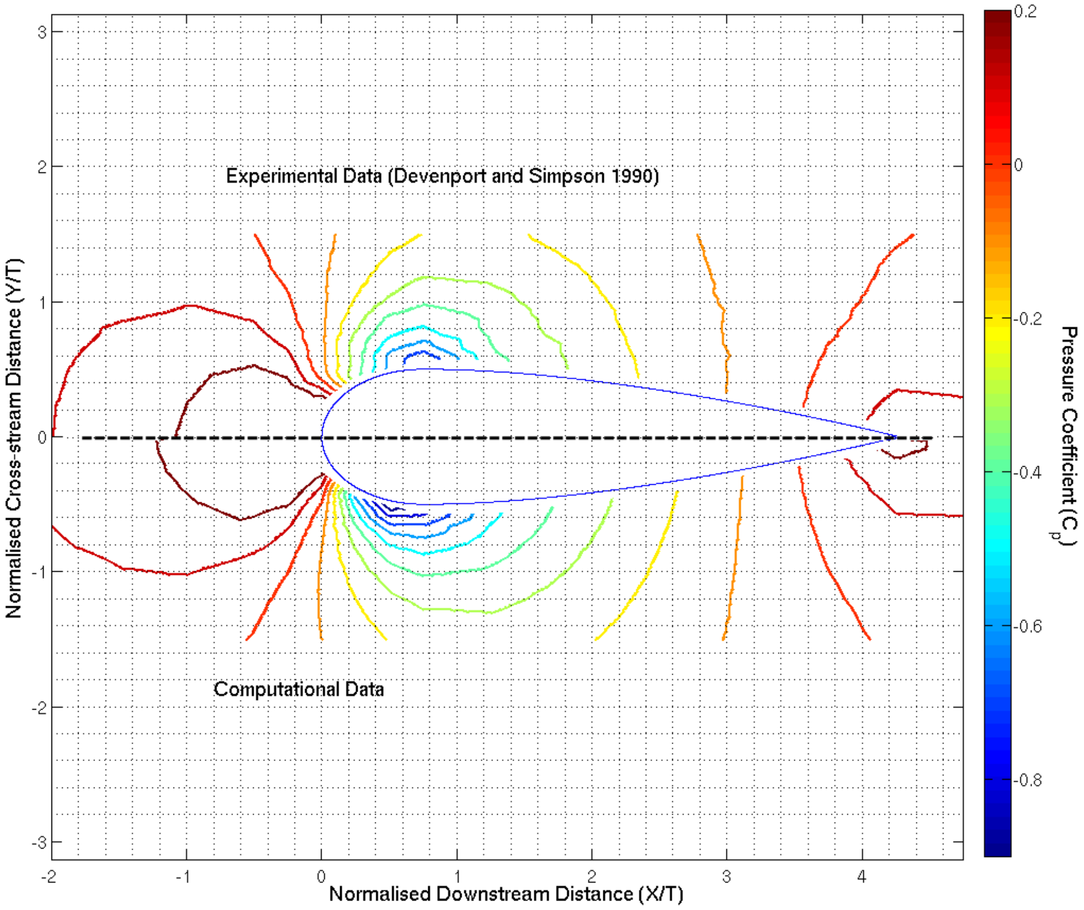

Figure A.37: Spalart-Allmaras model very-fine grid flat plate pressure coefficient plot.

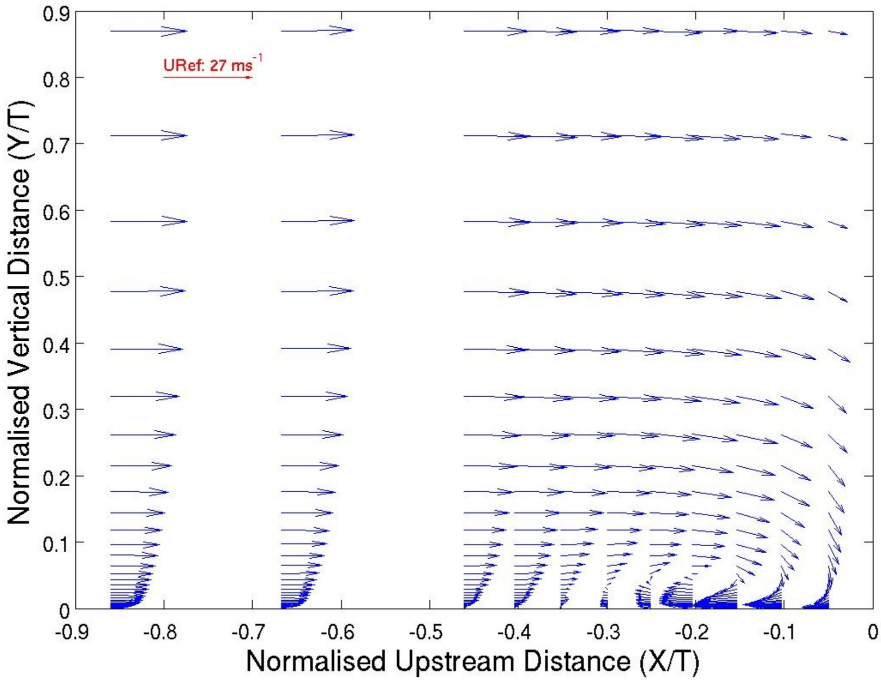

(a) Devenport and Simpson (1990) upwind symmetry plane velocity vector plot.

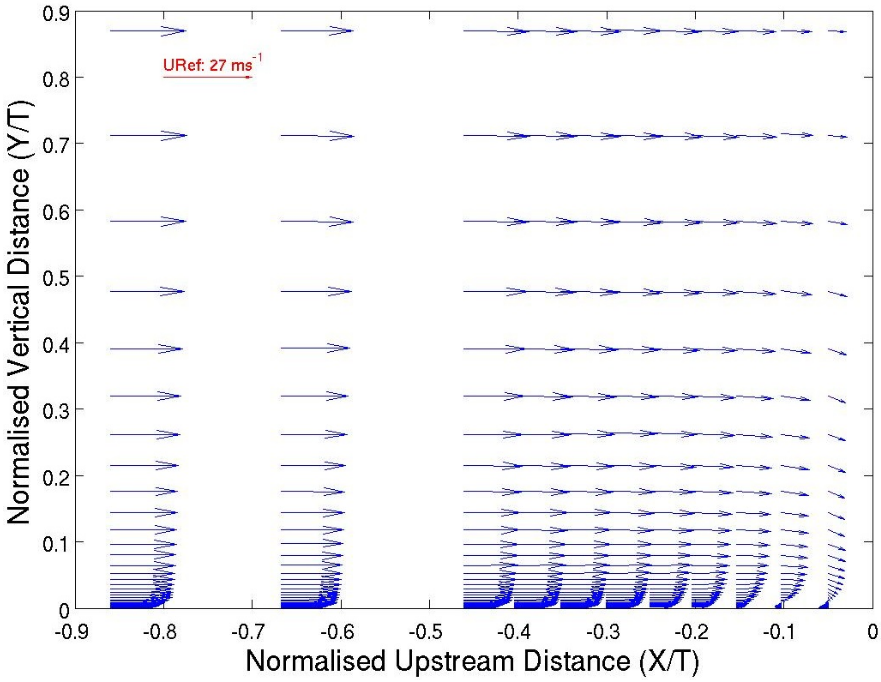

(b) Spalart-Allmaras model upwind symmetry plane velocity vector plot.

Figure A.38: Spalart-Allmaras model upwind symmetry plane velocity vector plot compared with Devenport and Simpson (1990) experiment.

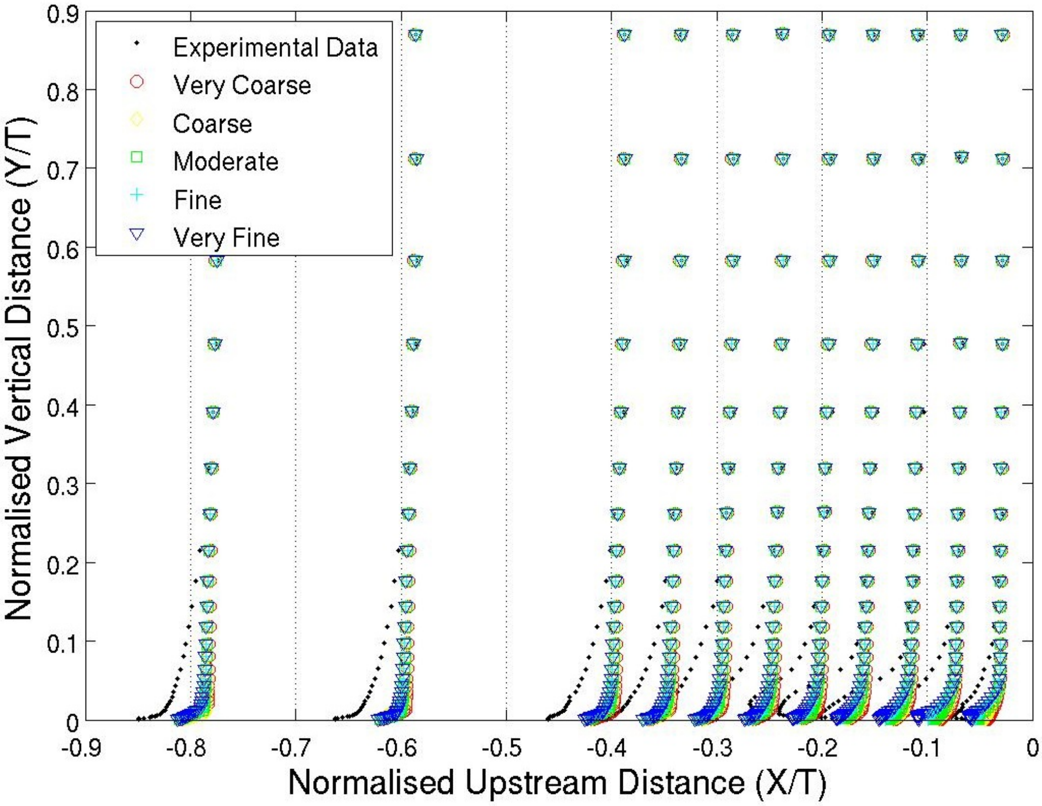

Figure A.39: Spalart-Allmaras model grid dependence of upstream symmetry plane velocity profiles.

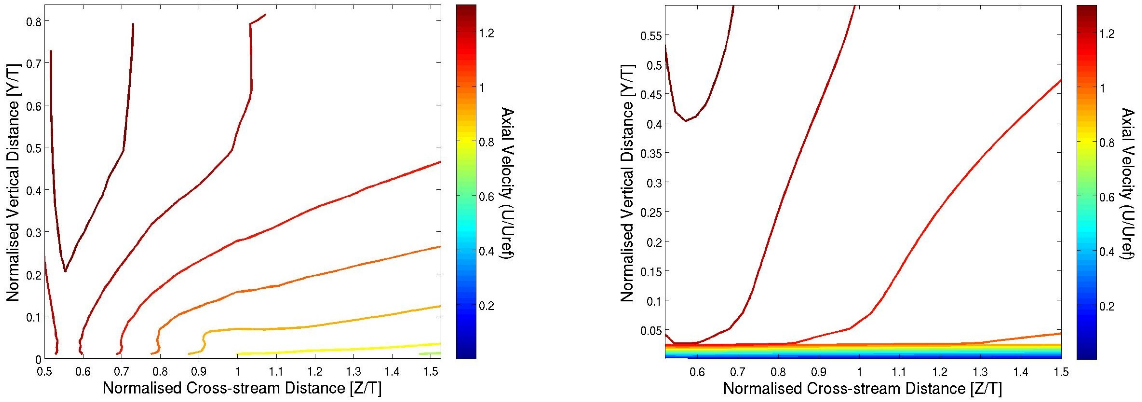

(a) Devenport and Simpson (1990) experiment plane 05 axial velocity contour plot.

(b) Spalart-Allmaras model plane 05 axial velocity contour plot.

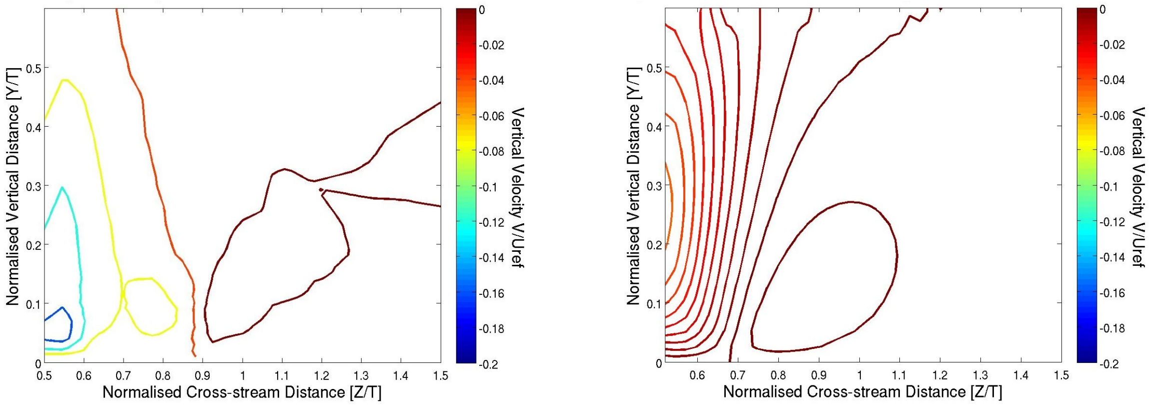

(c) Devenport and Simpson (1990) experiment plane 05 vertical velocity contour plot.

(d) Spalart-Allmaras model plane 05 vertical velocity contour plot.

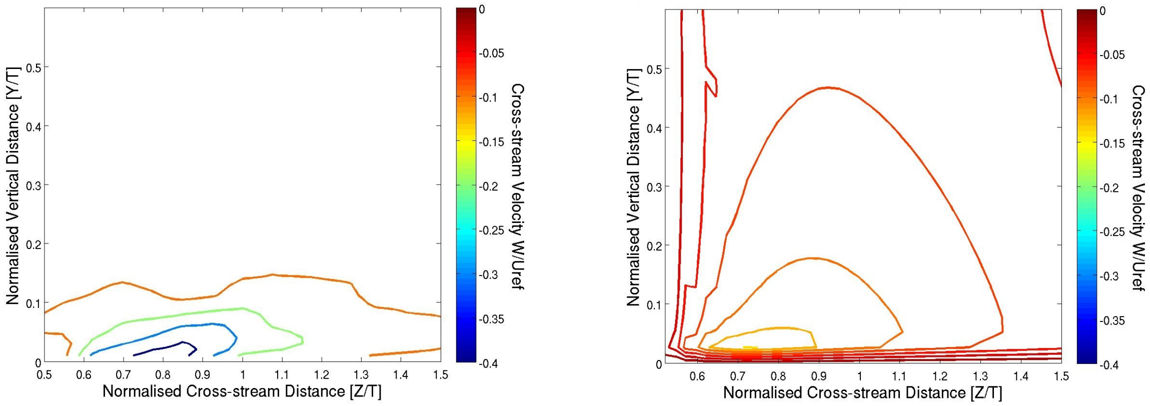

(e) Devenport and Simpson (1990) experiment plane 05 cross-stream velocity contour plot.

(f) Spalart-Allmaras model plane 05 cross-stream velocity contour plot.

Figure A.40: Spalart-Allmaras model plane 05 velocity contour plots compared with Devenport and Simpson (1990) experiment.

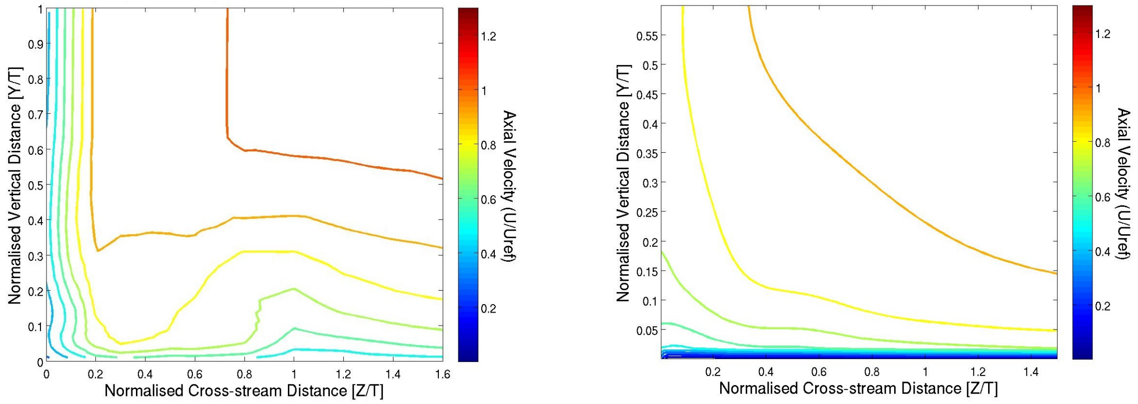

(a) Devenport and Simpson (1990) experiment plane 10 axial velocity contour plot.

(b) Spalart-Allmaras model plane 10 axial velocity contour plot.

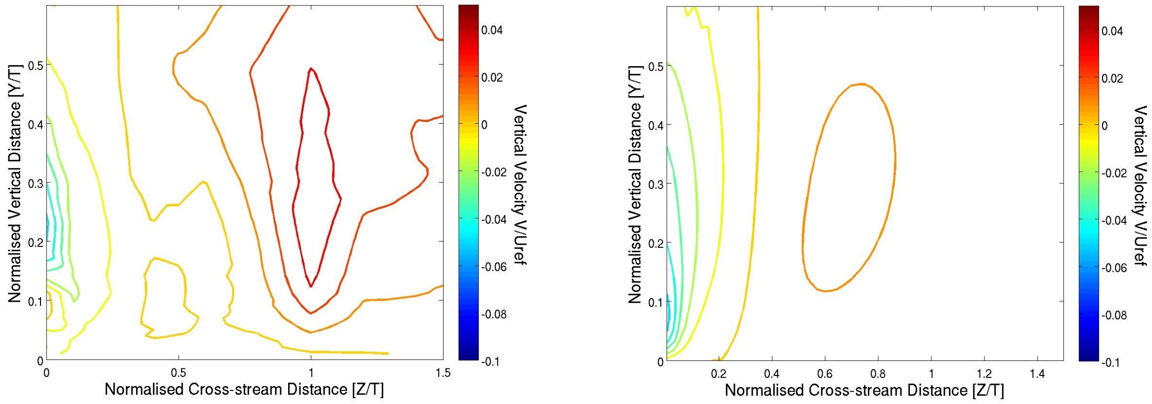

(c) Devenport and Simpson (1990) experiment plane 10 vertical velocity contour plot.

(d) Spalart-Allmaras model plane 10 vertical velocity contour plot.

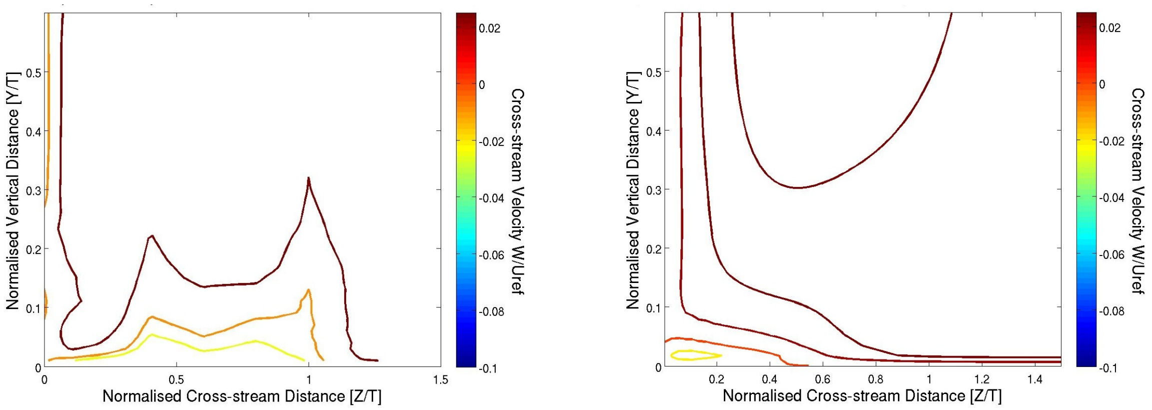

(e) Devenport and Simpson (1990) experiment plane 10 cross-stream velocity contour plot.

(f) Spalart-Allmaras model plane 10 cross-stream velocity contour plot.

Figure A.41: Spalart-Allmaras model plane 10 velocity contour plots compared with Devenport and Simpson (1990) experiment.

B Noise Modelling Verification and Validation Results Figures

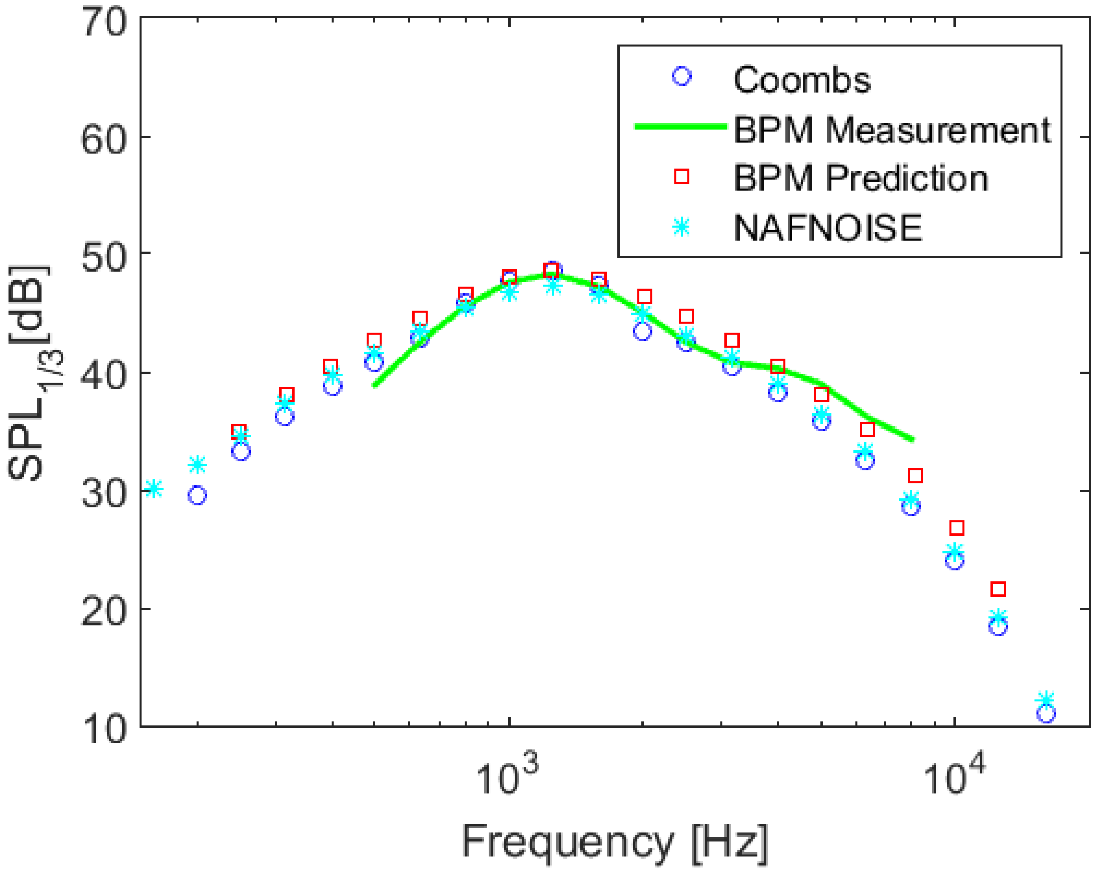

Figure B.1: BPM tip noise implementation verification

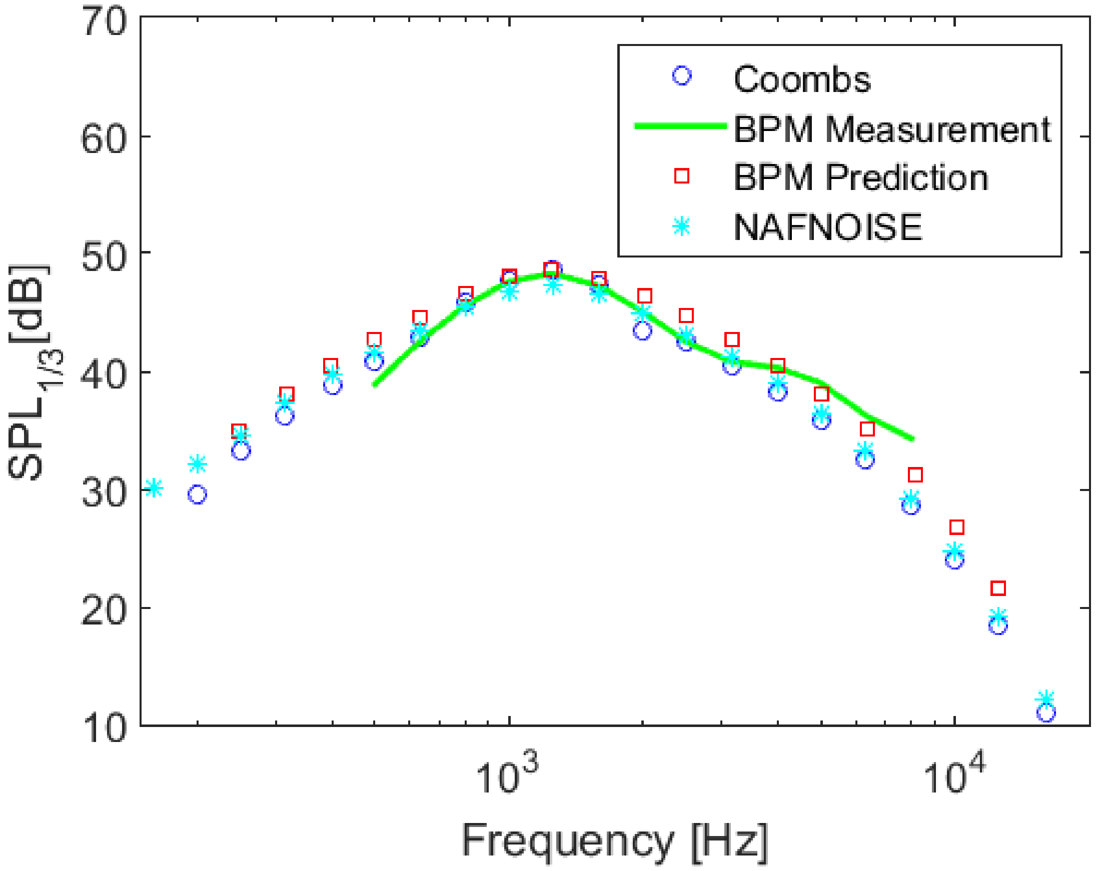

Figure B.2: BPM TE noise model implementation verification

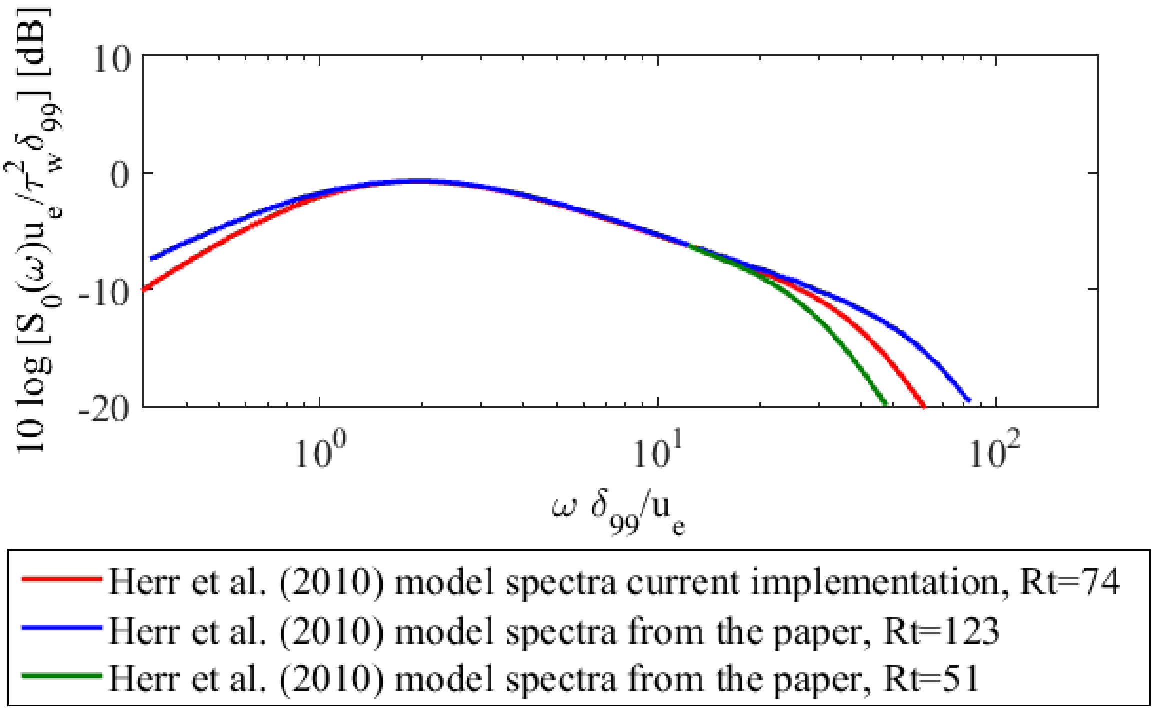

Figure B.3: Equation 3.35 implementation verification

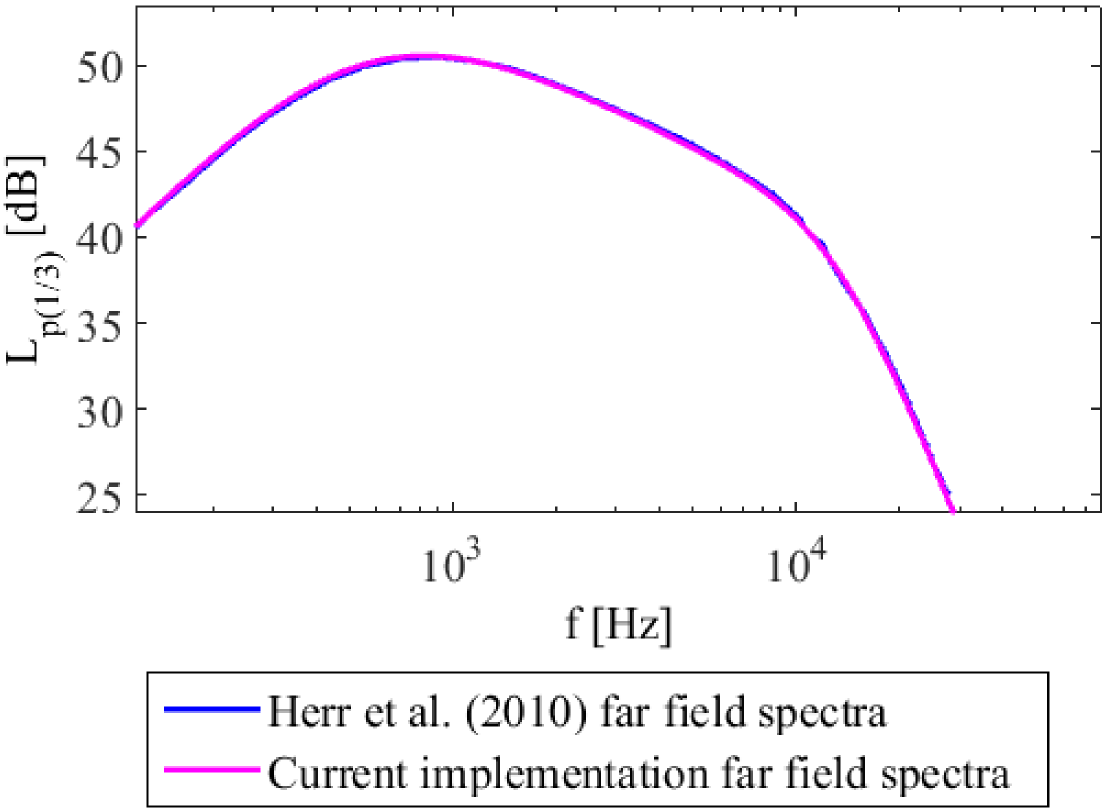

Figure B.4: Herr method farfield spectra implementation verification

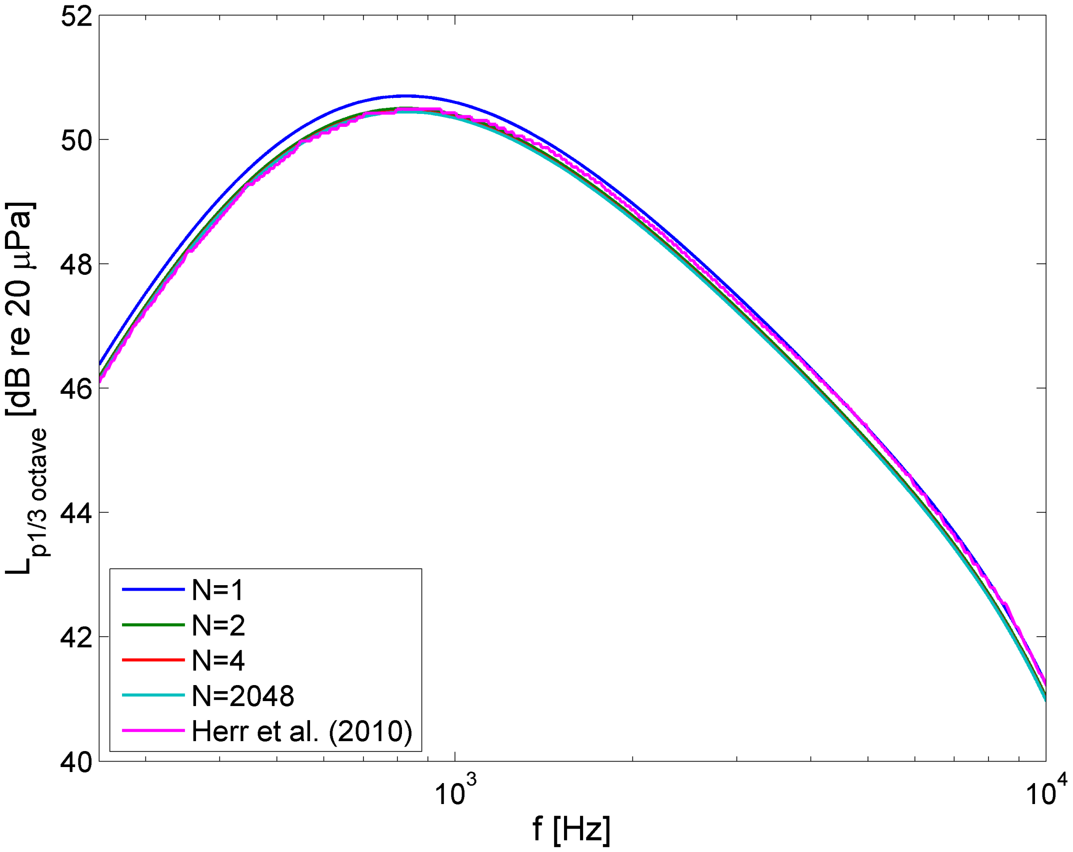

Figure B.5: Herr extension method farfield spectra implementation validation

C Turbulence Models: Formulation and Performance

C.1 The Boussinesq Hypothesis

In order to solve for the Reynolds-stress tensor $-\rho\overline{u_i'u_j'}$ Joseph Boussinesq (Boussinesq, 1877) proposed relating the stresses to the mean flow, by means of the concept of eddy viscosity, a scale which characterises the transport and dissipation of energy in the smaller-scale flow. Namely

$$\begin{aligned} \tau_{ij} &\propto \nu_t, \overline{u_i}, \overline{u_j} \\ &= 2 * \nu_t * s_{i,j} - \frac{2}{3} K \delta_{i,j} \end{aligned} \tag{C.1}$$

where $K = \frac{1}{2}\overline{u_i'u_j'}$ is the turbulent kinetic energy and $\delta_{i,j}$ is the Kronecker delta. Models based on this are known as eddy viscosity models.

C.2 Model Classifications

Algebraic Models

Algebraic models are the simplest and least computationally intensive of all turbulence models. Algebraic models seek to solve for the kinematic eddy viscosity as a function of a characteristic mixing length. An algebraic relationship is used to connect the eddy viscosity and the characteristic mixing length, and a function for the characteristic mixing length for the flow is determined, typically by comparison with experimental data. Although simple, algebraic models will only work effectively for the flows which fall within the range of data from which the model was calibrated. It is this loss of generality which limits their application and usefulness.

One-Equation Models

One equation models neglect the turbulent kinetic energy component of the Reynolds stress tensor, under the claim that it does not have a "major effect in thin shear flows" (Spalart and Allmaras, 1994). An equation for the turbulent viscosity is then proposed and closure complete. The Spalart-Allmaras model is one of the more frequently used one-equation models, especially for aircraft applications for which its performance is optimised (Wilcox, 2006).

Two-Equation Models

The two most popular two-equation models are the standard k-ϵ and k-ω models (Wilcox, 1988). These models provide equations for determining both the turbulent kinetic energy and turbulent viscosity variables needed for closure. Both of these models use an eddy viscosity that is a function of the two variables that form their names, and as such, require two additional equations to solve. These two models are used extensively (Apsley and Leschziner, 2001; Devenport and Simpson, 1992; Wilcox, 2008; Franke et al., 2005; Menter, 1994), and because of this they are still often considered the baseline for comparison with the more recent two-equation models and stress-transport models (Franke et al., 2005; Apsley and Leschziner, 2001; Menter, 1994), such as the also commonly used two-equation Realisable k-ϵ model (Shih et al., 1995).

Stress-Transport Models

Reynolds Stress-Transport Models (RSTM(s)) are also commonly referred to as second-order closure or second-moment closure models. Although much more complex, and with a corresponding computational cost, RSTMs hold promise for more accurate predictions of three-dimensional flows, since, unlike one-equation and two-equation models, RSTMs do not assume an isotropic eddy viscosity. The isotropic eddy viscosity assumption is unsuitable for three-dimensional flows, as there can be significant variations between the viscosities of flow in the stream-wise and cross-flow directions (Wilcox, 2006). Being the focus of ongoing research and development, there are many stress transport models. Of particular interest are the Launder-Reece-Rodi (LRR) RSTM (Launder et al., 1975) and the Launder Gibson RSTM (Gibson and Launder, 1978).

C.3 One Equation Models

C.3.1 Spalart-Allmaras

The Spalart-Allmaras model has accuracy issues for flows involving free shear regions, such as jets, or shock-induced separation, however it is still a valuable engineering tool, especially for aerodynamic applications such as flow past wings, for which it has been optimised.

The formulation of the Spalart-Allmaras model is as follows, where d is the distance to the nearest wall

Kinematic Eddy Viscosity

$$\nu_T = \tilde{\nu} f_{v1} \tag{C.2}$$

Eddy Viscosity Equation

$$\frac{\partial \tilde{\nu}}{\partial t} + U_j \frac{\partial \tilde{\nu}}{\partial x_j} = c_{b1} \tilde{S} \tilde{\nu} - c_{w1} f_w \left(\frac{\tilde{\nu}}{d} \right)^2 + \frac{1}{\sigma} \frac{\partial}{\partial x_k} \left[(\nu + \tilde{\nu}) \frac{\partial \tilde{\nu}}{\partial x_k} \right] + \frac{c_{b2}}{\sigma} \frac{\partial \tilde{\nu}}{\partial x_k} \frac{\partial \tilde{\nu}}{\partial x_k} \tag{C.3}$$

Auxiliary Relationships and Closure Coefficients

$$\begin{array}{rlll} c_{b1} = 0.1355 & c_{b2} = 0.622 & c_{v1} = 7.1 \\ \kappa = 0.41 & \sigma = \frac{2}{3} & \\ c_{w1} = \dfrac{c_{b1}}{\kappa^2} + \dfrac{1 + c_{b2}}{\sigma} & c_{w2} = 0.3 & c_{w3} = 2 \\ \chi = \dfrac{\tilde{\nu}}{\nu} & r = \frac{\tilde{\nu}}{\tilde{S} \kappa^2 d^2} & g = r + c_{w2}(r^6 - r) \\ f_{v1} = \dfrac{\chi^3}{\chi^3 + c_{v1}^3} & f_{v2} = 1 - \frac{\chi}{1 + \chi f_{v1}} & f_w = g \left[\dfrac{1 + c_{w3}^6}{g^6 + c_{w3}^6} \right]^{1/6} \end{array} \tag{C.4}$$

C.4 Two Equation Models

C.4.1 (Standard) k-ϵ

Having risen to prominence first, the k-ϵ model, although in recent times to an extent superseded by the k-ω model, is still extensively used and considered a baseline for comparison. The model, although only coincidentally, is formulated in such a way as to almost entirely avoid the sensitivity to free steam parameters that troubles the k-ω model. However, the k-ϵ model fails to accurately reproduce the law of the wall without the use of viscous corrections, and is difficult to integrate through the viscous sublayer (Wilcox, 1988).

The formulation of the standard k-ϵ model (Launder and Sharma, 1974) is as follows:

Kinematic Eddy Viscosity

$$\nu_T = C_\mu k^2/\epsilon \tag{C.5}$$

Turbulent Kinetic Energy

$$\frac{\partial k}{\partial t} + U_j \frac{\partial k}{\partial x_j} = \tau_{ij}\frac{\partial U_i}{\partial x_j} - \epsilon + \frac{\partial}{\partial x_j}\left[\left(\nu + \nu_T/\sigma_k\right)\frac{\partial k}{\partial x_j}\right] \tag{C.6}$$

Dissipation Rate

$$\frac{\partial \epsilon}{\partial t} + U_j \frac{\partial \epsilon}{\partial x_j} = C_{\epsilon 1}\frac{\epsilon}{k}\tau_{ij}\frac{\partial U_i}{\partial x_j} - C_{\epsilon 2}\frac{\epsilon^2}{k} + \frac{\partial}{\partial x_j}\left[\left(\nu + \nu_T/\sigma_k\right)\frac{\partial \epsilon}{\partial x_j}\right] \tag{C.7}$$

Auxiliary Relationships and Closure Coefficients

$$\begin{aligned} C_{\epsilon 1} &= 1.44 \quad C_{\epsilon 2} = 1.92 \quad C_\mu = 0.09 \\ \sigma_k &= 1.0 \quad\ \ \sigma_\epsilon = 1.3 \\ \omega &= \frac{\epsilon}{C_\mu k} \quad l = C_\mu k^{3/2}/\epsilon \end{aligned} \tag{C.8}$$

C.4.2 (Standard) k-ω

From Kolmogorov's own (Kolmogorov, 1942) to current day versions such as Wilcox's most current (Wilcox, 2008), there have been many k-ω model formulations. However, due to lack of computing capabilities, Kolmogorov's formation was largely academic, and it is the Wilcox (1988) formulation that first found widespread implementation and in doing so came to be known as the Standard k-ω model. The k-ω model has several significant advantages over the k-ϵ model, and it has, as a result of these, superseded the k-ϵ model as the most widely-used two-equation model. The first advantage of the k-ω over the k-ϵ model is greater accuracy for flows with pressure gradients. The second significant advantage is that the k-ω model can be integrated through the viscous sublayer without the need for viscous corrections (Wilcox, 2006). The model has undergone several revisions since the original (Wilcox, 1988), and those of particular interest are the 1998 revision (Wilcox, 1998) as it is this version that is implemented in OpenFOAM and the more recent 2006 revision (Wilcox, 2006). The 2006 version of the model incorporates additional auxiliary equations, refined closure coefficients, a cross diffusion term to the Specific Dissipation Rate equation, which removes the boundary-condition sensitivity of the model, as well as a stress-limiter modification in the Kinematic Eddy Viscosity definition, which greatly improves the performance of the model in adverse pressure gradient and shock-separated flows (Wilcox, 2006).

The formulation of the original (1988) k-ω model is as follows:

Kinematic Eddy Viscosity

$$\nu_T = k/\omega \tag{C.9}$$

Turbulent Kinetic Energy

$$\frac{\partial k}{\partial t} + U_j \frac{\partial k}{\partial x_j} = \tau_{ij} \frac{\partial U_i}{\partial x_j} - \beta^* k\omega + \frac{\partial}{\partial x_j} \left[\left(\nu + \sigma^* \nu_T \right) \frac{\partial k}{\partial x_j} \right] \tag{C.10}$$

Specific Dissipation Rate

$$\frac{\partial \omega}{\partial t} + U_j \frac{\partial \omega}{\partial x_j} = \alpha \frac{\omega}{k} \tau_{ij} \frac{\partial U_i}{\partial x_j} - \beta \omega^2 + \frac{\partial}{\partial x_j} \left[\left(\nu + \sigma \nu_T \right) \frac{\partial \omega}{\partial x_j} \right] \tag{C.11}$$

Auxiliary Relationships and Closure Coefficients

$$\begin{gathered} \alpha = \frac{5}{9} \quad \beta = \tfrac{3}{40} \quad \beta^* = \frac{9}{100} \\ \sigma = \frac{1}{2} \quad \sigma^* = \tfrac{1}{2} \quad \epsilon = \beta^* \omega k \end{gathered} \tag{C.12}$$

The differences between the original 1988 and updated 1998 k-ϵ models are limited to the closure coefficients and auxiliary relationships, and those of the updated 1998 model are as follows:

Auxiliary Relationships and Closure Coefficients

$$\begin{gathered} \alpha = \frac{13}{25} \quad \sigma_k = \sigma_\omega = \tfrac{1}{2} \\ \beta_o = \frac{9}{125} \quad \beta_o^* = 0.09 \\ \beta = \beta_o f_\beta \quad \beta^* = \beta_0^* f_{\beta^*} \\ \chi_\omega = \left| \frac{\Omega_{ij} \Omega_{jk} S_{ki}}{(\beta_o^* \omega)^3} \right| \quad \chi_k = \tfrac{1}{\omega^3} \tfrac{\partial k}{\partial x_j} \tfrac{\partial w}{\partial x_j} \\ f_\beta = \frac{1 + 70\chi_\omega}{1 + 80\chi_\omega} \\ f_{\beta^*} = \begin{cases} 1 & \chi_k \leq 0 \\ \frac{1+680\chi_k^2}{1+400\chi_k^2} & \chi_k \geq 0 \end{cases} \end{gathered} \tag{C.13}$$

where Ω_{ij} and S_{ij} take their usual definitions:

$$\Omega_{ij} = \frac{1}{2} \left(\frac{\partial U_i}{\partial x_j} - \frac{\partial U_j}{\partial x_i} \right), \quad S_{ij} = \tfrac{1}{2} \left(\tfrac{\partial U_i}{\partial x_j} + \tfrac{\partial U_j}{\partial x_i} \right)$$

Aside from the Turbulent Kinetic Energy equation, which remains unchanged from the original model, the formulation of the 2006 model is as follows:

Kinematic Eddy Viscosity

$$\nu_T = k/\tilde{\omega} \qquad \tilde{\omega} = max \left(\omega, \frac{7}{8} \sqrt{\frac{2 S_{ij} S_{ij}}{\beta^*}} \right) \tag{C.14}$$

Specific Dissipation Rate

$$\frac{\partial \omega}{\partial t} + U_j \frac{\partial \omega}{\partial x_j} = \alpha \frac{\omega}{k} \tau_{ij} \frac{\partial U_i}{\partial x_j} - \beta \omega^2 + \frac{\partial}{\partial x_j} \left[(\nu + \sigma \nu_T) \frac{\partial \omega}{\partial x_j} \right] + \frac{\sigma_d}{\omega} \frac{\partial k}{\partial x_j} \frac{\partial \omega}{\partial x_j} \tag{C.15}$$

Auxiliary Relationships and Closure Coefficients

$$\begin{array}{rcc} \beta = \beta_o f_\beta & \beta_o = 0.0708 & \beta^* = 0.09 \\ \sigma^* = \dfrac{3}{5} & \sigma = \frac{1}{2} & \sigma_{do} = \dfrac{1}{8} \\ \alpha = \dfrac{13}{25} & \epsilon = \beta^* \omega k & l = k^{0.5}/\omega \end{array}$$

$$f_\beta = \frac{1 + 85\chi_\omega}{1 + 100\chi_\omega} \quad \chi_\omega = \left| \tfrac{\Omega_{ij}\Omega_{jk}S_{ki}}{(\beta_o^* \omega)^3} \right|$$

$$\sigma_d = \begin{cases} 0 & \frac{\partial k}{\partial x_j}\frac{\partial \omega}{\partial x_j} \leq 0 \\ \sigma_d & \frac{\partial k}{\partial x_j}\frac{\partial \omega}{\partial x_j} > 0 \end{cases} \tag{C.16}$$

C.4.3 Re-normalisation Group Theory (RNG) k-ϵ

Turbulence models are developed upon the assumption of a single dominant characteristic turbulence length scale, and it is at this scale that turbulent diffusion is calculated. However, in reality, all of the scales of motion will make contributions. Re-Normalisation Group (RNG) theory was applied by Yakhot et al. (1992) to the Navier-Stokes equations, as well as enforceable physical requirements such as realisability (positivity) of terms such as the turbulent kinetic energy (K) and the turbulent dissipation rate (ϵ), and also Galilean invariance of the resulting model. This resulted in a model with the same form as the k-ϵ model, but with different constants.

The closure coefficients and auxiliary relationships for the RNG k-ϵ model are given by:

Auxiliary Relationships and Closure Coefficients

$$\begin{array}{rcl} C_{\epsilon 1} = 1.42 & \overline{C}_{\epsilon 2} = 1.68 & C_\mu = 0.085 \\ \sigma_k = 0.72 & \sigma_\epsilon = 0.72 & \beta = 0.0012 \\ \lambda_o = 4.38 & \lambda = \frac{k}{\epsilon}\sqrt{2S_{ij}S_{ji}} & C_{\epsilon 2} = \overline{C}_{\epsilon 2} + \dfrac{C_\mu \lambda^3 (1 - \frac{\lambda}{\lambda_o})}{1 + \beta \lambda^3} \end{array} \tag{C.17}$$

C.4.4 Shear-Stress Transport (SST) k-ω

The Shear-Stress Transport (SST) k-ω model developed by Menter (1994) is a hybrid of the k-ω and the k-ϵ models, with a modification to the definition of the eddy viscosity to account for the effect of the principal turbulent SST. The k-ω model is used in the inner region of the boundary layer while the k-ϵ model is used in the outer region as well as in free shear flows. This hybridisation was developed so as to benefit from superior performance of the original k-ω model within the inner boundary layer region, without its greater sensitivity on free-stream parameters.

The SST k-ω model is as follows:

Kinematic Eddy Viscosity

$$\nu_T = \frac{a_1 k}{\max(a_1\omega, \Omega F_2)} \qquad \Omega = \frac{\partial u}{\partial y}$$
$$F_2 = \tanh\left(arg_2^2\right) \quad arg_2 = \max\left(2\frac{\sqrt{k}}{\beta^*\omega y}, \frac{500\nu}{y^2\omega}\right) \tag{C.18}$$

Turbulent Kinetic Energy

$$\frac{D\rho k}{Dt} = \tau_{ij}\frac{\partial u_i}{\partial x_j} - \beta^* k\rho\omega + \frac{\partial}{\partial x_j}\left[\left(\mu + \sigma_k\mu_t\right)\frac{\partial k}{\partial x_j}\right] \tag{C.19}$$

Specific Dissipation Rate

$$\frac{D\rho\omega}{Dt} = \frac{\gamma}{\nu_t}\tau_{ij}\frac{\partial u_i}{\partial x_j} - \beta\rho\omega^2 + \frac{\partial}{\partial x_j}\left[\left(\mu + \sigma_\omega\mu_t\right)\frac{\partial \omega}{\partial x_j}\right] + 2(1-F_1)\rho\sigma_{\omega 2}\frac{1}{\omega}\frac{\partial k}{\partial x_j}\frac{\partial \omega}{\partial x_j} \tag{C.20}$$

Auxiliary Relationships and Closure Coefficients

$$\begin{aligned} \beta_1 &= 0.075 & a_1 &= 0.31 \\ \beta^* &= 0.09 & \kappa &= 0.41 \\ \gamma_1 = \frac{\beta_1}{\beta^*} &- \sigma_{\omega 1}\kappa^2/\sqrt{\beta^*} & F_1 &= \tanh\left(arg_1^4\right) \\ \sigma_{k1} &= 0.85 & \sigma_{\omega 1} &= 0.5 \\ \beta^* &= 0.09 & \kappa &= 0.41 \\ \beta_2 &= 0.0828 & \sigma_{k2} &= 1.0 \\ \gamma_2 = \frac{\beta_2}{\beta^*} &- \sigma_{\omega 2}\kappa^2/\sqrt{\beta^*} & \sigma_{\omega 2} &= 0.856 \end{aligned}$$

$$CD_{k\omega}\max\left(2\rho\sigma_{\omega 2}\frac{1}{\omega}\frac{\partial k}{\partial x_j}\frac{\partial \omega}{\partial x_j}, 10^{-20}\right)$$
$$arg_1 = \min\left(\max\left(\frac{\sqrt{k}}{0.09\omega y}, \frac{500\nu}{\omega y^2}\right), \frac{4\rho\sigma_{\omega 2}k}{CD_{k\omega}y^2}\right) \tag{C.21}$$

C.4.5 Realisable k-ϵ

The Realisable k-ϵ model was developed to improve upon the Standard k-ϵ model, which is known to have trouble with flows with a high mean shear rate or massive separation due to its tendency to over-predict the eddy viscosity in such situations (Shih et al., 1995).

The Realisable k-ϵ model is as follows:

Eddy Viscosity Equation

$$\begin{aligned}
\nu_T &= C_\mu \frac{k^2}{\epsilon} \\
C_\mu &= \frac{1}{A_0 + A_s \frac{kU^*}{\epsilon}} \\
U^* &= \sqrt{S_{ij}S_{ij} + \tilde{\Omega}_{ij}\tilde{\Omega}_{ij}} \\
\tilde{\Omega}_{ij} &= \Omega_{ij} - 2\epsilon_{ijk}\omega_k \\
\Omega_{ij} &= \overline{\Omega_{ij}} - \epsilon_{ijk}\omega_k
\end{aligned} \tag{C.22}$$

where $\overline{\Omega_{ij}}$ is the mean rate-of-rotation tensor when viewed in a reference frame rotating with angular velocity ω_k. The parameters needed to calculate the above are:

$$\begin{aligned}
A_s &= \sqrt{6}\cos(\phi) \quad & \phi &= \tfrac{1}{3}\arccos\left(\sqrt{6}W\right) \\
W &= \frac{S_{ij}S_{jk}S_{ki}}{\bar{S}^3} & \bar{S} &= \sqrt{S_{ij}S_{ij}}
\end{aligned} \tag{C.23}$$

where S_{ij} takes its usual definition $S_{ij} = \frac{1}{2}\left(\frac{\partial U_i}{\partial x_j} + \frac{\partial U_j}{\partial x_i}\right)$.

Turbulent Kinetic Energy

$$\frac{\partial k}{\partial t} + U_j \frac{\partial k}{\partial x_j} = \frac{\partial}{\partial x_j}\left[\left(\frac{\nu_T \frac{\partial k}{\partial x_j}}{\sigma_k}\right)\right] - \overline{u_i u_j}\frac{\partial U_i}{\partial x_j} - \epsilon \tag{C.24}$$

Dissipation Rate

$$\frac{\partial \epsilon}{\partial t} + U_j \frac{\partial \epsilon}{\partial x_j} = \frac{\partial}{\partial x_j}\left[\left(\frac{\nu_T \frac{\partial \epsilon}{\partial x_j}}{\sigma_\epsilon}\right)\right] + C_1 S\epsilon - C_2 \frac{\epsilon^2}{k + \sqrt{\nu\epsilon}} \tag{C.25}$$

Auxiliary Relationships and Closure Coefficients

$$\begin{aligned}
\frac{\partial k}{\partial t} &= -\epsilon \\
\frac{\partial \epsilon}{\partial t} &= -C_2 \frac{\epsilon^2}{k} \\
C_1 &= \max\left(0.43, \frac{\eta}{\eta + 5}\right) \\
\eta &= \frac{Sk}{\epsilon} \\
C_2 &= 1.9 \\
\sigma_k &= 1 \\
\sigma_\epsilon &= 1.2
\end{aligned}$$

C.5 Stress-Transport Models

C.5.1 Launder-Reece-Rodi (LRR)

Sometimes called the LLR-IP (where IP stands for isotropisation of production), to differentiate it from the LRR-QI (quasi-isotropic), as the most widely known and extensively tested stress-transport models, the ϵ equation based LRR model has been used as the base for many other stress-transport models (Wilcox, 2006).

The LRR model is as follows:

Reynolds-Stress Tensor

$$\overline{\rho}\frac{\partial \tau_{ij}}{\partial t} + \overline{\rho}\tilde{u}_k \frac{\partial \tau_{ij}}{\partial x_k} = -\overline{\rho}P_{ij} + \frac{2}{3}\overline{\rho}\epsilon\delta_{ij} - \overline{\rho}\Pi_{ij} - C_s \frac{\partial}{\partial x_k}\left[\frac{\overline{\rho}k}{\epsilon}(\tau_{im}\frac{\partial \tau_{jk}}{\partial x_m} + \tau_{jm}\frac{\partial \tau_{ik}}{\partial x_m} + \tau_{km}\frac{\partial \tau_{ij}}{\partial x_m})\right] \tag{C.26}$$

Dissipation Rate

$$\overline{\rho}\frac{\partial \epsilon}{\partial t} + \overline{\rho}\tilde{u}_j \frac{\partial \epsilon}{\partial x_j} = C_{\epsilon 1}\frac{\overline{\rho}\epsilon}{k}\tau_{ij}\frac{\partial \tilde{u}_i}{\partial x_j} - C_{\epsilon 2}\frac{\overline{\rho}\epsilon^2}{k} - C_\epsilon \frac{\partial}{\partial x_k}\left[\frac{\overline{\rho}k}{\epsilon}\tau_{km}\frac{\partial \epsilon}{\partial x_m}\right] \tag{C.27}$$

Pressure-Strain Correlation

$$\begin{aligned}\Pi_{ij} = {} & C_1\tfrac{\epsilon}{k}\left(\tau_{ij} + \tfrac{2}{3}k\delta_{ij}\right) - \hat{\alpha}\left(P_{ij} + \tfrac{2}{3}P\delta_{ij}\right) - \hat{\beta}\left(D_{ij} + \tfrac{2}{3}P\delta_{ij}\right) - \hat{\gamma}k\left(S_{ij} + \tfrac{1}{3}S_{kk}\delta_{ij}\right) \\ & + \left[\tfrac{0.125\epsilon}{k}\left(\tau_{ij} + \tfrac{2}{3}k\delta_{ij}\right) - 0.015\left(P_{ij} - D_{ij}\right)\right]\tfrac{k^{3/2}}{\epsilon n}\end{aligned} \tag{C.28}$$

Auxiliary Relationships:

$$P_{ij} = \tau_{im}\frac{\partial \tilde{u}_j}{\partial x_m} + \tau_{jm}\frac{\partial \tilde{u}_i}{\partial x_m}, \quad D_{ij} = \tau_{im}\frac{\partial \tilde{u}_m}{\partial x_j} + \tau_{jm}\frac{\partial \tilde{u}_m}{\partial x_i}, \quad P = \frac{1}{2}P_{kk} \tag{C.29}$$

Updated Closure Coefficients

$$\begin{aligned} \hat{\alpha} = (8 + C_2/11) \quad & \hat{\beta} = (8C_2 - 2)/11 \quad & \hat{\gamma} = (60C_2 - 4)/55) \\ C_1 = 1.8 \quad & C_2 = 0.6 \quad & C_s = 0.11 \\ C_\epsilon = 0.18 \quad & C_{\epsilon 1} = 1.44 \quad & C_{\epsilon 2} = 1.92 \end{aligned} \tag{C.30}$$

Original Closure Coefficients (Launder et al., 1975)

As above except for:

$$\begin{aligned} C_1 = 1.5 \quad & C_2 = 0.4 \\ C_\epsilon = 0.15 \quad & C_{\epsilon 2} = 1.90 \end{aligned} \tag{C.31}$$

C.5.2 Launder Gibson with Wall-Reflection Terms

Pope (2000) describes the Gibson-Launder RSTM model as an extension of the LRR-IP model, discussed previously, to include additional redistribution terms to account for wall reflections, and goes on to explain that these wall reflection terms, although negligible far from the wall, are significant at the near wall for ensuring log-law region behaviour.

Based on the LLR model, Gibson and Launder (1978) proposed additional slow $R_{ij}^{(s,w)}$ and rapid $R_{ij}^{(r,w)}$ pressure-rate-of-strain terms to better account for the pressure-echo or wall-reflection effect. The slow term is given by

$$R_{ij}^{(s,w)} = 0.2\frac{\epsilon}{k}\frac{L}{y}\left[\langle u_l u_m\rangle n_l n_m \delta_{ij} - \frac{3}{2}\langle u_i u_l\rangle n_j n_l - \frac{3}{2}\langle u_j u_l\rangle n_i n_l\right], \tag{C.32}$$

where the turbulence lengthscale L is given by

$$L = \frac{k^{\frac{3}{2}}}{\epsilon}. \tag{C.33}$$

D Turbulence Models: Wall Function Details

Wall Functions

Following is a description of the wall functions used in this study, namely the epsilonWallFunction, continousEpsilonWallFunction, the kRqWallFunction, the omegaWallFunction and the nutkWallFunction.

epsilonWallFunction

Calculates ϵ according to

$$\epsilon = \frac{C_\mu^{0.75} \times k^{1.5}}{\kappa y_d} \tag{D.1}$$

where $C_\mu = 0.09$, $\kappa = 0.41$ are constants and y_d is the distance to the wall.

omegaWallFunction

Calculates ω by blending laminar (viscous region) and log-law (logarithmic region) approximation components as developed by Metner and Esch (2001) and given by

$$\omega = \sqrt{\omega_{vis}^2 + \omega_{log}^2} \tag{D.2}$$

$$\omega_{vis} = \frac{6 \times (\nu_t + \nu)}{\beta y_d^2} \tag{D.3}$$

$$\omega_{log} = \sqrt{\frac{k}{C_\mu^{0.25} \times \kappa y_d}} \tag{D.4}$$

where $C_\mu = 0.09$, $\kappa = 0.41$ and $\beta = 0.075$ are constants and y_d is the distance to the wall.

continuousEpsilonWallFunction

A custom wall function, not included in OpenFOAM$^{\mathrm{TM}}$ by default, created to help eliminate problems caused by overresolving into the viscous region when using the epsilonWallFunction and High-Re turbulence models on cases which impinge on the $y^+ > 30$ wall function limit for High-Re turbulence modelling. Transforms from ω (as calculated using the omegaWalFunction), into ϵ by means of:

$$\epsilon = C_{mu} \times k \times \omega \tag{D.5}$$

kRqWallFunction

The kRqWallFunction for the k R and q variables, is only a place-name-holder and evaluates as though zeroGradient type boundary condition.

nutkUSpaldingWallFunction

The nutUSpaldingWallFunction calculates turbulent (kinematic) viscosity using Spalding's law of the wall to evaluate y^+ as given by

$$y^+ = u^+ + \frac{1}{E} \times (exp(u^+\kappa) - 1 - u^+\kappa - \frac{(u^+\kappa)^2}{2} - \frac{(u^+\kappa)^3}{6}) \tag{D.6}$$

where $\kappa = 0.41$ and E and are respectively the von Karman constant and integration constant based on the wall's roughness. The term inside the bracks in Equation D.6 is the exponential function minus the first 4 terms of its Taylor-series expansion; more terms may be used if greater accuracy is required.

nutkWallFunction

The nutkWallFunction calculates turbulent (kinematic) viscosity by using turbulent kinetic energy (k) to evaluate y^+ as given by

$$y^+ = \frac{C_\nu^{0.25} \times y_d \times \sqrt{k}}{1 + ln(E \times y^+)} \tag{D.7}$$

where $C_\nu = 0.09$, $\kappa = 0.41$ and E and y_d are integration constants based on the wall's roughness and the distance from the wall, respectively.

E Richardson Extrapolation

Although Richardson extrapolation was initially used with grid doubling or halving, Roache (1998) noted that it is not limited to such, and that for arbitrary solution quantity ϕ that a generalised theory can be expressed as

$$\phi_{exact} \approx \phi_{exacth} + \frac{\phi_{rh} - \phi_h}{r^p - 1} \tag{E.1}$$

where p is the order of the finite-difference scheme used, ϕ_h is the solution at the initial grid spacing h and ϕ_{rh} is the solution on alternative grid spacing rh where r is the refinement ratio between grids. For example, given a fine grid solution has cell spacing h, and a coarse grid solution spacing $2h$ then the cell refinement ratio $r = \frac{course}{fine} = \frac{2h}{h} = 2$, showing that a refinement ratio of 2 corresponds to explicit halving of cell spacing from the coarse to fine grids in line with normal Richardson extrapolation. The order of accuracy, p, of the solution for quantity ϕ, can be determined using

$$p = \frac{ln|\frac{phi_{rh} - \phi_{r^2h}}{phi_{rh} - \phi_h}|}{ln(r)} \tag{E.2}$$

where ln is the natural logarithm. However it is not sensible for the order of accuracy to exceeed that of the discretisation scheme used, and so the order of accuracy should be limited to that of the discretisation scheme employed if necessary.

Extending Richardson extrapolation, Roache (Roache, 1998) developed the concept of Grid Convergence Index to provide uniform reporting of a grid refinement study. The GCI is defined as

$$GCI = F_s \frac{|\epsilon_h|}{r^p - 1} \tag{E.3}$$

where ϵ_h, the fractional error for the grid with spacing h is in turn defined as

$$\epsilon_h = \frac{phi_h - phi_{rh}}{phi_h} \tag{E.4}$$

and F_s is a safety factor, an appropriate value for which for a three grid study is 1.25, and a GCI result of less than 5% is generally considered sufficient (Wilcox, 2006).

To evaluate a Richardson extrapolation value the convergence conditions of the system must be first determined and these convergence conditions are;

- $R < -1$: oscillatory divergence
- $-1 < R < 0$: oscillatory convergence
- $R = 0$: converged
- $0 < R < 1$: monotonic convergence
- $R > 1$: divergence

where R is the convergence ratio and given by

$$R = \frac{phi_h - phi_{rh}}{phi_{rh} - phi_{r^2h}} \tag{E.5}$$